INFLUENCE OF CLIMATE CHANGE ON HYDROLOGICAL DROUGHT IN THE VOLTA RIVER BASIN, WEST AFRICA

BY

ODOOM PETER ROCK EBO

(MET/19/3756)

October, 2023

INFLUENCE OF CLIMATE CHANGE ON HYDROLOGICAL DROUGHT IN THE VOLTA RIVER BASIN, WEST AFRICA

BY

ODOOM PETER ROCK EBO

B.Sc. (Agricultural Engineering),

MTech (Climate Change and Adapted Land Use),

(MET/19/3756)

A Thesis of the Doctoral Research Programme of the West African Climate Systems, under the West Africa Science Service Centre on Climate Change and Adapted Land Use, in the Department of Meteorology and Climate Science submitted to the School of Postgraduate Studies in partial fulfilment of the requirements for the award of the degree of Doctor of Philosophy in Meteorology and Climate Science of the Federal University of Technology, Akure, Nigeria

October, 2023

DECLARATION

I hereby declare that this Thesis was written by me and is a correct record of my own research work. It has not been presented in any previous application for any degree of this or any University. All citations and sources of information are clearly acknowledged by means of references.

Candidate's Name: ODOOM, Peter Rock Ebo

Signature: Date

CERTIFICATION

We certify that this Dissertation ENTITLED "Influence of Climate Change on Hydrological Drought in the Volta River Basin" is the outcome of the research carried out by ODOOM, Peter Rock Ebo under the WASCAL DRP-WACS in the Department of Meteorology and Climate Science of the Federal University of Technology, Akure.

Prof. P. G. Oguntunde **……**

(Major Supervisor) Signature Date

Department of Agricultural & Environmental Engineering
Federal University of Technology,
Akure, Nigeria

Prof. I. A. Balogun **……**

(Co-Supervisor) Signature Date

Department of Meteorology and Climate Science
Federal University of Technology,
Akure, Nigeria

Prof. B. J. Abiodun **……**

(Advisor) Signature Date

Department of Environment and Geographical Science
University of Cape Town,
South Africa

Prof. Zachariah Debo Adeyewa **……**

(Director) Signature Date

Doctoral Research Program – West African Climate Systems
West Africa Science Service Centre on Climate Change and
Adapted land Use (DRP-WACS),
Federal University of Technology,
Akure, Nigeria

ABSTRACT

This study investigates the influence of climate change on hydrological drought in the Volta River Basin. The specific objectives were to assess; the potential impacts of climate change on meteorological drought over the basin, the ability of the SWATplus model in simulating the water balance of the basin, and the impact of future climate on hydrological droughts. The datasets used were the observation data (GMFD and CRU) and projected climate dataset (CMIP6 and NEX-GDDP), a digital elevation model, land use and the FAO digital soil map (2003). The Standardized Precipitation-Evapotranspiration Index at 12- and 24-month scales were used to characterise meteorological drought and the Standardized Streamflow Index (SSFI) for hydrological drought at a 12-month scale. The principal component analysis (PCA) and the wavelet analysis were utilised to assess the spatiotemporal patterns of drought using SPEI computed from GMFD. PCA was also performed on the SPEI of the CMIP6 and NEX-GDDP to determine the spatiotemporal patterns of droughts. The SWATplus was calibrated and evaluated using streamflow records at some selected stations. The calibrated model was employed to assess the future climate change impacts using the ACCESS-CM2 output. The SSFI were then computed using the simulated streamflow output as input data. Results showed that NEX-GDDP model captured the climate of VRB accurately as compared to CMIP6. GMFD and CRU perform reasonably well in the stations evaluated. Four drought modes (DM1 – north, DM2 – south, DM3 – east, and DM4 – west) obtained from 12- and 24-month SPEI explained 85 % and 87 % of variance in the VRB. The wavelet analysis reveals cycles with periodicities ranging from 1–16 years in all DMs which corresponded to periods of drought and wetness. Most CMIP6 and NEX-GDDP models were able to capture the spatial patterns of DM1 and

DM2. The comparison of the CMIP6 and NEX-GDDP model's ability suggests that bias correction can either improve or reduce the models' performance in reproducing the drought modes. Some NEX-GDDP models performed better than the CMIP6 counterpart. Climate change assessment in the VRB suggests an increment in temperature (1–4 °C) and a decrease of 0–2.5 mm/year^2 in precipitation. Most models projected wetter conditions under SSP5-8.5 in the Near term (2021–2050) and Far term (2081–2100) while more precipitation is expected under SSP2-4.5 in the MF (2051–2080). The calibration of the SWATplus model revealed- good performance in Nawuni, Sabari and Saboba with NSE scores of 0.7, 0.68 and 0.81, R^2 of 0.72, 0.69 and 0.91, and Pbias (PBIAS) of -9.1, -1.9 and -18 respectively. Bamboi had a poor NSE (0.101) but good PBIAS (22.7) and R^2 (0.52). The validation statistics were satisfactory for all stations. Projected streamflow show significant increase in the future in line with projected precipitation. Projections indicate reduced drought events and intensities under certain scenarios. Consequently, the VRB is expected to face increased flood risks due to projected increasing streamflow, posing significant threats to agriculture, infrastructure, and human well-being. More efforts should prioritize flood risk management in the VRB to address these challenges.

DEDICATION

This work is dedicated to God Almighty who gave me the strength and inspiration to pursue, persevere and complete this work successfully.

This work is also dedicated to my sweet mom and sisters, Elizabeth Egyir, Joyce Mary Agyemang, Gloria Odoom and Roberta Egyir who have played an instrumental role in my life.

To my brothers, Stephen Adomako and Robert Odoom.

I also dedicate this work to my late father, James Ben Odoom.

ACKNOWLEDGEMENTS

I want to thank God Almighty, the creator of the universe, for aiding and strengthening me to complete this Ph.D. research work. I want to also express my profound gratitude to the Federal Ministry of Education and Research (BMBF), Germany, for fully sponsoring my PhD degree through the West Africa Science Service Centre on Climate Change and Adapted Land Use (WASCAL).

My sincerest appreciation goes to my team of supervisors: the major supervisor, Prof. P.G. Oguntunde; the co-supervisor, Prof. I. A. Balogun; and my advisors, Prof. H. Paeth and Prof. B. J. Abiodun. I am dumbfounded by the immense support, encouragement, productive criticism, comments, and insightful suggestions.

I would like to express my gratitude to the Executive Director and Capacity Building Director of WASCAL, Accra, Ghana. I wish to also express my profound gratitude to the Director of the Doctoral Research Programme (DRP) West African Climate Systems (WACS), Prof. Z. Debo Adeyewa, the Deputy Director, Prof. I. A. Balogun, the Coordinator, Prof. A. Oluleye, and the entire staff of DRP-WACS for their support and coordination towards the successful completion of this program.

I wish to thank the staff of the Department of Meteorology and Climate Science for their encouragement and words of affirmation.

My special thanks go to Prof. B. J. Abiodun for introducing me to the SWATplus working group in the Climate System Analysis Group (CSAG) at the University of Cape Town. This group became my bedrock by assisting in debugging model errors and providing insightful suggestions, which ultimately contributed to the improvement of this research. I express

special thanks to members of this group, especially Dr. Mariam Nguvava, for her supervision, advice, and friendship throughout this period.

I wish to also thank Prof. Wilson A. Agyare and Prof. L. Amekudzi for motivating me to apply and pursue this degree in the first place.

I would like to express my deepest gratitude to my friends, Richard Adade, Andrews Addai, Kojo Adom Quagraine, Dr. Isaac Larbi, Dr. Marian A. Osei, Dr. Enoch Bessah, Dr. Daniel Kwawuvi, Dr. Derrick K. Danso, Dr. Gloria C. Okafor, Dr. Eric Mortey, Dr. Paul M. Iboko, and Dr. Ragatoa S. Dakega, for their constant encouragement, technical support, and always checking up on me.

I would like to acknowledge my colleagues; Gildas Guidigan, Pouwerou Nimon, Assa Tapily, Teeda Njie, Michael Ochei, Laouali Ibrahim Tanimoune, Modou Pouye, Idelbert Behanzin, Boubacar Doumbia and Peace Awoleye. They became a family that I would always cherish and part of my support system.

My profound thanks go to Lt. Col. F. A. K. Tenteh and Major Fred D. Agyemang (in-law) for supporting me and always being there for me. I pray the good Lord blesses you.

Finally, I would like to thank my family for all the help, support, financial aid, and encouragement throughout my life, especially Elizabeth Egyir, Joyce M. Agyemang, Stephen Adomako, Robert K. Odoom, Gloria Odoom, and Ben Odoom.

TABLE OF CONTENTS

LIST OF FIGURES

LIST OF TABLES

LIST OF ACRONYMS

Acronym	Meaning
ACCESS-CM2	Australian Community Climate and Earth System Simulator Climate Model Version 2
ACCESS-ESM	Australian Community Climate and Earth System Simulator Earth System Model
AEJ	African Easterly Jet
AMO	Atlantic Multi-decadal Oscillation
APFM	Associated Programme on Flood Management
BCC-CSM2-MR	Beijing Climate Center (BCC) Climate System Model, medium-resolution version
CanESM5	The Canadian Earth System Model version 5
CCLM	Climate Limited-area Modelling Community
CCZ	Coastal Climatic Zone
CMCC	Euro-Mediterranean Centre on Climate Change
CMIP5	Coupled Model Intercomparison Project Phase 5
CMIP6	Coupled Model Intercomparison Project Phase 6
CO_2	Carbon Dioxide
CORDEX	Coordinated Regional Downscaling Experiment
CRU	Climate Research Unit
CSAG	Climate System Analysis Group
CSFR	Climate Forecast System Reanalysis
CSIRO	Commonwealth Scientific and Industrial Research Organisation

DEM	Digital Elevation Model
DM	Drought Mode
DRP	Doctoral Research Programme
EEA	European Environment Agency
ENSO	El Niño–Southern Oscillation
ESA CCI-LC	European Space Agency Climate Change - Initiative Land Cover
ESGF	Earth System Grid Federation
ESM	Earth System Model
FAO	Food and Agriculture Organization
FCZ	Forest Climatic Zone
FF	Far Future/ Far term
FUTA	Federal University of Technology, Akure
GCM	General Circulation Model / Global Climate Model
GISS	Goddard Institute for Space Studies
GMET	Ghana Meteorological Agency
GMFD	Global Meteorological Forcing Dataset for Land Surface Modeling
GPCP	Global Precipitation Climatology Project
GRACE	Gravity Recovery and Climate Experiment
GRDC	Global Runoff Database Centre
GSWP	Global Soil Wetness Project
HadGEM3	Hadley Centre Global Environment Model version 3
HRU	Hydrological Response Unit
HSD	Hydrological Service Department

INCA	Integrated Catchments model
IPCC	Intergovernmental Panel on Climate Change
ITD	inter-tropical discontinuity
IWRM	Integrate Water Resource Management
KGE	Kling-Gupta efficiency
LSU	Landscape Unit
MF	Mid Future or Mid term
MIROC	Model for Interdisciplinary Research on Climate
MIROC-ES2L	Model for Interdisciplinary Research on Climate, Earth System version 2 for Long-term simulations
MPI	Max Planck Institute
MRI-ESM2	Meteorological Research Institute-Earth System Model Version 2
MSDI	Multivariate Standardized Drought Index
NASA	National Aeronautics and Space Administration
NASM	Northern fringe of the Asian summer mon soon region (NASM) in China
NCEP-NCAR	National Centers for Environmental Prediction - National Center for Atmospheric Research
NESM3	Nanjing University of Information Science and Technology Earth System Model (NESM) version 3
NEX-GDDP	NASA Earth Exchange Global Daily Downscaled Projections
NF	Near Future or Near term
NOAA	National Oceanic and Atmospheric Administration

NCEI	National Centers for Environmental Information
NorESM2	Norwegian Earth System Model version 2
NSE	Nash-Sutcliffe efficiency
PCA	Principal Component Analysis
PEC	Performance Evaluation Criteria
PET	Potential Evapotranspiration
PGF	Princeton
QBO	Quasi-Biennial oscillation
RAPID	Routing Application for Parallel Computation of Discharge
RCM	Regional Climate Model
RCP	Representative Concentration Pathway
RMSE	Root Mean Square Error
RSR	Ratio of RMSE to standard deviation
SCZ	Savannah Climatic Zone
SPEI	Standardized Precipitation Evapotranspiration Index
SPI	Standardized Precipitation Index
SRI	Standardized Runoff Index
SSFI	Standardized Streamflow Index
SSI	Soil Moisture Index
SSP	Shared Socioeconomic Pathway
SST	Sea Surface Temperature
SWAT	Soil & Water Assessment Tool
TEJ	Tropical Easterly Jet

TNA	Tropical Northern Atlantic
TRMM	Tropical Rainfall Measuring Mission
TSA	Tropical Southern Atlantic
ub-pwm	unbiased probability weighted moment
UNEP-GEF	The United Nations Environment Programme - Global Environment Facility
UNESCO	United Nations Educational, Scientific and Cultural Organization
USDA-ARS	United States Department of Agriculture - Agriculture Research Service
VIC	Variable Infiltration Capacity
VRA	Volta River Authority
VRB	Volta River Basin
VRB	Volta River Basin
WEAP	Water Evaluation And Planning System
WMO	World Meteorological Organization

CHAPTER ONE

1.0 INTRODUCTION

1.1 Background

Drought plays a crucial role in the hydrodynamic processes in any basin because it is directly related to precipitation which is one of the key factors that control river flow. Drought is a phenomenon whose signals can be identified as a deficiency in the average and frequency of precipitation usually for a longer period. It is projected that West Africa may experience a significant reduction in the length of the rainy season, longer dry spells and more intense extreme precipitations (Sylla *et al*., 2016). These changes in precipitation might lead to possible severe water shortages or flooding events in West African river basins (Sylla *et al*., 2018). The longer duration of dry spells may transition into droughts (Zhang *et al*., 2015a). This situation will likely adversely affect socio-economic activities such as rainfed agriculture in West Africa. According to Adefisan *et al*. (2007) and Leroux *et al*. (2016), agriculture in West African countries continues to be dominated by rainfall which is the only factor whose onset determines the planting season. The variability in rainfall and increase in mean temperature over West Africa increases the exposure of farmers to the risk of crop failure and loss of capital (Sultan and Gaetani, 2016). According to Nicholson (1979), drought has been a recurring phenomenon since the year 1960 in West Africa. The occurrence of drought generally compromises food security through the destruction of crops, reduces yield and increases in mortality rate of animals; eventually culminating in famine. For instance, droughts occurrence in 1981 to 1983 resulted in poor crop yield as a result of reduced rainfall leading to food insecurity in Ghana (Ofori-Sarpong,

1986). Reduction in groundwater level, surface water shortage, water supply problems, reduction in water quality and saline water intrusion are some known impacts of drought (European Environment Agency, 2015). Causes of meteorological and hydrological drought globally have been linked to global warming, atmospheric circulations such as El-Nino Southern Oscillation (ENSO) (La Nina anomalies), tropical sea surface temperature (SST) triggering La Nina-like conditions over the Tropical Pacific Ocean, SST warming variations on the tropical Atlantic Ocean, Indian Ocean, Land cover changes and local feedbacks (Dai, 2011). Reduction in vegetation cover (such as forest and grassland) plays a significant role during droughts as it affects evaporation and relative humidity and may enhance and prolong droughts activated by tropical SSTs and atmospheric circulations (Dai, 2011).

Forest is generally known to have a direct interaction with rainfall (Sheil and Murdiyarso, 2009). Evapotranspiration produced by forests increases the moisture in the atmosphere. Forest significantly modulates rainfall patterns and atmospheric moisture over land (Ellison *et al*., 2017). Findings by Meher-Homji (1988) suggest that forest cover changes can affect the intensity and number of dry spells of tropical storms. Also, Ellison *et al*. (2017) suggest that deforestation can influence temperature at the local scale leading to changes in rainfall and availability of water as well as the release of carbon into the atmosphere. Afforestation has been suggested to possess the potential to increase precipitation and reduce drought events in the Savanna part of West Africa (Diasso and Abiodun, 2018). Despite the important roles of forests, deforestation continues to be one of the major challenges in West Africa (Cotillon and Tappan, 2016; Kossi *et al*., 2019). Deforestation may contribute to a reduction in rainfall amount and an increase in its variability as well as the consequent impacts on micro-scale hydrology and soil conservation (Meher-Homji, 1991).

Global warming refers to the gradual continuous rise in temperature of the earth system. Global warming is evidence of climate change which is caused by increasing concentration of greenhouse gases in the earth's atmosphere. According to the recent Intergovernmental Panel on Climate Change (IPCC) report, global warming plays a crucial role in shifting climatic zones over many areas globally, leading to the expansion of arid climate zones and the contraction of polar zones (Arneth *et al*., 2019). Thus, global warming may likely cause an increase in the frequency and severity of drought mainly as a consequence of decreased precipitation and increasing evaporation driven by increasing global temperatures (Sheffield and Wood, 2008; Dai, 2011).

The Volta River Basin is an important transnational watershed in West Africa. It is relied upon majorly for agricultural activities, hydropower generation, domestic water supply (Barry *et al.*, 2005) and a rich source of biodiversity (flora and fauna). There are five hydroelectric dams located in the Volta River Basin, namely: Akosombo Dam, which has the largest man-made lake in Africa; Kpong Dam; Bui Hydroelectric Power at Bui Gorge in Ghana; Bagre Dam; and Kompienga in Burkina Faso. The basin provides hydrological and ecosystem services to more than 30 million inhabitants (Liersch *et al*., 2023). In light of the importance of the basin, global warming poses a serious threat to the occurrence of drought and other extreme events in the future.

General Circulation Models (GCMs) are useful tools which have been applied to study climate systems, weather forecasting and understanding climate change effect on the atmospheric composition in the climate systems (Ford *et al.*, 2010; Zhou *et al.* 2013; Mechoso and Arakawa, 2015; Miao *et al*., 2016). GCMs application has improved our understanding of the global climate system and influences of atmospheric phenomena such as Southern Oscillation and storm formation (Ghosh and Misra, 2010; Cotton *et al.*, 2011).

GCMs have been a constant feature in the IPCC reports which analyse the impact of climate change on a multisector scale across the globe (Knutti and Sedláček, 2013). Despite these advantages of GCMs, their inability to accurately account for subgrid processes such as the influences of topographic features and small-scale processes (land surface processes, cloud formation and hurricanes) due to the spatial resolution of their grid system introduces uncertainties and biases in their output (Salvi *et al*., 2011; Flato *et al*., 2014; Fang *et al*., 2015). Most of these subgrid processes are parameterised which also introduces some uncertainties in their outputs. Statistical and dynamic downscaling in association with bias correlation approaches have been proposed by several studies to reduce the systematic biases and uncertainties in the GCM outputs (Li *et al.*, 2010; Li *et al*., 2014; Miao *et al*., 2016; Navarro-Racines *et al*., 2020) These downscaling techniques improved the spatial resolution of GCM outputs from their coarser resolution (Brands *et al*., 2011; Gutiérrez *et al*., 2013). For instance, Li *et al*. (2014) applied a joint bias correction technique on precipitation and temperature outputs of the CMIP5 model ensemble and found that the bias correction method was able to improve the distribution of the variables individually, their variances, mean and the correlation between them. In addition, Miao *et al*. (2016) employed bias correlation methods on CMIP5 outputs. Their findings revealed that the modified nonstationary bias correction method substantially reduces the biases in CMIP5 model outputs and corrects the distribution of air temperature and precipitation throughout the validation period thereby reducing the uncertainties in the GCM projections. Also, Navarro-Racines *et al*. (2020) demonstrated that the delta bias correction technique was able to reduce 50 to 70 % of the systematic biases present in the CMIP5 model projections of maximum and minimum temperature and precipitation. The focus of this study is not to evaluate the merits of statistical downscaling over dynamical downscaling methods but to

explore CMIP6 outputs and statistically downscaled CMIP6 datasets to understand drought patterns in the Volta River Basin.

Many studies have highlighted the impact of drought in this basin. Studies such as Bekoe and Logah, (2013) and Oguntunde *et al*. (2017), Oguntunde *et al*. (2020) have investigated the drought characteristics in the Volta River Basin. Nevertheless, it is essential to understand the basin's drought patterns and analyse the ability of GCM models to mimic these patterns. This study aims to spatiotemporal characteristics of historical drought in the Volta River Basin. The study also evaluates how well CMIP6 models and bias-corrected CMIP6 can reproduce the identified drought patterns in the Volta River Basin.

Several studies such as Bekoe and Logah (2013), Ndehedehe *et al*., (2016), Oguntunde *et al*. (2017), Oguntunde *et al*. (2020) and Gebrechorkos *et al*. (2021) have projected that there is a high likelihood of drought occurring in the future in the Volta River Basin. There has not been a lot of studies conducted to improve the knowledge of hydrological drought in the basin. Ndehedehe *et al*., (2016), Oguntunde *et al*. (2017) and Gebrechorkos *et al*. (2021) have sought to provide answers to the influence of climate change on the occurrence of hydrological drought using both GCMs and Regional Climate Models (RCMs). This study seeks to enrich the existing knowledge on the impact of anthropogenic warming on the Volta River Basin using the latest CMIP6 models coupled with a hydrological model that has proven very useful in understanding future drought frequency by applying drought indices (Kang & Sridhar, 2017). Knowledge from this study will be useful to the river basin managers and decision-makers to understand drought modes and plan accordingly to adapt to this extreme event in future

1.2 Statement of the Problem and Justification

Water supports all life processes of plants, animals and humans. As population growth increases worldwide, the demand for water resources and ecosystem services for domestic and industrial usage also increases. In West Africa, the population is estimated to grow from 132.2 million in the year 1980 (Fuwape and Onyekwelu, 2011) to 430 million in 2022 (United Nations, Department of Economic and Social Affairs, Population Division, 2022). These population growths will drive demand for more food and water which may directly lead to intensification and expansion of agriculture. In the quest to increase agriculture production, the forest and natural vegetation are cleared to make way for agriculture expansion in the Sahel, Savannah and Guinea Coast climate zones of West Africa. This phenomenon was observed by Ouedraogo *et al*. (2010) who showed that forest land cover is usually converted to agriculture to increase food production. As forest cover reduces, it may not only impact precipitation characteristics of the area but also the hydrodynamics of the catchment which may likely lead to drought as the microclimatic effect of the trees is gradually lost and might have a feedback effect on agriculture production. Also, this condition can be exacerbated by climate change as anthropogenic-induced CO_2 concentrations can change the fluxes of latent and sensible heat, and evapotranspiration processes which can alter the climate (Oguntunde, 2004).

Climate change poses a major existential threat to hydrological resources which may lead to climate extremes such as floods and droughts. According to Rummukainen (2012), anthropogenic increases in CO_2 will affect the intensity and frequency of extreme weather events such as floods, storms and droughts. This implies that climate change directly or indirectly affects the characteristics of meteorological and hydrological drought in West Africa. West Africa has been projected to be one of the most vulnerable areas on the globe

to the impact of climate change as several economic activities are still reliant on climatic conditions (IPCC, 2007). Climate change is identified as a major cause of precipitation change in West Africa which may likely lead to extreme events such as droughts or floods. Increasing changes in the characteristics of drought could have dire consequences on the availability of food and impact the health and living conditions of human beings, making it imperative to conduct further research to better understand how natural systems and processes are affected by climate change in the future. Apart from agriculture, extreme precipitation events may adversely impact the population (Peirce et al., 2022) in the VRB. Therefore, this study seeks to understand the influence of climate change on drought (meteorological and hydrological) duration, severity and intensity over the Volta River basin in West Africa.

Oguntunde *et al*. (2020) studied meteorological drought in the VRB and suggested the application of hydrological models such as SWAT will enhance understanding of hydrological resources and the response to climate change in the basin. This study will employ the use of the hydrological model and CMIP6 outputs to assess these changes. The outcome of this study will be useful to the basin managers to understand how climate change will affect the hydrodynamics of the basin. This will also provide valuable information to basin managers on how anthropogenic warming may affect the characteristics of droughts in the basin.

1.3 Aim of the Study

The aim of this study was to investigate the influence of climate change on hydrological drought in the Volta River basin.

The specific objectives of this study are to:

i. assess the potential impacts of climate change on meteorological drought over the basin;
ii. examine the performance of the SWATplus Model in simulating the hydrological variables and water balance of the basin; and
iii. assess the impact of future climate on hydrological droughts.

1.4 Research Questions

The study investigates climate change's impact on the characteristics of drought in the Volta River Basin. To achieve the objectives of this study, the following research questions are addressed:

i. What are the spatiotemporal characteristics of meteorological drought in the past and their relationship with climate change in the future?
ii. Can the SWATplus model adequately simulate the hydrology of the Volta River Basin?
iii. How does climate change affect hydrological drought characteristics in the Volta River Basin?

1.5 Innovation

Few studies have applied the new SWATplus model to investigate the hydrological regime of the Volta River Basin as well as study the impact of climate change on streamflow and hydrological drought in the Volta River Basin. In addition, this study provides insight into the projections of meteorological and hydrological drought by the CMIP6 datasets over the Volta River basin. Also, this research investigated the added value of bias correction statistical downscaling of the CMIP6 datasets in understanding the past spatiotemporal characteristics of drought in the VRB.

CHAPTER TWO

2.0 LITERATURE REVIEW

2.1 Definition of Drought

Many authors have tried to define drought. For example, Wilhite and Pulwarty (2017) define drought as an insidious natural hazard that occurs as a result of precipitation deficiency from average or normal amounts that, when extended over a season or longer results in water supplies that are insufficient to meet the demands of human activities and the environment. Droughts are not only dependent on precipitation alone but affected by other climatic factors such as temperature, wind and low humidity which might equally have the same influence or have even more importance than rainfall in some regions (Dai, 2011). Therefore, Sivakumar *et al*. (2011) integrate these factors in defining drought as a normal and natural recurrent climatic feature which results from natural deficiency in precipitation amount over a longer period usually a season or more in length and is also influenced by climatic factors such as high temperature, high winds and low relative humidity which can significantly aggravate drought severity in many regions of the world. Consequently, drought leads to water shortages for human activities and the environment, and further impacts the economic sectors. Drought is also associated timing of the principal season of occurrence, delays in the onset of the rainy season, onset of rains in principal growing crop growth stages and number of rainfall events and its intensity (Sivakumar *et al*., 2011). Generally, four types of droughts have been identified which are agricultural, meteorological, hydrological and socioeconomic droughts (Mishra and Singh 2010). The American Meteorological Society defines the four types of drought:

Meteorological Droughts are defined in terms of the deficiency of precipitation and the duration of this shortfall in precipitation persists.

Agricultural or Soil Moisture Droughts: Agricultural drought occurs as a result of soil moisture deficit and is most commonly applied to non-irrigated agricultural regions. The water demands of plants depend on the weather conditions, the plant type and the growth stage of the plant as well as the soil's physical and biological features.

Hydrological Droughts: Hydrological drought is a broad term which refers to the consistent below-normal levels of water found in lakes, declining wetland areas and decreased river discharge (van Loon, 2015). It takes a longer time for Precipitation deficits to be felt in the hydrological system. As a result, the effects are not concurrent with those in other economic sectors. Where irrigation is required for agriculture, hydrological drought is used to determine agricultural drought. Hydrological drought lags both agricultural and soil moisture drought. The reasons attributed to the occurrence of hydrological droughts are complex since they are not only atmospherically dependent but also involve hydrological processes that feed moisture to the atmosphere and cause storage of water and runoff to streams (Mishra and Singh, 2011).

Socio-economic Droughts: Socio-economic drought is associated with the supply and demand of some economic goods, which are influenced by the elements of the other types of drought.

2.2 Impact of Historical Drought

Over the past few decades, the Earth's climate has become more unbalanced due to the escalation of atmospheric greenhouse gases (Shahbazi, 2015), which continues to manifest itself in the form of extreme events such as drought, floods, heatwaves, aberrant rainfall

regimes, fires and other catastrophic occurrences worldwide (Arora, 2019). Among weather-related disasters, drought is known for its comparatively gradual onset and consequential time-intensive manifestation of damaging effects (Davarpanah *et al*., 2021). Unfortunately, the IPCC (2014) projects climate change to modify the frequency and severity of droughts, causing intensified impacts in certain regions and seasons. In addition, studies like Im *et al*. (2017) and Arora (2019) have lent support to the prevailing scientific consensus that the earth's ecosystems have not only been altered but are also persistently influenced by climate change. As a result, it is anticipated that there will be an augmentation in unusual weather patterns like droughts due to the relationship between water and climate (Leng *et al*., 2015).

Globally, the number and duration of droughts have increased by 29% since the year 2000. Drought affected about 1.4 billion people between 1998 and 2017, resulting in $124 billion in economic losses (United Nations Convention to Combat Desertification, 2022; Cui *et al*., 2023). For instance, the Great U.S. Drought of 2012, which coincided with a heat wave and cost more than $33 billion in damages, was the most severe drought to affect the country since the 1930s (National Oceanic and Atmospheric Administration – National Centers for Environmental Information (NOAA–NCEI), 2018). In addition, the related summer heatwave directly contributed to 123 fatalities (Masters, 2013; NOAA–NCEI, 2018). In the 1900s, Europe experienced 45 major drought events which affected adversely affected millions of people and led to economic losses amounting to about $27.8 billion. In recent times, an annual average of 15 percent of the land area and 17 percent of the population within the European Union has been affected by drought (Guha-Sapir *et al*., 2021; European Environment Agency, 2017). The megadrought in Australia contributed to 'mega-fires from 2019 to 2020 that resulted in the most dramatic loss of habitat for threatened species in

postcolonial history (Wintle *et al*., 2020); about three billion animals were killed or displaced in the Australian wildfires (van Eeden *et al*., 2020; Haque *et al*., 2021; Allard *et al.*, 2023). In the northern fringe of the Asian summer monsoon region (NASM) in China, the severe drought that occurred from 1927 to 1929 led to a drastic reduction in streamflow and water level in the Yellow River and Daihai Lake, respectively (Yang et al., 2014), which consequently resulted in drought-induced famine and diseases and led to the deaths of more than 4 million people in the provinces of Shanxi, Gansu, Ningxia, Qinghai, and Inner Mongolia (Xu et al., 1997, as cited in Yang *et al.*, 2014). In Brazil, drought conditions with a 16-month duration led to the drastic reduction of the Cantareira Reservoir water level to about 5 % of its capacity from the years 2013/2014 to 2014/2015 (Nobre *et al*., 2016; Pattnayak *et al*., 2018).

The African continent is also deemed highly susceptible to droughts owing to the great inconsistency in precipitation (Shiru *et al*., 2020). Regrettably, the majority of countries in the continent have limited adaptive capacity to cope with the impacts of climate change. Recent years have seen a large number of severe droughts, which led to devastating famines and the loss of countless lives in Africa (Masih *et al*., 2014). Historical records show that drought is highly prevalent in Africa experiencing about 44 % of total global drought events which represent more than 300 events reported within 100 years. Sub-Saharan Africa has recently seen the catastrophic effects of climatic disasters increasing in frequency and intensity (Guha-Sapir, *et al*., 2021). In the West African region for instance, drought events have caused numerous deaths and destroyed properties, hampering development and economic development in the region since the major economic activity in the region is rainfed agriculture. In Southern Africa, an escalation in the spatial extent of drought has been experienced since the 1970s (Rouault and Richard, 2005) and remains a risk to water

management and agriculture in the region (Ayugi *et al*., 2022). For instance, Blamey *et al*. (2018) found that more droughts occurred from the 1970s to 2017 than witnessed in the 1950s and preceding years during the summer rainfall season in several regions in South Africa. Severe drought from 2015 to 2018 that occurred in the Western Cape of South Africa adversely impacted the population resulting in the area being classified as a disaster zone (Pienaar and Boonzaaier, 2018; Mahlalela *et al*., 2020).

Several studies investigated Sahel droughts and have however attributed the Sahel drought to factors such as sea surface temperatures (SSTs). For example, Hoerling *et al*. (2006), and Caminade and Terray (2010) studies attributed changes in sea surface temperature (SST) as the main factor affecting Sahel drought decadal-scale and interannual variations. Particularly, a strong relationship was observed between the tropical Pacific and Indian oceans SSTs and inter-hemispheric (north-south) temperature gradients in the tropical Atlantic (Ayugi *et al*., 2022). The north-south SST gradient (the south and north oceans warmed and cooled after 1970) relationship is the underlying factor which induced the Sahel drought on a decadal timeline (Ayugi *et al*., 2022). Bader and Latif (2011) found that the high Indian Ocean SST which could be a residue of the 1983 and 1983 El Nino events had a strong relationship to the Sahel drought of 1983. They also show that the Indian Ocean SST play a crucial role in the rainfall of the West Sahel by regulating the interannual variability of rainfall. Gore *et al*. (2020) examined the impact of ENSO on drought in Southern Africa and found that drought conditions are associated with the strength of the El Nino while La Nina induced wetness over the region. They also found that drought is driven by the weakening of the Walker circulation due to El Nino events across the region while the Atlantic and Indian Oceans influence the intensity and spatial patterns of drought. Drought trends in Northern Africa have been caused by the interaction of complex

processes and feedback mechanisms. Some of these processes are El Nino events, increased vertical thermal instability from the warming troposphere, and changes in the SST of the Atlantic Ocean which can induce low rainfall amounts in the summer months (Dai and Zhao, 2017). Other studies have suggested that Sahel droughts are also driven by the warming of the Atlantic Ocean as well as the Indian Ocean warming. Moulin and Chiapello (2004) also suggested that the impact of aerosol emissions could play a crucial role in the characteristics of droughts in the Sahel.

2.3 Climate Change and Drought

Numerous studies have investigated and affirmed the influence of climate change on drought frequency, duration and severity drought. Climate change possess the ability to alters the behaviour of climatic parameters such as precipitation, temperature and many more. With increasing greenhouse gases in the atmosphere leading to climate change, extreme events are projected to increase concurrently. Studies like Wang *et al*. (2011) investigated the soil moisture drought from 1950 – 2006 in China. Their study illustrates an increasing trend in drought frequency with varying degrees and duration and ascribes climate change as a possible phenomenon inducing that in China. Yuan et al. (2016) found that runoff reduced under a balanced emphasis on all energy sources (A1B) of the Special Report on Emissions Scenarios, leading to fewer hydrological droughts with longer persistence and severity, which will deteriorate the historical hydrological conditions in the Weihe River basin in China. Nosrati *et al*. (2018) studying climate change impacts on the minimum hydrological drought found that climate change will induce more drought events and increase its severity and drought-prone areas in the Atrak River basin in Iran. Zhiña *et al*. (2019) identified that there is variability in the impact of hydrological drought in the

near and far future under RCP 4.5 and 8.5 in the Puate River basin in Ecuador. They discovered that generally the frequency and duration reduce in both the near and future under both RCP 4.5 and 8.5 but the severity of the drought was seen to increase as compared to the baseline period. Some areas in their study area also had drought severity reduced under both scenarios. They recognise the complexity of terrain processes as a factor for the variation and GCM's inability to simulate convective systems as a limitation. Oguntunde *et al*. (2017) studied the characteristics of drought in the Volta River basin and found that the frequency of drought may magnify in the future. The study considered runoff from Regional Climate Models which occurs during precipitation event but does not account for the characteristics and complex processes which influences streamflow in the river basins as streamflow does not depend on precipitation events alone.

2.4 Impact of Land Use Change (Forestation or Deforestation) on Droughts

There are two schools of thought on the interactions of forest cover and precipitation. The first school of thought views forest as a net producer of water and the other considers it as a net user of water in the hydrological cycle. The net producer (supplier) side argues that forest acts as a generator or recycler of water which increases and improves the overall water balance while the net user (demand) side school of thought argues that forest is net users of water which lead to loss of water in the water balance to the atmosphere and advocates for policies to manage and regulate forest cover to maximise streamflow in a region (Bennett and Barton, 2018). Studies like Ellison *et al*. (2017) which champion the net producer side explains that evapotranspiration produced by forest increases the moisture in the atmosphere. Forest has a significant modulating effect on rainfall patterns and

atmospheric moisture over land deforestation increases temperature at the local scale and causes changes in rainfall and water. The net user (demand) side views trees in forest cover as contributing to water loss in catchment through the transpiration process and forests do not have any endearing link to precipitation formation and the concept of relief rainfall is not an inducement of forest cover but rather the relief (mountain) of the land surface (Bennett and Barton, 2018).

Other studies looking to verify the substance of these two claims have gone further to analyse forest influence on rainfall and drought using climate models or climate models coupled with hydrological models. Such studies are Diasso and Abiodun (2018) show that the influence of reforestation over the Savanna region of West Africa could affect drought patterns in future under the RCP 4.5 scenario. Their findings revealed that reforestation reduces temperature and frequency of drought by -0.1 to -0.8 °C and 1 – 2 events per decade respectively over the reforested region and increases rainfall by 0.8 – 1.2 mm/day. They also realised that reforestation also induced feedback in the Sahel by increasing drought frequency by 1 event per decade during the monsoon season. Abiodun *et al*. (2013) investigated the influence of afforestation on climate change and climate extreme events over Nigeria and discovered that afforestation induces positive feedback over afforested areas and coastal regions by enhancing precipitation. They observed the reverse effect over the north-eastern part of the country which enhanced warming and reduced precipitation. Also, they note that more heatwaves and drought are likely to occur in the semi-arid regions and these enhancements of rainfall in the other parts may lead to flooding along the coastal regions. Lawrence and Vandecar (2015) investigated the impact of deforestation on climate and agriculture in the tropics and found that there exists a threshold for deforestation beyond which significant changes in rainfall are observed. Their findings also showed that with

increasing rates of deforestation, a high incidence of heat extremes as a result of the increase in mean temperature and, a decline in rainfall (average and frequency) may occur which will subsequently affect agriculture. Naik and Abiodun (2016) discovered that warming and rainfall increased in the afforested area and induced cooling in different places in the possible future under climate change. They associated the warming to albedo characteristics of forest cover and the cooling to the feedback effect of localised warming induced by the forest cover. This situation induces wetness and dryness in different locations in their study area. They observed that forestation created variation in summer drought frequency suggesting that forestation utilisation as a climate change mitigation option can cause undesirable results. Lima *et al*., 2014 observed that deforestation increased the dry season length while affecting streamflow which eventually led to hydrological drought in some basins in the Amazon forest region in South America. Takata and Hanasaki (2020) studies identified that afforestation increased drought risk during the dry season as a result of the increment in the evaporation process in Chao Phraya. Their study also revealed that afforestation has a less profound impact than climate change and afforestation reduced streamflow during the wet season. They conclude that afforestation aids in flood risk reduction in the wet season. Therefore, consideration must be taken in using afforestation as a mitigation option. Bonnesoeur *et al*. (2019) review of studies relating to forestation impacts on hydrological services in the Andes revealed that generally numerous studies have highlighted that forestation reduces streamflow and water supply downstream but enhances hydrological regulation and reduces erosion in degraded soils. They identified that forestation was associated with high water usage which leads to a decrease in downstream.

2.5 Hydrological Drought in the Volta River Basin

The hydrology of a basin is dependent on spatial variables such as topology, land cover/use and climate inputs. Three challenges emerge when assessing water balances in the Volta River Basin. First, demand for water for power generation has approached the supply stored in the water reservoir. Second, water management would require international or transboundary cooperation as water becomes increasingly scarce. Third, the dam's modulated outflow has a negative impact on downstream water users (Andreini *et al*., 2000; Kasei, 2009).

According to Associated programme on Flood Management (APFM) (2020), the Volta River basin is very vulnerable to water-related disasters due to a lack of mitigation techniques. Over the previous two decades, climate change has contributed to disasters such as floods and droughts which incurred social, economic and environmental losses to almost two million people.

van de Giesen *et al*. (2010) reported that climate models suggest there will be a shift in the onset of the rainy season roughly from April towards May in the Volta basin in the near future. At the same time, the total amount of rainfall and the end of the rainfall season will remain fixed. In a related study, Mul *et al*. (2015) stated that the Volta River Basin is characterized by high seasonal rainfall variability with a distinct dry season during which rivers in the majority of the northern part dry up. Furthermore, the drying up of streams and wells in the communities during the dry season leads to frequent water shortages in the White Volta Basin.

In another study, Gebrechorkos *et al.* (2022) used streamflow data simulated using the Variable Infiltration Capacity (VIC) and vector-based routing (RAPID) modelling system for 10,300 river reaches to assess the changes in drought duration and severity in the Volta

River Basin. They found that drought severity exhibited an increasing trend in the southern part of the basin while decreasing in the northern part of the basin. Furthermore, the trend analysis indicated a general decreasing trend (up to 5% per event) in drought duration in the northeastern part of the basin but showed an increasing trend in the southern parts of the basin.

Oguntunde *et al*. (2006) conducted a study on the hydrological variability and trends in the Volta River Basin over the period 1901–2002. The study showed that the Rainfall variability index in the last three decades over the period 1901-2002 have been drier, with 1983 being the driest year and 1968 being the wettest year. Runoff, on the other hand, has increased significantly at the rate of 0.8 mm/yr^2 or 23 mm/ yr^2 since 1970. Runoff before dam construction was higher (87.5 mm/ yr^2) and varied more, with a coefficient of variation of 41.5% but the runoff post-dam period was 73.5 mm/ yr^2 with a coefficient of variation of 23.9%.

Furthermore, Kasei (2009) reported that the increase in low-flow events in the Volta River Basin will lead to an increase in droughts despite certain regional models projecting an increase in rainfall. This would have a major impact on the agricultural and energy sectors of communities in countries that rely on the Volta River basin for their needs.

2.6 Impact of Climate Change on the Hydrology and Hydrological Drought in the Volta Basin

Various studies have been conducted on the impact of climate change on hydrological drought in the Volta basin. For example, Dembélé *et al*. (2022) evaluated the impact of climate change on water resources in the Volta river basin under three Representative Concentration Pathways (RCP2.6, RCP4.5, and RCP8.5). They reported that although

potential evaporation and air temperature were increasing under the three representative pathways, an increase in the magnitude of soil moisture, total runoff, actual evaporation, groundwater recharge and terrestrial water storage is projected under RCP8.5 scenario. Furthermore, the analysis of high and low flows indicated a potential increased in hydrological drought frequency in the Black Volta under RCP2.6 and RCP4.5 beginning in the mid-21st century. On the contrary, more frequent flooding was projected in the White Volta under RCP8.5 over the 21st century.

In addition, Oguntunde *et al*. (2017) investigated the projected impacts of future climate change on drought in the Volta River Basin, as well as how the drought influences streamflow. They used the Standardized Precipitation Index (SPI) and Standardized Precipitation and Evapotranspiration Index (SPEI) to characterize drought, and the Standardized Runoff Index (SRI) to quantify hydrological drought. Their findings indicated that drought frequency (events per decade) when compared to the present-day episodes may be amplified by a factor of 1.2 in the year 2046–2065 and 1.6 in the year 2081–2100. Furthermore, precipitation was highly sensitive to runoff and a time lag of about 2 to 3 months was observed between stream flow and drought indices in the Volta River Basin.

In another study, Oguntunde *et al*. (2020) investigated the impact of global warming levels on drought characteristics in the Volta River basin and Niger River basin by employing two indices namely the Standardized Precipitation-Evapotranspiration Index (SPEI) and Standardized Precipitation Index (SPI). They found that with Standardized Precipitation-Evapotranspiration Index (SPEI), severe drought frequency and magnitude are projected to increase across all basins (Volta River and Niger River basins), with the increase in consonance with higher global warming levels. On the other hand, the projected changes in severe drought frequency and magnitude are weaker for SPI than for SPEI.

Furthermore, Ndehedehe *et al*. (2016) examined the utility of standard indicators (Standardised Soil moisture index (SSI), standardised precipitation index (SPI), standardised runoff index (SRI), multivariate standardised drought index (MSDI) as well as Gravity Recovery and Climate Experiment (GRACE) to assess the characteristics of drought over the Volta River basin. They found that SPI and SRI showed a nonlinear relationship for wet periods, indicating that river discharge responds slowly to precipitation, especially after a previous extreme dry period. On the other hand, SPI and SSI exhibited a linear relationship with a correlation of 0.63 (that is on a 12-month scale) at a 95% confidence level indicating consistency in observed wet and dry periods.

Yeboah *et al*. (2022) assessed climate projections in the Volta river basin using the CORDEX-Africa climate simulations under the Representative Concentration Pathways (RCPs) 4.5 and 8.5 scenarios. Their findings indicated that the Volta Basin would experience warmer days and night temperatures, as well as frequent drought and extreme precipitation events under RCPs 4.5 and 8.5 scenarios. However, RCP 4.5 showed a relatively lower magnitude of these extremes when compared to RCP 8.5.

According to Kasei (2009), analysis of climate data in the Volta River basin indicated that the months where precipitation exceeds evapotranspiration typically occur in June, July, August, and September. Furthermore, temperature has been increasing over years leading to an increase in evapotranspiration and hence annulling any surplus amount gained from increased rainfall.

McCartney *et al*. (2012) conducted a study utilizing a dynamic regional climate model (CCLM), a hydrological model (SWAT) and a water resource model (WEAP) to evaluate the impact of a downscaled 'middle impact' climate change scenario on existing and planned irrigation and hydropower schemes in the Volta River basin. Their results indicated that,

under a midrange climate change scenario, the CCLM model predicts a 9% decline in the basin-wide mean annual rainfall by 2050 and a 20% decrease by 2100. In addition to an increase in potential evapotranspiration, there would be a 24% and 45% decline in average annual basin flow by 2050 and 2100, respectively.

In a related study, Jin *et al*. (2018) assessed changes in flow in the Volta river system by 2050s and 2090s under the RCP8.5 scenarios by using High-resolution climate scenarios downscaled from three different Global Climate Models to drive the Integrated Catchment Model (INCA). Their findings reported that peak flows during the monsoon months could increase by up to 50% by the 2090s at the Black Volta River outflow and 10% by the 2090s at the Volta Lake outflow. Furthermore, the duration of drought in the Black Volta River may increase until the 2050s, after which overall wetter climatic circumstances may lead to less drought at the end of the century. Also, the future drought duration in Lake Volta is projected to be less frequent due to the climate pattern and long residence time of the lake system. Furthermore, they asserted that the impacts of changing socio-economic scenarios on flow are minor when compared to the impact of climate change.

2.7 Impacts of Climate Change and land use on river basins using Hydrological models

Hydrological models are potent in studying the combined effect of climate change and land use change on streamflow. The output from these models could be used to study the hydrological processes and how these two factors affect the cycle as well as understanding hydrological drought. Zhang *et al*. (2016) coupled a climate model with a hydrological model to study climate change and land use change in the Heihe River Basin located in China. The authors found that climate change was more significantly correlated to the

changes observed as it had enhanced the hydrologic response tremendously as compared to land use alone which was linked to reduced runoff, streamflow and groundwater recharge. The combined effect of both factors produced outputs similar to that obtained from climate change alone. Guo *et al*. (2008) also coupled a climate and hydrological model together and found that annual streamflow correlates with climate change while seasonal streamflow was sensitive to land use change in the Xinjiang River basin located in China. The combined effect produces unique results different from that obtained from land use change or climate change alone which underlined the need to factor both climate and land use changes in assessment studies. Dong *et al*. (2014) reported that runoff is more sensitive to land use change than to climate change in the Jinghe River basin in China using the SWAT model coupled with a sequential cluster and separation approach. Yin *et al*. (2017) applied the SWAT model to investigate the combined effect of climate and land use change on surface runoff and indicated that land use change and climate change influence runoff differently in different decades. They also observed that runoff fluxes are more sensitive to land use change than climate change. These studies have affirmed the capability of hydrological models to quantify changes that occurred as a result of climate and land use change.

From these various reviews above, some effort has been made to analyse the impact of climate change on meteorological and hydrological drought. Especially, studies like Oguntunde *et al*. (2017) and Ndehedehe *et al*. (2016) have explored the impact of climate change using RCMs outputs nested in CMIP5 models. This study will utilise a statistically downscaled and bias correction method on the latest CMIP6 models to enhance current knowledge on climate change's impact on meteorological and hydrological drought in the Volta Basin. This study also aims to evaluate the relationship between meteorological and

hydrological drought. This approach will be applied to this study by coupling the hydrological model (SWATplus) and CMIP6 data outputs.

CHAPTER THREE

3.0 MATERIALS AND METHODS

3.1 Study Domain

The Volta River Basin is a transnational basin shared between six West African countries: Burkina Faso, Ghana, Togo, Benin, La Côte D'Ivoire and Mali (Figure 3.1). The Volta River Basin (VRB) is located in West Africa and lies between longitudes 5° 30' W and 2° E and latitudes 5° 30' N to 14° 30' N (Biney, 2010). The basin has a total surface area of 409,000 km^2 and three main tributaries (Williams *et al*., 2016). The tributaries are the White Volta which takes its source from the northern part of Burkina Faso, the Black Volta which takes its source from the southwestern part of Burkina Faso, and the Oti Basin which originates from the northern part of Benin (Williams *et al*., 2016). The Red Volta is a major tributary to the White Volta in Burkina Faso. The Lower River Basin is found in the south of the VRB. The Black Volta, White Volta and Oti Basin flows into the Lower Volta. Appendix 1 shows a map of the main subbasins found in the VRB. The length of the river is 1850 km flowing southwardly till it empties into the Gulf of Guinea. Most of the catchment lies within Burkina Faso and Ghana with 43 % and 41.6 % of land areas of the Volta River Basin respectively (Volta Basin Authority, 2010; Darko *et al*., 2019). This represents 67 % and 65 % of the total land mass of Burkina Faso and Ghana respectively (Ampomah *et al*., 2008). 6.4 %, 3.1 %, 3.4 and 2.5 % of the VRB lies in Togo, Mali, Benin and Côte D'Ivoire respectively (Barry *et al*., 2005). The Black Volta, Oti and White Volta River Basins contribute 18 %, 20 %, and 25 % respectively to the water stored in the Volta Lake (Kasei, 2009). The Lower Volta and Oti Basins have the highest flow contribution

coefficient to the VRB, even though they have the smallest areas when compared with the Black and White Volta (Table 3.1). The Volta Lake is the largest artificial lake in West Africa. The Volta Lake stores water used for hydropower generation at the Akosombo dam. Bagré, Kompienga, Kpong, and Bui dams are other hydropower generation plants constructed in the VRB. Bui, Bagré and Kompienga dams are reservoir-operated dams. Kpong Dam is a run-of-river hydropower plant located in the Lower Volta south of the Akosombo dam. There are some protected ramsar sites such as *Lac Dem*, *Barrage de Bagré*, *Barrage de la Kompienga*, *Lac Bam* and *La Vallée du Sourou* in Burkina Faso; Keta Lagoon Complex and Songor in Ghana; *Parc National de la Keran* and *Bassin versant Oti-Mandouri* in Togo; and *Zone humide de la rivière Pendjani* in Benin.

The major economic activity of the inhabitants of the VRB is agriculture. About 70 % of inhabitants are dependent on rainfed agriculture (Kuntsmann and Jung, 2005). The demand for water in the Basin has short-up and is driven by hydropower, agriculture, mining, recreation, industrial consumption, transportation and domestic use (Amisigo, 2005; Mul *et al*., 2015). Urbanisation as a result of population growth and some economic activities such as agriculture and mining may lead to pollution that could affect water quality and destruction of ecosystem. Recently, both legal and illegal mining activities within the basin have increased, which if not managed adequately, may cause land degradation, increased sedimentation load and heavy metal pollution.

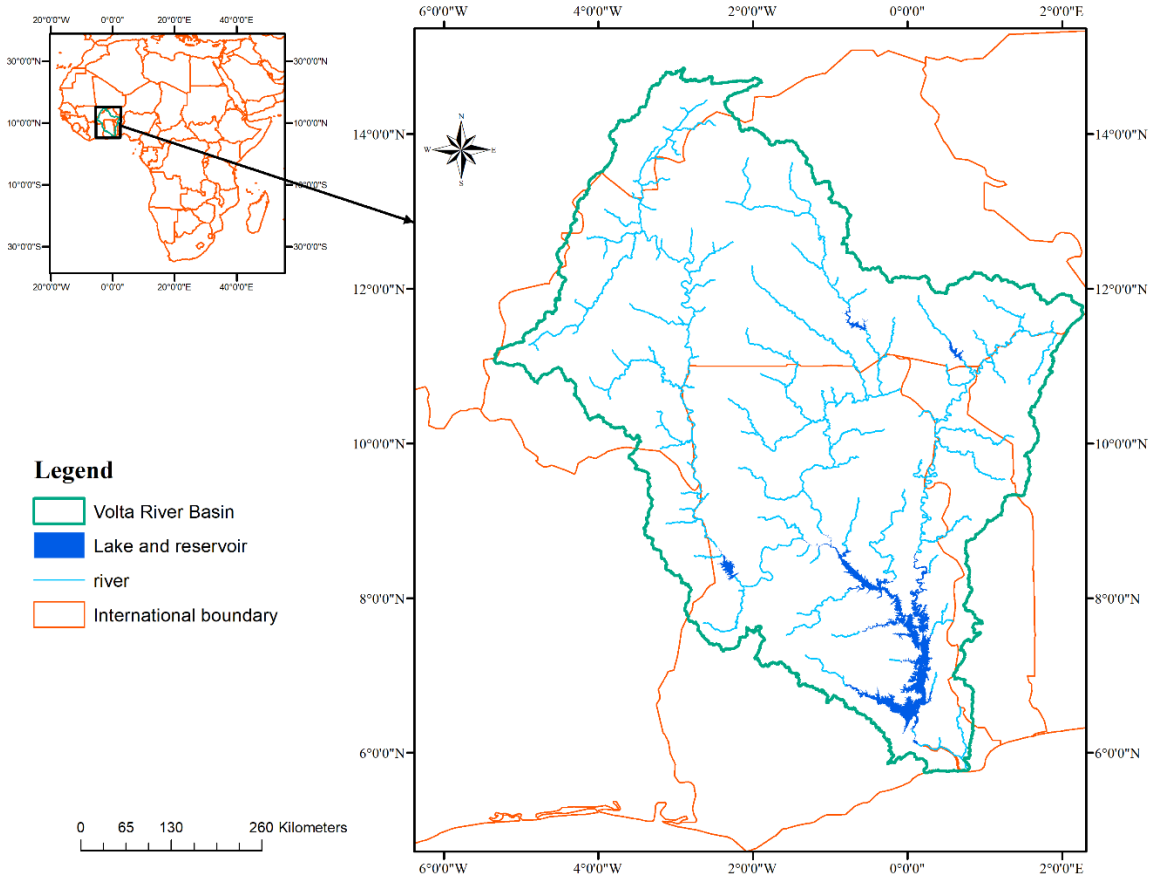

Figure 3.1: Map of the Volta River Basin, West Africa

Table 3.1: Area and annual flow of main tributaries (Subbasins) of the Volta River Basin

Subbasin	Area (km^2)	Mean Annual Flow ($\times 10^6$ m^3)	Flow Coefficient (%)
White Volta (Nawuni)	104,749	7,673	8.3
Black Volta (Bamboi)	149,015	9,565	10.8
Oti (Sabari)	72,778	11,215	14.8
Lower Volta (Senchi)	62,651	9,842	17.0
Total	400,710		

Source: Barry *et al*. (2005)

3.1.1 Climate

Generally, the northern part and a portion of the central part of the VRB are characterized by a mono-modal rainfall pattern from latitude 8 °N where The major rainfall season occurs in June, July and August while December, January and February characterise the dry season also known as *harmattan*. the southern part of the basin experiences a bimodal pattern of rainfall with two major rainfall seasons occurring in May-June-July and August-September-October and a little dry season in August. The West African Monsoon system influences the climate of the basin. The convergence of moist south-westerlies from the Atlantic Ocean and the dry north-easterlies in West Africa forms the Inter-tropical discontinuity (ITD). The migration of the ITD influences moisture influx into West Africa. The ITD, Tropical Easterly Jet (TEJ) and the African Easterly Jet (AEJ) influence rainfall characteristics over the basin (Omotosho and Abiodun, 2007; Gebrechorkos *et al*., 2022). The rainfall follows a north-south gradient where the least amount of rainfall occurs in the north (400 mm/year) and the highest in the south (1600 mm/year) (Obuobie, 2008; Gebrechorkos *et al*., 2022). According to Amisigo (2005) was subdivided into the humid southern zone, the tropical transition zone and the tropical northern zone. These also correspond to the Guinea Savannah, Sudanian Savannah and the Sudano-Sahelian zones (Darko *et al*., 2019). The Guinea Savannah is characterised by 2 rainy seasons which peak in June and September, the Sudano-Sahalien and Sudanian Savannah zones have a mono-modal rainfall season which peaks in August/September (Amisigo, 2005; United Nations Environmental Programme - Global Environment Facility (UNEP-GEF), 2013; Darko *et al*., 2019).

Annual potential evapotranspiration ranges between 1800 mm and 2500 mm in the coastal and the north of the basin respectively. There is a negative deficit between mean monthly rainfall and potential evapotranspiration (Amisigo, 2005).

Temperature also demonstrates a north-to-south gradient where the highest temperature is recorded in the north and the south also records a relatively lower temperature. The mean monthly temperature in the north varies from 36 °C to 27 °C while that of the south varies from 30 °C to 24 °C in March and August respectively (Oguntunde, 2004).

3.1.2 Topography

A greater portion of the elevation of the VRB ranges between 200 m and 300 m with a mean elevation of 257 m (Obuobie, 2008). The highest peak in the VRB is found in the Oti Basin at 920 m (Barry *et al*., 2005). The Akuapem Mountains, Fazao Mountains, Togo Mountains and Atakora Ranges in Benin rise from the sea northeastwards and the Kwahu Plateau extends northwestwards after the Akosombo Gorge (Barry *et al*., 2005). The Banfora Plateau located in Burkina Faso in the Black Volta is another relief that flanks the western part of the VRB (Barry *et al*., 2005).

3.1.3 Geology and soil

Two major geological formations characterize the geology of the Volta River Basin. They are the Proterozoic to Paleozoic ages consolidated sedimentary formations also known as the Voltaian Formation and the Precambrian basement crystalline rocks associated with the West African Shield (Obuobie, 2008; Barry *et al*., 2005; Mul *et al*., 2015). They occupy more than 90 % of the Volta River Basin (Mul *et al*., 2015; Aziz, 2017). The Volta River Basin is comprised primarily of these two geological formations (Figure 3.2). The Precambrian formations in the VRB are also categorized into the Birimian group, Tarkwan, Dahomeyan formation, and Buem and Togo formations (Obuobie, 2008). The Voltaian system comprises the Lower Voltaian (basal sandstone), Middle Voltaian (Obosom and Oti

beds) and the Upper Voltaian formation which are located in the Oti basin and Lower Volta, and the lower part of the Black and White Volta (Mul *et al.*, 2015). Other Voltaian formations are the Quarternary alluvia deposits mostly found around the Volta Lake and the metasediments or volcanic sedimentary located bounded by the Middle Voltaian formation to the west and along the Volta delta, Togo and the northern part of Benin. The tertiary sandstones and the sedimentary formations are localised in the northern part of the Basin. The Precambrian basement crystalline rocks consist of igneous rocks, metamorphic rocks, anorogenic intrusions and granite-gneiss-greenstone rocks (Mul *et al*., 2015; Obuobie *et al*., 2016; Aziz, 2017). The sedimentary formations comprise sandstone, politic schist, shale, mudstones, arkose, dolomitic limestone and conglomerate, sandy and pebbly beds and limestones. The lithology and thickness of the weathered layer of the basement crystalline rocks vary (Martin, 2005; Obuobie *et al*., 2016). The thickness of the weathered layer was due to factors such as the structural properties of the rocks, topography, vegetation, climatic conditions and erosion (Obuobie *et al*., 2016).

The soils of the Volta River Basin are formed as a result of the weathering of the various parent rock types identified in the basin (Andah *et al*., 2003; Obuobie, 2008). Using the Food and Agriculture Organisation and United Nations Educational, Scientific and Cultural Organization (FAO-UNESCO) (1974) soil classification system, eleven dominant soil types were identified in the VRB (Table 3.2). The soils are Acrisols, Arenosols, Cambisols, Fluvisols, Gleysols, Lithosols, Luvisols, Nitosols, Planosols, Regosols and Vertisols. The major soil type identified in the Volta River Basin is the Luvisols (59.896 %) (Obuobie, 2008). Generally, the soils in the northern part of the basin are lower in organic content than the soils found in the south, especially in the forest zones. In the northern part, the soil structure of Luvisols is unstable and has low nutrient content thereby making them highly

susceptible to erosion when the slope gradient is not gentle (Obuobie, 2008). The Regosols (10.609 %) and Lithosols are the next dominant soil types (10.01 %) (Table 3.2) that are located in the northern part of the VRB. Regosols are highly porous and have poor water retention ability. In the VRB, the largest type of Regosols is the Eutric Regosols (Re33-1a-1677) which has a sandy-loam textural class. Aresonols of the VRB are also high in sandy textured with low soil productivity and poor water retention capacity (Appendix 2). Luvic Arenosols (Ql1-1a-1614) which have a sandy textural class are the largest amongst the Arenosols soil types in the VRB (Appendix 2).

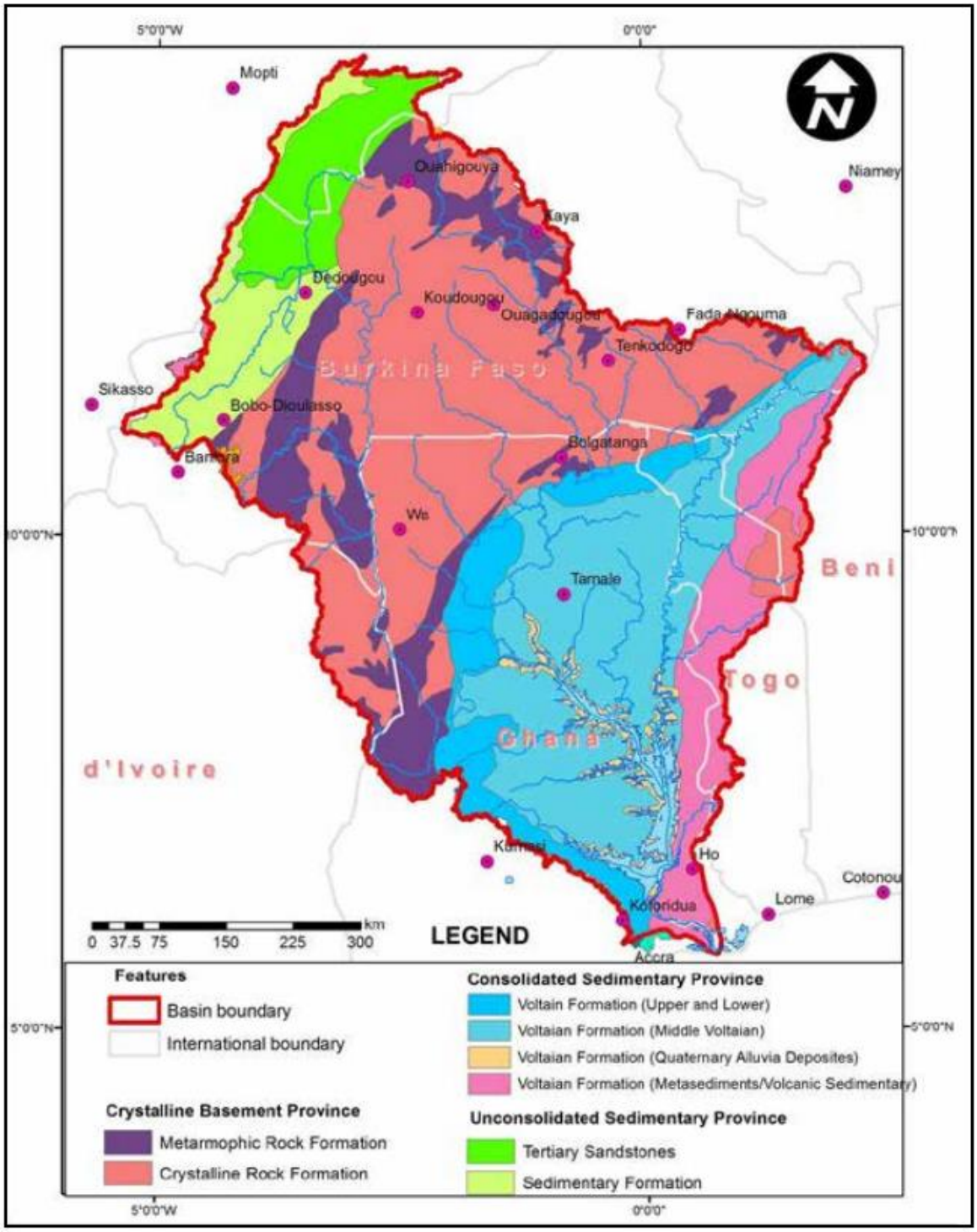

Figure 3.2: Geology map of the Volta River Basin

Source: GLOWA-Volta project, adapted from Mul *et al*. (2015)

Table 3.2: Soil types of the Volta River Basin

Soil Type	**Area Covered (km^2)**	**PERCENTAGE (%)**
Acrisols	7479.045065	1.814
Arenosols	13756.10074	3.337
Cambisols	12353.77977	2.996
Fluvisols	5676.060983	1.377
Gleysols	2604.310329	0.632
Lithosols	41268.30222	10.01
Luvisols	**246942.0414**	**59.896**
Nitosols	5742.838173	1.393
Planosols	4874.734727	1.182
Regosols	43739.05817	10.609
Vertisols	15959.74795	3.871
Water	11886.33947	2.883
Grand Total	412282.359	**100**

Luvisols is the most dominant soil in the VRB (in Bold)

Source: FAO-UNESCO (2003)

3.1.4 Land use/ cover

The VRB is dominated by Savannah land cover (Obuobie, 2008) which is characterised by grasses interspaced by shrubs. According to Obuobie (2008), 86 % of the basin is covered by the savannah, with croplands, wetlands, natural vegetation, built-up and forest cover. The savannah was subdivided into wooded (found in the south) and grassy (found in the north) savannah. The dominant land use in the VRB is agriculture (Obuobie, 2008).

3.2 Data collection

3.2.1 Spatial datasets

The spatial datasets used in this study include the gridded climate variables, soil, land cover, and Digital Elevation Map (DEM). These datasets are required as input into the SWATplus model. A 90m hydrological conditioned DEM was obtained from HydroSHEDS version 1 (http://www.hydrosheds.org). The HydroSHEDS was developed by Lehner *et al*. (2008) and was based on the Shuttle Radar Topography Mission (SRTM) elevation data. The digital soil map from the Food and Agriculture Organisation (FAO, 2003) and a land cover map for the year 1992 were obtained from the European Space Agency's Climate Change Initiative Land Cover project (ESA CCI-LC) (ESA, 2017). The ESA land cover map was reclassified into similar land cover classes found in the SWATplus database using Defourny *et al*. (2017), Reinhart *et al*. (2021) and Tew *et al*. (2022). Sixteen SWATplus land use classes were used for this study. Table 3.3 shows the reclassification of ESA land cover type to correspond to SWATplus land cover types. The spatial datasets used to set up the SWATplus model are illustrated in Figure 3.3.

Table 3.3: Land cover types of the ESA CCI-LC data and its corresponding land cover types in SWATplus Database

ID	ESA Landuse	SWAT+ Landuse	SWAT+ Landuse Long name
10	Cropland, rainfed	AGRR	agricultural_land_row
11	Herbaceous cover	CRGR	cropland/grassland_mosiac
12	Tree or shrub cover	CRWO	cropland/woodland_mosiac
20	Cropland, irrigated or post-flooding	CRIR	irrigated_cropland_and_pasture
30	Mosaic cropland (>50%) / natural vegetation (tree, shrub, herbaceous cover) (<50%)	AGRL	agricultural_land_generic
40	Mosaic natural vegetation (tree, shrub, herbaceous cover) (>50%) / cropland (<50%)	CRWO	cropland/woodland_mosiac
50	Tree cover, broadleaved, evergreen, closed to open (>15%)	FRSE	forest_evergreen
60	Tree cover, broadleaved, deciduous, closed to open (>15%)	FRSD	forest_deciduous
61	Tree cover, broadleaved, deciduous, closed (>40%)	FRSD	forest_deciduous
62	Tree cover, broadleaved, deciduous, open (15-40%)	FRSD	forest_deciduous
70	Tree cover, needleleaved, evergreen, closed to open (>15%)	FRSE	forest_evergreen
71	Tree cover, needleleaved, evergreen, closed (>40%)	FRSE	forest_evergreen
72	Tree cover, needleleaved, evergreen, open (15-40%)	FRSE	forest_evergreen
80	Tree cover, needleleaved, deciduous, closed to open (>15%)	FRSD	forest_deciduous
81	Tree cover, needleleaved, deciduous, closed (>40%)	FRSD	forest_deciduous
82	Tree cover, needleleaved, deciduous, open (15-40%)	FRSD	forest_deciduous
90	Tree cover, mixed leaf type (broadleaved and needleleaved)	FRST	forest_mixed
100	Mosaic tree and shrub (>50%) / herbaceous cover (<50%)	FRST	forest_mixed
110	Mosaic herbaceous cover (>50%) / tree and shrub (<50%)	GRAS	grassland
120	Shrubland	SHRB	shrubland
121	Shrubland evergreen	SHRB	shrubland
122	Shrubland deciduous	SHRB	shrubland
130	Grassland	GRAS	grassland
140	Lichens and mosses	BSVG	barren_or_sparsley_vegetated
150	Sparse vegetation (tree, shrub, herbaceous cover) (<15%)	BSVG	barren_or_sparsley_vegetated

ID	ESA Landuse	SWAT+ Landuse	SWAT+ Landuse Long name
151	Sparse tree (<15%)	BSVG	barren_or_sparsley_vegetated
152	Sparse shrub (<15%)	BSVG	barren_or_sparsley_vegetated
153	Sparse herbaceous cover (<15%)	BSVG	barren_or_sparsley_vegetated
160	Tree cover, flooded, fresh or brackish water	WETF	wetlands_forested
170	Tree cover, flooded, saline water	WETF	wetlands_forested
180	Shrub or herbaceous cover, flooded, fresh/saline/brakish water	WETL	wetlands_mixed
190	Urban areas	URBN	urban
200	Bare areas	BARR	Barren_Land
201	Consolidated bare areas	BARR	Barren_Land
202	Unconsolidated bare areas	BARR	Barren_Land
210	Water bodies	WATR	Water
220	Permanent snow and ice	WATR	Water

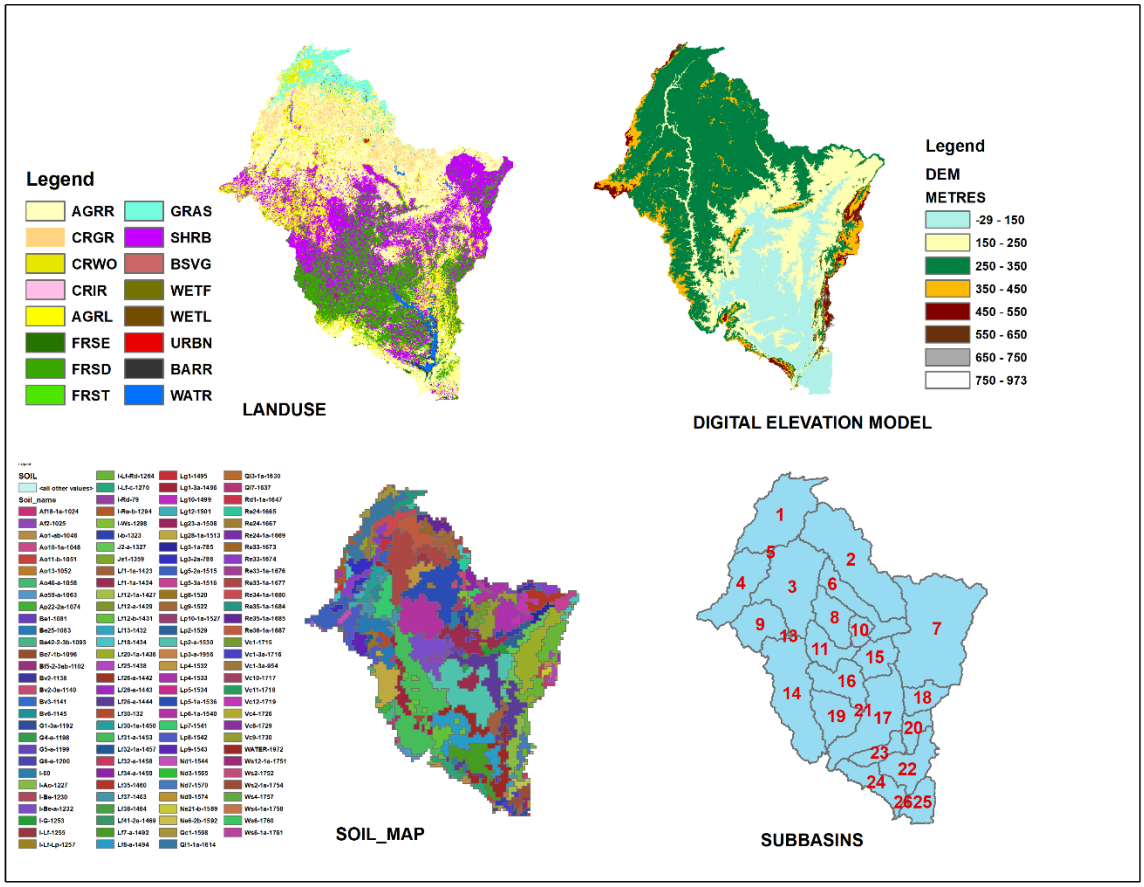

Figure 3.3: Land Cover, Soil map, Digital Elevation Model and Subbasins used in the SWATplus model for the Volta River Basin

3.2.2 Climate datasets

3.2.2.1 Observation Data

Global Meteorological Forcing Datasets for Land Surface Modelling (GMFD) and Ghana Meteorological Agency. The GMFD is a reanalysis dataset published by Sheffield. *et al*. (2006) and is also known as Princeton Global Forcing (PGF) datasets. The GMFD was produced by the combination of the National Centers for Environmental Prediction–National Center for Atmospheric Research (NCEP–NCAR) reanalysis, the World Meteorological Organization (WMO) Solid Precipitation Measurement Intercomparison, Global Precipitation Climatology Project (GPCP) daily product, Climate Research Unit (CRU TS3.0) and Tropical Rainfall Measuring Mission (TRMM) and evaluated against the Global Soil Wetness Project (GSWP-2). The dataset has been updated from 1948-2010 to 1948-2016 at a horizontal resolution of both 0.5° X 0.5° and 0.25° X 0.25° covering the globe between longitude 180 °W to 180 °E and latitude 90 °N to 90 °S, and available at 3-hourly, daily and monthly time steps. In this study, version 3 of the GMFD datasets is used. Precipitation, temperature (Mean, Maximum and Minimum), wind speed, downward shortwave at the surface and Specific humidity.

Historical precipitation data was obtained from the Ghana Meteorological Agency and compared against the precipitation records of the GMFD. Precipitation is highly variable in West Africa therefore it is essential to assess the performance of any gridded spatial datasets against in-situ data. The description of the in-situ data used in this study is shown in Appendix 3. The new agro-climatology zones presented in Bessah *et al*. (2022) was used to classify the in-situ data during the evaluation of the GMFD and CRU precipitation data with GMET precipitation data. Also, the climatic zoning illustrated in Dotse *et al*. (2023)

was used throughout this study. The climatic zones are Guinea Coast (5 – 8 °N), Savanna (8 – 12 °N) and Sahel (12 – 16 °N).

3.2.2.2 Climate change data

The Sixth Model Intercomparison Phase (CMIP6) uses a scenario which integrates the Shared Socioeconomic Pathway (SSP) with Representative Concentration Pathway (RCP) (Meinshausen *et al.*, 2019). The RCPs have been expanded to seven scenarios with forcings 1.9, 3.4 and 7.0 W m−2 added to the already existing forcings (8.5, 6.0, 4.5 and 2.6 W m−2). The various SSPs are SSP1 referring to sustainability (taking the green road), SSP2 is middle of the road, SSP3 is regional rivalry (a rocky road), SSP4 referes to inequality (a road divided) and SSP5 is fossil-fuelled development (taking the highway) (Grose *et al*., 2020). Simulated climate change scenario outputs from the NASA Earth Exchange (NEX) Global Daily Downscaled Projections (GDDP) (Thrasher *et al*., 2022) were downloaded for the study area to study the future occurrence of drought. The future climate years were from 2060 to 2100. The CMIP6 datasets were also downloaded and used for comparison between the NEX-GDDP datasets. The NEX-GDDP datasets are statistically downscaled and bias-corrected CMIP6 datasets using GMFD which is spatially aggregated to the horizontal resolution of the GMFD at 0.25° X 0.25°. The historical, SSP1-2.6, 2-4.5 and 5-8.5 were obtained to conduct this study. A total of 15 global CMIP6 and their NEX-GDDP counterparts were downloaded from Earth System Grid Federation (ESGF) and NASA Earth Exchange (NEX) websites (https://www.nccs.nasa.gov/services/data-collections/land-based-products/nex-gddp-cmip6). Only the historical scenario of the CMIP6 model outputs were downloaded on daily and monthly time steps. Table 3.4 shows the individual models used in this study.

Table 3.4: Description of CMIP6 GCM models used for the study

Model	Institution	Country	Land resolution	Short name	Reference
ACCESS-CM2	Commonwealth Scientific and Industrial Research Organisation (CSIRO)	Austrialia	250 km	ACCESS-CM2 or ACCESS_CM2	
ACCESS-ESM1	Commonwealth Scientific and Industrial Research Organisation (CSIRO)	Austrialia	250 km	ACCESS-ESM1	
BCC-CSM2-MR	Beijing Climate Center	China	100 km	BCC	Wu *et al.* (2019)
CanESM5	Canadian Centre for Climate Modelling and Analysis, Environment and Climate Change Canada, Victoria	Canada	500 km	CanESM5/ CanESM	Swart *et al.* (2019)
GISS-E2-1-G	Goddard Institute for Space Studies (GISS), New York, NY, USA	United States of America	250 km	GISS	Kelley *et al.* (2020)
HADGEM3-GC31-LL	Met Office Hadley Centre, Exeter, Devon, UK	United Kingdom	250 km	HADGEM3-LL / HadGEM_LL	Williams *et al.* (2018)
MIROC6	Japan Agency for Marine-Earth Science and Technology (JAMSTEC), Kanagawa, Japan, Atmosphere and Ocean Research Institute (AORI), The University of Tokyo, Chiba, Japan, National Institute for Environmental Studies (NIES), Ibaraki, Japan, and RIKEN Center for Computational Science, Hyogo, Japan (MIROC)	Japan	500 km	MIROC6	Hajima *et al.* (2020)
MIROC-ES2L	Japan Agency for Marine-Earth Science and Technology (JAMSTEC), Kanagawa, Japan, Atmosphere and Ocean Research Institute (AORI), The University of Tokyo, Chiba, Japan, National Institute for Environmental Studies (NIES), Ibaraki, Japan, and RIKEN Center for Computational Science, Hyogo, Japan (MIROC)	Japan	500 km	MIROC-ES2L/ MIROC_ES2L	Hajima *et al.* (2020)

Model	Institution	Country	Land resolution	Short name	Reference
CMCC-ESM2	Fondazione Centro Euro-Mediterraneo sui Cambiamenti Climatici (CMCC), Lecce, Italy	Italy	100 km	CMCC-ESM2/ CMCC	Lovato *et al.* (2022)
MPI-ESM1-HR	Max Planck Institute for Meteorology (MPI-M), Hamburg, Germany	Germany	100 km	MPI-HR	
MPI-ESM1-LR	Max Planck Institute for Meteorology (MPI-M), Hamburg, Germany	Germany	250 km	MPI-LR	
MRI-ESM2-0	Meteorological Research Institute (MRI), Tsukuba, Ibaraki, Japan	Japan	100 km	MRI	Yukimoto *et al.* (2019)
NESM3	Nanjing University of Information Science and Technology (NUIST), Nanjing, China	China	250 km	NESM3	Cao *et al.* (2018)
NorESM2-LM	NorESM Climate modeling Consortium, Oslo, Norway	Norway	250 km	NorESM2-LM	Seland *et al.* (2020)
NorESM2-MM	NorESM Climate modeling Consortium, Oslo, Norway	Norway	100 km,	NorESM2-MM	Seland *et al.* (2020)

Short name refers to the names the models are renamed in this study

Source: Center for Earth System Research and Sustainability, University of Hamburg

3.2.2.3 Hydrological data

Observed hydrological gauge station records for the VRB were obtained from the Global Runoff Database Centre (GRDC) (https://portal.grdc.bafg.de). The GRDC is a global archived centre which aims to provide hydrological gauge streamflow watersheds across the World. Most of the streamflow records on the GRDC website were obtained from the Hydrological Service Department (HSD) of Ghana. These datasets were used for the calibration and validation of the SWATplus model and also for comparing the outputs. There were a lot of gaps in the datasets and therefore stations like Nawuni, Saboba and Sabari were considered as most suitable on a monthly scale for calibration. The Bamboi gauge records were eventually used to aid in the calibration of the Black Volta despite the amount of missing data in the records. The hydrological gauge stations used in this station are described in Table 3.5.

Table 3.5: Hydrological Gauge Stations Used in the Volta River Basin

Gauge Station	Country	Latitude	Longitude
Bamboi	Ghana	8.15	-2.03
Nawuni	Ghana	9.7	-1.08
Sabari	Ghana	9.28	-0.23
Saboba	Togo	9.76	-0.32

Source: Taylor *et al*. (2006)

3.3 Model Description

The Soil and Water Assessment Tool PLUS (SWATplus or SWAT+) is developed and maintained by the United States Department of Agriculture (USDA) Agricultural Research Service (USDA-ARS) and Texas A&M AgriLife Research which is part of Texas A&M University. SWATplus was developed based on the limitations and challenges faced by the earlier model SWAT after its usage for more than 20 years and throughout many parts of the globe. The principles used in the development of the SWAT model are not changed in the SWAT+ but the input data structure and gives users more flexibility to represent interactions spatially and processes spatially within the catchment or watershed. SWAT+ can model from small watershed to river basin scale by simulating the quantity and quality of surface and groundwater and forecast the impact of land use and land cover, management practices, and climate change on the environment. SWATplus has been developed based on the improvement and challenges faced by the earlier model SWAT. The SWAT model divides the watershed into sub-basins (which is the first level of subdivision). The sub-basins are subdivided into Hydrological Response Units (HRU) based on the land uses, soil and slope distribution in the watershed. The HRU signifies the basic unit of the watershed which is homogenous. The hydrology of the SWAT model is based on the water balance equation. The hydrology of the watershed model is divided into the land phase of the hydrology cycle and the water or routing of the hydrologic cycle. The land phase regulates the sediment, amount of water, pesticides and nutrient loadings of the main channel in each sub-basin. The routing phase comprises the movement of water, sediments, nutrients and pesticides through the main channel (Neitsch *et al*., 2011). Contrary to the SWAT model, the subbasins in the SWATplus are first divided into water areas and Landscape Units (LSUs) which aim to separate upland and floodplain processes and then after subdivided

into HRUs (Bieger *et al*., 2017). The new model improves model processes and interactions and also their spatial representation in the basin than observed in the old SWAT model (Bieger *et al*., 2017). Modelling of water HRUs has always been problematic in the SWAT model as a result of parametrisation and therefore, this issue has been resolved in the new model HRUs (Bieger *et al*., 2017). Additional spatial options that have been incorporated into the new model are water rights, outlets, animal herds, canals and pumps. Also, decision tables have been included in the SWAT+ which simulate the management, reservoir operations and irrigation (Arnold *et al*., 2018). The SWAT+ is more user-friendly and flexible in the spatial definition of processes such as reservoir or pond processing, HRU definition and their interactions. The model equations still remain the same

The basic model equations are described in equations 1 – 4.

The water balance equation is defined below:

$$SW_t = SW_o + \sum_{i=1}^{t}(R_{day} - Q_{surf} - E_a - W_{seep} - Q_{gw}) \qquad (3.1)$$

where SW_t is the soil water content during the beginning or the final stage (mmH_2O), SW_o is the soil water content during the beginning or the initial stage (mmH_2O), R_{day} is the precipitation amount recorded on a day i (mmH_2O), Q_{surf} refers to the surface runoff amount recorded on a particular day i (mmH_2O), t refers to the period (or time) (days), E_a is the recorded evaporation amount on a day i (mmH_2O)), W_{seep} refers to the quantity of water entering the vadose region from the soil profile on day i (mmH_2O), Q_{gw} the return flow amount on day i (mmH_2O)

$$Q_{surf} = \frac{(R_{day} - I_a)^2}{(R_{day} - I_a + S)} \qquad (3.2)$$

where Q_{surf} is accumulated runoff (rainfall excess) in mmH_2O, R_{day} is the rainfall depth

for the day in $\mathrm{mmH_2O}$, I_a is the initial abstraction which includes surface storage ; interception and infiltration before runoff

S is the retention parameter ($\mathrm{mmH_2O}$) which is defined as:

$$S = 25.4\left(\frac{1000}{CN} - 10\right) \tag{3.3}$$

Where CN is the curve number for the day. Ia is commonly given as 0.2S, hence the equation 4 is expressed as:

$$Q_{surf} = \frac{(R_{day} - 0.2S)^2}{(R_{day} + 0.8S)} \tag{3.4}$$

In this equation, runoff is generated when $R_{day} > I_a$. The SCS curve number is a function of the permeability of the soil, land use and antecedent soil condition (Arnold *et al.*, 2011).

3.4 Methods

3.4.1 Methods for Achieving Objective 1

3.4.1.1 Evaluation of GMFD with Ghana meteorological datasets (GMET)

The precipitation records of the GMFD and the GMET were compared with each other. A number of performance evaluation criteria (PEC) were used to assess the relation of the GMFD and GMET datasets. The results were also compared with CRU datasets which has been applied in the Basin by Taylor *et al*. (2006) and Oguntunde *et al*. (2006). The PECs used are the coefficient of determination (R^2), correlation (R), Kling-Gupta efficiency (KGE), Nash-Sutcliffe efficiency (NSE), percent bias (PBIAS), Root mean square error (RMSE) and ratio of RMSE to the standard deviation (RSR).

The PECs were also used during the SWATplus model's calibration and validation.

$$R^2 = \frac{\left[\sum_{i=1}^{n}(Qm_{ob,i} - \overline{Qm}_{ob})(\,Qm_{s,i} - \bar{Q}m_s)\right]^2}{\sum_{i=1}^{n}(Qm_{ob,i} - \bar{Q}m_{ob}\,)^2\ \sum_{i=1}^{n}(Qm_{s,i} - \overline{Qm}_s\,)^2} \quad (3.5)$$

$$NSE = 1 - \frac{\sum_{i=1}^{n}(Qm_{s,i} - Qm_{ob,i}\,)^2}{\sum_{i=1}^{n}(Qm_{ob,i} - Qm_{ob}\,)^2} \quad (3.6)$$

$$PBIAS = 100 \times \frac{\sum_{i=1}^{n}(Qm_{ob} - Qm_s\,)_i}{\sum_{i=1}^{n} Qm_{ob,i}} \quad (3.7)$$

$$\mathrm{KGE} = 1 - \sqrt{(\mathrm{r}-1)^2 + \left(\frac{\mathrm{SD_s}}{\mathrm{SD_{ob}}} - 1\right)^2 + \left(\frac{\bar{\mathrm{Q}}\mathrm{m_s}}{\bar{\mathrm{Q}}\mathrm{m_{ob}}} - 1\right)^2} \quad (3.8)$$

$$r = \frac{\sum_{i=1}^{n}\left(Qm_{ob,i} - \bar{Q}_{ob}\right) \times \left(Qm_{s,i} - \bar{Q}_s\right)}{\sqrt{\left[\sum_{i=1}^{n}\left(Qm_{ob,i} - \bar{Q}m_{ob}\right)^2 \times \sum_{i=1}^{n}\left(Qm_{s,i} - \bar{Q}m_s\right)^2\right]}} \quad (3.9)$$

$$RMSE = \sqrt{\frac{\sum_{i=1}^{n}\left(Qm_{\,s,i} - Qm_{\,ob,i}\right)}{N}} \quad (3.10)$$

$$RSR = \frac{RMSE}{SD_{ob}} \quad (3.11)$$

Where:

Qm_{ob} is the observed streamflow or rainfall ($m^3/_S$), Qm_s is the simulated streamflow or rainfall amount ($m^3/_S$), *i* refers to the time step of the observed and simulated, $\bar{Q}m_{ob}$ is the mean of the observed rainfall or streamflow, $\bar{Q}m_{\,s}$ is the mean of the simulated rainfall or streamflow, *n or N* is the total number of time steps in the data records of the observed and

simulated rainfall or streamflow. SD_s is the standard deviation of the observed and SD_{ob} is the standard deviation of the simulated.

The R^2 ranges from 0 to 1 with the best-fitted model having a value approximately 1 and zero being the worse fitted model. r ranges from -1 to 1. The best r value is one that approaches 1 when comparing models with observed data. NSE ranges from -∞ to 1 with 1 indicating the best-fitted models. The PBIAS ranges from -100 to 100 with the best-fitted model having a value of zero indicating no difference between the observed and simulated datasets.

3.4.1.2 Computation of standardised precipitation evapotranspiration index (SPEI)

SPEI was introduced by Vicente-Serrano *et al*. (2010) to analyse drought characteristics. The SPEI was introduced to overcome the limitation of the Standardised Precipitation Index (SPI) by accounting for water balance. In this study, a three parameter log-logistic distribution was applied to the GMFD datasets. The SPEI package (Begueria *et al*., 2023) was employed in R software to compute SPEI indices spatially. The unbiased probability weighted moment (ub-pwm) which was recommended by Begueria *et al*. (2014) was used as the method for fitting the log-logistics distribution to the climatic water balance (P-PET) outputs. They report that the ub-pwm is able to resolve the problem of no solution and computed SPEI indices computed at different time scales are consistent and with equal variance. The rectangular kernel was used in the computation of the SPEI indices. The log-logistic probability distribution is applied by normalising the water balance. The SPEI was compute at 12- and 24-month scales. The climatic water balance (WB) is computed by the equation below:

$$WB_n^k = \sum_{i=0}^{k-1} P_{n-1} - PET_{n-1} \quad (3.12)$$

The calculated WB values are aggregated at different timescales below

Where P is precipitation, PET is the evapotranspiration, k is the month or timescale of aggregation.

The probability distribution function is given as:

$$F(x) = \left[1 + \left(\frac{\alpha}{x - \gamma}\right)^{\beta}\right]^{-1} \quad (3.13)$$

where α, β and γ refer to the scale, shape and location parameters for $\gamma > x > \infty$ (Begueria *et al*., 2014) and are estimated from WB.

After computing the F(x), the Abramowitz and Stegun (1965) classical approximation is used to compute the SPEI indices.

$$SPEI = W - \frac{C_0 + C_1 W + C_2 W^2}{1 + d_1 W + d_2 W^2 + d_3 W^3} \quad (3.14)$$

$W = \sqrt{-2\ln(p)}$ for $p \leq 0.5$ where $p > 0.5$ then p is replaced by 1-p and the sign reversed (3.15)

p defines the probability of exceedance determined WB_i value and given as p = 1 - F(x) (Vicente-Serrano *et al*., 2012).

where C_0 = 2.515517, $+C_1$= 0.802853, C_2 = 0.010328, d_1= 1.432788, d_2 = 0.189269, and d_3 = 0.001308 (Vicente-Seranno *et al*., 2012).

The SPEI indices were calculated for the GMFD, CMIP6 and NEX-GDDP datasets from 1960 to 2014 during the historical assessment period. For the future estimation of drought indices, the SPEI indices were computed for the NEX-GDDP datasets from 1960 to 2100 using a climatic reference period from 1971 to 2000 on a monthly time step.

3.4.1.3 Computation of Principal Component Analysis (PCA) and wavelet analysis

The Principal component analysis is a dimension-reducing technique that tries to uncover hidden structures in the datasets by summarising them into uncorrelated orthogonal and accounting for the majority of the variance. PCA has been applied by Ujeneza and Abiodun (2015), Oguntunde *et al*. (2020) and Mohammed *et al*. (2022) to SPEI data to understand the spatiotemporal characteristics of drought. In this study, the rotated PCA was employed to understand the spatiotemporal characteristics of drought in the VRB using the computed SPEI indices. The Hargreaves method (Hargreaves and Samani, 1985) of estimating evapotranspiration (PET) was used. Following the approaches of Diasso and Abiodun (2017) and Ujeneza and Abiodun (2015), the first four PCA factors were retained during the computation of the PCA. The first four PCA factors were the dominant factors which had the highest explained variance in the observed SPEI indices of the observed data. The study also applied wavelet analysis to understand the possible atmospheric cycles that control drought and wet events in the VRB. The PCA scores obtained for each factor were detrended and used as input for the wavelet analysis. The Morlet wavelet was used during

the computation of the wavelet power spectrum (Torrence and Compo, 1998; Oguntunde *et al*., 2017).

3.4.1.4 Mann-Kendall trend test and Thiel's Sens slope estimator

The Mann-Kendall (MK) test (Mann, 1945; Kendall, 1975) is a non-parametric test that is used to detect monotonic trends in a dataset. This test has been widely used in environmental science as it does not require the data series to be normally distributed and can also accommodate missing values.

The Mann-Kendall test is computed by the following equations below:

$$S_k = \sum_{i=1}^{N} \sum_{j=i+1}^{N} \text{sgn}(X_j - X_i) \tag{3.16}$$

Where X_j and X_k are sequential data values of length N in years such that k is greater than *i* and where sgn function is defined as:

$$\text{sgn}(X_j - X_i) = \begin{cases} 1 \text{ if } (X_j - X_k) > 0 \\ 0 \text{ if } (X_j - X_k) = 0 \\ -1 \text{ if } (X_j - X_k) < 0 \end{cases} \tag{3.17}$$

The Mann-Kendall statistic's variance is determined using the following formulas under the null hypotheses of no trend and independence of the series:

$$Var(S_k) = \frac{N(N-1)(2N+5) - \sum_{p=1}^{g} t_p(t_p-1)(2t_p+5)}{18} \tag{3.18}$$

g represents the number of tied groups and Where tp refers to the number of data values in the Pth group. If the data series contains tied values, only then is the summing term in the numerator applied. The standard normal test statistic Z_s is calculated using the statistic S_k,

which assumes a normal distribution for samples with n ≥ 10 and sample sizes greater than 10.

$$Z_s = \begin{cases} \dfrac{S_k - 1}{\sqrt{VAR(S_k)}}, \text{for } S_k > 0 \\ 0, \quad \text{for} \quad S_k = 0 \\ \dfrac{S_k + 1}{\sqrt{VAR(S_k)}}, \quad S_k < 0 \end{cases} \tag{3.19}$$

Compute the probability associated with this normalised test statistic. The probability density function for a normal distribution with a mean of 0 and a standard deviation of 1 is given by the following equation:

$$f(Z_s) = \frac{1}{\sqrt{2\pi}} e^{-\frac{Z_s^2}{2}} \tag{3.20}$$

If Z_s is negative and the computed probability exceeds the level of significance, the trend is considered to be decreasing. If the Z_s is positive and the computed probability is above the level of significance, the trend is said to be increasing. There is no trend if the estimated probability is lower than the level of significance.

3.4.1.5 Modified Mann Kendall Test

Autocorrelation or serial correlation in a data series affects the power of the Mann-Kendall test and may increase the likelihood of type 1 error (Yue *et al.* 2004). The method of removing serial correlation proposed by Yue and Wang (2004) was applied to the Mann-Kendall test by using the correction approach of Yue and Wang (2004).

$$Var^*(S_{mk}) = Var(S_{mk}) \times \frac{N}{N^*} \tag{3.21}$$

Where N is the actual sample size of data (ASS), N^* is the effective or equivalent sample size (ESS) and $\frac{N}{N^*}$ is the correction factor for correcting the serial dependence. Additional equations explaining how the effective sample size was obtained is presented in Yue and Wang (2004).

The Theil-Sen's slope estimator has been used to establish the true slope magnitude of the monotonic trend detected by the MK test statistics wherever it is present in the time series. It is a robust method for fitting a line to a time series data by utilising the median of the slopes of all through pairs of two-dimensional sample points. An unbiased median slope estimator approach is used to estimate the magnitude of the trend which was proposed by Sen (1968) and further modified by Hirsch *et al.* (1982). The modified Mann-Kendall and Sen's slope estimates were computed for each spatial grid of the GMFD data. These statistics were also computed for the NEX-GDDP datasets for both the historical and future periods. Future periods were subdivided into Near term (NF) which ranges from the year 2021 to 2050, Mid term (MF) from 2051 to 2080, and Far term (FF) from 2081 to 2100. These time slices of the future were inspired by a simple division based on a 20-year climatology. In this study, a 30-year climatology was utilised in defining the NF and MF while 20 years for FF due to the availability of records. The baseline period (Historical reference) selected was between 1971 to 2000. This was influenced by the availability of GMFD datasets.

3.4.1.6 Runs theory

The runs theory proposed by Yevjevich (1967) was applied to the SPEI drought indices to extract the drought characteristics of both the past and the future. This was used to estimate

the Severity, Intensity, Duration and Return period of drought using the SPEI indices as input. An R software package called drought_features found on GitHub (adrHuerta/ drought_features) and developed by Adrian Huerta was utilised. This package was developed based on the definition of drought characteristics in Le *et al*. (2019) and Ogunrinde *et al*. (2020).

The drought characteristics are defined below:

The focus of this study was to study the moderate to extreme drought event in the VRB which is defined by the SPEI index below -1.

Duration (Du) of an event refers to the duration of a drought event is known as the consecutive months where SPEI indices were below -1.

Cumulative Intensity (CI) refers to the cumulative SPEI indices during the drought event.

Severity (S): It is the cumulative drought intensities during the drought event.

Interarrival time or Return period (T) of droughts is the interval between the start of two successive drought events, regardless of their length, within the same drought where the SPEI is below -1. It covers both the current drought and subsequent non-drought periods.

Intensity (I) of drought refers to the magnitude of drought of a particular month that was below -1.

3.4.2 Methods for Achieving Objective 2

This presents the methods used to achieve objective 2 which aims to calibrate and validate a SWATplus model for the VRB.

3.4.2.1 SWATplus model set-up, calibration and validation

The VRB was subdivided into 26 subbasins, 304 landscape units (LSU), 17909 HRUs and 238 channels. The watershed was delineated with a channel threshold of 141851 sq. km

channel threshold. A shapefile of five reservoirs was created and added to the SWATplus model during the watershed delineation. The DEM inversion method was applied to create the landscape unit in the VRB. Five slope classes were utilised to define slope based on the Canadian Soil Information Service. Slopes of 0 - 4 % represent flat land, 4 – 9 % presents moderate slope, 9 – 15 % represent gentle slope, 15 – 30 % represent steep slope and > 30 % refer to extremely to excessively steep slopes. During the HRU definition, no area filter method was used. From the land cover map utilised in the VRB, 51 % of the land use/cover was associated to agricultural use (CRIR (0.39 %), AGRR (31.84 %), AGRL (7.3 %), CRGR (4.55 %) and CRWO (6.91 %)), 19.1 % was forested land (FRST (0.08 %), FRSD (18.73 %) and FRSE (0.26%)), sparsely vegetated (BSVG) was 0.03 %, Barren or bareland (BARR) 0.02%, and Urban (URBN) was 0.06 %. In the SWATplus editor, the Variable storage flow routing method and the Hargreaves PET method were used after the HRU definition. Also reservoir information was included into the model setup. The Kpong dam was the only run of river dam in the VRB. Reservoir information incorporated in the SWATplus editior are listed in the Table 3.6. The principal spillway volume and area were estimated from reservoir volume and head information obtained from the Volta River Authority (VRA) using appropriate regression equations. The climatic parameters (i.e. temperature, precipitation, wind speed, humidity, and solar radiation) from the GMFD were included into the model. After the above, the SWATplus model was simulated before calibration was performed.

The calibration of the SWATplus model was conducted in the SWAT+ Toolbox software. Calibration was performed on a monthly time step from 1985 to 1995 with the first four years of simulation as warmup years. Validation of the model performed with streamflow records from 1996 to 2002. The Nash-Sutcliffe efficiency was used as the target objective

function during the calibration of the model. The PBIAS and R^2 are the other performance evaluation criteria that were used to evaluate the goodness of fit of the model during calibration and validation. A number of 30 parameters which were related to streamflow, groundwater, management and hydrological response unit were considered. The selection of the parameters was influenced by Obuobie (2008), Aziz (2017) and the SWATplus manual. The sensitivity analysis conducted in this study is presented in the next section.

After calibration and validation, best-fitted parameters were adapted into the model and simulated to obtain streamflow for the period between 1970 and 2005. Also, climatic parameters of the ACCESS-CM2 model were used to simulate streamflow from 1970 to 2100. The streamflow is then used to compute the Standardised Streamflow Index.

Table 3.6: Characteristics of reservoirs found in the Volta in the SWATplus

Reservoir	MORES (month)	IYRES (year)	RES_ESA (ha)	RES_EVOL (*10E4 m3)	RES_PSA (ha)	RES_PVOL (*10E4 m3)	RES_VOL (m3)	Source
Bagre	February	1995	43900	336300	25200	168900	168900	Obuobie (2008)
Kompienga	January	1984	19038.55	190385.49	16555.26	165552.6	165552.6	Generated in SWATplus except MORES and IYRES which were obtained from Sandwidi (2007)
Bui	May	2013	44000	1257000	35000	772000	694800	Aziz (2017)
Akosombo	August	1965	848200	148000000	509179.91	7859571.24	7859571.24	obtained from Volta River Authority (VRA)
Kpong	January	1981	3620.026	36200.26	3147.85	31478.49	165552.6	Generated in SWATplus except MORES and IYRES which were obtained from VRA

MORES = Month the reservoir became operational, IYRES = Year of the simulation the reservoir became operational, RES_ESA = Reservoir surface area when the reservoir is filled to the emergency spillway, RES_EVOL = Volume of water needed to fill the reservoir to the emergency spillway, RES_PSA = Reservoir surface area when the reservoir is filled to the principal spillway, RES_PVOL = Volume of water needed to fill the reservoir to the principal spillway, and RES_VOL = Initial reservoir volume

3.4.2.2 Sensitivity analysis

Sensitivity analysis is used often in environmental science to identify model parameters or parameter sets which have a greater influence on the model output before calibration. This analysis helps to understand which model parameters have significant contributions to the model output (Zhang *et al*., 2015b) and thereby aids in the selection of a considerably small number of parameters as compared with the utilization of all model parameters during calibration. Sensitivity analysis has been widely used in fields, such as risk assessment, economics, engineering and hydrology, and it has become instrumental in the systems pharmacology arena to guide the understanding and development of a complex model. SWAT-CUP has been widely used by most users to perform SWAT model sensitivity analysis, calibration and evaluation. Two methods of sensitivity analysis were performed namely; one-at-a-time sensitivity analysis and global sensitivity. The first sensitivity test was performed before model calibration by varying a particular parameter over a number of simulations. The latter sensitivity analysis was performed after the calibration runs had been completed to measure the sensitive parameters as they vary and interact with each other. In contrast, the SWAT+ Toolbox recommend that sensitivity analysis should be performed before model calibration. In this study, sensitivity analyses were performed before and after calibration was carried out. This was done because the authors recognized that the sensitivity analysis might have no direct impact on model calibration because it could be an independent process like in the SWAT-CUP where it is performed after calibration or before calibration using algorithms like SOBOL, Morris OAT and Fourier Amplitude. Due to the size and computing facility available (Laptop), the recommended number of seeds and sample sizes required to perform the sensitivity analysis in SWAT+ Toolbox was computationally expensive for the whole Volta River Basin. Therefore, this

influenced the decision to use Morris's One-At-Time (OAT) elementary effects screening method (MOAT) approach (Morris, 1991) in R-SWAT to perform global sensitivity analysis after the model had been calibrated. The advantage of the R-SWAT method relies on its ability to enable parallel processing which reduces the computational time significantly. The Morris method uses a one-at-a-time sampling approach where a single parameter is modified at a particular step. The MOAT method was applied with two different repetition times (*r*). In the first analysis an *r* value was set at 4 with a time jump at 3 and level set at 5 to define the intervals in the parameter range which was applied to 35 parameters found in the SWATplus model. The MOAT approach was obtained from the sensitivity package (Iooss *et al.,* 2022) in R software. The repetition times for the second analysis was increased to 20 based on the findings of Gan *et al.* (2014). The determination of sampling combinations which define the number of simulations is based on the expression below:

$$\mathrm{N} = \mathrm{r} \times (\mathrm{p} + 1) \tag{3.22}$$

Where N is the total number of simulations to be performed, r is the repetition times and p is the number of parameters under evaluation. The MOAT approach are illustrated in equation 3.23 to 3.27 as found in Gan *et al*. (2014).

For n-dimension s-level orthogonal point space, where each a_i may take on values from 0, {1/(s-1), 2/(s-1),…,1}. The elementary effect of the *i*th input is defined as m_i.

$$m_i = (f(a_1, \ldots, a_{i-1}, a_i + \Delta, a_{i+1}, \ldots, a_n) - f(a))/\Delta \tag{3.23}$$

Δ is determined by the 1/(s-1). In cases where s is an even number, it is normally = p/[2(p-1)]. The final Morris measures for the *i*th input when the process is repeated *r* times.

$$\mu_i = \sum_{j=1}^{r} \frac{m_i(j)}{r} \tag{3.24}$$

And

$$\sigma_i = \sqrt{\sum_{j=1}^{r} \frac{(m_i(j) - \mu_i)^2}{r}} \tag{3.25}$$

Where μ_i and σ_i define the mean and standard deviation of m_i respectively.

$$\mu_i^* = \sum_{j=1}^{r} \frac{|m_i(j)|}{r} \tag{3.26}$$

For the Morris OAT (MOAT) method, the higher the μ_i (or μ_i^*) value, the more sensitive is input parameter a_i. On the other hand, the higher the standard deviation (σ_i) the more interaction input parameter a_i has with other inputs.

The multi-regression approach employed in SWAT-CUP was also used to detect the parameters which were sensitive. The regression equation is given below.

$$\mathrm{g} = \sum_{i=1}^{m} \beta_i b_i \tag{3.27}$$

g is the average value of the objective function which is the NSE, b_i is the parameter and β_i is the coefficient of the parameter. The Student t-test and the p-value were used to evaluate the sensitivity of a parameter. The more sensitive parameters have a p-value less than 0.05 and a comparably larger Student t-test value (Abbaspour *et al*., 2007).

Finally, the SOBOL algorithm was used to assess the sensitivity of some parameters using the Nawuni streamflow station by creating a small watershed with the SWATplus model as its catchment alone. The creation of the subcatchment of Nawuni significantly reduced the

size and files that would be analysed when using the entire Volta River Basin for the SOBOL analysis. A seed of 50 which corresponds to 2400 sample size was set in the SWAT+ Toolbox software to run this sensitivity analysis. The parameters considered were SCS condition II curve number (cn2), Pothole evaporation coefficient (cn3_swf), Manning's 'n' value for overland flow (ovn), Average slope steepness in HRU in m/m (slope), Average slope length for erosion in m (slope_len), Lateral flow travel time (days) (lat_ttime), Slope length for lateral subsurface flow (lat_len), Lateral soil flow coefficient (latq_co), Maximum canopy storage (canmx), Soil evaporation compensation factor (esco), Plant water uptake compensation factor (epco), Average distance to stream (dis_stream), Soil percolation coefficient (perco), PET coefficient (petco), Depth from soil surface to bottom of layer in mm (z), Moist bulk density (bd), Available water capacity of the soil layer (awc), Saturated hydraulic conductivity in mm/hr (k), Clay content % soil weight (clay), Silt content in % soil weight (silt), Moist soil albedo (alb), Moist soil albedo (alb), Surface runoff lag coefficient (surlag), Channel depth (chd), Channel slope (chs), Channel length (chl), Channel Manning's n (chn), Channel bottom conductivity (chk), Channel clay percent of bank and bed (ch_clay), channel dry bulk density (ch_bd), Channel side slope (chss), Baseflow alpha factor (alpha), maximum daily baseflow when all channels are contributing (bf_max), Minimum aquifer storage to allow return flow in metres (flo_min) and Groundwater "revap" coefficient (revap_co), Threshold depth of water in the shallow aquifer for “revap” or percolation to the deep aquifer to occur (revap_min).

3.4.3 Methods for Achieving Objective 3

Computation of standardised streamflow index (SSFI) and cross correlation analysis

The standardised streamflow index was first introduced by Modarres (2007) which aimed to produce an index based assessment of hydrological drought. The structure and computation of the SSFI was further expanded by Telesca *et al*. (2012). They investigated the appropriate distribution suitable to compute the SSFI and recommended log-logistic distribution. The SSFI follows the computation of the Standardised Precipitation Index (SPI) except that the streamflow records replace the precipitation input in the SPI. The R software package SPEI was applied in computing the SSFI. In this study, the log-logistic distribution was applied. The reference climatic reference period was 1971 to 2000. The SSFI was computed for the simulated historical period from 1960 to 2005 and 1960 to 2100 for the ACCESS-CM2 model.

The Pearson cross-correlation was performed on the SPEI drought indices and the SSFI drought indices to understand the propagation of drought from meteorological to hydrological drought.

CHAPTER FOUR

4.0 RESULTS AND DISCUSSION

4.1 Evaluation of Climate Data with Observation

4.1.1 Evaluation of spatial observation data

Precipitation is arguably the key climatic variable in West Africa that controls economic activities such as Agriculture. Unfortunately, the weather stations in West Africa remain inadequate and poorly distributed. Aside from the spatial distribution, the temporal records of some stations have a considerable percentage of missing data which presents a major challenge when utilising these data records in research studies. Therefore, Precipitation records of GMET, CRU and GMFD were evaluated using some statistical performance criteria. Table 4.1 presents the results of the statistical evaluation computed between the monthly GMET stations' precipitation records and the precipitation records of the two gridded datasets (CRU and GMFD) extracted for each GMET stations. Generally, CRU slightly performs better than GMFD in most of the criteria considered across stations. The two spatial climate datasets performed better in Bole, Wa, Tamale and Yendi, located in the Northern part of Ghana. These stations had the least PBIAS between -4.3 % and 1.3 %, NSE value greater than 0.5, KGE greater than 0.75 and RSR less than 0.7. The two spatial climate datasets performed satisfactorily among the coastal stations (Accra, Takoradi, Axim, Ada Foah and Tema). The computed NSE values for both CRU and GMFD at Accra, Takoradi, Axim and Tema (CRU only) were greater than or equal to 0.5 while that of Ada Foah and Tema (GMFD) were lower than the 0.5 (NSE threshold). KGE values of most of the coastal stations were less than 0.5 except for Accra and Takoradi which had values

greater than 0.5 indicating a good skill of the CRU and GMFD. The percentage bias within the Coastal Climatic Zone (CCZ) ranges between -29.9 and 56.2 % for GMFD and -29.3 and 64.2 % for CRU. The GMFD's highest overestimation of rainfall occurred at Tema (56.2 %) but it was still closer to CRU (53.4 %), and the highest underestimation of rainfall at Axim (-29.9 %) which was also closer to the CRU value of -29.3 %. The CRU's highest overestimation of rainfall occurred at Ada Foah (64.2 %) which was bigger than the 39 % obtained with GMFD at the same location, and the highest underestimation of rainfall at Axim (-29.3 %). Extracted values of stations (i.e. Wenchi, Sunyani, Kumasi, Akim Oda, Koforidua, Akuse, Akatsi and Ho) located in the Forest Climatic Zone (FCZ) of the country showed good skill but their statistics were lower when compared with the stations in the Savanna Climatic Zone (SCZ). In the FCZ, Akatsi, Akim Oda and Akuse which were closer to the CCZ had NSE less than 0.5 for both CRU and GMFD except for Akuse (CRU only). On the contrary, their KGE values were greater than or equal to 0.6 demonstrating a good agreement with the GMET records except for Akatsi. The KGE of the rest of the stations in the FCZ was greater than or equal to 0.67. Both GMFD and CRU NSE values at Koforidua, Kumasi, Sunyani and Wenchi satisfied the 0.5 thresholds. Only NSE values computed with GMFD were lesser than the threshold at Ho (0.49). Majority of the computed percentage bias in the FCZ ranged from -14.5 to 2.9 % for CRU and -15.9 to 1.2 % for GMFD. The Akatsi was the only station with higher PBIAS for both CRU (41.3 %) and GMFD (45.8 %). According to Knoben *et al.* (2019), KGE values do not have an appropriate benchmark but KGE = -0.41 (or 1- $\sqrt{2}$) is an acceptable benchmark rather than using the concept of KGE = 0 (similar to NSE = 0) because they are inherently different. They indicate that any KGE value within the range of $-0.41 < KGE \leq 1$ is acceptable. From the results of Table 4.1, the KGE values computed between the GMET and both CRU and GMFD for all

stations fall within this acceptable range. Even though CRU performed slightly better than GMFD at most of the stations considering all the performance evaluation criteria (PEC) used, GMFD was slightly better than CRU in several stations when certain PECs were considered. For example, comparing RMSE obtained for CRU and GMFD, Ada Foah and Axim were the only stations where GMFD was better than CRU. Also, at Axim, the RSR value of GMFD (0.7) was slightly better than CRU (0.71). The NSE values of GMFD at Ada Foah (0.43) and Axim (0.51) were greater than that of CRU (0.33 for Ada Foah and 0.5 for Axim). PBIAS of GMFD at Ada Foah, Akuse, Kete Krachi, Kumasi, Takoradi and Wa were also slightly better than that of CRU. KGE of GMFD at Ada Foah, Axim, Kete Krachi, Kumasi, Takoradi and Wenchi were also slightly better than that of CRU at the same stations. These results were similar to Hassan *et al.* (2020) who evaluated the performance of Climate Forecast Station Reanalysis (CFSR), CRU and GMFD against in-situ data in the Niger Delta using RMSE, R^2 and Mean Bias Error (MBE) They observed that GMFD and CRU performed better than CFSR. They concluded CRU generally performed slightly better than GMFD. The differences between GMFD and CRU were not huge, therefore GMFD and CRU are good spatial substitutes for GMET stations. GMFD was used in this study because it had been used to downscaled and bias correct the NEX-GDDP CMIP6 datasets.

Table 4.1: Statistical result of performance evaluation criteria used to assess the ability of CRU and GMFD to represent GMET station data

	GMFD						CRU					
Station/ PEC	RMSE	PBIAS %	RSR	NSE	R^2	KGE	RMSE	PBIAS %	RSR	NSE	R^2	KGE
Accra	48.4	37	0.68	0.53	0.63	0.55	42.02	34.8	0.59	0.65	0.73	0.6
Akim Oda	65.14	-15.9	0.78	0.4	0.46	0.6	63.84	-11.2	0.76	0.42	0.5	0.67
Akatsi	67.58	45.8	1.04	-0.09	0.34	0.37	61.45	41.3	0.95	0.1	0.4	0.45
Ada Foah	62.13	39	0.75	0.43	0.52	0.47	67.47	64.2	0.82	0.33	0.6	0.32
Akuse	53.54	1.2	0.74	0.44	0.48	0.66	48.43	2.9	0.67	0.54	0.56	0.72
Axim	112.19	-29.9	0.7	0.51	0.67	0.43	114.37	-29.3	0.71	0.5	0.66	0.41
Bole	57.87	1.3	0.7	0.51	0.59	0.76	51.33	1.3	0.62	0.61	0.66	0.81
Ho	55.86	-8.8	0.71	0.49	0.53	0.69	48.88	-5	0.62	0.61	0.62	0.74
Kete Krachi	61.1	-9.2	0.54	0.71	0.72	0.71	57.33	-10	0.51	0.74	0.77	0.68
Koforidua	53.53	-15.6	0.7	0.51	0.57	0.67	46.47	-14.5	0.61	0.63	0.67	0.71
Kumasi	47.47	-3.5	0.56	0.68	0.69	0.77	46.37	-3.9	0.55	0.7	0.7	0.75
Sunyani	53.12	-0.8	0.68	0.54	0.57	0.75	45.72	0.4	0.58	0.66	0.66	0.77
Takoradi	56.07	20.8	0.62	0.62	0.68	0.72	53	24.3	0.58	0.66	0.72	0.7
Tamale	48.29	-2.9	0.53	0.72	0.73	0.84	37.93	-2.4	0.42	0.83	0.83	0.87
Tema	53.2	56.2	0.79	0.37	0.58	0.38	47.26	53.4	0.71	0.5	0.68	0.43
Wa	42.61	-0.9	0.51	0.74	0.75	0.86	36.18	-4.3	0.43	0.82	0.82	0.86
Wenchi	49.24	-10.1	0.6	0.64	0.67	0.77	44.01	-8.7	0.53	0.71	0.73	0.75
Yendi	49.61	-4.1	0.49	0.76	0.76	0.84	41.86	-2.8	0.42	0.83	0.83	0.84

PEC = performance evaluation criteria, RMSE = Root Mean Square Error, RSR = Root Mean Standard Deviation Ratio, R^2 = coefficient of determination, NSE = Nash-Sutcliffe efficiency, Kling-Gupta efficiency

4.2 Evaluation of Spatiotemporal relationship between Observation and Climate Model Outputs

Annual Precipitation in the Volta River Basin has a North-South gradient where the Southern part records the highest total annual rainfall amount (1200 mm) and the basin's northern part records the least rainfall (Figure 4.1). Generally, the model ensemble of the NEX-GDDP performed slightly better than the CMIP6 model ensemble when compared to the observed (GMFD). The model of the CMIP6 and the NEX-GDDP were able to reproduce the rainfall pattern with correlation values of 0.99 and 1 respectively during the reference period. NEX-GDDP ensemble precipitation records showed a spatial bias of -10 mm to -20 mm throughout the whole basin. In contrast, a positive bias greater than 5 mm in the central and southern parts of the basin was exhibited by the CMIP6 ensemble. Similarly, the northern and eastern parts of the basin had a negative bias greater than -20 mm. High evaporative demand was present in the basin's northern part, which gradually declined southwards in the observation data and the ensembles of both CMIP6 and NEX-GDDP. Both models underestimated the potential evapotranspiration with the largest underestimation occurring in the CMIP6. A -10 mm to 1 mm bias was found in the NEX-GDDP ensemble mean while a bias value between 1 mm to -210 mm in the CMIP6 ensemble mean. Even with these biases, both CMIP6 and NEX-GDDP models have a positive spatial correlation of 0.96 and 1 respectively. The ability of the models to account for the climatic water balance followed similar trends where the statistically downscaled and bias-corrected NEX-GDDP output performed reasonably better than the CMIP6 output (Figure 4.1). NEX-GDDP ensemble models also outperformed CMIP6 model ensemble mean when temperature records were assessed (Figure 4.2). The average, maximum and minimum temperature records of NEX-GDDP had a better spatial pattern with a correlation

value of 1.0 and the least bias as against the CMIP6 ensemble. Taylor's diagram representing the spatial characteristics (normalized spatial standard deviation and pattern correlation) of individual CMIP6 and NEX-GDDP models is illustrated in Figure 4.3. All the NEX-GDDP outputs converge near the observation for all variables (precipitation, average, maximum and minimum temperature). This demonstrated how efficient the bias-correction technique was in improving the model outputs. In contrast, CMIP6 individual models deviate from the observed in all variables assessed. Performing a peer-to-peer assessment, some CMIP6 such as CMCC, MRI, ACCESS-CM2, GISS, NorESM2-LM and HadGEM-LL models were good at simulating the patterns of precipitation (correlation (**r**) ranging from 0.7 to 0.95 and normalised standard deviation (σ) between 0.6 and 1.4). In addition, CMCC, ACCESS-ESM1, ACCESS-CM2, GISS, MPI-LR, MPI-HR, NESM3, MRI and HadGEM-LL also performed better than their peers in simulating spatial patterns of maximum temperature (**r** ranging from 0.8 to 0.95 and σ between 0.6 and 1.4) as compared to the others. Also, CMCC, ACCESS-ESM1, ACCESS-CM2, GISS and HadGEM-LL were better at simulating average temperature (**r** ranging from 0.5 to 0.8 and σ between 0.6 and 1.4). ACCESS-ESM1, ACCESS-CM2, MIROC6, CanESM5, GISS and MIROC-E2SL were relatively better in simulating minimum temperature (**r** ranging from 0.3 to 0.5 and σ between 0.6 and 1.4). ACCESS-CM2 and GISS were the only CMIP6 models that exhibited good performance in all climatic variables evaluated.

The ability of the models in capturing the annual cycle of rainfall was assessed (Fig. 4.4). In general, CMIP6 models capture the unimodal annual cycles of precipitation in the Savannah and Sahel zones in the Volta River Basin (Fig 4.4). As observed in the GMFD, the major rainfall seasons of the Savannah and the Sahel occur between July and September with the peak rainfall recorded in August (Figure 4.4a). This occurs due to the movement

of the intertropical Discontinuity (ITD) to its northmost position (20 – 22 °N) in West Africa in August encouraging moisture advection from the Gulf of Guinea penetrating more inland of West Africa (Omotosho and Abiodun, 2007). In addition, the strength of the African Easterly Jet (AEJ) and Tropical Easterly Jet (TEJ) highly affect rainfall amounts in West Africa (Jung, 2006). A model's ability to capture the influence of these jet streams also enhances its ability to simulate precipitation in West Africa reasonably well. Most CMIP6 models capture the unimodal rainfall pattern in these zones with peak rainfall occurring in August in the Savannah zone. For instance, all models except BCC (in July), MRI (in May) and CanESM5 (in July) have their highest rainfall in the month of August. MRI, GISS, HadGEM-LL and ACCESS-CM2 underestimated rainfall while all other models overestimated the peak rainfall season in the Savannah zone. A similar pattern was seen in the Sahel with NorESM2-MM and MIROC6 overestimating peak rainfall. This result is in agreement with Dotse *et al.* (2023) who also found that NorESM2-MM overestimates precipitation in the VRB. Precipitation pattern in the Guinea Coast zones was characterised by a bimodal pattern with the peaks of the major season and the minor season occurring in June and September respectively.

In the Guinea Coast zone, rainfall exhibits a bimodal pattern with two peak records occurring in June (major season) and September/October (minor season). CMIP6 models; MIROC6, NorESM2-MM and HadGEM-LL captured the bimodal precipitation patterns that are characteristic of the zone but could not capture the characteristics of the rainfall peaks except NorESM2-MM. For instance, MIROC6, NorESM2-MM and HadGEM-LL simulated the two rainfall peaks in July (minor season) and September (major season), June (major season) and September (minor season), and April (minor season) and August (major

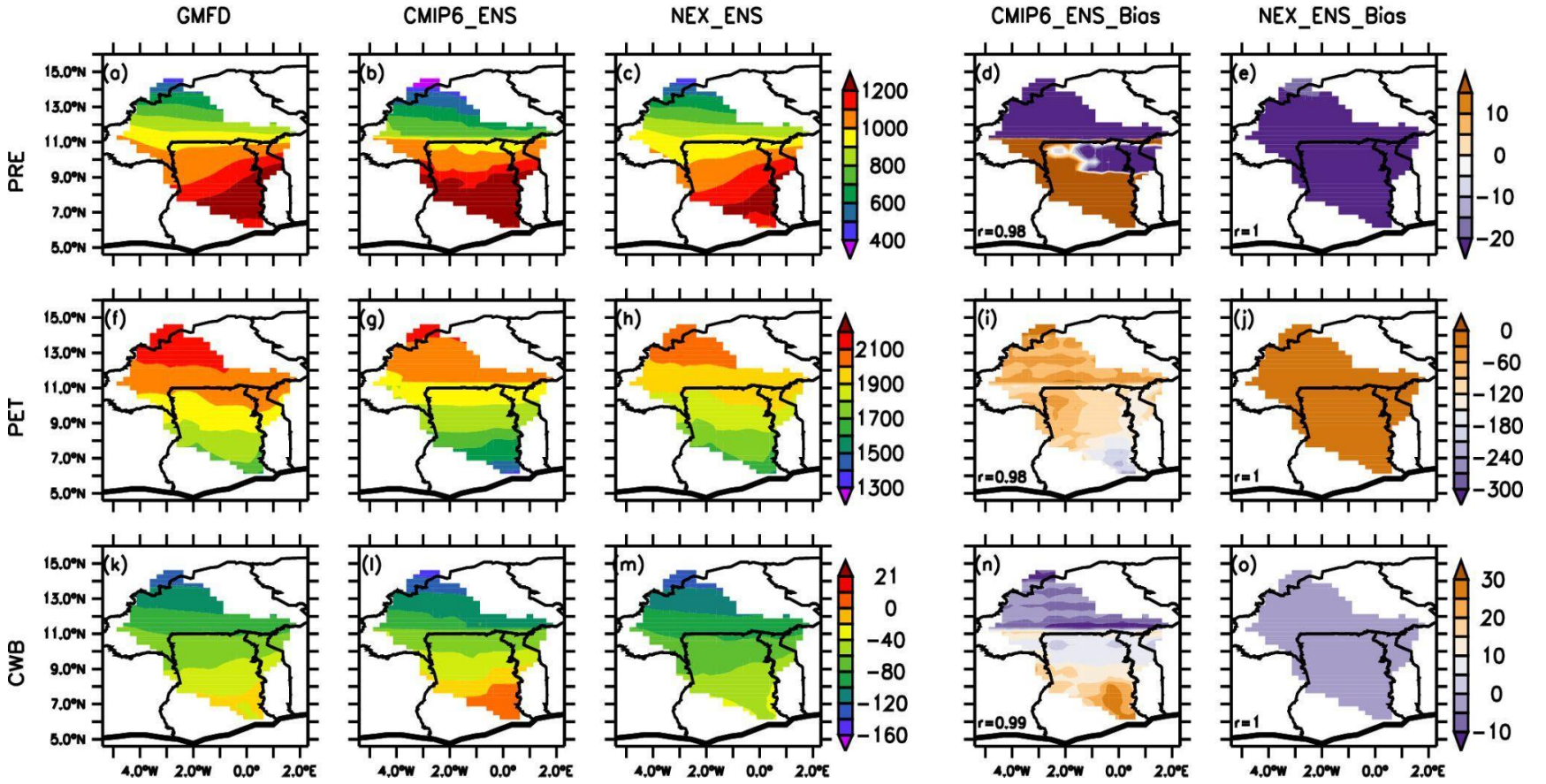

Figure 4.1: Spatial patterns of averaged values from 1960 to 2014 of climatic variables (Precipitation, Potential Evapotranspiration and Climatic Water balance) for Observed (GMFD), CMIP6 model ensembles and NEX-GDDP multi model ensembles

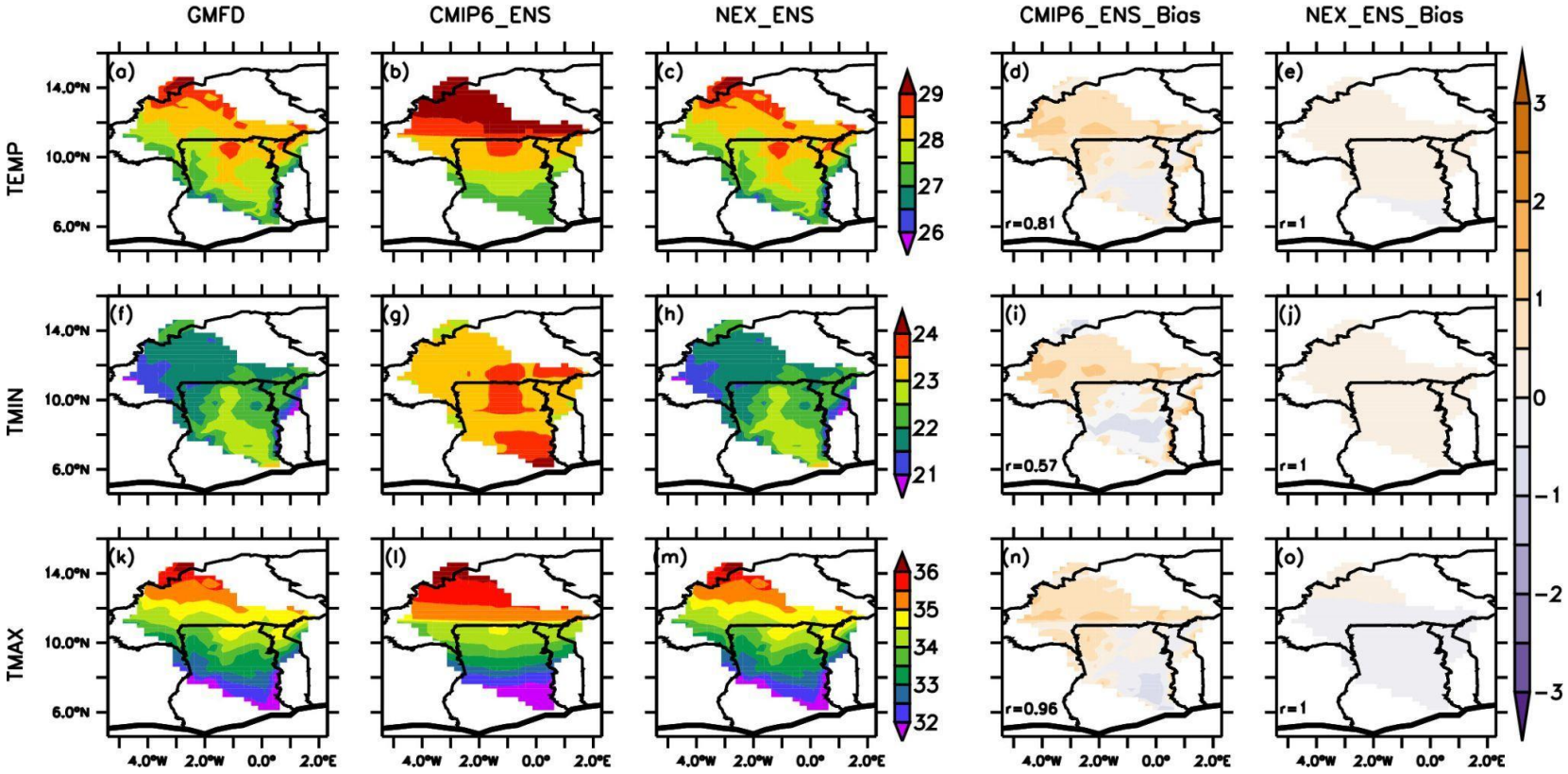

Figure 4.2: Spatial patterns of averaged values from 1960 to 2014 of climatic variables (mean, maximum and minimum temperature) for Observed (GMFD), CMIP6 model ensembles and NEX-GDDP multi-model ensembles

season), respectively. Only NorESM2-MM could correctly capture the bimodal rainfall pattern in the Guinea Coast zone with some overestimation. All CMIP6 models overestimate the minimum temperature during the Northern Hemisphere summer which is also the rainy season in the Volta River basin.

CMIP6 models capture the annual cycle of minimum, average and maximum temperature with either overestimation or underestimation during different months in the year with the peak temperature in some models having a 1-month lag. MIROC6 and NESM3 simulated a higher overestimation and underestimation of maximum temperature than other models in all the climatic zones, respectively. In agreement with the findings of Limantol *et al.* (2023), NorES2-MM, BCC and MPI-HR overestimate the average temperature in all the climatic zones. Akinsanola *et al*. (2020) reported that GCM models generally struggle to capture processes of the West African Monsoon system very well. GCMs are not able to capture fine-scale processes such as complex topography, land cover processes, coastal lines, and mesoscale convection as a result of their coarse horizontal resolution (Dosio *et al*. 2021). The bias-corrected NEX-GDDP models improved all models' ability to capture the annual cycle significantly (Figure 4.4b). The bias-correction method performed remarkably in all the zones in the river basin. This was because the bias correction was able to not only correct the spatial distribution of model outputs but also significantly reduce model biases (Guo *et al.*, 2018).

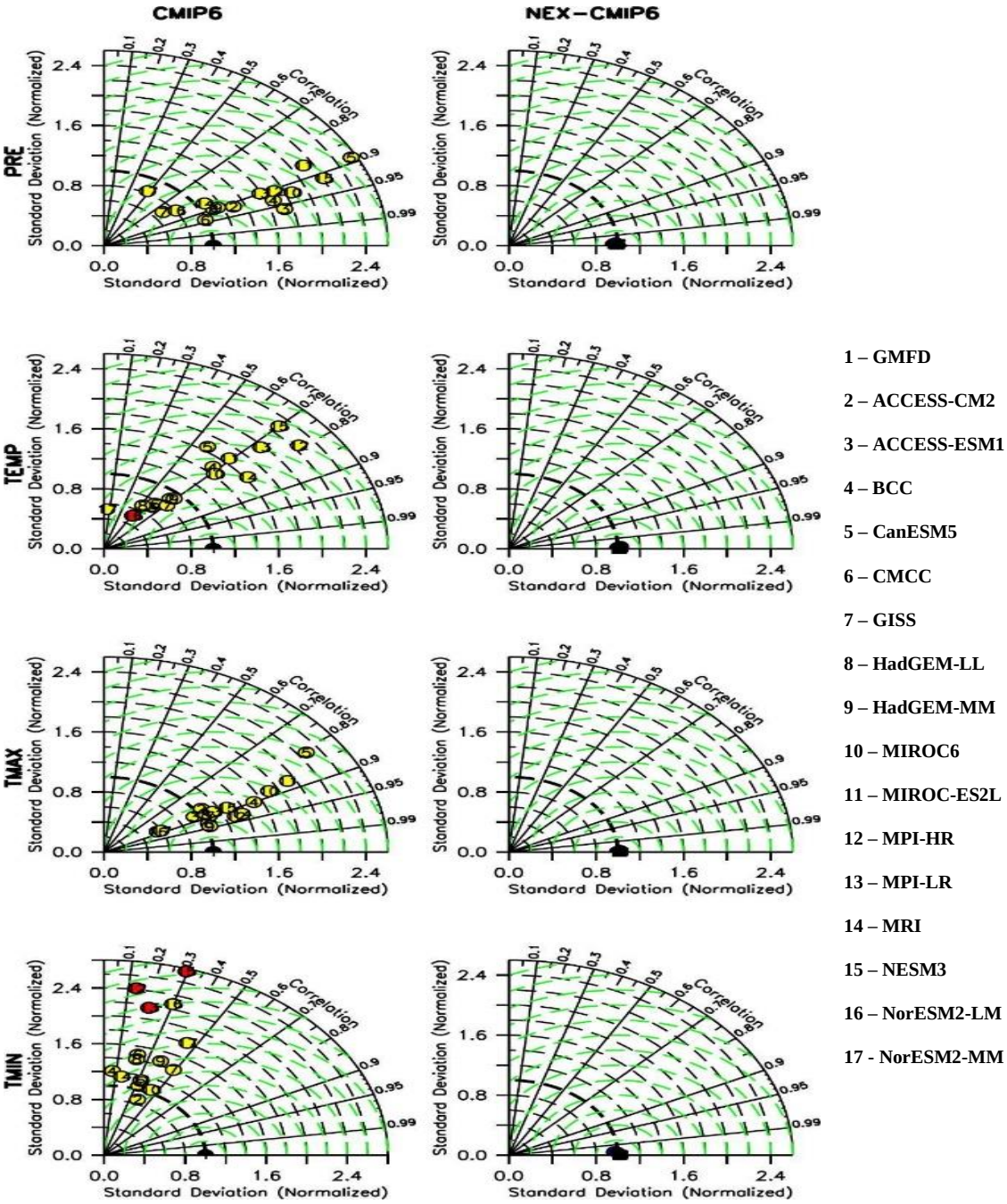

Figure 4.3: Taylor diagram of CMIP6 and NEX model data for average values of climatic variables (average, maximum and minimum temperature and precipitation) for the study period (1960-2014). Red coloured dots are negatively correlated to the observed, and yellow (CMIP6) and blue (NEX) dots are positively correlated with the observed

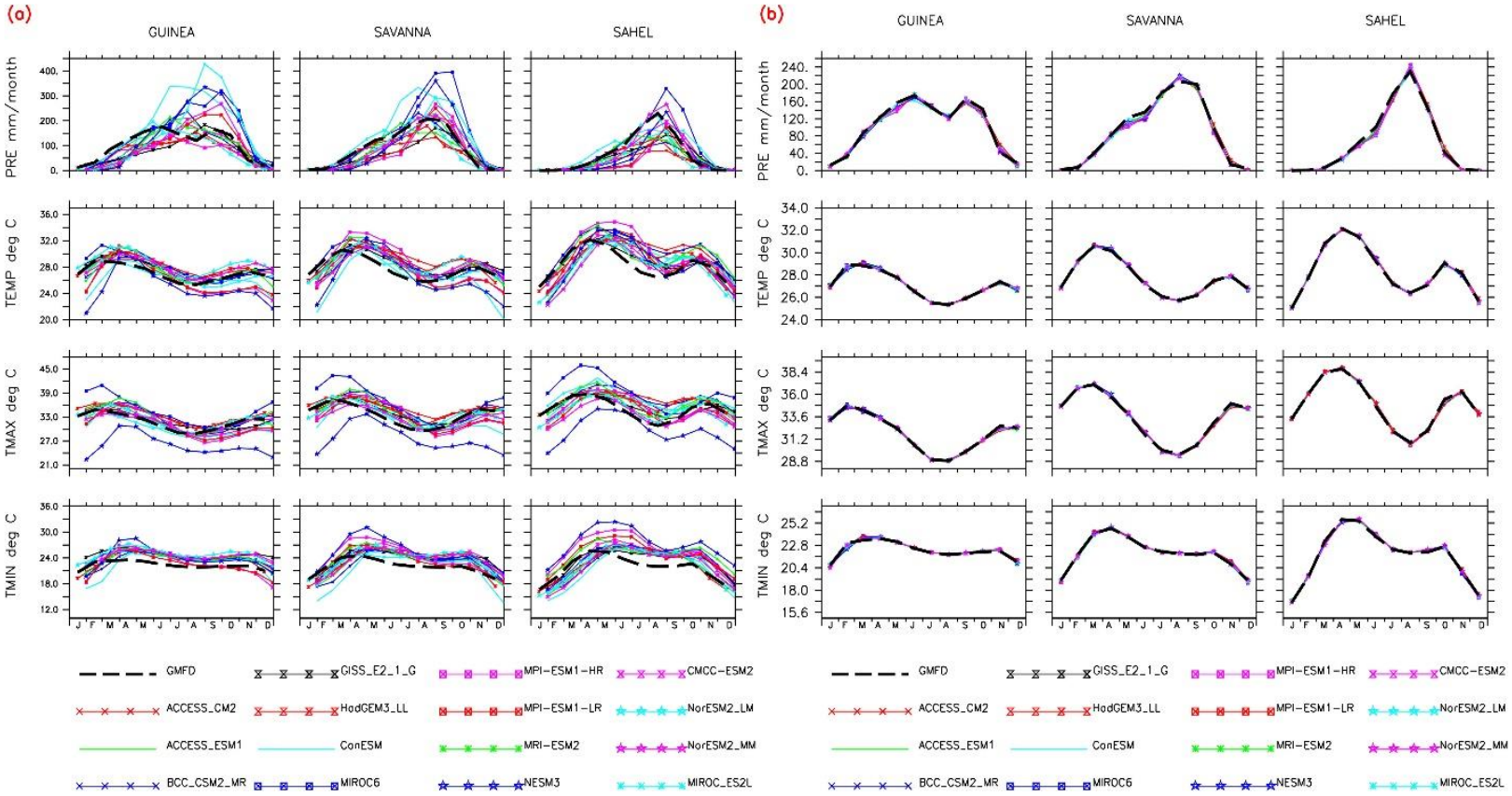

Figure 4.4: The climatological (1960-2014) annual cycle of average monthly Precipitation (PRE), Mean temperature (TEMP), Maximum Temperature (TMAX) and Minimum Temperature (TMIN) for both CMIP6 and NEX outputs. The (a) represents CMIP6 outputs and (b) refers to the NEX-GDDP outputs

4.3 Drought Patterns in the Volta River Basin

Figure 4.5 and 4.6 illustrate the results of principal component analysis for 12- and 24-month accumulated SPEI drought computed using the observed (GMFD). The first four PCA loadings identified during the analysis were referred to as the distinct drought modes present in the Volta River Basin (hereafter DM1, DM2, DM3, and DM4). The four principal components explained about 85 and 87 % of drought variability in the 12- and 24-month scale respectively. Each drought mode (DM) exhibits unique spatiotemporal characteristics. DM1 explains 24 and 22.1 % of the 12- and 24-month scale SPEI respectively. Its highest positive loading (≥ 0.8) was seen in the northern part of Burkina Faso and south-eastern Mali which is also the northern part of the basin. The climatic zone of the area is Sahel where the PCA scores show the highest correlation ($r = 96$) with the SPEI time series. This is the driest part of the basin with the least annual rainfall amount of 600 mm (Obuobie *et al.*, 2017). Drought has been reported in some studies to have occurred in this area (Nicholson and Grist, 2001; Nicholson, 2013). Studies like Graetz (1991), Nicholson *et al.* (1998) and Nicholson (2013) have also reported drought in the 1970s which lasted throughout most of the 1980s and led to severe economic losses and affected food security and livelihoods of the population in the region. The drought variability in 12- and 24-month are very similar spatially and temporally and hence the 12-month scale will be mostly discussed.

The SPEI time series over the area indicates a historical dry period spanning from the 1960s to the late 1970s. The drought ended in 1978 when a short wet period was observed till 1981, followed by a short dry period lasting till around 1984. This was followed by an intermittent longer wet period and shorter dry period from 1984 to 2006. A general wet period was observed from 2006 to 2014. The drought frequency was the highest in the

1960s (47 events per decade) and 1970s (50 events per decade) and reduced to its lowest in the 1980s to 0 events per decade, 1990s to 3 events per decade and 2000s to 2 events per decade (Fig. 4.7). The DM2 was located at the southern part of the Basin, in an area where the Volta Lake was constructed and extending to the point where the Volta River drains into the Gulf of Guinea. This was where it shows its highest PCA loadings of between 0.8 to 1 and explains about 29 % of the SPEI variance. A strong correction of 0.91 exists between this region's SPEI and the PCA scores. The SPEI shows a wet condition from 1960 to 1970 followed by a predominantly dry condition from 1972 to 2003 with some notable wet periods from 1979 to 1981, 1984 to 1986 and 1991 to 1993. This was followed by a predominantly wet period till 2014. From Figure 4.7, the drought frequency was at its highest in the 1970s (38 events per decade) and reduced to 16 events per decade in the 2000s. The DM2 results were in agreement with the results of Diasso and Abiodun (2017). For instance, the region corresponds to the fourth drought mode they identified where southern Ghana experienced the worst drought conditions in the 1980s. However, there were notable differences in the drought frequency computed per decade and magnitude owing to the difference in the reanalyses data (CRU) used as observed. The third drought mode (DM3) has its highest loading (PCA value from 0.8 to 1) over the eastern part of the VRB and northeastern, southeastern, northwestern and north of Ghana, Burkina Faso, Benin and Togo respectively. The PCA score has a strong correlation of 0.79 with the SPEI over the region. The drought indices show drought conditions occurring in each decade during the period of analysis. The longest drought duration occurred between 1984 and 1990 while the longest wet period was between 2007 and 2013 (Fig. 4.5). The highest drought magnitude occurred in 1962 (Fig 4.5) but had its highest frequency in the 1980s (33 events per decade) (Figure 4.7a). The drought frequency identifies an alternating cyclical pattern

within the basin in adjacent decades (Figure 4.7a). For instance, the drought frequency was 22 events per decade in the 1960s which declined to 19 events per decade in the 1970s which then recorded its highest frequency of 33 events per decade in the 1980s and later declined to 12 events per decade in the 1990s, then finally increased in the 2000s (28 events per decade). DM4 explains 13.9 and 15.3 % of the variance in 12 and 24-month SPEIs respectively and shows positive loadings (0.6) over northwestern Ghana and western Burkina Faso. The main drought occurred in the 1960s, 1970s and 2000s. The drought frequency decreased from 26 events per decade to 6 events per decade on the 12-month scale and 25 events per decade to 4 events per decade on the 24-month scale. An alternating dry and wet period was present from 1960 to 1978 followed by a prolonged wet period up till 2001. The longest prolonged drought occurred from 2001 to 2013.

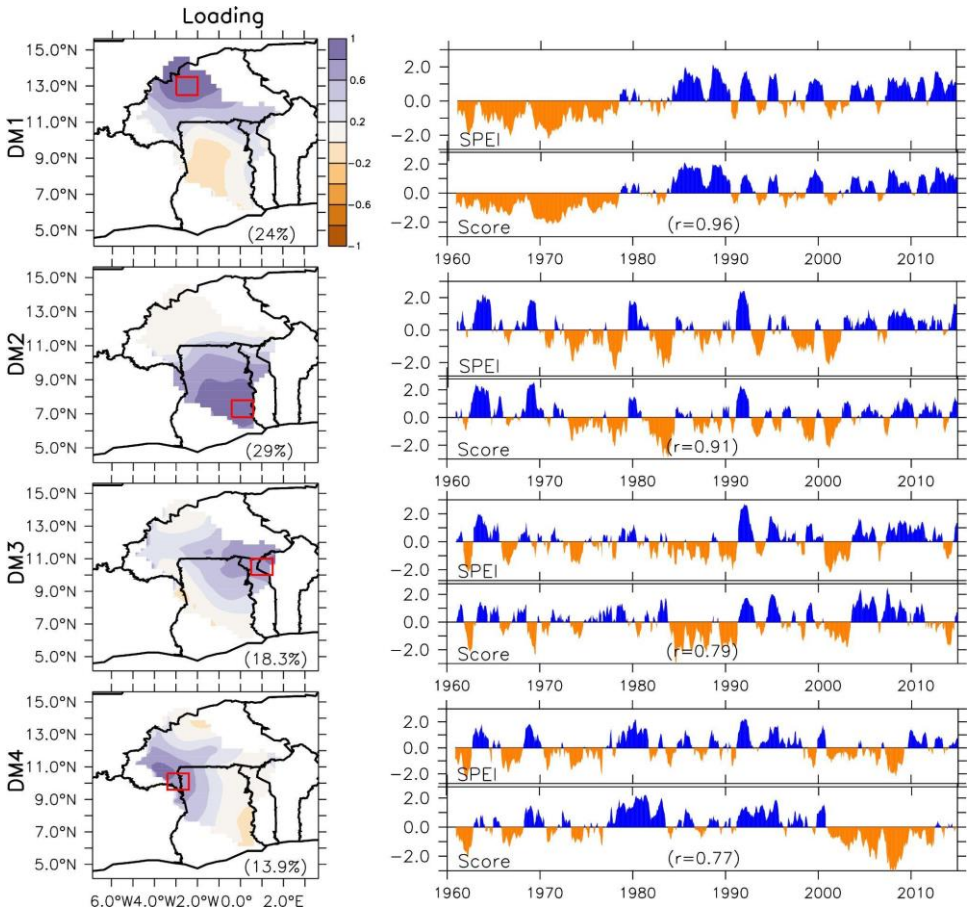

Figure 4.5: Principal component loadings on the left panel illustrate spatial patterns of 12-month scale drought and temporal SPEI and PCA scores on the right. The correlation "r" between the PCA scores and the SPEI from the region in the red box is found in the bracket.

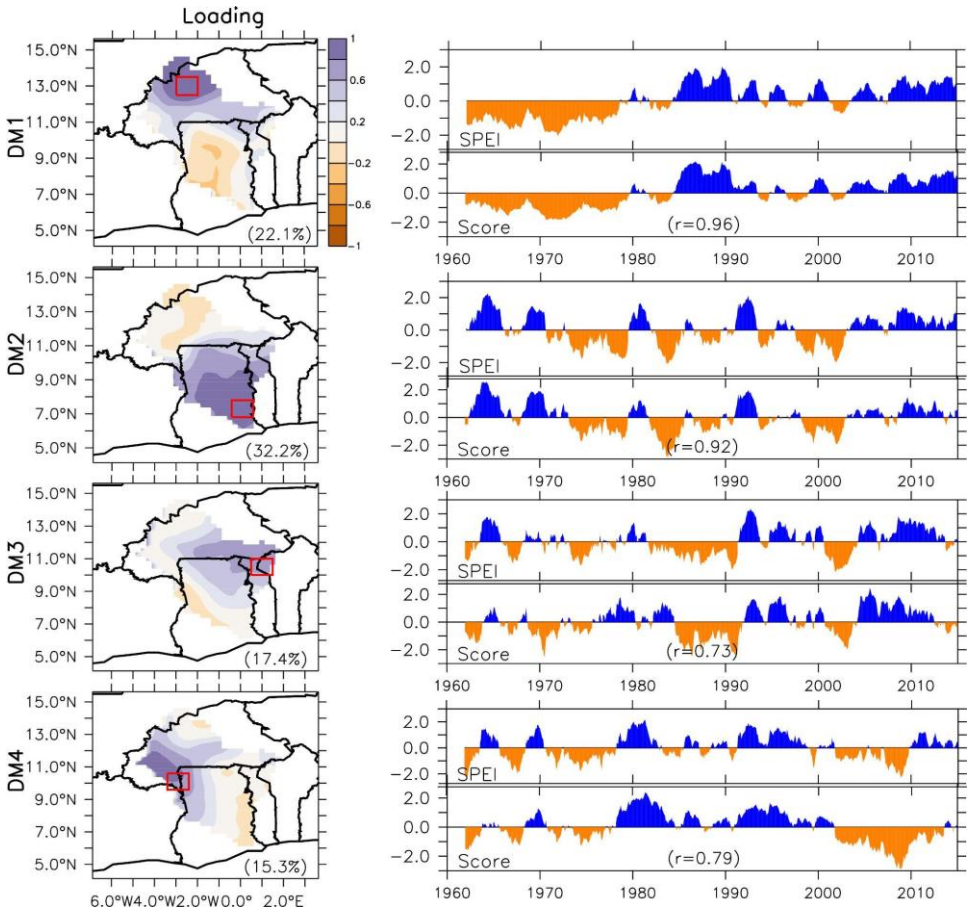

Figure 4.6: Principal component loadings on the left panel illustrate spatial patterns of 24-month scale drought and temporal SPEI and PCA scores on the right. The correlation "r" between the PCA scores and the SPEI from the region in the red box is found in the bracket.

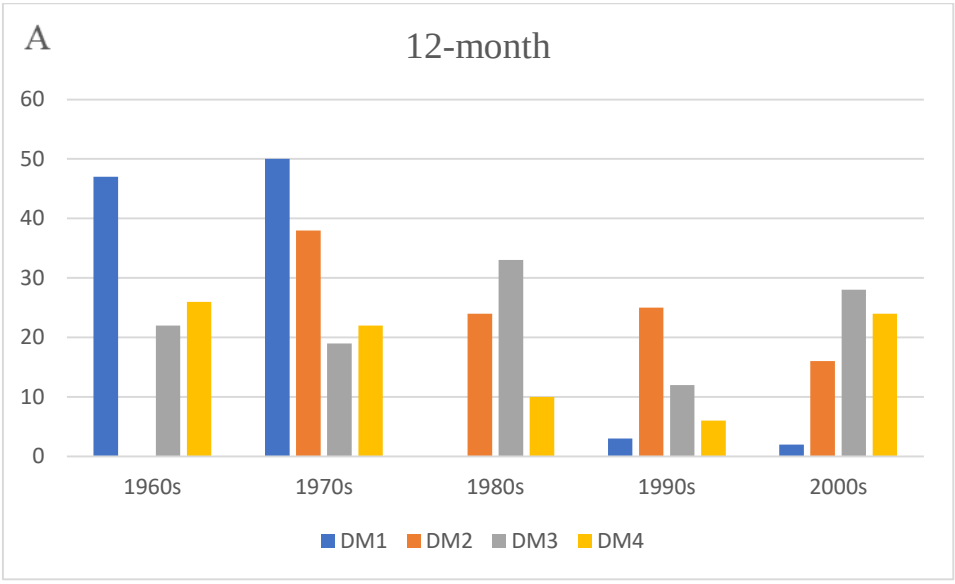

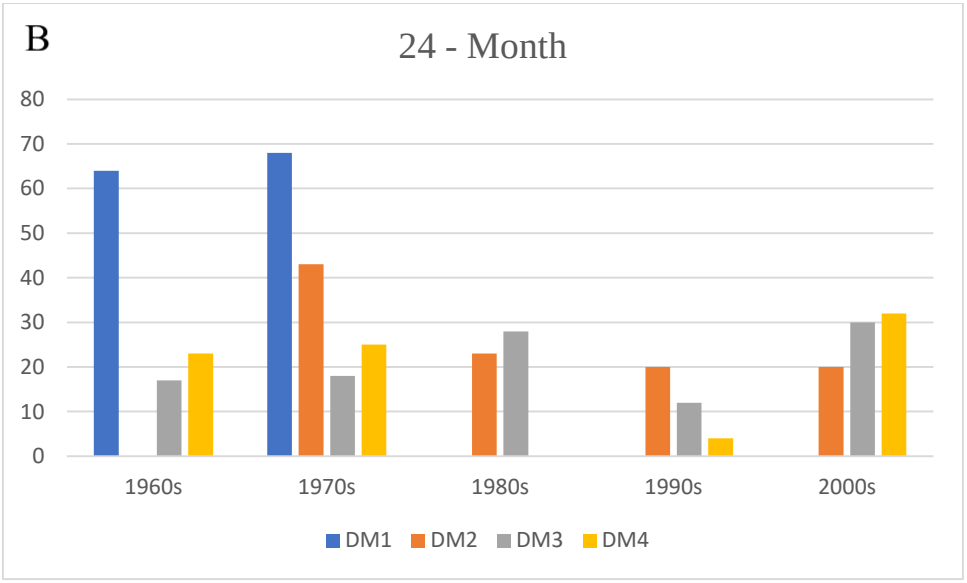

Figure 4.7: Decadal Variation of 12- and 24-month drought frequencies over DMs regions indicated with red boxes in Fig. 4.5 and 4.6

Figure 4.8 illustrates the wavelet power spectrum of all drought modes' PCA scores for the 12-month scale SPEI using a significance value of 0.5 to identify deviations in regions that were areas with black contours (Fig. 4.8). The score1, score2, score3 and score4 corresponding to DM1, DM2, DM3 and DM4 respectively. Generally, there was a 1- to 4-year cycle existing in the wavelet power spectrum in all the drought modes. The wavelet power spectrum of DM1 shows a significant 4- to 8-year cycle which occurred from 1970 to 1985. During this period, drought conditions were most prevalent in the region (Fig. 4.5). This cycle could have a direct influence on the drought variability during that period. This was followed by a cycle with a periodicity of 1 to 4 years (Fig. 4.8) which was present from 1985 to 2014, and was predominantly wet (Fig. 4.6). In the wavelet power spectrum of DM2, 4 major cycles were visible (Fig. 4.8). Two cycles were identified between 1960 and 1973, the first with a 1- to 2-year cycle and a 2- to 4-year cycle. These 2 distinct cycles corresponded to years where the region was predominantly wet (Fig. 4.6). This 2- to 4-year cycle is associated with the Quasi-Biennial Oscillation (QBO) (Torrence and Webster, 1999; Diasso and Abiodun, 2017; Oguntunde *et al.*, 2017). Conversely, Diasso and Abiodun (2017) found that QBO did not correlate with the 2- to 4-year cycle identified in the wavelet analysis of the drought modes in eastern Sahel and northern Nigeria. They indicated that the cycle had significant coherence with the Atlantic Multi-decadal Oscillation (AMO) and Tropical Southern Atlantic (TSA) in the eastern Sahel drought mode and AMO and Tropical Northern Atlantic (TNA) in the drought mode located in northern Nigeria. The third cycle which was a 4- to 8-year cycle existed from 1977 to 1993. From Fig. 4.6, this range of years was predominantly characterised by drought conditions in the region. The fourth cycle was present from 1990 to 2010. It has a 1- to 4-year cycle and overlaps with the third cycle between 1990 to 1993. Except for the overlapping years of the third and fourth cycles where

a wet condition exists, the range of years was characterised by predominantly drought conditions (1991 to 2003) and predominantly wet conditions from 2003 to 2010 (Fig. 4.6). In the wavelet power spectrum of DM3, three major cycles were visible (Fig. 4.8). The first had a 1- to 4-year cycle, which was predominantly wet when compared with Fig. 4.6. This cycle overlapped with the 1- to 2-year cycle from 1968 to 1972, resulting in dry conditions. The 1- to 4-year cycle (Fig. 4.8) was also observed from 1982 to 2001, where a predominantly dry condition persisted and interfaced with wet conditions between 1992 and 1999 (Fig. 4.6). These predominant wet conditions correspond to the period where the cycle overlapped with a 12- to 16-year cycle (1990–1997). The 1- to 2-year cycle was also observed between 1978–1981 and 2003–2010, where there were dry and wet conditions respectively (Fig. 4.6). DM4's wavelet power spectrum identified three cycles. The first cycle was a 1- to 4-year cycle, which was observed in the years 1963–1970, 1981–1987, 1996–2002 and 2005–2011. These ranges of years corresponded to dry conditions, wet conditions, wet conditions, and dry conditions in Fig. 4.6 respectively. The second cycle was a 2- to 6-year cycle that persisted from 1966 to 1975. It corresponded to a predominantly dry condition (Fig. 4.6). The second cycle overlapped with the first cycle between 1967 and 1969, which resulted in wet conditions within that period. The last cycle was a 1- to 2-year cycle that persisted in the years 1992–1996 and 2011–2012 (Fig. 4.8), corresponding to wet and dry conditions, respectively (Fig. 4.6). The non-uniqueness of the cycles could be a result of the interactions of these cycles with other atmospheric indices.

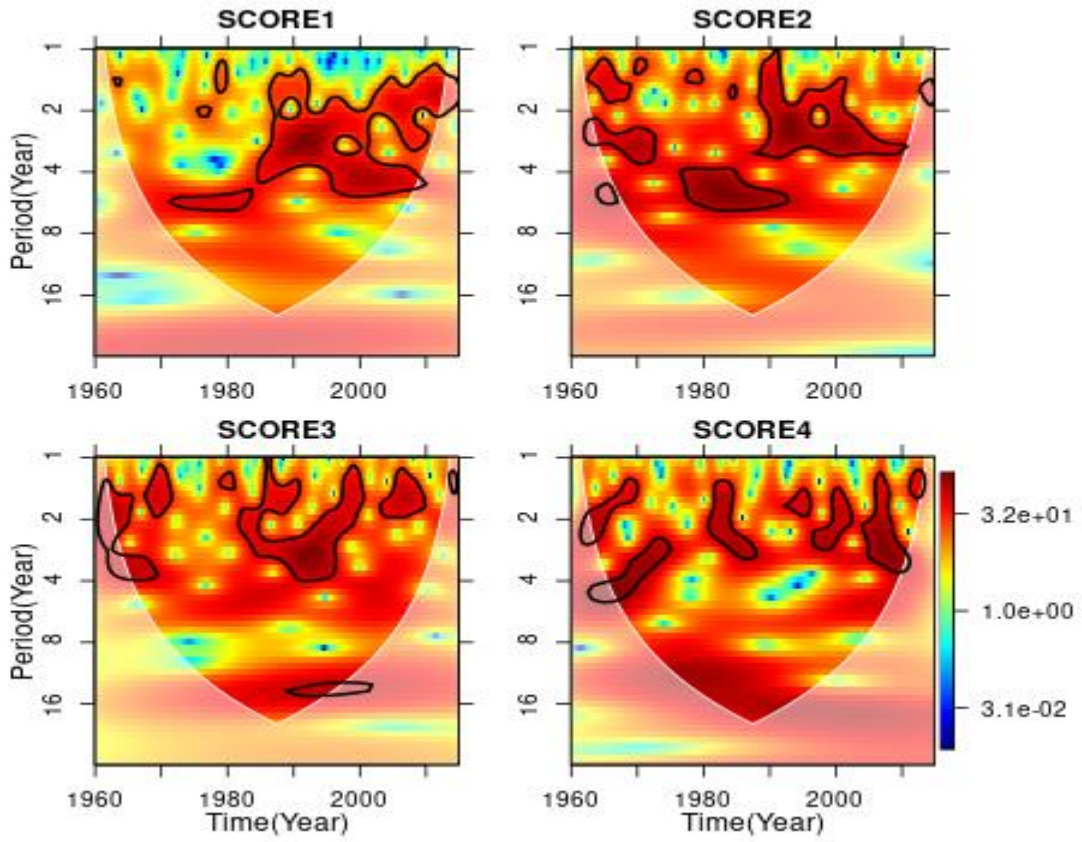

Figure 4.8: The wavelet power spectrum of 12-month SPEI drought mode over the Volta River Basin. The cone of influence is indicated by the white areas. The significant areas are marked by black contours.

4.4 Representation of Drought Patterns in CMIP6 and NEX-GDDP Model Outputs

The ability of Global models to represent drought patterns identified in the observed data was important to its application in understanding drought projection in the future. It indicates the

skill of the Global models to simulate inherent characteristics of the climate system over the Volta River Basin. Figures 4.9a and 4.9b compare the PCA loadings of the 12-month SPEI simulated drought modes (DMs) by the CMIP6 models with observed (GMFD). The PCA loadings simulated by the CMIP6 models were arranged based on their similarities with the observed drought modes identified from PCA loadings of the observed (Fig. 4.5) and were not arranged based on the increasing or decreasing order of the explained variance of the models. In general, all models reproduce DM1 and DM2 well similar to the observed pattern with varying explained variance and spatial extent. About 67 % of the CMIP6 models, namely ACCESS-CM2, ACCESS-ESM, BCC, CanESM5, GISS, HadGEM-LL, MIROC6, MIROC-ES2L, CMCC-ESM and NorESM2-MM were able to reproduce all the drought modes. For DM1, CMCC-ESM, BCC, GISS, MIROC6, ACCESS-ESM1 and HadGEM-LL outperformed other models with correlations greater or equal to 0.9 and a normalized standard deviation (σ) between 0.8 to 1.2 (Fig. 4.11). The best models were BCC and ACCESS-ESM1 which had normalized standard deviations of approximately 1. From Figure 4.11, models such as ACCESS-CM2, NorESM2-MM, CanESM5, NorESM2-LM and MIROC-ES2L also exhibited good performance in reproducing DM1 with a pattern correlation ranging from 0.8 to 0.89 and normalized standard deviation of between 0.8 and 1.2. MRI ($r = 0.85$, $\sigma = 0.66$) MPI-HR ($r = 0.8$, $\sigma = 0.77$) showed a reasonable performance when compared to the DM1 region of the observed (Fig. 4.11). The least performing

models were MPI-LR (r = 0.73, σ = 0.85) and NESM3 (r = 0.76, σ = 0.583). In DM2, NorESM2-MM, NorESM2-LM and CMCC were the best-performing models with pattern correlation equal to or greater than 0.95 and a normalized standard deviation of approximately 1.0. This was followed by GISS and ACCESS-ESM which had a pattern correlation of 0.9 and normalized standard deviation of approximately 1. BCC and HadGEM-LL also performed well with a pattern correlation of 0.9 and a normalized standard deviation ranging between 0.8 and 1.2 (Fig. 4.11). ACCESS-CM2 (r = 0.87, σ = 0.7), MPI-HR (r = 0.88, σ = 0.77), MIROC6 (r = 0.89, σ = 1.186), MIROC-ES2L (r = 0.79, σ = 0.834) and MRI (r = 0.91, σ = 0.674) also performed reasonably well with a correlation greater than 0.79 and normalized standard deviation greater than 0.6.MPI-LR and CanESM5 were the least performing models with a correlation of 0.75 and normalized standard deviation of 0.71 and 1.067 respectively. NESM3 had a strong correlation of 0.85 but had a lower normalized standard deviation of 0.576.

In DM3, the CMCC, GISS, HadGEM-LL and MIROC6 outperformed all the models with a correlation greater than 0.85 and a normalized standard deviation of approximately 1 (Figure 4.11). Subsequently, ACCESS-CM2, NorESM2-MM and ACCESS-ESM1 also performed reasonably well with a normalized standard deviation between 0.8 and 1.2 and a correlation greater than 0.7. BCC showed a strong correlation (0.89) with the observed pattern but had a normalized standard deviation of 1.39 further away from the observed. The worst-performing models were NESM3, MPI-HR and MPI-LR which had a lower correlation of less than 0.5. Even though MRI could not reproduce the DM3 observed in the GMFD, it exhibited a drought pattern that was present in the central part of the basin and extended to the eastern and western boundaries of the basin. Thus, MRI performed fairly in reproducing DM3 when compared with observation.

In DM4, CMCC, GISS, HadGEM-LL, ACCESS-CM2, ACCESS-ESM1 and MIROC6 were the best performing models with correlations greater than 0.7 and normalized standard deviations between 0.8 and 1.2. HadGEM-LL outperformed all the models in reproducing the DM4. BCC also had a correlation greater than 0.7 but had a normalized standard deviation greater than 1.2, similar to its behaviour in DM3. The worst-performing models were NESM3, MPI-LR, MPI-HR and MRI, with correlations less than 0.2. In general, all models' performance decreased in their ability to reproduce DM3 and DM4.

From Figure 4.9a and 4.9b, all the models show that DM1 had the greatest explained variance except for BCC, GISS, HadGEM-LL and CMCC where DM2 had the greatest explained variance as seen in the observation. ACCESS-CM2 (88 %) and HadGEM-LL (81 %) had a total explained variance closer to that of GMFD (85 %). The rest of them had a total explained variance greater than 88 % except for BCC which had a total explained variance of 78 %.

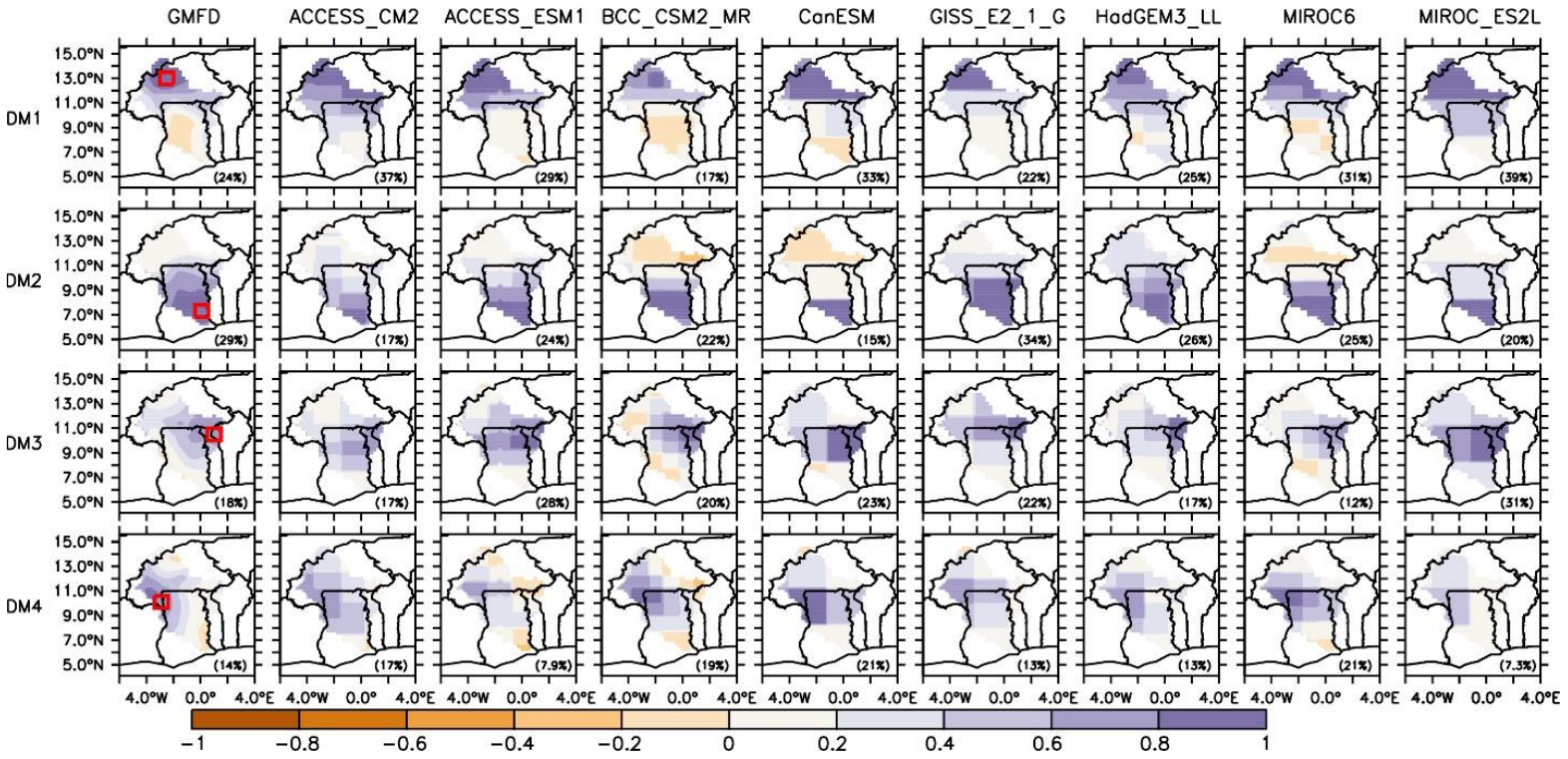

Figure 4.9a: The PCA loadings of 12-month SPEI for the observed (GMFD) and CMIP6 models over the Volta River Basin from 1960 to 2014. The percentage of the variance explained by each DM is indicated in the lower right corner. The PCA loadings of the models were not in increasing or decreasing order of the variance explained but arranged according to their similarities with the PCA loadings of the observed

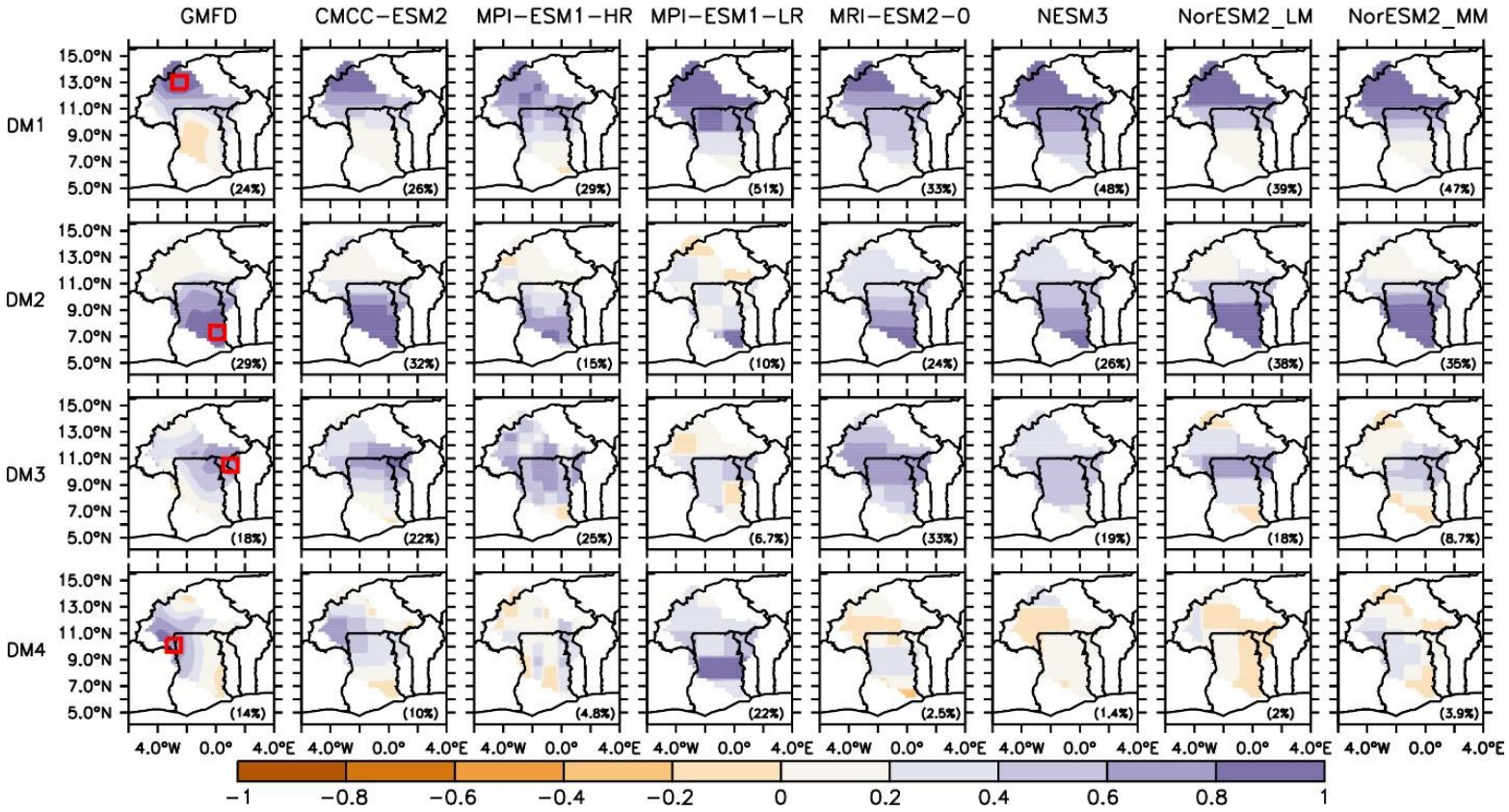

Figure 4.9b: Same as Figure 4.9a for models CMCC-ESM2, MPI-ESM1-HR, MPI-ESM1-LR, MRI-ESM2-0, NESM3, NorESM2-LM and NorESM2-MM

Figures 4.10a and 4.10b compare the PCA loadings of the 12-month SPEI simulated drought modes (DMs) by the NEX-GDDP models with observed (GMFD) similar to Figures 4.9a and 4.9b. Similar to the results seen in CMIP6, the NEX-GDDP models reproduce DM1 and DM2 well comparable to the patterns seen in the GMFD with varying explained variance and spatial extent. Unlike CMIP6, about 73 % of the models, namely ACCESS-CM2, ACCESS-ESM, BCC, CanESM5, GISS, HadGEM-LL, MIROC6, MIROC-ES2L, CMCC-ESM and NorESM2-MM, NorESM2-LM were able to reproduce all the drought modes. The noticeable difference was NorESM2-LM where statistical downscaling and bias correction were able to improve the model's ability to reproduce DM3 and DM4 patterns with a low PCA loadings value between 0.2 and 0.6. Figure 4.11 compares the CMIP6 and NEX-GDDP models' performances in reproducing the drought modes. Bias corrected and statistically downscaled either improves or reduces the performance of each model under different drought modes (DMs). For example, in DM1, ACCESS-CM2, HadGEM-LL, MIROC6, MPI-HR, MPI-LR and NESM3 saw improvement in their correlation value by a magnitude of 0.02 to 0.06. A slight increment of 0.01 was observed in the correlation values of CanESM5, ACCESS-ESM1, GISS, BCC and CMCC. On the contrary, the correlation values of MIROC-ES2L, NorESM2-MM, MRI and NorESM2-LM reduced by magnitudes 0.01, 0.01, 0.03 and 0.04 respectively. Also, models such as MRI, NorESM2-MM, MPI-HR and MIROC-ES2L, MIROC6, ACCESS-ESM1 and CanESM5 slightly improved in their normalized standard deviation. In DM2, there were general improvements in the correlation of models except for MRI which decreased from 0.91 to 0.89. Although the correlation of MRI decreased, the normalized standard deviation improved. Models with the most significant improvements in their correlation were MIROC6 (0.89 to 0.97), MPI-LR (0.67 to 0.95), ACCESS-CM2 (0.87 to

0.92), MIROC-ES2L (0.79 to 0.93) and CanESM5 (0.74 to 0.89). There were no changes in the correlation of NorESM2-MM and CMCC but a slight reduction in their normalized standard deviation. In DM3, there were improvements in the correlations and the normalized standard deviation of ACCESS-CM2, ACCESS-ESM1, BCC, CanESM5 and MIROC6. GISS, HadGEM-LL, MIROC-ES2L and NorESM2-LM models' correlation improved but reduced slightly in their normalized standard deviation. Models that saw a reduction in their correlation but improvement in the normalized standard deviation were NorESM2-MM and CMCC. The MRI model's correlation and normalized standard deviation were reduced. Bias correlation was not able to improve the model's ability to reproduce DM3. In DM4, ACCESS-ESM1, BCC, CanESM5, MIROC6 and NorESM2-LM improved in both their correlations and the normalized standard deviations. ACCESS-CM2 model's correlation improved but the normalized standard deviations reduced. Similarly, the correlation of GISS, MIROC-ES2L, CMCC and NorESM2-MM increased but reduced slightly in their normalized standard deviation. The bias correlation did not improve the ability of MPI-HR, MPI-LR and NESM3 to reproduce DM3 and DM4 as observed in the CMIP6.

From Figure 4.10a and 4.10b, all the NEX-GDDP models show that DM1 had the highest explained variance except for GISS, HadGEM-LL and CMCC where DM2 had the highest explained variance as seen in the observation and BCC where DM4 had the highest explained variance. After statistical downscaling and bias correction, the total variance explained by all the DMs increased higher than the total variance observed in their original CMIP6 models.

In summary, NEX-GDDP models such as MIROC6, ACCESS-CM2, ACCESS-ESM1, CanESM5, GISS and BCC were generally better than their CMIP6 counterparts in reproducing drought modes over the Volta River Basin.

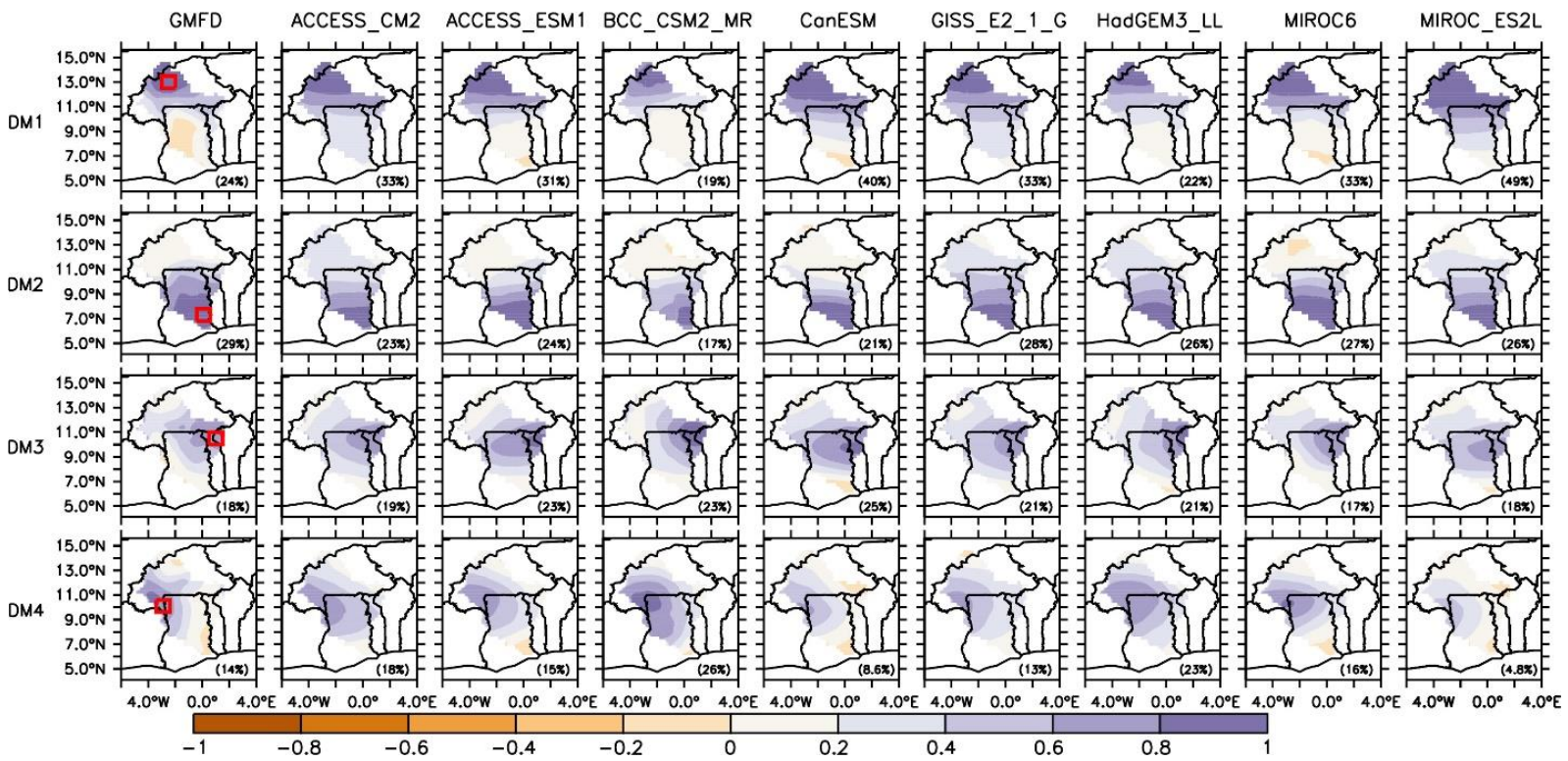

Figure 4.10a: The PCA loadings of 12-month SPEI for the observed (GMFD) and NEX-GDDP models over the Volta River Basin from 1960 to 2014. The percentage of the variance explained by each DM was indicated in the lower right corner. The PCA loadings of the models were not in increasing or decreasing order of the variance explained but arranged according to their similarities with the PCA loadings of the observed

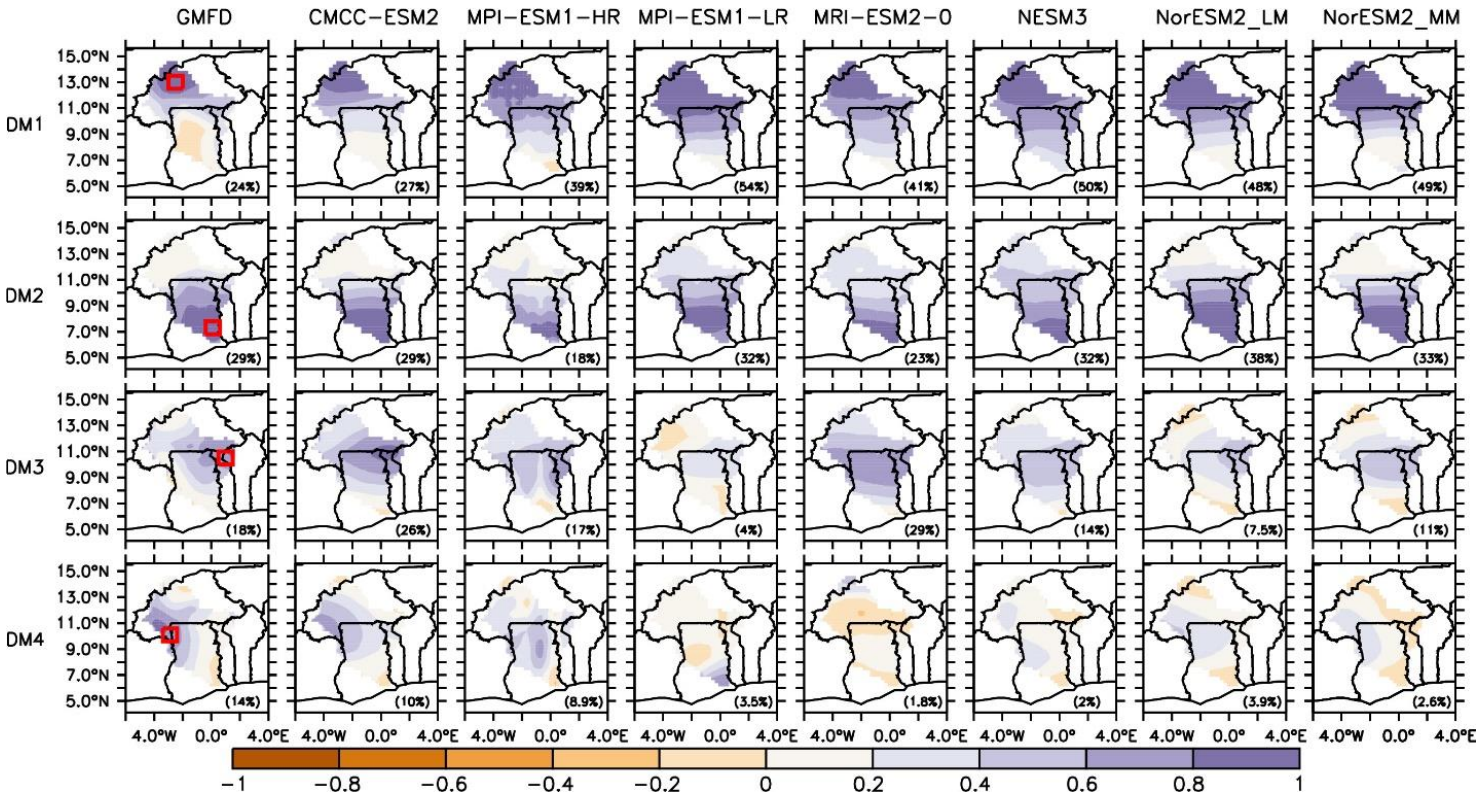

Figure 4.10b: Same as Figure 4.10a for models CMCC-ESM2, MPI-ESM1-HR, MPI-ESM1-LR, MRI-ESM2-0, NESM3, NorESM2-LM and NorESM2-MM

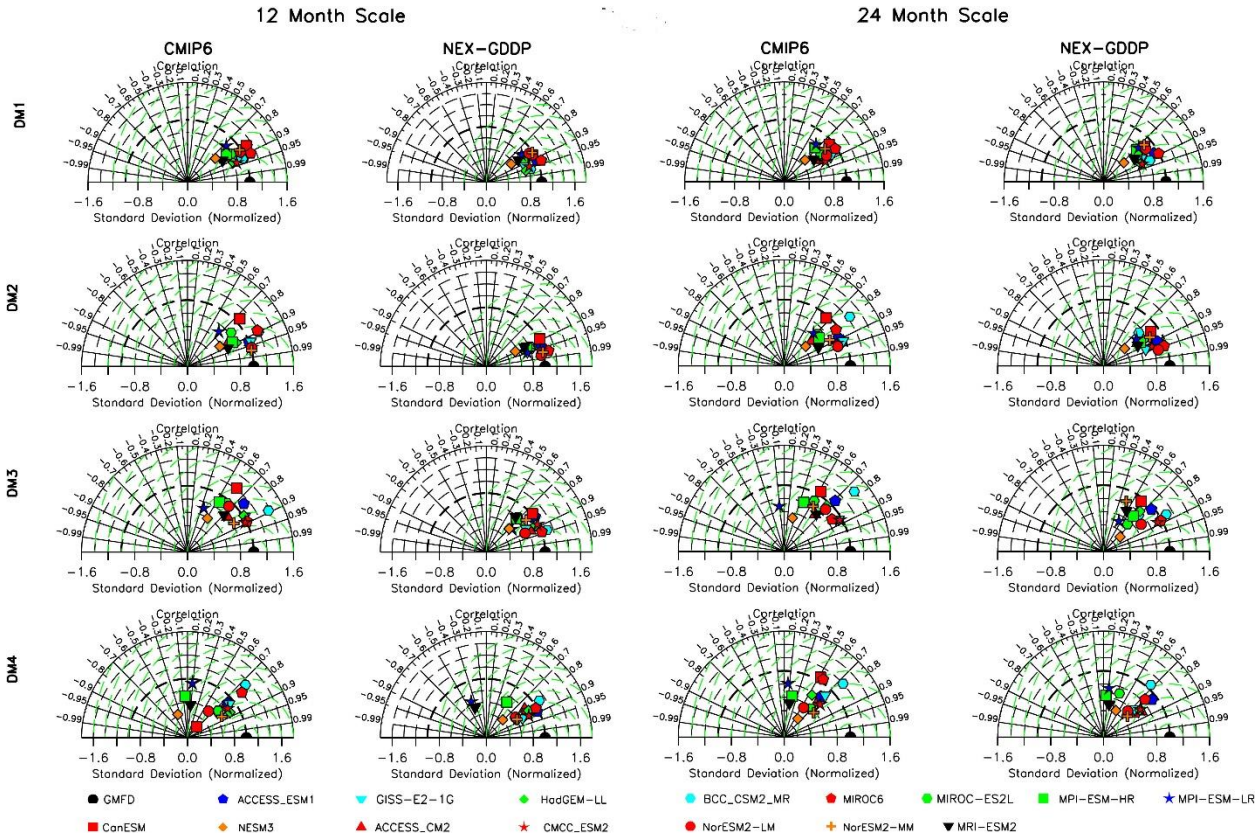

Figure 4.11: The Taylor diagram comparing pattern correlation and spatial normalized standard deviation of observed and simulated DMs for both CMIP6 and NEX-GDDP models

4.5 Climate Change and Variability in the Volta River Basin

This section assessed climate change using Theil Sen's slope analysis on annual temperature and rainfall data for both GMFD (observed data and NEX-GDDP data for the historical, Near, Mid and Far term.

4.5.1 Analysis of Historical Trends in Climatic Variables

Figure 4.12 illustrates the historical trends in precipitation performed using Thiel Sen's Slope analysis using observations (CRU and GMFD) and 15 NEX-GDDP models datasets, and their ensemble mean. From the graph, GMFD and CRU show that precipitation has been decreasing in most parts of the Volta River Basin (VRB) at a magnitude of about -2.5 mm/year^2 during the historical period. Only the trends in some eastern parts of VRB were statistically significant at a p-value of 0.05 in the CRU datasets. In the GMFD, statistically significant trends were observed in some areas in the eastern, southwestern, central part and western parts of the basin. Positive trends in precipitation of about 2.5 mm/year^2 were in the central and northern part of the basin but they were not statistically significant. Unlike CRU, GMFD identified more areas in the VRB which has experienced a reduction in historical precipitation amount. The result is in agreement with Oguntunde *et al.* (2006) in which rainfall in the VRB experienced a decreasing trend of magnitude 6 mm/year^2 from 1970 to 2002. The difference in the magnitude of change could be a result of the difference in rainfall product use and the slight differences in study periods. The results also revealed that statistically significant precipitation increments were observed in the majority of the NEX-GDDP models such as ACCESS-CM2, ACCESS-ESM1, MIROC-ES2L, MPI-HR, MPI-LR, MRI, NorESM2-MM, NorESM2-LM, NESM3 and the Ensemble mean of the models which occurred almost throughout the entire basin. The NESM3 model recorded

the highest precipitation increment ranging from 2.5 to 10 mm/year^2 with the eastern part of the VRB having the greatest change amount ranging between 7.5 to 10 mm/year^2. Additionally, the NorESM2-LM was the second-highest model with an increment in precipitation amount between 2.5 to 7.5 mm/year^2 after NESM3 followed by NorESM2-MM. The GISS model was the only model that simulated a general statistically significant decrease in precipitation (0 to -2.5 mm/year^2) throughout the entire basin. Models like BCC, HadGEM-LL and MIROC6 slope analyses show a dipole change pattern where most of the northern part of the basin had an increasing precipitation trend between 0 to 2.5 mm/year^2 and the southern part experienced a decreasing trend between 0 to -2.5 mm/year^2 during the period of analysis. The Ensemble mean of the NEX-GDDP models showed a statistically significant increasing trend in precipitation with a magnitude of between 0 to 2 mm/year^2 throughout the whole basin.

Historical average temperature records present an increasing trend pattern in both CRU and GMFD with most changes occurring in the northmost and eastern part of the VRB (Figure 4.13) which was statistically significant at a p-value of 0.05. The northern and eastern parts increased by a magnitude of 0.03 to 0.04 °C/year while the rest of the basin saw increments of 0.01 to 0.02 °C/year. From Figure 4.13, all the NEX-GDDP models simulated increasing temperature trends during the historical period. The warmest models were ACCESS-ESM1 and CMCC which had significant positive trends of magnitudes between 0.04 to 0.05 °C/year for most parts of latitude 10 °N upwards and magnitudes between 0.03 to 0.04 °C/year south of latitude 10 °N. The Ensemble mean of the models features a positive trend of magnitudes 0.03 to 0.04 °C/year spanning from east to west of the basin north of latitude 10 °N and 0.02 to 0.03 °C/year in most parts of the basin. The results obtained for the observed were in agreement with Okafor *et al.* (2019) who examined changes in historical

climate within the rainy season (May to October for VRB, Sahel and Soudano Sahel), minor rainy season, major and minor dry season in the VRB by using Mann Kendall trend test and Thiel Sen's Slope. In the overall VRB, precipitation and temperature change were 0.44 mm/season and 0.02 °C/season in the rainy season and 0.10 mm/year^2 and 0.03 °C/season in the dry season respectively, only temperature changes were within the 95 % confidence level. More than 75 % of rainfall amounts are recorded during the rainy season (May to October). In the Sahel and Soudano Sahel region (similar to this study Sahel and Savannah zones) temperature changes were 0.02 °C/season in the rainy season and 0.03 °C/season in the dry season while precipitation changes ranged from 0.53 to 0.99 mm/ season and 0.0 to 0.15 mm/season in the wet and dry season respectively. They observed that, in the Guinea Coast, changes in precipitation and temperature range between -1.33 to 0.83 mm/season and 0.02 to 0.03 °C/season in both the wet and dry seasons. Their result falls within the range of values obtained in this study.

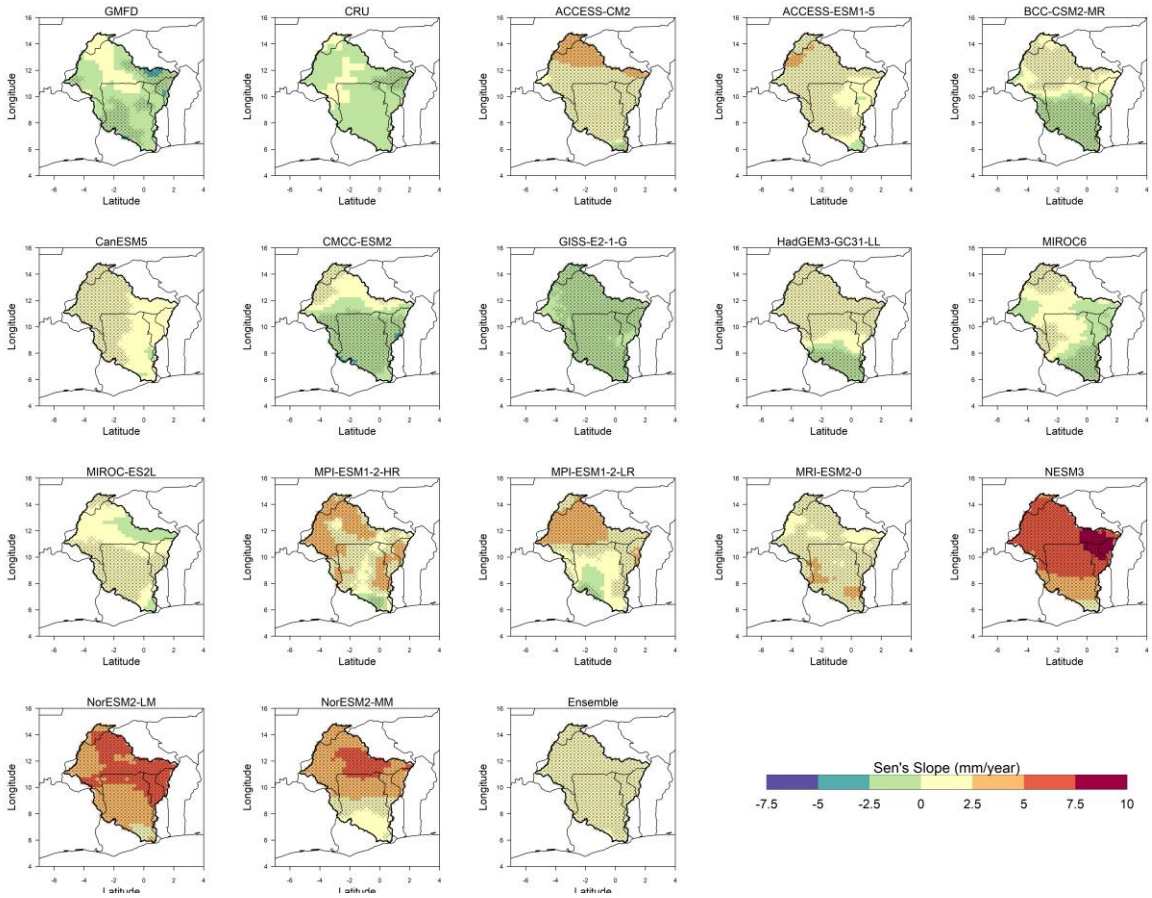

Figure 4.12: Comparison of historical (from 1960 to 2014) precipitation trends of observation (GMFD and CRU) and NEX-GDDP models using Thiel Sen's slope. The black crosses represent areas with trends that are significant at a 95 % confidence level

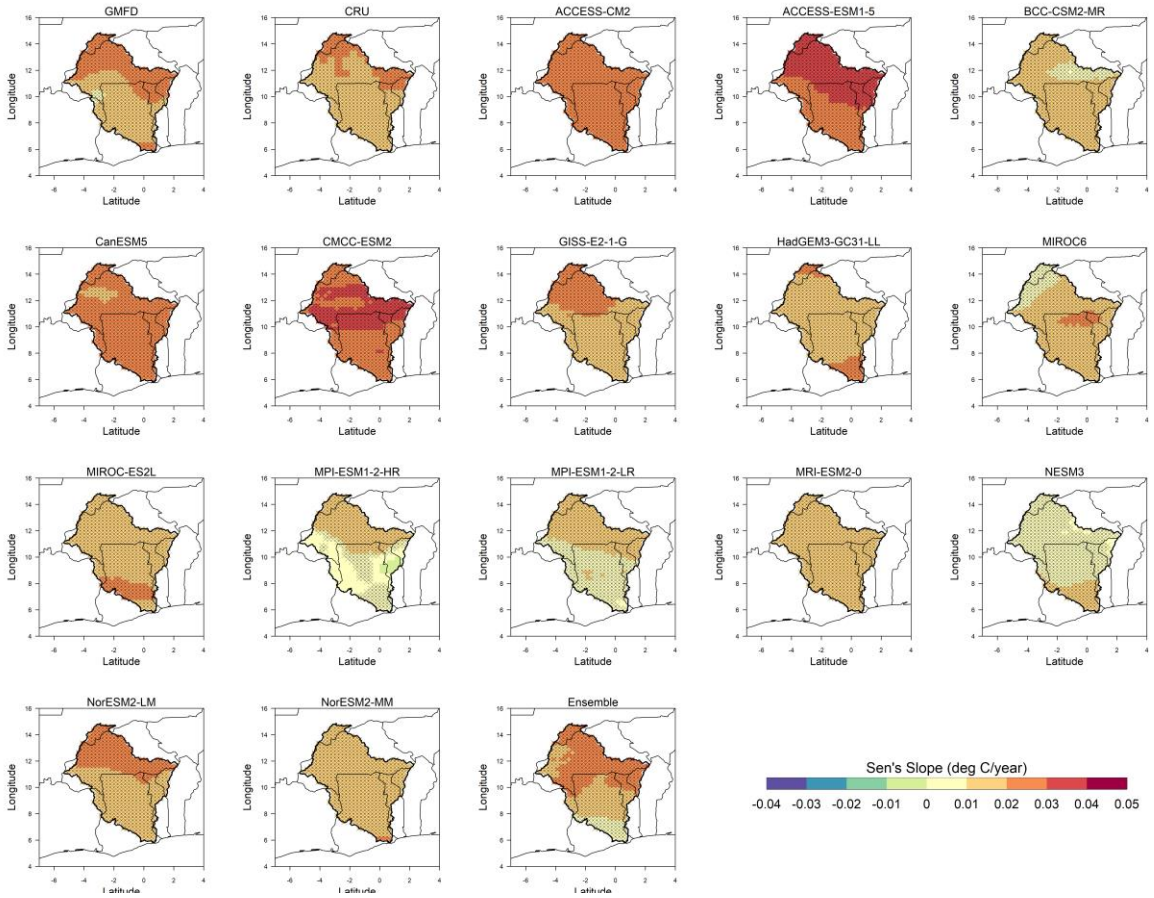

Figure 4.13: Comparison of historical (from 1960 to 2014) average temperature trends of observation (GMFD and CRU) and NEX-GDDP models using Thiel Sen's slope. The black crosses represent areas with trends that are significant at a 95 % confidence level

4.5.2 Future trends in climatic variables

4.5.2.1 Future trends in precipitation

Figures 4.14, 4.15 and 4.16 present the results of the estimated slope and trend detected in precipitation under SSP 1-2.6 emission scenario for the Near term (NF), Mid term (MF) and Far term (FF). From Figure 4.14, ACCESS-CM2, CanESM5, HadGEM-LL, CMCC, and MRI projected a potential increase in precipitation amount in the NF occurring from the central part of the basin and moving northward. In HadGEM-LL and MRI, this increment in precipitation will occur across the Black Volta, White Volta and Oti Basin while models such as ACCESS-CM2, CanESM5 and CMCC suggest that precipitation will increase in all the subbasins of the VRB Black Volta, White Volta, Oti and Lower Volta Basin. These changes were statistically significant at a p-value of 0.05. NESM3 and MIROC-ES2L projected decreasing precipitation in VRB. In NESM3, all the subbasins of the VRB will experience a statistically significant reduction in precipitation with most changes occurring in part of White and Black Volta (between -10 to -15 mm/year^2). ACCESS-ESM1, MPI-LR, NorESM2-LM, NorESM2-MM and GISS models projection of precipitation changes were not widespread within the VRB. Most noticeable among these models were GISS which projected decreasing precipitation in the Black Volta and NorESM2-MM which shows significant reductions in small portions of Black and White Volta. MIROC-ES2L shows that precipitation in most parts of the Lower Volta and some areas of the Black Volta will decrease. MIROC6 projected a decrease in precipitation in the northern and eastern parts, and increasing precipitation in the Black Volta of the VRB. In the MPI-LR model, only the northern part of the VRB will see an increment in precipitation while some parts of the Black Volta, White and Oti Basin will under precipitation reduction.

From these results, there was less agreement between models on the projection of precipitation in the NF. In the Ensemble mean of the models, there was a projected decrease in precipitation in most parts of the Black Volta and some areas in Lower Volta while a little part of the eastern and northern portion of the VRB might have a positive precipitation change.

In the Mid term (Figure 4.15), most of the models projected a statistically significant decrease in precipitation in VRB. Models that projected statistically significant changes covering more than 50 % of the VRB were ACCESS-CM2, ACCESS-ESM1, BCC, GISS, MPI-HR and the Ensemble Mean. The NorESM2-MM projected a statistically significant decrease in precipitation in most of the VRB from latitude 9 °N northwards and positive gains of 5 to 15 mm/year^2 south of latitude 8 °N. The Ensemble Mean shows that most part (more than 75 %) of the basin will experience a reduction in precipitation of magnitude -5 to -10 mm/year^2 and 0 to 5 mm/year^2 gains around the river mouth and southern edge. The models that simulated statistically significant gains in precipitation were the CMCC and HadGEM-LL. While changes were cut across the entire basin in CMCC with major gains around the river mouth and southern edge, gains were localised between latitude 13 °N and 7 °N in the HadGEM-LL. Almost the entire VRB basin experienced any change in the CanESM5, the only significant positive change was seen at the northmost edge of the VRB where the international border between Mali and Burkina Faso.

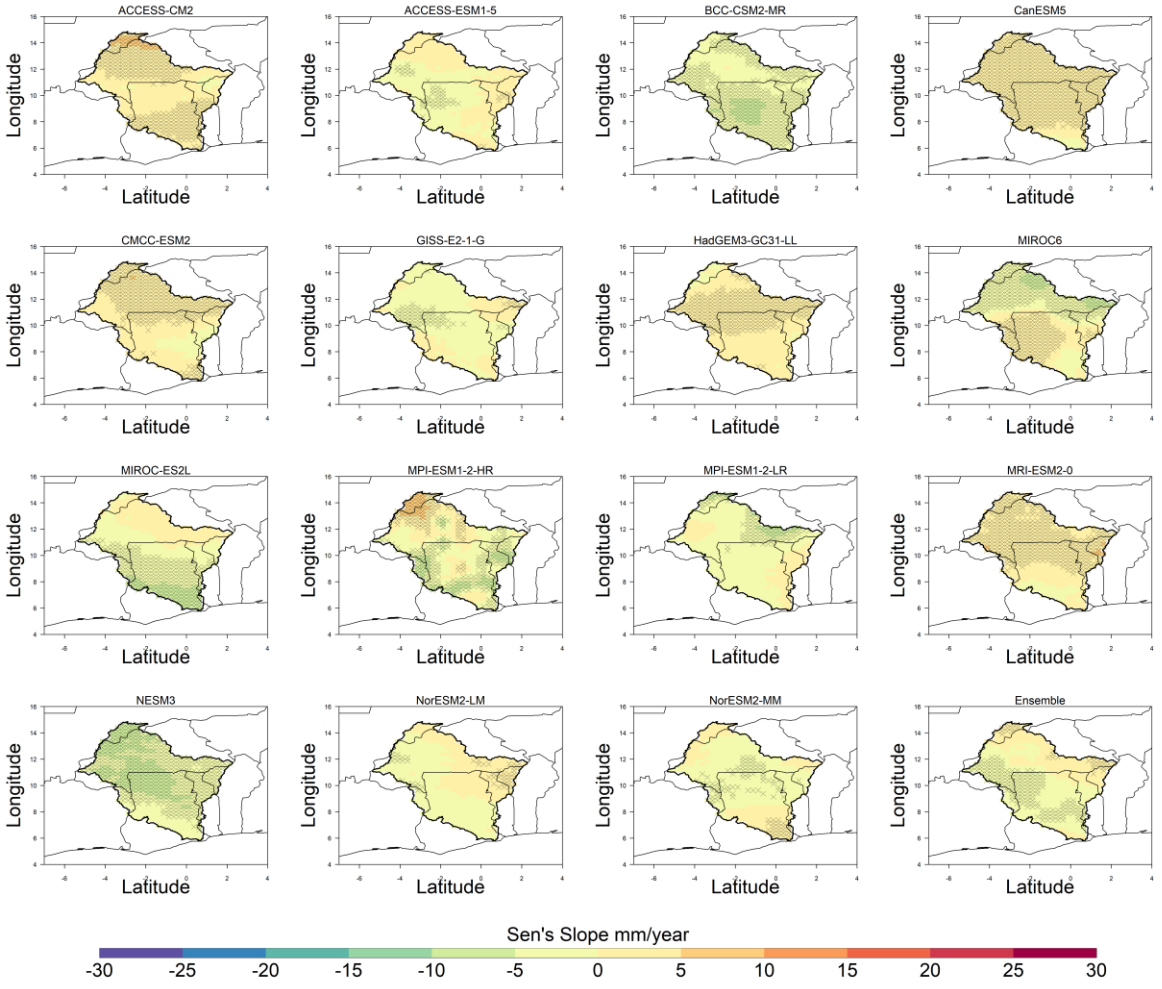

Figure 4.14: Comparison of Near term (from 2021 to 2050) precipitation trends of NEX-GDDP models under Socioeconomic Shared Pathways SSP 1-2.6 scenario using Thiel Sen's slope. The black crosses represent areas with trends that are significant at a 95 % confidence level

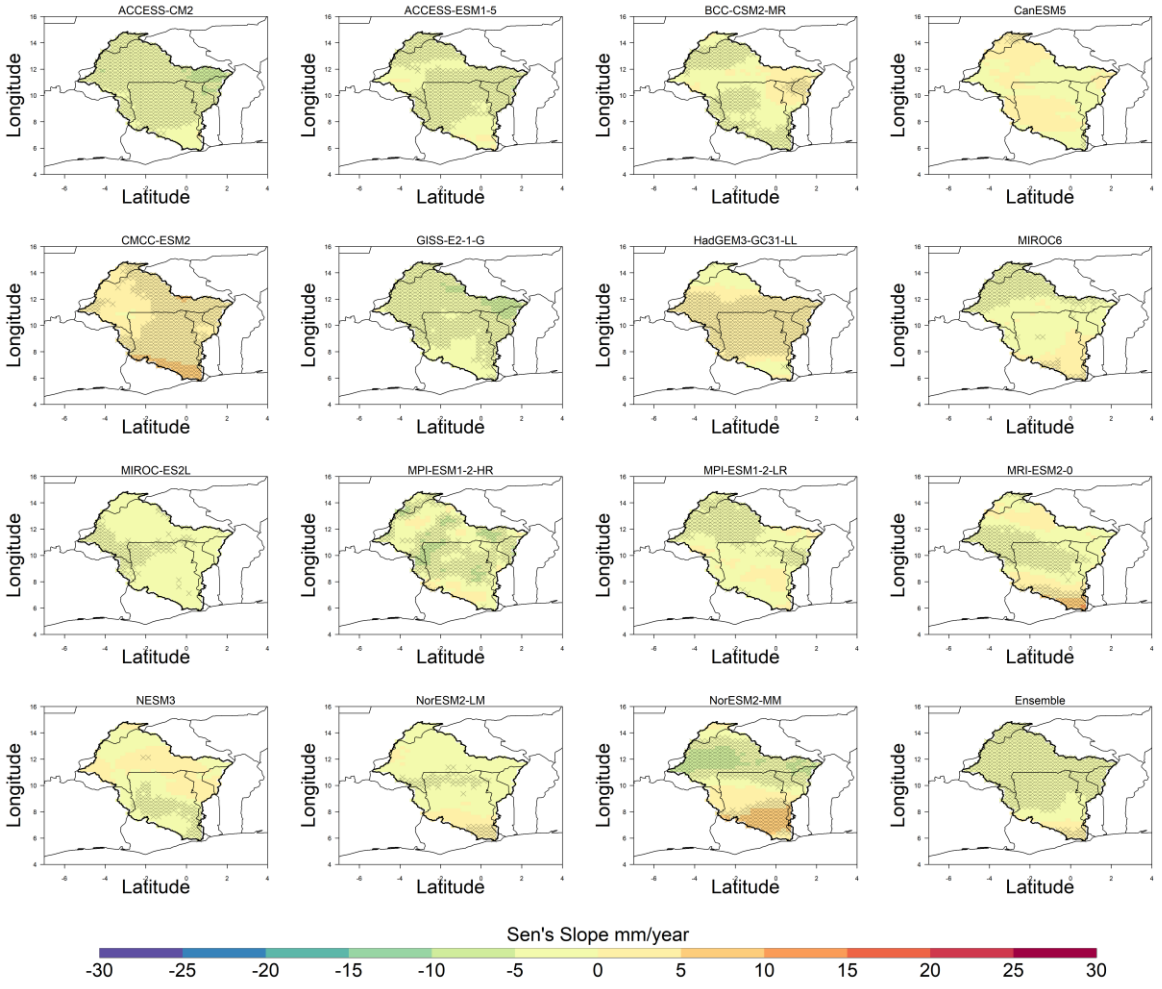

Figure 4.15: Comparison of Mid term (from 2051 to 2080) precipitation trends of NEX-GDDP models under Socioeconomic Shared Pathways SSP 1-2.6 scenario using Thiel Sen's slope. The black crosses represent areas with trends that are significant at a 95 % confidence level

In the Far term (Figure 4.16), most of the models projected a statistically significant increase in precipitation in most regions of the VRB. Models that projected statistically significant changes covering about 50 % or more of the VRB were ACCESS-ESM1, CanESM5, MIROC-ES2L, MPI-HR, MPI-HR, MRI and the Ensemble Mean. Most of the statistically significant changes occur throughout the entire VRB. In the GISS, there was a statistically significant decrease (0 to 5 mm/year^2) in precipitation in the northern part of the VRB and an increase (0 to 5 mm/year^2) in precipitation in the southern part from about latitude 10 °N. Similarly, the CMCC models exhibit similar characteristics to the GISS. The observed decrease in the precipitation extends towards the eastern part of the VRB which highlights some of the difference between the spatial pattern of the two models. The magnitude of the decrease in precipitation ranges between 0 to 15 mm/year^2 while the increase ranges from 0 to 20 mm/year^2. Unlike in the Near and Mid term, the MPI-HR projected had a statistically significant positive change in precipitation over the VRB.

The Ensemble means projections of precipitation change defer from that of the Near and Mid term. Positive changes were projected in the Far term which spreads over almost the entire basin. In the Near and Mid term, a decrease in precipitation of similar magnitude was projected over the VRB which affects more areas in the Mid term than in the Near term under SSP1-26.

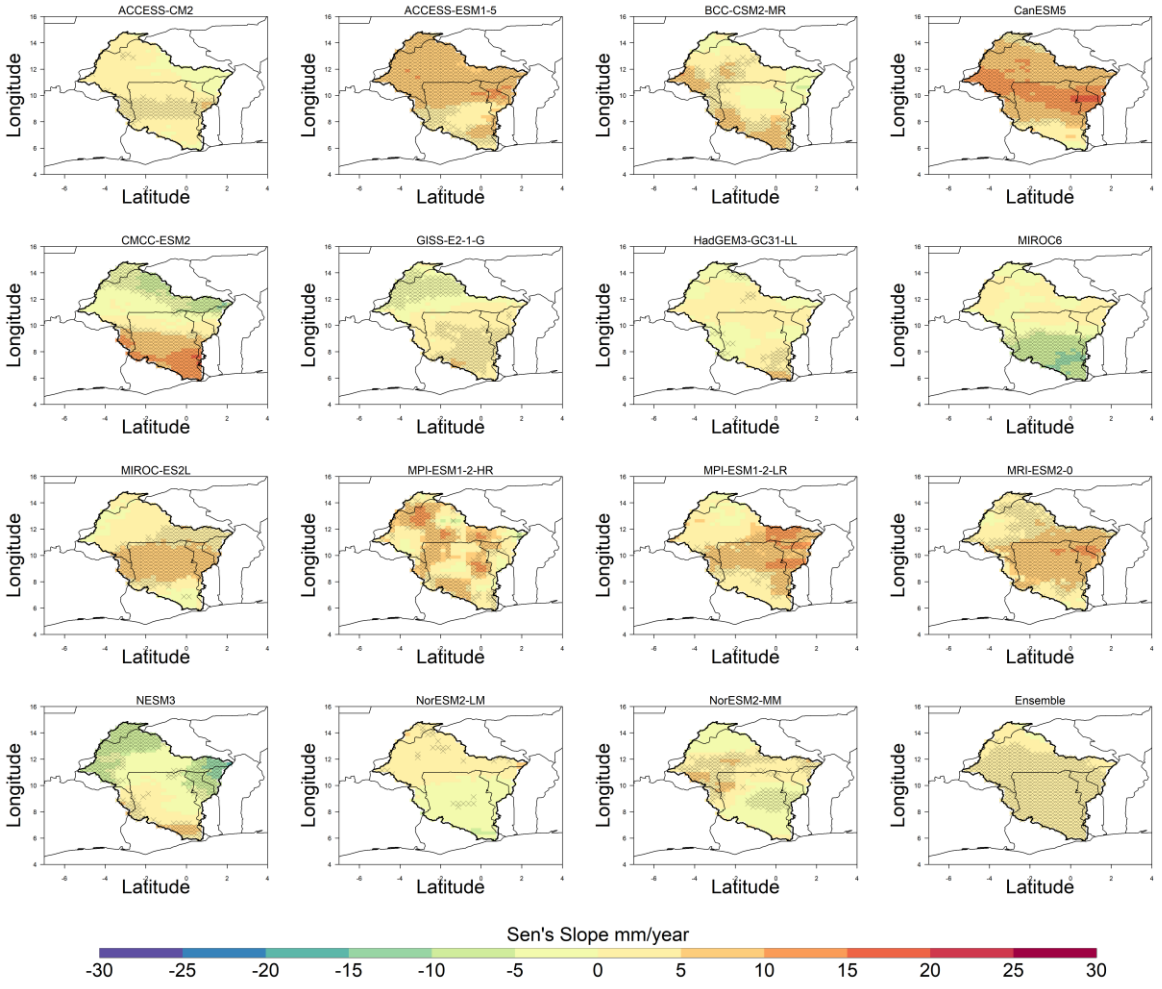

Figure 4.16: Comparison of Far term (from 2081 to 2100) precipitation trends of NEX-GDDP models under Socioeconomic Shared Pathways SSP 1-2.6 scenario using Thiel Sen's slope. The black crosses represent areas with trends that are significant at a 95 % confidence level

Figures 4.17, 4.18 and 4.19 present the results of the estimated slope and trend detected in precipitation under SSP 2-4.5 emission scenario for the Near term (NF), Mid term (MF) and Far term (FF). From Figure 4.17, the models ACCESS-CM2, ACCESS-ESM1, CanESM5, CMCC, NESM3, NorESM2-LM and NorESM2-MM projected more statistically significant positive change in precipitation than negative trends. In ACCESS-CM2, positive gains in precipitation were projected over the northern part of the VRB from latitude 11 °N extending from the east to the west part of the VRB. The gains range from 5 to 15 mm/year^2 with the highest at the northern edge of the basin around the border of Mali and Burkina Faso. There were positive changes (0 - 5 mm/year^2) around the southern edge of the VRB and Akosombo dam areas while a negative trend (0 – 5 mm/year^2) extends from the central part of the VRB to the eastern part. In ACCESS-ESM1, a statistically significant positive change (0 – 10 mm/year^2) was present between latitude 10 °N and 7 °N extending from the east to west. There also existed a negative trend (0 – 15 mm/year^2) around the southern edge of the VRB and Kpong dam areas. In CanESM5, the positive trend occurred throughout the entire VRB and they were statistically significant. In CMCC, statistically significant changes occurred only in the northern part of VRB from latitude 10 °N. In NESM3, a statistically significant positive trend existed around the eastern part of VRB over northeastern Ghana, southeastern Burkina Faso and northern Togo and Benin. In NorESM2-LM, a statistically significant positive trend (5 – 25 mm/year^2) was detected in the southern part of the VRB from latitude 8 °N. In NorESM2-MM, a statistically significant positive trend (5 – 20 mm/year^2) was found in the northern part from latitude 11 °N and the southern part of latitude 10 °N of the VRB.

Models such as BCC, GISS, HadGEM-LL, MIROC-ES2L, MPI-HR and MRI projected more negative trends than positive trends in the VRB. In the BCC model, statistically

significant negative changes (5 – 15 mm/year^2) mostly occurred in the southern part of the VRB from latitude 8 °N southward. Some small areas in the north of the VRB also showed a statistically significant negative trend (0 – 5 mm/year^2) and small areas in the east of the VRB over the border of Benin and Burkina Faso showed a statistically significant positive trend (0 – 5 mm/year^2). In GISS, most parts of the basin were projected to experience changes ranging from 0 – 15 mm/year^2 from latitude 11 °N southwards while some areas in the north were projected to experience positive changes (0 – 5 mm/year^2). The HadGEM-LL model was projected to have statistically significant negative changes (0 – 15 mm/year^2) extending from the north to south of the entire basin which was localised along the central and western parts of the VRB. There was a statistically significant positive trend (0 – 10 mm/year^2) in the eastern part of the VRB around southeastern Burkina Faso. Most parts of the MIROC-ES2L model projected a major statistically significant decrease in precipitation (0 – 20 mm/year^2) in the central and northern parts of the VRB from latitude 9 °N. Some parts of the southern parts from latitude 8 °N southwards. In MPI-HR more than 60 % of the basin might experience statistically significant negative trends (5 to 30 mm/year^2). In MRI, almost the entire VRB was projected negative trends (5 to 20 mm/year^2) which were statistically significant. The greatest decrease (10 – 15 mm/year^2) occurred around the Lake Volta area and central Togo. The MPI-LR model showed less than 10 % of the VRB experienced any kind of change in the precipitation. The MIROC6 model showed the northern part of the VRB from latitude 10.5 °N might experience statistically significant positive trends (0 – 15 mm/year^2) and statistically significant negative trends (0 – 10 mm/year^2) in the southern part of the basin from latitude 10 °N. In the Ensemble mean, statistically significant negative trends exceeded the statistically significant positive trends. The statistically significant negative trends (0 – 10 mm/year^2) occurred from the east to

west part of the VRB between latitude 11 °N and 6 °N. The positive statistically significant change occurred in the northern and eastern parts of the VRB from latitude 11 °N.

In the Mid term (Figure 4.18), ACCESS-CM2, CanESM5, CMCC, HadGEM-LL, MPI-HR, NorESM2-LM and NorESM2-MM projected more statistically significant positive change in precipitation more than negative trends while BCC, GISS, MIROC6, MIROC-ES2L, MPI-LR and MRI projected more statistically significant negative change in precipitation more than positive trends in the VRB. In ACCESS-CM2, a positive statistically significant change (0 – 10 mm/year^2) throughout the entire VRB. This is different from the patterns observed in the NF where the areas projected to experience changes were not basinwide but less than 50 % of the VRB as observed in the MF. Similarly, CanESM5 changes were similar to that of the CanESM5 model in the NF where a positive statistically significant change was projected basinwide. The only difference between them is the magnitude where CanESM5 in MF had a higher range of 5 to 25 mm/year^2. Major precipitation gains were observed at Black Volta, White Volta and Oti Basin along the Upper West region and Oti Region of Ghana, south and central Burkina Faso. The changes (0 – 10 mm/year^2) in HadGEM-LL were also found throughout the VRB and were statistically significant. The changes occurred in all the subbasins. In CMCC, a positive statistically significant change (0 – 10 mm/year^2) localised from within latitude 13 °N to 8 °N from the east to west of the VRB. More areas showed statistically significant changes in the CMCC MF than NF. In MPI-HR, a positive statistically significant change (0 – 15 mm/year^2) in all the subbasins occurring in the east, west south and north of the VRB. This is different from changes in the NF where changes show a decrease in precipitation. The statistically significant changes occurred in less than 40 % of the VRB. In NorESM2-LM, a positive statistically significant change (5 – 20 mm/year^2) occurred in most parts from latitude 12 °N southwards while a

positive statistically significant change (5 – 15 mm/year^2) was observed in most parts from latitude 9 °N northwards extending from east to west in the VRB projected by NorESM2-MM. More areas showed statistically significant positive changes in the NorESM2-LM MF than NF. The case is different from NorESM2-MM where more areas showed statistically significant positive changes in the NF than MF.

In BCC, a projected negative significant change (0 – 15 mm/year^2) was observed in most parts of the basin. These changes were seen in the White Volta, Lower Volta and Oti basins. More areas showed significant changes in the BCC MF than NF. In GISS, a negative statistically significant change (0 – 10 mm/year^2) was projected over most parts of the VRB from latitude 8 °N northwards. In the MF, changes are more skewed to the north unlike in the south as seen in NF. The magnitude is also higher in the NF than in MF. In MIROC6, negative changes were observed within latitudes 11 °N and 7 °N which was skewed more towards the east of the VRB. Comparing the NF and MF, the MF only showed negative significant trends while positive and negative trends were observed in NF. MIROC-ES2L projected a negative statistically significant trend from the central to northern parts of the VRB. This was different from patterns observed in the NF which exhibited both negative and negative trends. In MPI-LR, a projected negative significant trend (5 – 20 mm/year^2) from latitude 8 °N. There were more negative significant changes in the MF than observed in the NF. MRI projected negative significant changes in the northern parts from latitude 13 °N northwards and southern parts from latitude 8 °N of the basin. NESM3 projected almost equal portions of the basin that might experience negative and positive significant changes. Positive significant changes occurred from the central to eastern parts around latitudes 8 °N and 11 °N of the VRB and negative significant changes in the western around latitudes 7 °N and 9 °N. There were more areas projected to experience significant changes

in the MF than in the NF. Similar to NESM3, the ACCESS-ESM1 also projected almost equal portions of the basin that might experience negative and positive significant changes. The difference between them was that ACCESS-ESM1 projected significant negative changes (5 – 15 mm/year^2) from latitude about 10 °N northwards and significant positive changes (5 – 15 mm/year^2). This deviates from the patterns observed in the NF which had fewer areas projected to experience significant changes. Also, a lot more areas might experience decreased precipitation. In the Ensemble mean, more areas were projected to experience significant positive changes (0 – 5 mm/year^2) in more than 70 % of the VRB which is skewed southwards from latitude 12 °N and extended from the east to the west. This differs from the NF where there were more negative significant changes and positive significant changes in the north extending to the east.

In the FF (Figure 4.19), the models ACCESS-CM2, CMCC, HadGEM-LL, MIROC6, MIROC-ES2L, NESM3 and NorESM2-MM projected more areas with a positive statistically significant increase in precipitation than negative changes in the VRB. Precipitation in the ACCESS-CM2 model is projected to decrease in the north and increase around the central to the eastern part of the VRB and the border between Ghana and Burkina Faso, and in the south, from latitude 9 °N in the FF. The changes in these areas were statistically significant. The model projected more areas becoming wetter in the MF than in the NF and the FF. The NF will also be wetter than the FF. In CMCC, the projected positive statistically significant changes (10 – 30 mm/year^2) occurred from latitude 10 °N, propagating southward and statistically significant negative changes (5 – 20 mm/year^2) from latitude 12 °N in the northern part of the VRB, which extends from the east to the west. Precipitation was projected to increase in the FF more than in the MF and in the MF more than in the NF. In HadGEM-LL, statistically significant positive changes were

localised within latitudes 9 and 11 °N and extended from the central to western parts of the VRB. Precipitation was projected to increase in the MF more than in the FF and in the FF more than in the NF. In the MIROC6, most areas of the VRB were projected to experience statistically significant positive changes (0 – 15 mm/year^2) with the greatest magnitude occurring in northern Ghana around the Upper East and West Regions, and northern Togo (around the *Savanes* Region) and Benin. Precipitation was projected to be greater during the FF, followed by the NF, and lastly the MF. MIROC-ES2L generally projected statistically significant gains (5 – 30 mm/year^2) in rainfall in most parts of the basin with the highest magnitude of change (25 – 30 mm/year^2) anticipated around the Bui Dam, Bamboi and their environs. Precipitation was projected to be greater during the FF, followed by the MF, and lastly the NF. In the NESM3, the statistically significant positive changes (5 – 20 mm/year^2) were localised around the Volta Lake areas. Precipitation was projected to be greater during the NF, followed by the FF, and lastly the MF, but more areas might experience significant changes during the MF than the NF and in the MF than the FF. In NorESM2-LM, projected statistically significant positive changes (5 – 20 mm/year^2) from latitude 9 °N northwards with most change areas skewed from the central towards the west of the VRB. Statistically significant negative changes (5 – 20 mm/year^2) might occur in the southern parts of the VRB from latitude 8 °N southward. Overall precipitation gains were projected to occur more in the MF than in the FF and in the FF than in the NF.

The models ACCESS-ESM1, BCC, CanESM5, GISS, MPI-HR, MPI-LR and MRI projected more areas with a negative statistically significant increase in precipitation than positive changes in the VRB in the FF (Figure 4.19). For example, the ACCESS-ESM1 model projected that the majority of areas in the VRB would experience a reduction of 5–20 mm/year^2 in rainfall, especially in the northern and eastern parts. It is projected that more

areas will experience a reduction in rainfall in the FF than in the MF, and the MF more than in the NF, where there will be more areas with an increase than a decrease. In BCC, significant changes occurred in more areas in the northern part from latitude 10 °N northward than in the southern part between latitude 6.5 °N and the mouth of the VRB. In the BCC model, more areas would undergo rainfall reduction in the MF than in the FF, and the MF more than in the NF. In CanESM5, a reduction in precipitation might occur in greater parts of the VRB, which was mostly observed from latitude 13 °N southward and extends from east to west. More reductions in precipitation were anticipated to occur in the eastern and southern parts of the basin. There would be more gains in precipitation in the MF than the NF and will shift to reduce in the FF. The GISS model projected a statistically significant negative change in the southern part of the basin from latitude 6.5 °N to the mouth of the river. The Model projected more areas with significant reductions in precipitation in the NF than the MF, and in the MF than the FF. MPI-HR projected a loss in precipitation of 5 – 20 mm/year^2 in more than 50% of the VRB. These changes are statistically significant. Comparing precipitation patterns during the different future periods, more gains are expected in the MF, followed by the NF, and then the FF. Precipitation decreased significantly in the FF. In MPI-LR, projected statistically significant losses in precipitation of 5 – 30 mm/year^2 in the northern and eastern parts of the VRB. The biggest magnitude of change (23 – 30 mm/year^2) was in the northern part of Benin. There would be more gains in precipitation in the MF than the FF and will shift to reduce in the NF.

The NorESM2-MM projected that almost 99 % of the changes in rainfall observed in the VRB were not statistically significant in the FF. A very small part of the northmost edge of the VRB exhibited statistically significant negative changes. The Ensemble mean of the

models projected statistically significant negative changes from latitude 10 °N northward and statistically significant positive changes from about 10 °N southward which is skewed towards the western part of the VRB. Comparing precipitation patterns during the different future periods, more gains are expected in the MF, followed by the FF, and then the NF.

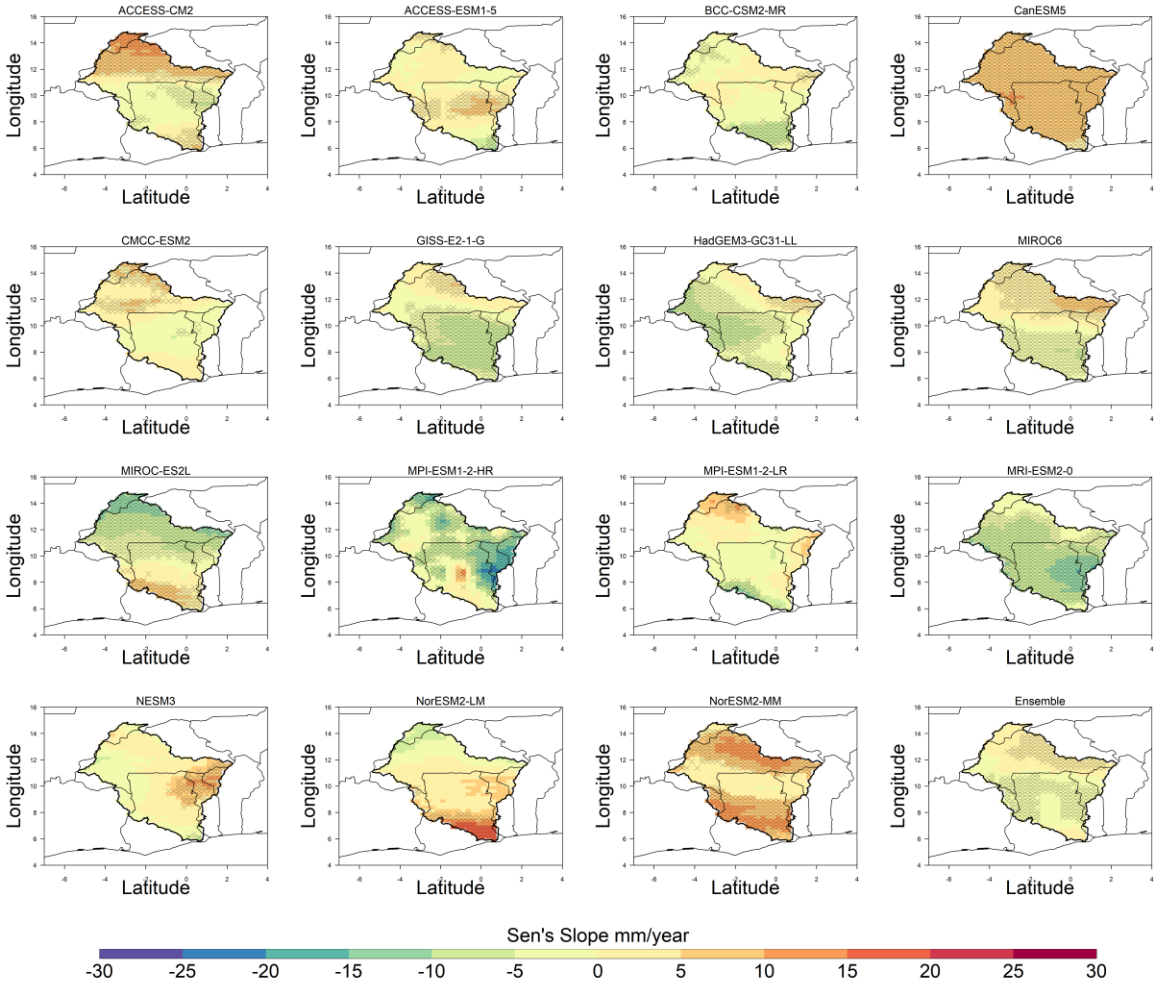

Figure 4.17: Comparison of Near term (from 2021 to 2050) precipitation trends of NEX-GDDP models under Socioeconomic Shared Pathways SSP 2-4.5 scenario using Thiel Sen's slope. The black crosses represent areas with trends that are significant at a 95 % confidence level

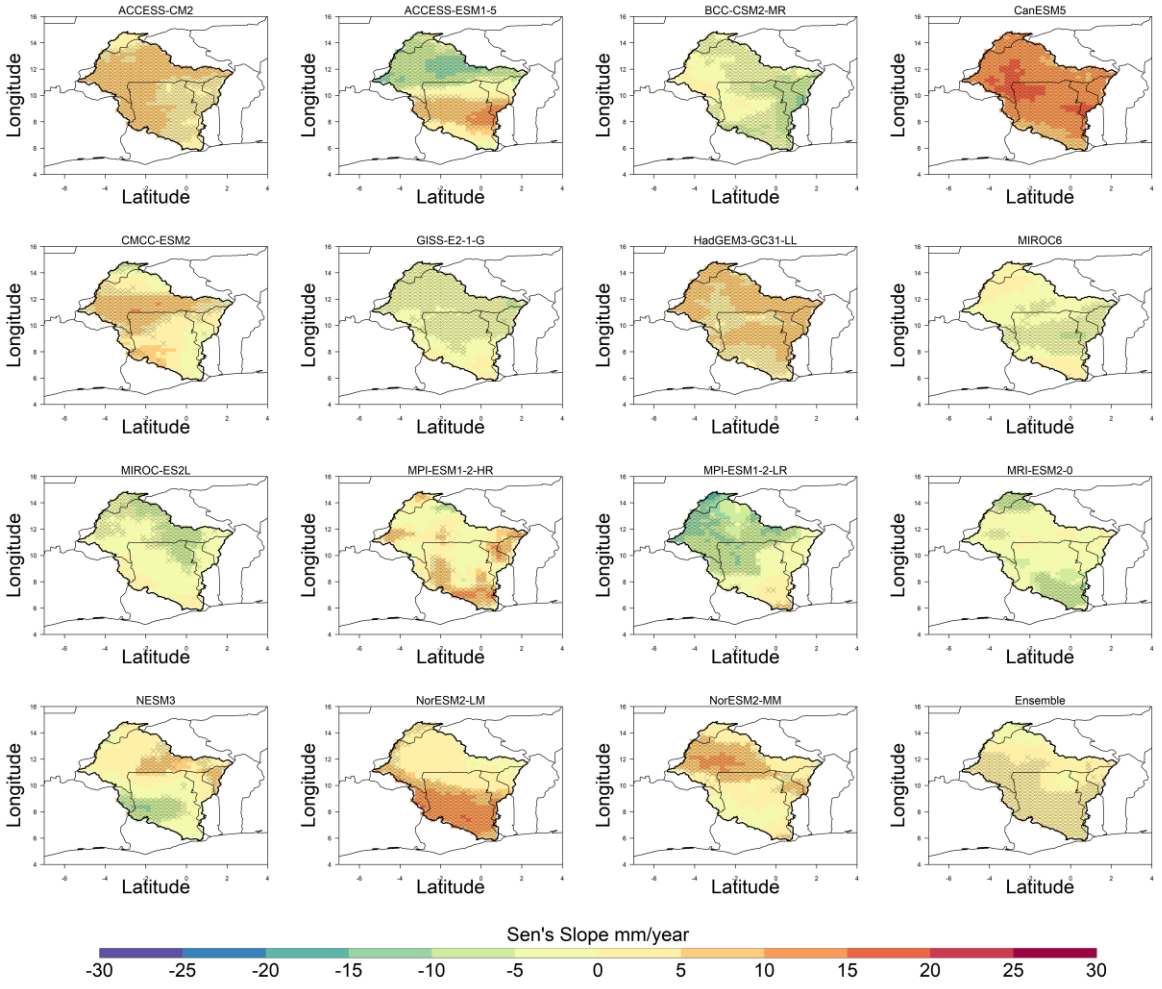

Figure 4.18: Comparison of Mid term (from 2051 to 2080) precipitation trends of NEX-GDDP models under Socioeconomic Shared Pathways SSP 2-4.5 scenario using Thiel Sen's slope. The black crosses represent areas with trends that are significant at a 95 % confidence level

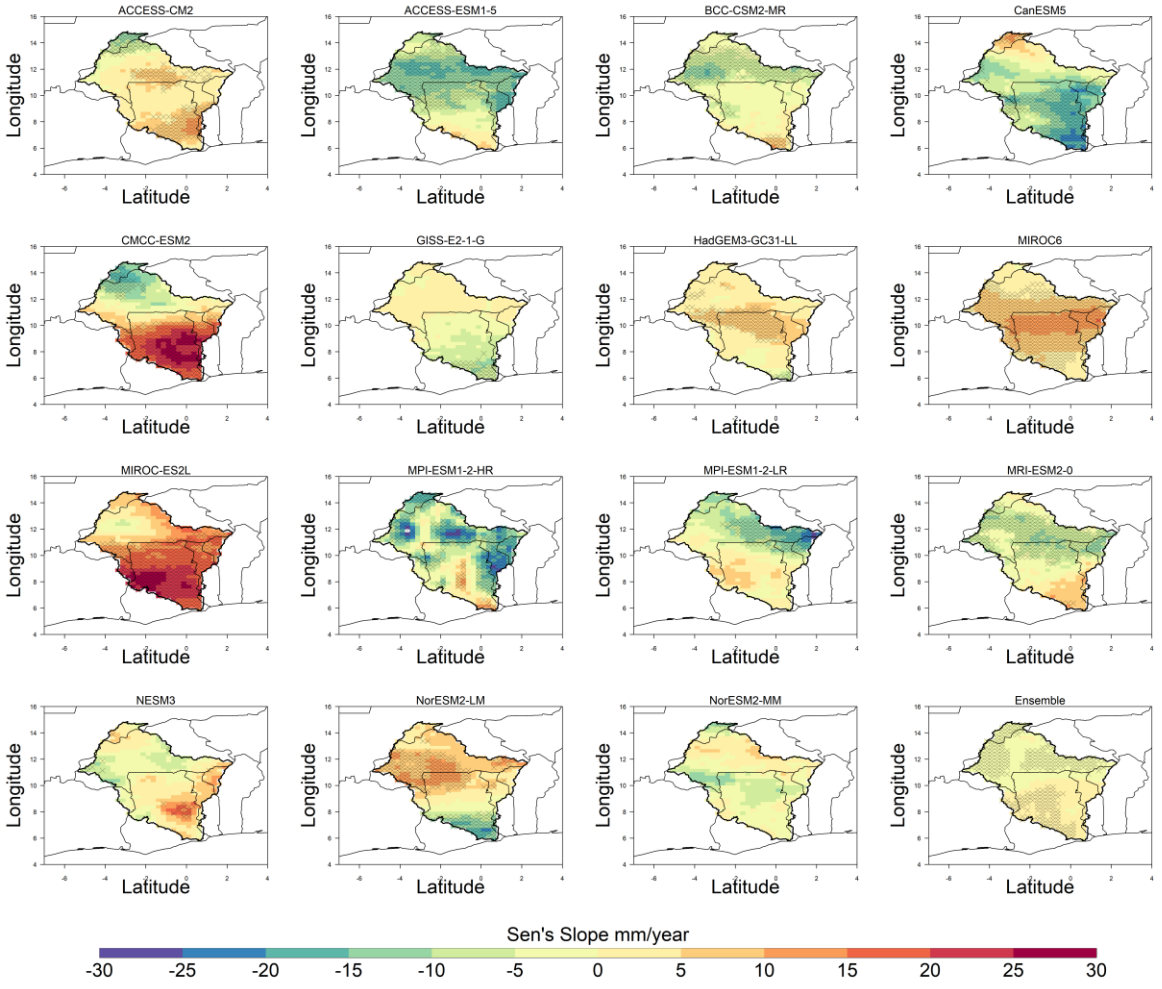

Figure 4.19: Comparison of Far term (from 2081 to 2100) precipitation trends of NEX-GDDP models under Socioeconomic Shared Pathways SSP 2-4.5 scenario using Thiel Sen's slope. The black crosses represent areas with trends that are significant at a 95 % confidence level

Figures 4.20, 4.21 and 4.22 present the results of the estimated slope and trend detected in precipitation under SSP 5-8.5 emission scenario for the Near term (NF), Mid term (MF) and Far term (FF) respectively. From Figure 4.20, the models CanESM5, CMCC, MIROC6, MPI-HR, and MRI projected more statistically significant positive changes in precipitation than negative trends, while the models like ACCESS-CM2, ACCESS-ESM1, BCC, GISS, HadGEM-LL and NorESM2-LM projected the opposite in the NF. Other models, such as MIROC-ES2L, MPI-LR, NESM3 and NorESM2-MM, projected statistically significant negative and positive changes with almost equal areas of significant change in the VRB. Their spatial patterns differ from model to model. For instance, NorESM2-MM projected more areas (> 60 % of the VRB) that will experience changes in precipitation while MIROC-ES2L, MPI-LR and NESM3 projected less than 40 % of the VRB will experience changes. The CanESM5, CMCC and MPI-HR projected that more than 60 % of the basin would experience an increase in rainfall. The models with high precipitation biases were CanESM5 and MPI-HR with most areas of change values between 10 and 30 mm/year^2. The model with less precipitation bias was GISS with statistically significant decreases in precipitation in the NF.

On the contrary, the models ACCESS-CM2, CMCC, MPI-HR, MPI-LR and NorESM2-LM projected more significant positive changes in precipitation than negative trends, while the models like ACCESS-ESM1, BCC, CanESM5, GISS, HadGEM-LL, MIROC-ES2L, NESM3, MRI and NorESM2-MM projected the opposite in the MF (Figure 4.21). The number of areas projected to undergo positive significant changes increased appreciably in ACCESS-CM2, MPI-LR and NorESM2-LM, where areas with positive significant areas became dominant in the VRB in the MF, unlike as projected in the NF. Similarly, CanESM5, MIROC-ES2L, NESM3, NorESM2-MM and MRI also projected more areas to

experience negative statistically significant changes different from the spatial patterns observed in the NF. MIROC6 projected almost equal proportions of areas that would experience negative and positive change, which were significant. This was different from spatial patterns in the NF, where most of the changes projected were significant positive changes. In the MF, the wettest model was MPI-HR and the driest was MRI.

Additionally, the models ACCESS-CM2, BCC, CanESM5, CMCC, HadGEM-LL, MPI-LR, MRI, NESM3 and NorESM2-MM projected more significant positive changes in precipitation than negative trends, while the models like ACCESS-ESM1, GISS, MIROC6, MIROC-ES2L, MPI-HR and NorESM2-LM projected the opposite in the FF (Figure 4.22). The model with high precipitation bias was NESM3, with most areas of change values between 10 and 50 mm/year^2. The model with less precipitation bias was MPI-HR, with most areas experiencing significant decreases in precipitation between -10 and 60 mm/year^2. The ACCESS-ESM1 and GISS models were projected to have more significant negative changes throughout the NF, the MF and the FF. For instance, in the ACCESS model, more spatial areas experienced significant changes in the MF, followed by the FF, and then the NF. The highest change in precipitation magnitude was recorded in the FF, ranging from -30 to -40 mm/year^2. Also, in the GISS model, significant changes occurred throughout the VRB in both the NF and the MF, which was more than spatial changes in the FF. The highest change in precipitation was recorded in the FF, ranging from -20 to -30 mm/year^2. The CMCC was the only model that showed gains in precipitation throughout all future periods. There were more statistically significant areas of change and the highest magnitude of change (30 – 40 mm/year^2) in the FF, followed by the NF, and then the MF. The HadGEM-LL and the BCC projected dominantly significant negative spatial changes in the NF and the MF and statistically significant positive spatial changes in the FF. The

vice-versa is seen in MPI-HR, where it projected dominantly significant positive changes in the NF and the MF and the opposite in the FF. ACCESS-CM2 and NorESM2-LM also projected dominantly significant negative spatial changes in the NF and significant positive spatial changes in the MF and the FF. On the contrary, CanESM5 and MRI projected dominantly significant positive spatial changes in the NF and the FF and significant positive spatial changes in the MF.

The Ensemble means of the models in the NF (Figure 4.20), the MF (Figure 4.21) and the FF (Figure 4.22) showed distinct spatial patterns of change in the basin. For example, the Ensemble mean in the NF (Figure 4.20), projected significant positive changes (0 – 10 mm/year^2) from latitude 9 °N northwards and significant negative changes (0 – 5 mm/year^2) from latitude 8 °N southward, both changes spread from the eastern to the western edges of the VRB. Conversely, the spatial patterns are different revealing dominant significant negative changes (0 – 10 mm/year^2) originating from latitude 12 °N southward and covering most of the basin below this 12 °N latitude in the MF. On the contrary, the Ensemble mean in the FF projected more significant positive changes (0 – 5 mm/year^2) majorly localised around the eastern, the northern and some areas in the central part of the VRB.

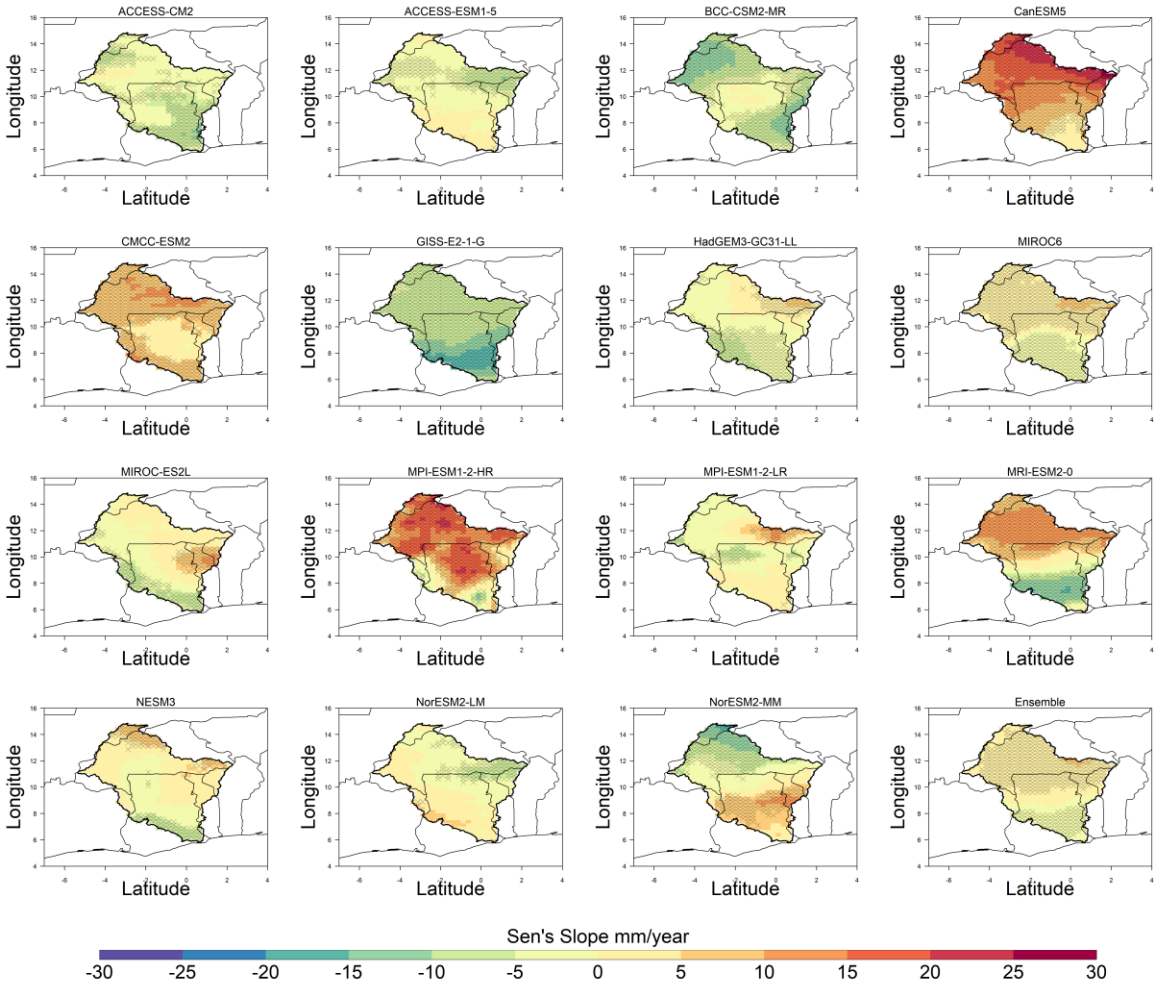

Figure 4.20: Comparison of Near term (from 2021 to 2050) precipitation trends of NEX-GDDP models under Socioeconomic Shared Pathways SSP 5-8.5 scenario using Thiel Sen's slope. The black crosses represent areas with trends that are significant at a 95 % confidence level

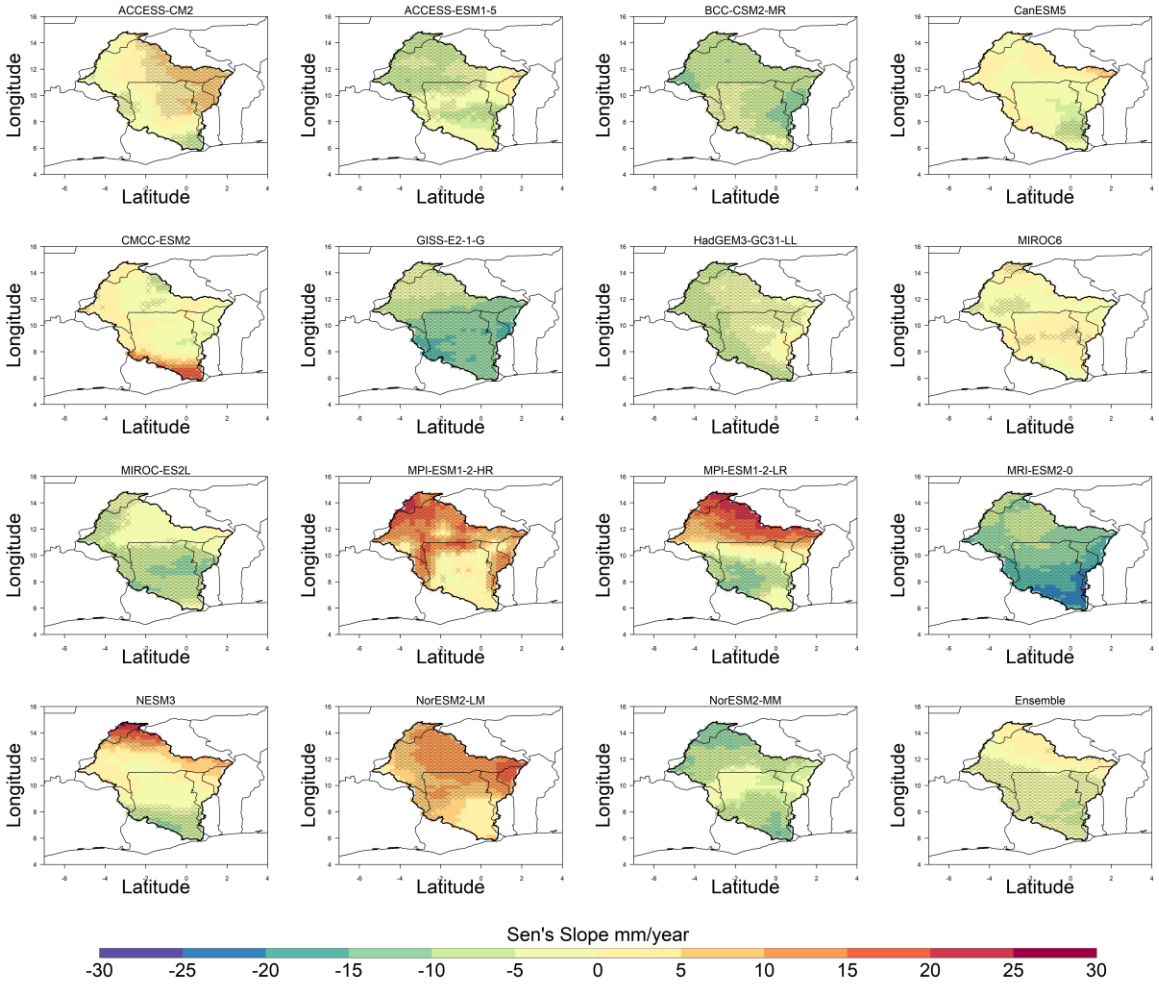

Figure 4.21: Comparison of Mid term (from 2051 to 2080) precipitation trends of NEX-GDDP models under Socioeconomic Shared Pathways SSP 5-8.5 scenario using Thiel Sen's slope. The black crosses represent areas with trends that are significant at a 95 % confidence level

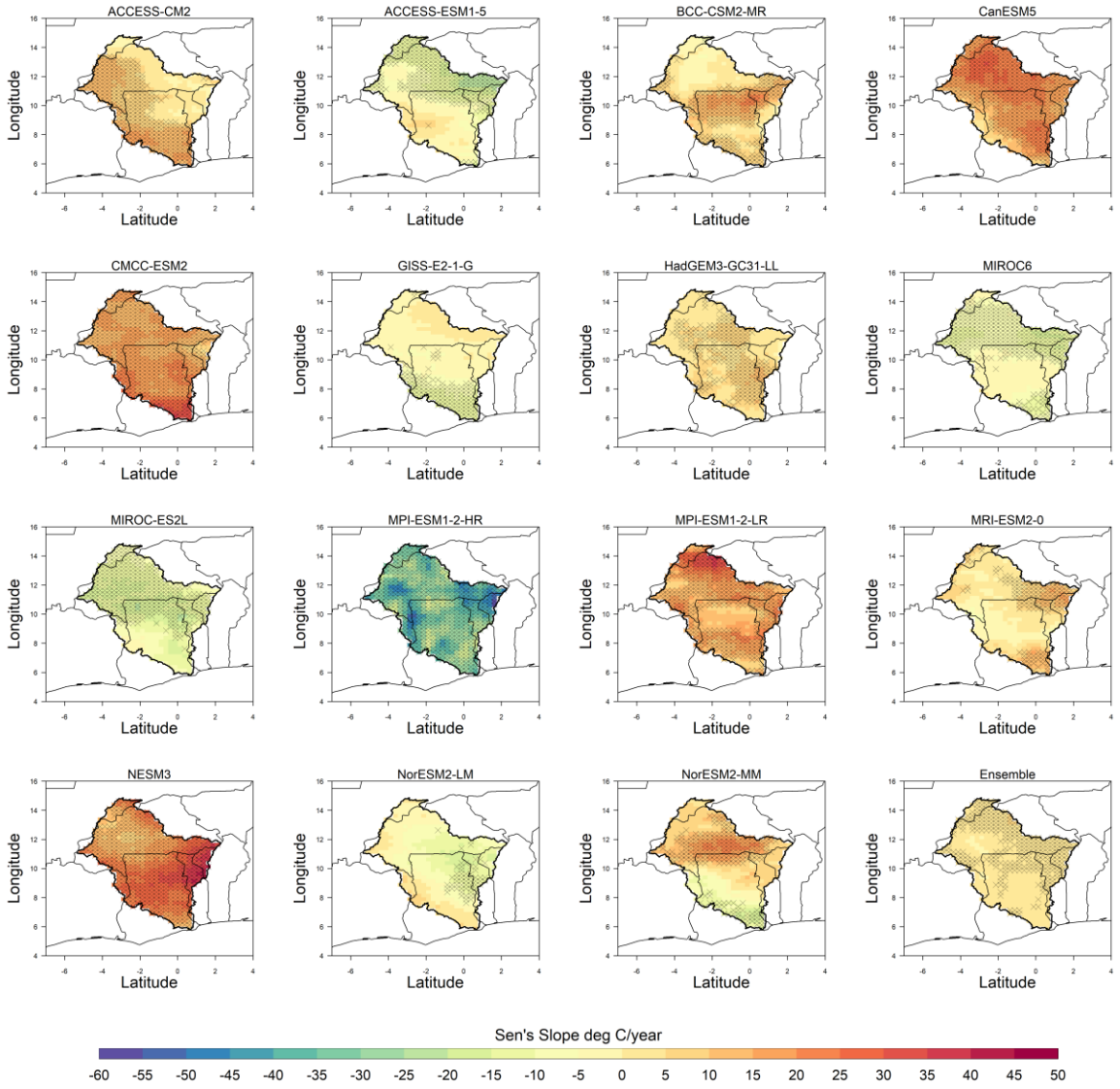

Figure 4.22: Comparison of Far term (from 2081 to 2100) precipitation trends of NEX-GDDP models under Socioeconomic Shared Pathways SSP 5-8.5 scenario using Thiel Sen's slope. The black crosses represent areas with trends that are significant at a 95 % confidence level

4.5.2.1 Future trends in temperature

Figures 4.23 to 4.31 presents the results of the Modified Mann Kendall and Sen's Slope trend of temperature for SSP1-26, SSP2-45 and SSP5-85, and the different period (NF, MF and FF).

Figures 4.23, 4.24 and 4.25 illustrate Sen's Slope computation for average temperature in the VRB, at NF, MF and FF respectively. From Figure 4.23, all the models except NorESM2-LM projected statistically significant temperature increase in most parts (more than 80%) of the VRB in the Near term (NF). All models had statistically significant changes ranging from 0 to 0.06 °C/year. The warmest model was CMCC with a change magnitude of 0.045 to 0.06 °C/year in the north of VRB from latitude 10 °N northwards and 0.03 to 0.045 °C/year southwards. Other models like ACCESS-CM2, GISS and MIROC-ES2L also projected more increase in temperature magnitude of 0.03 to 0.045 °C/year throughout the entire VRB. The NESM3 was the least warm model. There were no statistically significant changes observed in the NorESM2-LM in the NF. The Ensemble mean of the models projected statistically significant temperature increase (0.03 to 0.045 °C/year) throughout the entire VRB.

Figure 4.24 presents Sen's Slope result for the Mid term (MF). The ACCESS-ESM1, CanESM5, MRI and NorESM2-MM projected significant increases in temperature (0 to 0.03 °C/year) in most parts of the VRB in the Mid term (MF). CMCC projections were in this range but covered less than 50 % of the VRB. HadGEM-LL and NorESM2-LM projected no significant changes in temperature despite the former and the latter projecting decreases and increases in temperature in most of VRB respectively. The NESM3 projected decreases in temperature trend (-0.015 to 0 °C/year) in less than 50 % of the basin. This was the less warm model because it had mostly significant negative changes. The BCC

model also projected a significant decreasing temperature (-0.015 to 0 °C/year) in the east and an increasing temperature (0 to 0.015 °C/year) change in the north and south of VRB. ACCESS-CM2 and MPI-LR showed projected significant decreases in temperature, while MPI-HR also projected significant temperature increase in less than 10 % of the VRB. The warmest models were CanESM5 and MRI. The Ensemble mean of the models projected significant increases (0 to 0.015 °C/year) over the entire VRB.

In the Far term (FF) (Figure 4.25), most of the models projected a significant decreasing temperature change in the VRB except ACCESS-CM2, CMCC, MPI-LR, MRI and NorESM2-MM. ACCESS-CM2, MPI-LR and MRI showed no significant change in temperature in the VRB. CMCC and NorESM2-MM showed significant temperature increase of magnitudes 0.015 to 0.03 °C/year and 0.15 to 0.045 °C/year over less than 50 % and more than 70%, respectively. The coldest models were the BCC, CanESM5 and MIROC-ES2L with change magnitude ranging between -0.06 to -0.015 °C/year in most parts of VRB. In the Ensemble mean of the models, projected significant decreases in temperature (-0.015 to 0 °C/year) were observed basinwide in the VRB.

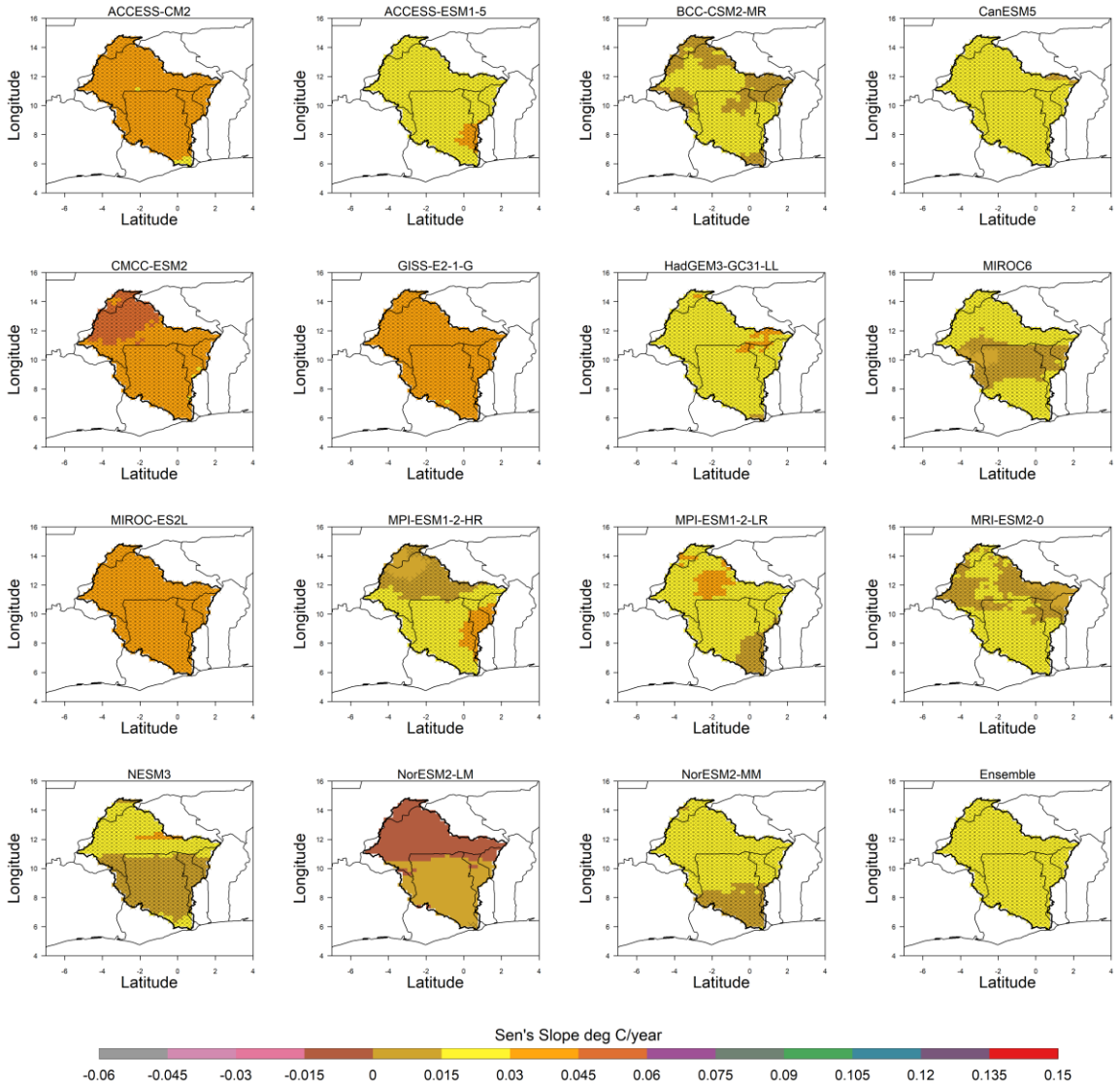

Figure 4.23: Comparison of Near term (from 2021 to 2050) temperature trends of NEX-GDDP models under Socioeconomic Shared Pathways SSP 1-2.6 scenario using Thiel Sen's slope. The black crosses represent areas with trends that are significant at a 95 % confidence level

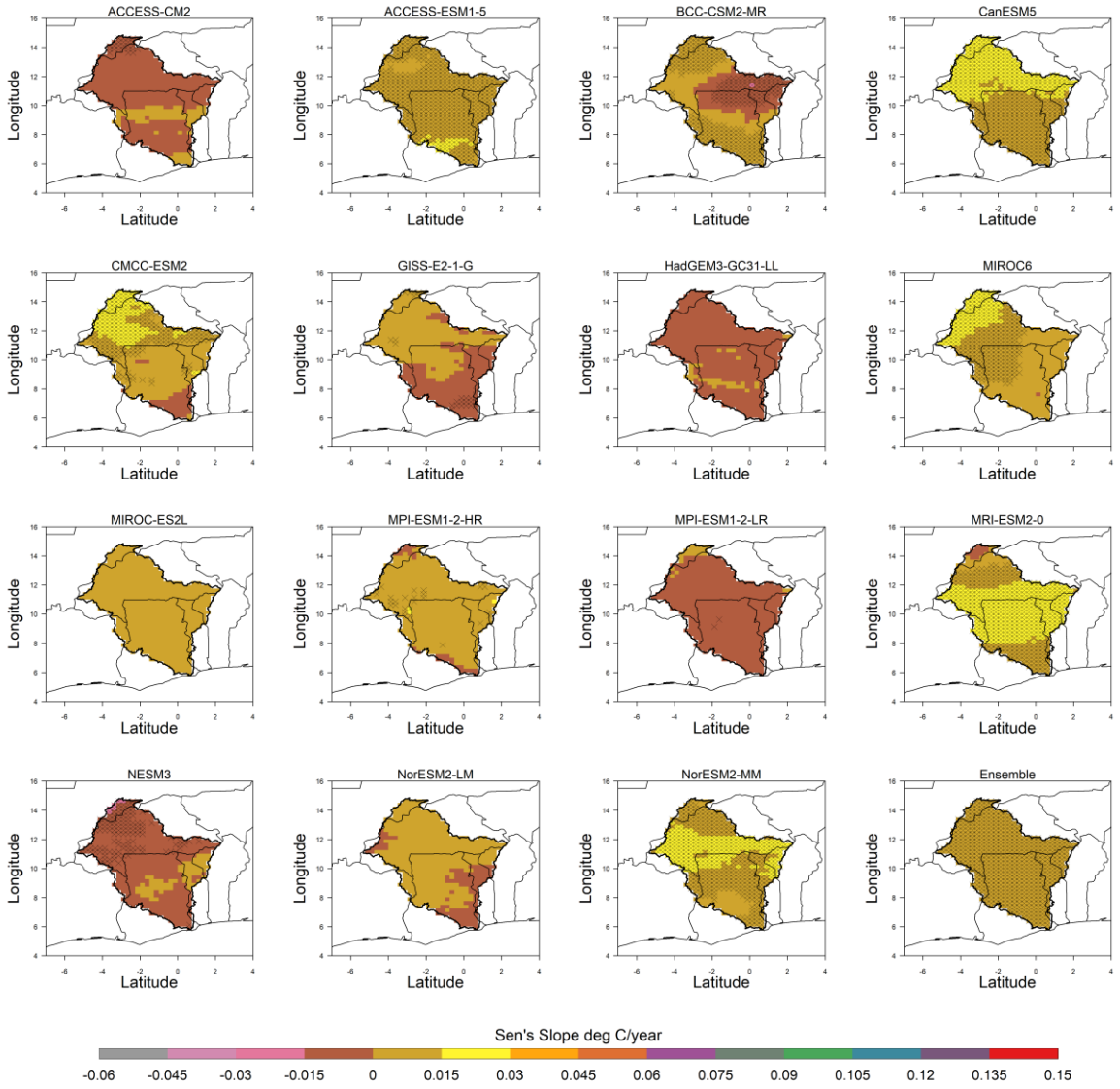

Figure 4.24: Comparison of Mid term (from 2051 to 2080) temperature trends of NEX-GDDP models under Socioeconomic Shared Pathways SSP 1-2.6 scenario using Thiel Sen's slope. The black crosses represent areas with trends that are significant at a 95 % confidence level

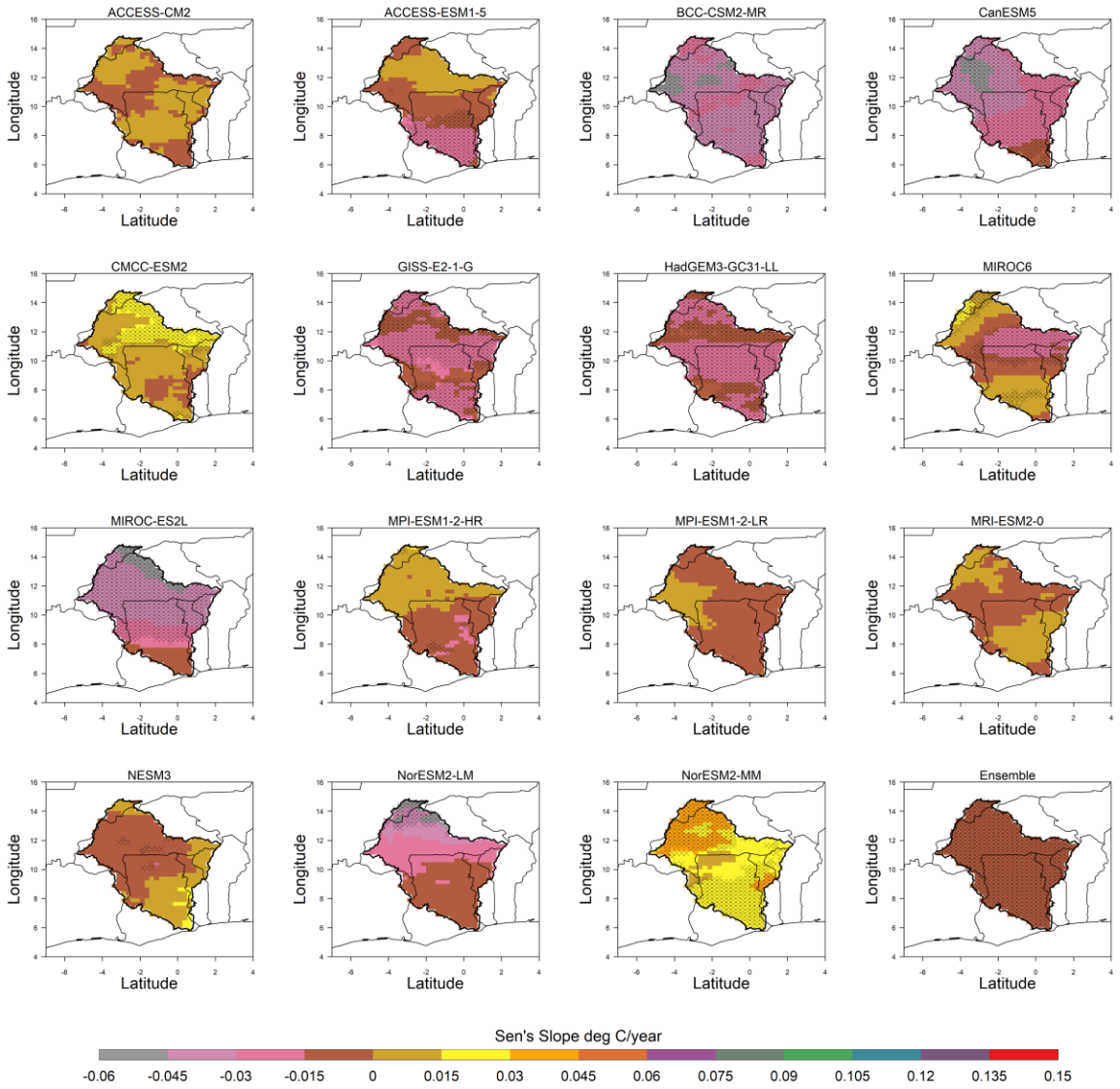

Figure 4.25: Comparison of Far term (from 2081 to 2100) temperature trends of NEX-GDDP models under Socioeconomic Shared Pathways SSP 1-2.6 scenario using Thiel Sen's slope. The black crosses represent areas with trends that are significant at a 95 % confidence level

Figures 4.26, 4.27 and 4.28 illustrate Sen's slope computation for average temperature in the VRB at NF, MF and FF, respectively, under SSP2-4.5. From Figure 4.26, all the models projected statistically significant temperature increase between 0 and 0.06 °C/year in the entire VRB in the Near term (NF). This is similar to the spatial patterns observed in the NF under SSP1-26, where most of the models except NorESM2-LM projected statistically significant changes. The model with the highest statistically significant temperature increase (0.03 to 0.06 °C/year) was ACCESS-CM2. Other models with similar magnitudes of change were ACCESS-ESM1, CMCC, GISS, HadGEM-LL and NorESM2-LM. The least warm models were MIROC-ES2L and NESM3. The ensemble mean projected that more than 90 % of the VRB will experience 0.03 to 0.045 °C/year statistically significant increases and 0.015 to 0.03 °C/year along the southern edge of the VRB.

All the models projected statistically significant temperature increase between 0 and 0.06 °C/year in the entire VRB in the Mid term (MF) (Figure 4.27). This was similar to the spatial patterns in the NF except for differences in their magnitude and NorESM2-LM being statistically significant in the MF. The warmest model was HadGEM-LL, with more areas in the VRB having magnitudes of change between 0.03 and 0.045 °C/year. ACCESS-CM2, ACCESS-ESM1, BCC and MPI-LR, with more than 50 % of the basin having projected changes from 0.03 to 0.045 °C/year. The highest magnitudes of change (0.045 to 0.06 °C/year) were seen in the ACCESS-ESM1 and MPI-LR. The least warm model was MPI-HR, with most areas projecting magnitudes of change from 0 to 0.015 °C/year in more than 50 % of the basin. In the ensemble mean, projected statistically significant temperature increase (0.015 to 0.03 °C/year) throughout the entire basin

In the Far term (FF) (Figure 4.28), most of the models projected a significant increasing temperature change in the VRB except MROC-ES2L and NorESM2-MM, which showed no statistically significant changes in the VRB. BCC had the highest significant magnitude of change (0.06 to 0.075 °C/year), occurring in a very tiny fraction in the north of the VRB. Generally, significant changes occurred in less than 40 % of the VRB projections of the BCC model. ACCESS-ESM1 was the warmest model in the FF, with more areas having change values between 0.03 and 0.06 °C/year. Other models, such as CanESM5 and HadGEM-LL, also showed most areas of the VRB undergoing 0.03 and 0.06 °C/year, like ACCESS-ESM1, except that they also had more areas under 0.015 and 0.03 °C/year temperature change when compared to the latter. NESM3 showed less than 5 % of the VRB will experience a 0.015 to 0.03 °C/year temperature increase, occurring in the west of the VRB. The ensemble of the models projected statistically significant temperature increase (0.015 to 0.03 °C/year) throughout the VRB. This was similar to the patterns observed in the ensemble in the MF. Comparing the ensemble means of the different periods, the magnitudes projected in the NF were greater than those of the MF and FF.

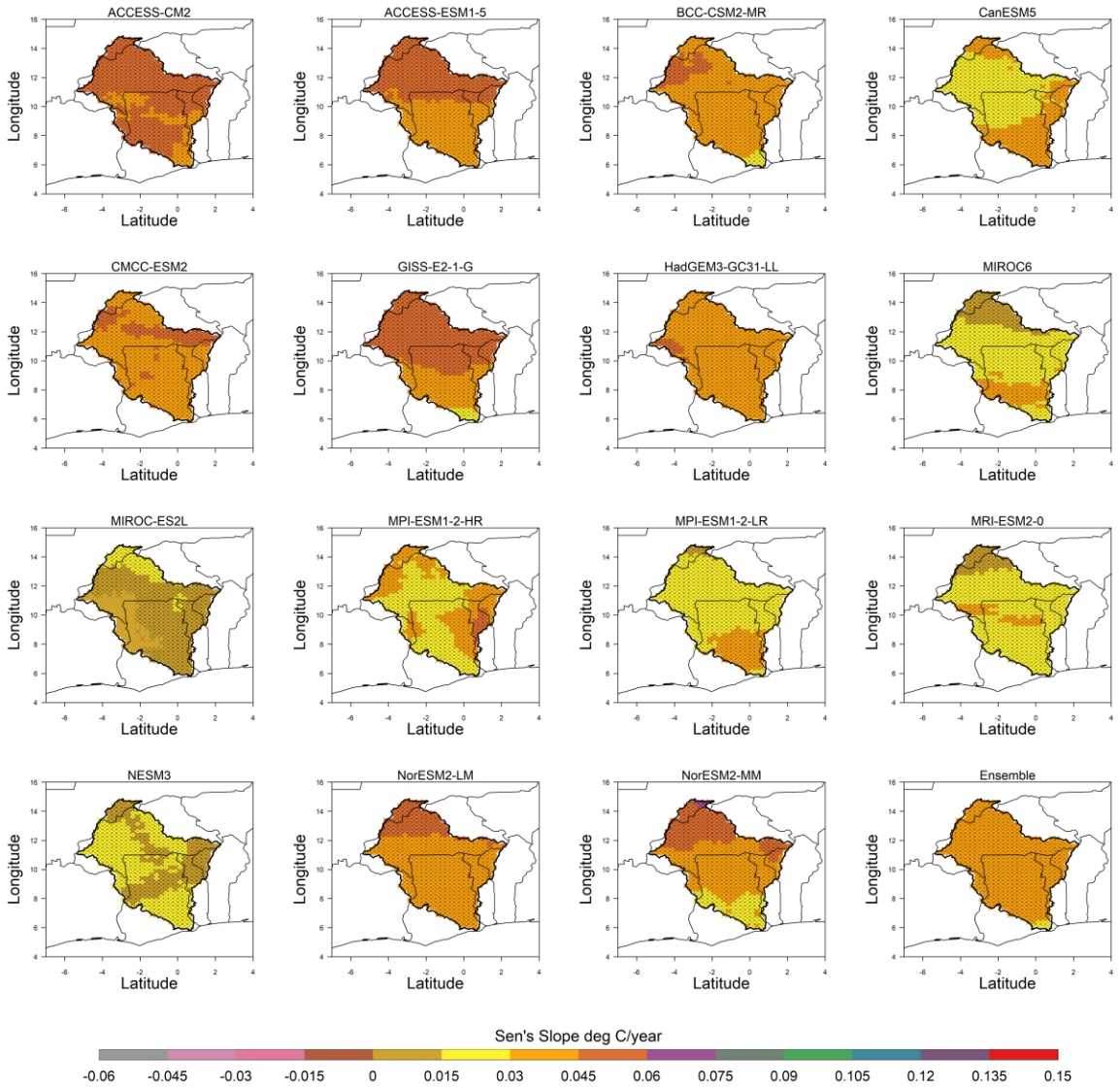

Figure 4.26: Comparison of Near term (from 2021 to 2050) temperature trends of NEX-GDDP models under Socioeconomic Shared Pathways SSP 2-4.5 scenario using Thiel Sen's slope. The black crosses represent areas with trends that are significant at a 95 % confidence level

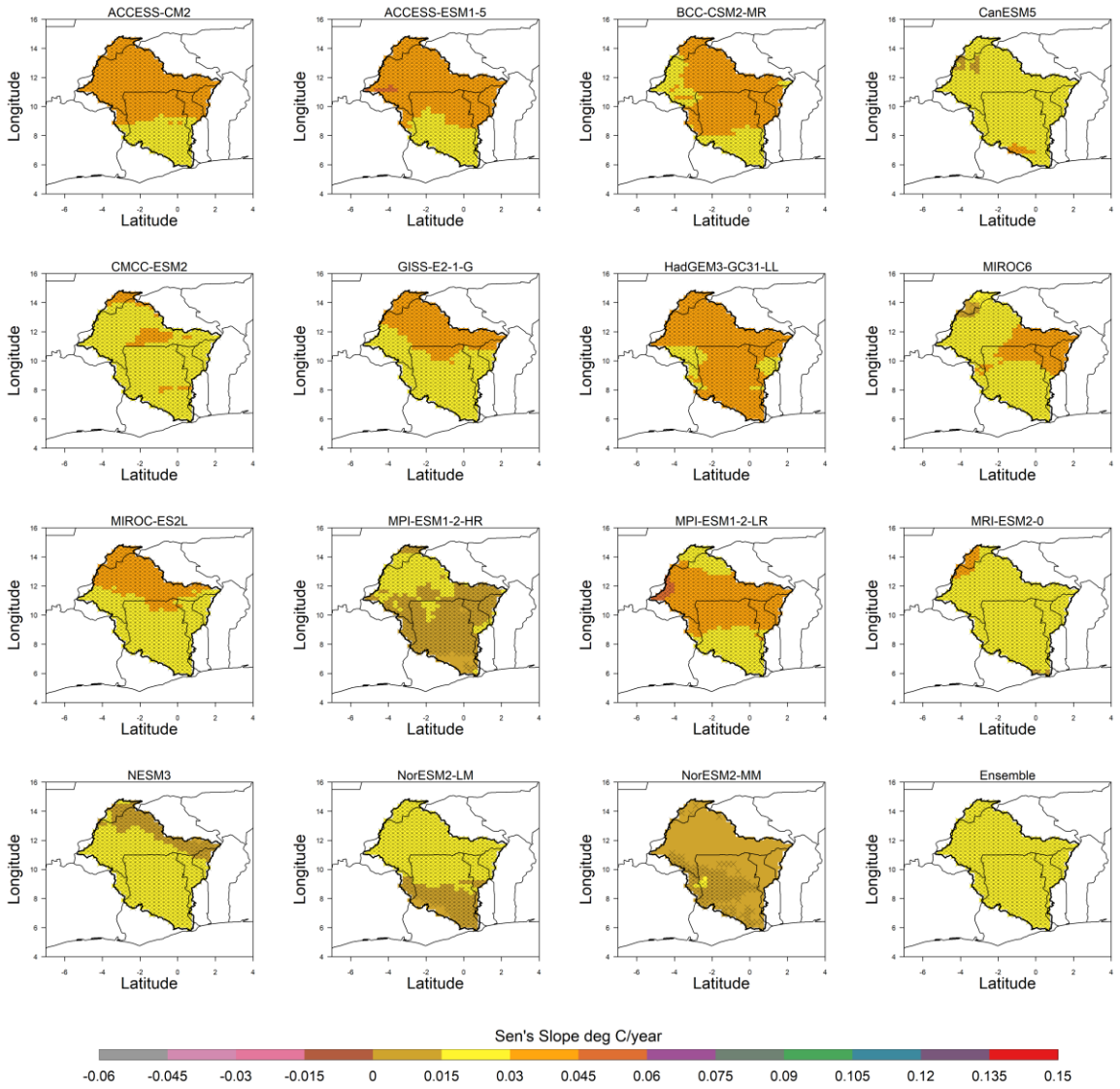

Figure 4.27: Comparison of Mid term (from 2051 to 2080) temperature trends of NEX-GDDP models under Socioeconomic Shared Pathways SSP 2-4.5 scenario using Thiel Sen's slope. The black crosses represent areas with trends that are significant at a 95 % confidence level

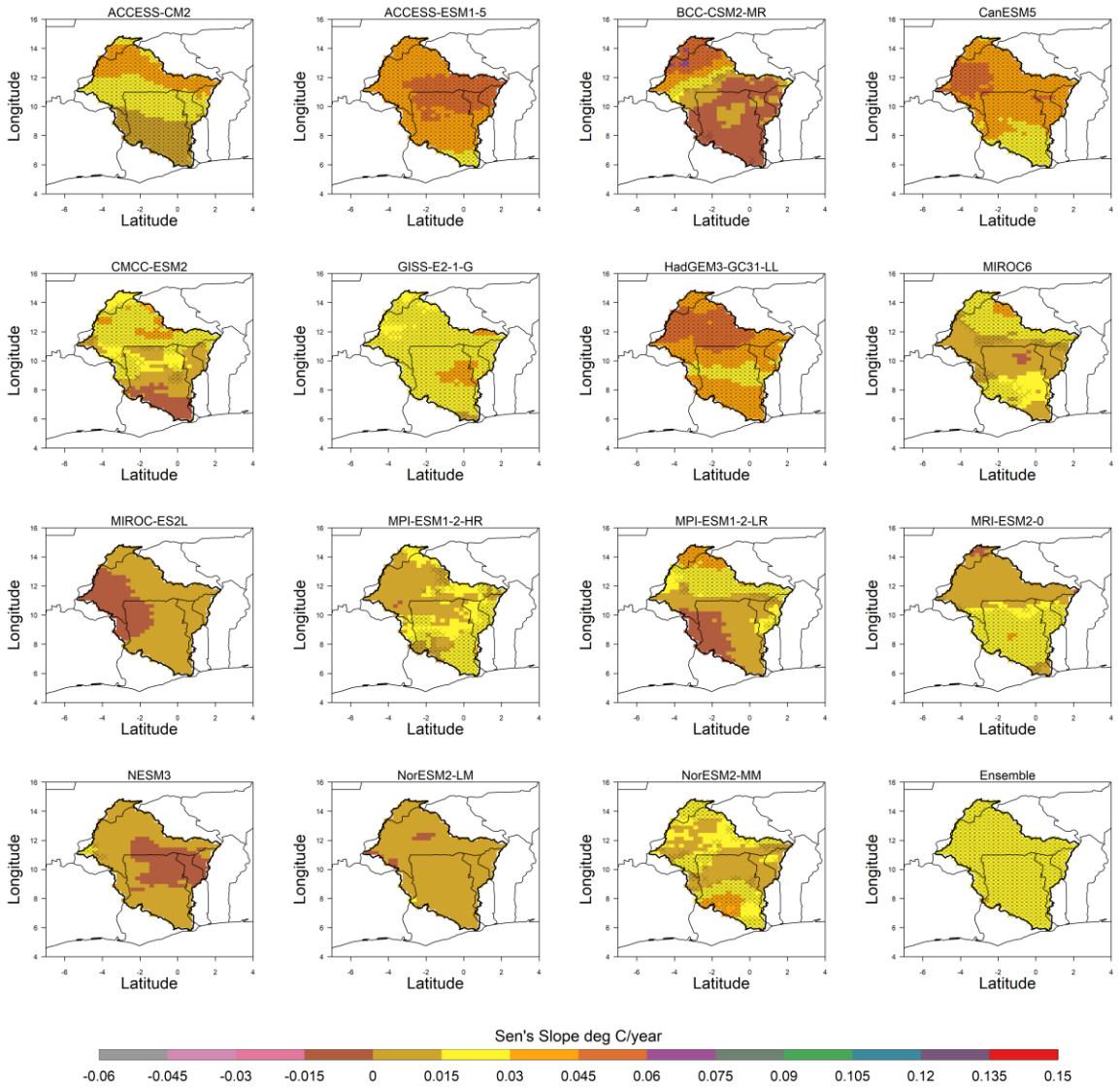

Figure 4.28: Comparison of Far term (from 2081 to 2100) temperature trends of NEX-GDDP models under Socioeconomic Shared Pathways SSP 2-4.5 scenario using Thiel Sen's slope. The black crosses represent areas with trends that are significant at a 95 % confidence level

Under the SSp5-8.5 scenario, temperature trends in the VRB increased in the NF (Figure 4.29), MF (Figure 4.30) and FF (Figure 4.31). In the NF, all the models and their ensemble mean projected statistically significant temperature increase between 0 and 0.09 °C/year throughout the entire VRB (Figure 4.29). Most of the models projected that temperature change would be higher in the northern half of the VRB. MRI and MIROC6 showed that the southern part of the basin would experience more prominent temperature changes than the northern part. The warmest model was GISS (0.045 – 0.09 °C/year), and the least warm model was MPI-HR (0 – 0.03 °C/year). Other warm models within the range of change of the GISS model were HadGEM-LL, ACCESS-CM2 and NorESM2-MM. The ensemble mean showed most areas in the VRB will experience a 0.045 to 0.06 °C/year temperature change. Only some small areas, from the mouth of the river to about latitude 6 °N in the south of VRB, exhibited a 0.03 to 0.045 °C/year temperature change.

In the Mid term (Figure 4.30), all the models generally projected warmer conditions (0.015 – 0.12 °C/year) than those observed in the NF (Figure 4.29). These temperature changes were significant throughout the VRB. The warmest model was CanESM5 (0.075 – 0.12 °C/year) and the least warm model was MPI-HR (0.015 – 0.06 °C/year). Other models, like the HadGEM-LL and MRI, also showed warmer trends with temperature changes between 0.06 and 0.105 °C/year. The ensemble mean projected that the entire VRB will experience 0.06 to 0.075 °C/year significant increases and 0.045 to 0.06 °C/year along the southern edge of the VRB. These temperature changes in the ensemble mean were greater in magnitude in the MF than in the NF.

In the Far term (Figure 4.30), all the models generally projected warmer conditions within magnitudes of 0.015 – 0.15 °C/year. About 60 % of the models, namely, ACCESS-CM2, ACCESS-ESM1, HadGEM-LL, CanESM5, GISS, MIROC6, MIROC-ES2L, MPI-HR and MPI-LR, were warmer in the FF than in the MF. Alternatively, about 40 % of the models, namely, BCC, CMCC, MRI, NESM3, NorESM2-LM and NorESM2-MM, were also less warm in the FF than in the MF. The warmest models were ACCESS-CM2 and HadGEM-LL, while the least warm model was BCC. The temperature changes observed in all the models were significant and occurred throughout the basin. The ensemble mean of the models projected that temperature might increase between 0.075 and 0.09 °C/year in the north of the basin from about latitude 10 °N northward and between 0.06 and 0.075 °C/year southwards of the same latitude. The ensemble projected more warming in the FF than in the MF and the MF than in the NF.

Generally, under the SSP1-2.6 scenario, ACCESS-ESM1, BCC, CanESM5, CMCC, GISS, HadGEM-LL, MIROC6, MPI-HR and MRI projected significant temperature changes between future periods, decreased from the NF, the MF and the FF. On the contrary, MPI-LR and NESM3 suggested the NF would be warmer than the FF and the FF warmer than the MF. Other models illustrated distinct temperature change patterns different from those mentioned above. For instance, the projection of the NF and MF by the NorESM2-LM model showed no significant temperature trends in the NF or the MF but negative significant temperature trends in the north of the VRB in the FF. In addition, ACCESS-CM2 showed different patterns of change, where the temperature of the VRB in the NF was significant, small areas were significant in the MF, and no significant temperature trends were seen in the FF. Also, MIROC-ES2L projected positive significant trends in the NF, but in the MF, there was a positive temperature trend throughout the basin, but it was not

statistically significant in the MF, while most of the VRB might be under negative significant trends in the FF. Finally, in the NorESM2-MM model, the FF, NF and MF define the order of decreasing significant temperature trends in the VRB.

Under the SSP2-4.5 scenario, ACCESS-CM2, ACCESS-ESM1, BCC, CMCC, GISS and MPI-HR projected that the NF would be hotter than the MF and the MF would be hotter than the FF. Alternatively, MIROC6, MPI-LR, MRI and NESM3 also projected that the MF would be hotter than the NF, and the NF would be hotter than the FF. On the contrary, CanESM5 and HadGEM-LL projected that the FF would be hotter than the NF, and the NF would be hotter than the MF. Models such as MIROC-ES2L, NorESM2-LM and NorESM2-MM portrayed distinct temporal patterns. For example, there was no significant temperature change in the FF, while the NF was warmer than the MF projected by the NorESM2-LM. In contrast, there was no significant temperature change in the FF, while the MF was warmer than the NF projected by the MIROC-ES2L. Alternatively, the NorESM2-MM projected that the NF was warmer than the FF, and the FF was warmer than the MF.

Under the SSP5-8.5 scenario, nine models, namely ACCESS-CM2, ACCESS-ESM1, CanESM5, GISS, HadGEM-LL, MIROC6, MIROC-ES2L, MPI-HR and MPI-LR, projected that the FF would be warmer than the MF and the MF would be hotter than the NF. On the contrary, BCC, MRI and NorESM2-LM also projected that the MF would be warmer than the FF and the FF would be hotter than the NF. Alternatively, CMCC and NorESM2-MM projected that the MF was warmer than the NF and the FF was warmer than the MF. The FF and MF of the NESM3 showed equivalent temperature trends but they were warmer than NF.

The temporal trends observed in the ensemble mean under the different scenarios were unique to each other. For example, the FF was warmer than the MF, and the MF was subsequently also warmer than the NF under SSP5-8.5. In addition, the NF was warmer than the MF and FF, and the MF and FF had equivalent magnitudes of temperature change and distribution under SSP2-4.5. Under SSP1-2.6, the NF was warmer than the MF and the MF was warmer than the FF.

Inter-SSP comparison of the significant temperature trends for FF revealed that all models except MIROC-ES2L, MPI-LR, MRI and NorESM2-MM identified SSP5-8.5 as warmer than SSP2-4.5 and SSP1-2.6, and SSP2-4.5 as warmer than SSP1-2.6. Conversely, MIROC-ES2L, MPI-LR, MRI and NorESM2-MM showed that SSP5-8.5 was warmer than SSP2-4.5 and SSP1-2.6, and SSP1-2.6 was warmer than SSP2-4.5. In MIROC-ES2L, significant temperature changes were observed only in SSP5-8.5 and SSP1-2.6, with SSP5-8.5 being warmer than SSP1-2.6. Alternatively, only SSP5-8.5 and SSP2-4.5 had significant temperature changes projected by the MPI-LR and MRI models. SSP5-8.5 was warmer than SSP2-4.5. Results in the MF revealed that 9 models had the same direction of trends observed in the FF, where projections for SSP5-8.5 were warmer, followed by SSP2-4.5, and then SSP1-2.6. NorESM2-LM, MPI-LR, HadGEM-LL, GISS and ACCESS-CM2 have similar patterns except that they simulated no significant temperature trends under the SSP1-2.6 in the MF. The NorESM2-MM patterns were similar to those observed in FF except that there were no significant temperature trends under the SSP2-4.5. Similar to MF and FF, the NF showed most models (ten) had the SSP5-8.5 as the warmest, followed by the SSP2-4.5 and the SSP1-2.6. CMCC and MIROC-ES2L in the NF had the same patterns as NorESM2-MM in the FF, while MPI-HR revealed that SSP2-4.5 would be warmer, followed by SSP1-2.6 and SSP5-8.5.

From the results, models exhibit different spatial patterns in precipitation which is consistent with the findings of Eyring *et al*. (2016). Eyring *et al*. (2016) indicated that models do not converge on their projections of the magnitude of change in rainfall characteristics for any given location but models could show more agreement on expected temperature change. Similarly, Dembélé *et al*. (2022) also identified the conflicting projections of GCM-RCM models under different Representative Concentration Pathways (RCP) in the VRB. Inter-SSP comparison revealed that most of the GCMs (MPI-HR, MPI-LR, MRI, MIROC-ES2L, NESM3, CanESM5 and CMCC) and the ensemble mean projected more rainfall under SSP5-8.5 than in all other scenarios in the NF. MIROC6, NorESM2-MM, NorESM2-LM, ACCESS-CM2, ACCESS-ESM1 and BCC projected more rainfall under SSP5-8.5 than in all other scenarios in the NF while GISS and HadGEM-LL showed that under SSP1-2.6, the VRB would become wetter than all the other scenarios. In the Mid term, most of the models namely: NorESM2-MM, ACCESS-CM2, ACCESS-ESM1, CanESM5, CMCC, GISS and HadGEM-LL, and the ensemble mean projected more rainfall under SSP2-4.5 than all the scenarios while SSP5-8.5 was projected to be wetter by MIROC6, MPI-HR, MPI-LR, NESM3 and NorESM2-LM. Other models like MIROC-ES2L, MRI and ACCESS-CM2 also showed that SSP1-2.6 would be wetter than all the scenarios. In the Far term, most models namely: MPI-LR, NESM3, NorESM2-MM, ACCESS-CM2, BCC, CanESM5, HadGEM-LL and the ensemble mean simulated more rainfall under SSP5-8.5 while MPI-HR, MRI, ACCESS-ESM1 and GISS projected more rainfall under SSP1-2.6. Alternatively, GCMs like MIROC6, MIROC-ES2L, NorESM2-LM and CMCC projected more precipitation under SSP2-4.5. Overall, more precipitation was projected under SSP5-8.5 by majority of the models (7) and multi-model ensemble mean in the NF and FF than under SSP2-4.5 (6 in NF and 4 in FF), and under

SSP2-4.5 than in SSP1-2.6 (2 in NF and 4 in FF). Also, more precipitation was projected under SSP2-4.5 by majority of the models (7) and multi-model ensemble mean in the MF than under SSP5-8.5 (5), and under SSP5-8.5 than in SSP1-2.6 (3). This is consistent with the findings of Eyring *et al*. (2016), who reported that there would be a 16–24% increment in heavy precipitation intensity in most areas globally in the future. This increase can be attributed to the model's evapotranspiration process being accelerated by the increasing temperatures in SSP5-8.5, which increase the amount of moisture in the atmosphere and enhance moisture convergence at low levels, leading to an increase in precipitation events (Donat *et al*., 2016; Dembélé *et al*., 2022; Adeyeri *et al*., 2019). Increment in precipitation increases the probability of flood occurrence and also poses a major risk to agricultural production (Agyekum *et al*., 2022).

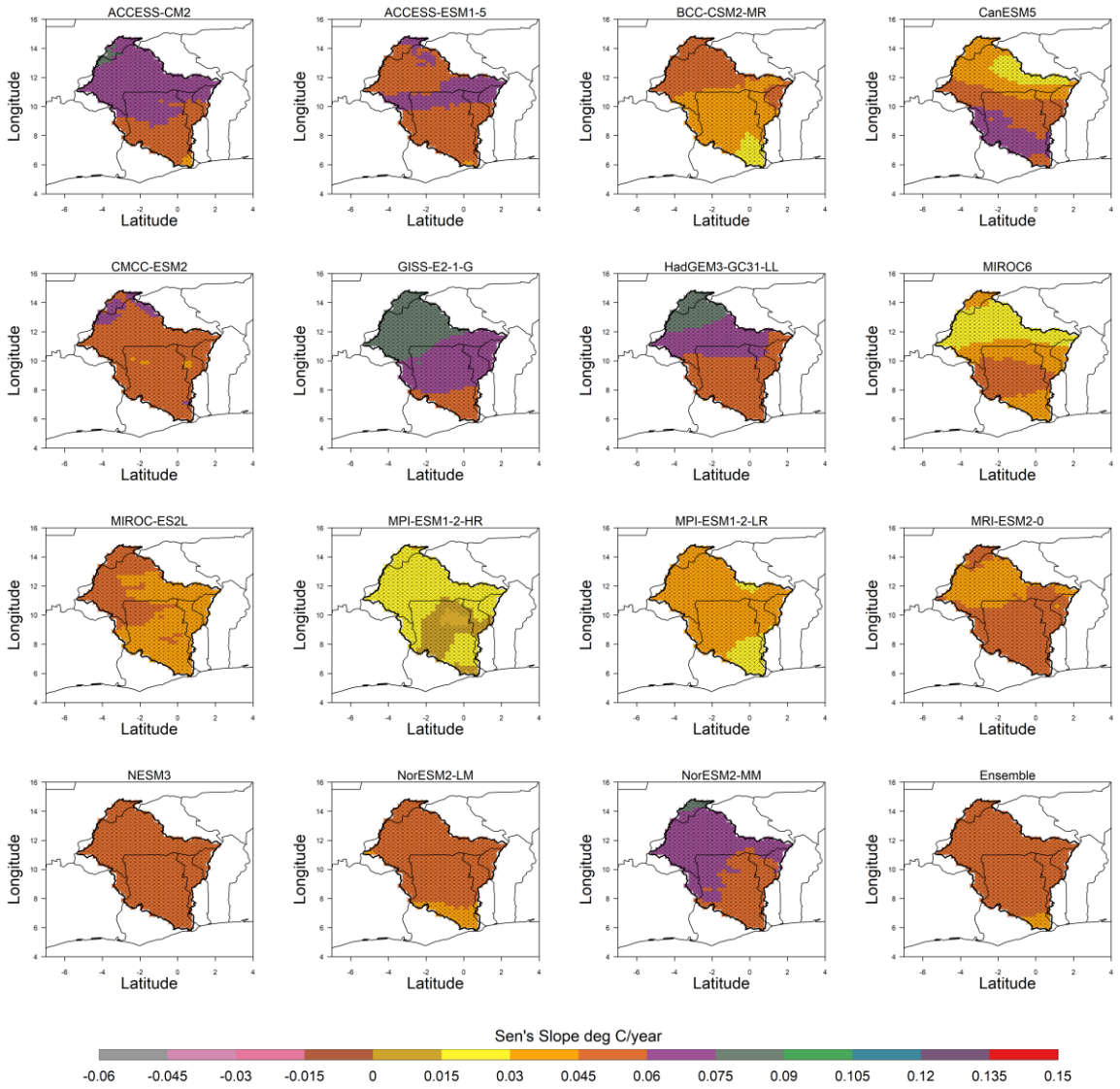

Figure 4.29: Comparison of Near term (from 2021 to 2050) temperature trends of NEX-GDDP models under Socioeconomic Shared Pathways SSP 5-8.5 scenario using Thiel Sen's slope. The black crosses represent areas with trends that are significant at a 95 % confidence level

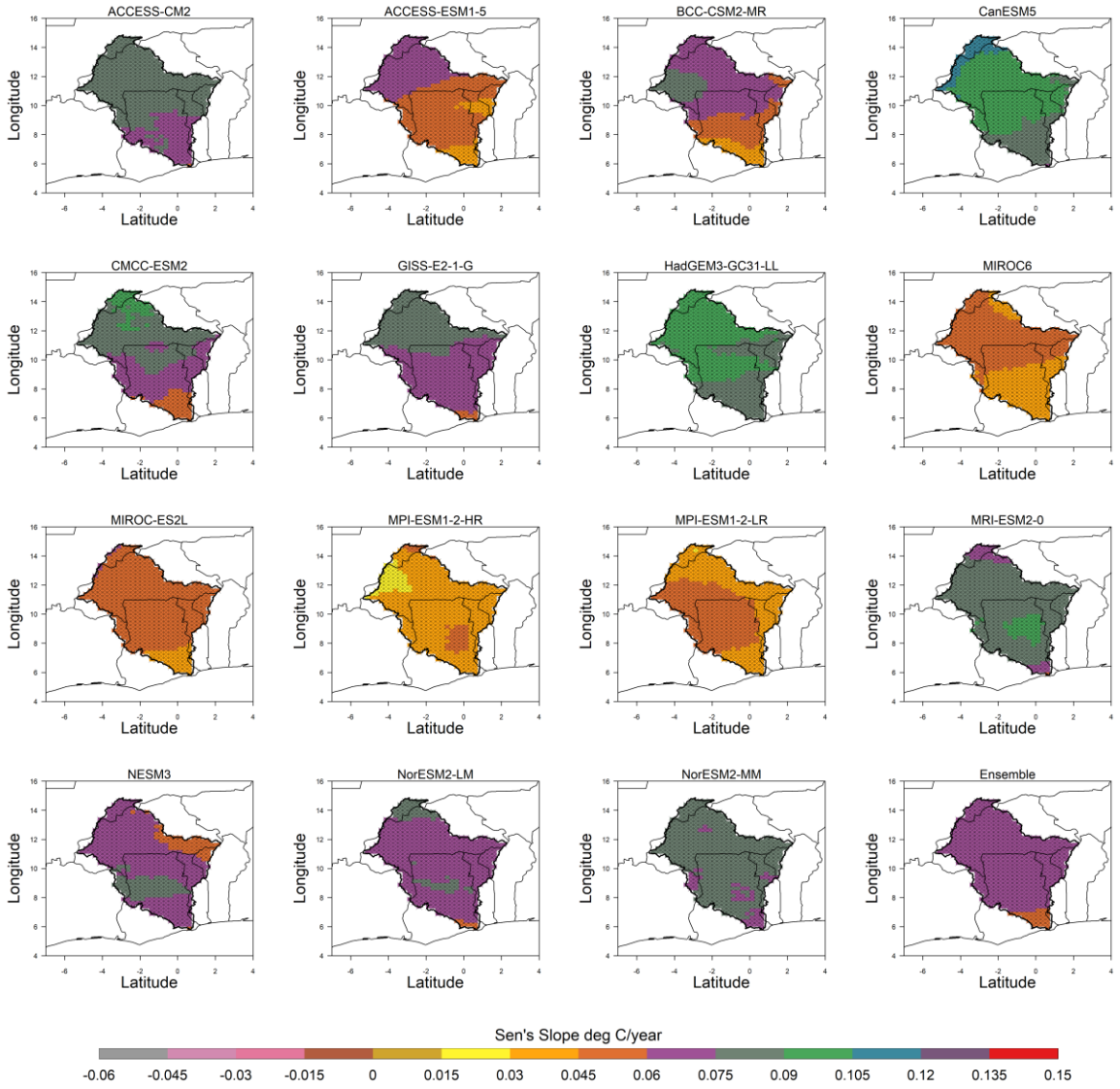

Figure 4.30: Comparison of Mid term (from 2051 to 2080) temperature trends of NEX-GDDP models under Socioeconomic Shared Pathways SSP 5-8.5 scenario using Thiel Sen's slope. The black crosses represent areas with trends that are significant at a 95 % confidence level

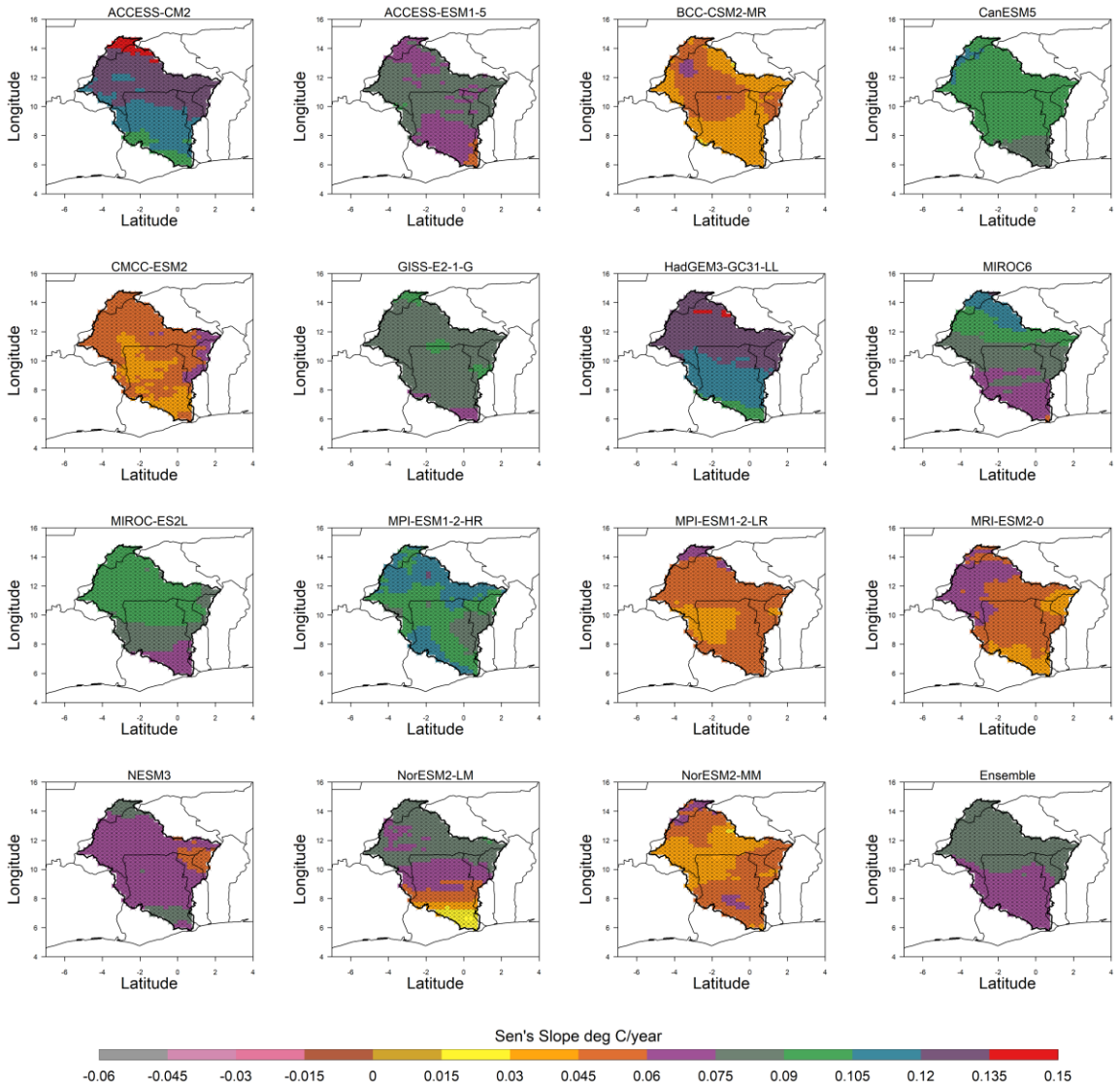

Figure 4.31: Comparison of Far term (from 2081 to 2100) temperature trends of NEX-GDDP models under Socioeconomic Shared Pathways SSP 5-8.5 scenario using Thiel Sen's slope. The black crosses represent areas with trends that are significant at a 95 % confidence level

4.5.3 Influence of climate change on meteorological drought in each drought modes

The boxplots shown in Figures 4.32, 4.33, 4.34 and 4.35 illustrate the changes in drought intensities (SPEI < -1) for DM1, DM2, DM3 and DM4 respectively. From Figure 4.32, the observed data (GMFD) during the historical reference period had an almost normal distribution with a little negative skewness and a median of approximately zero. Less than 25 % of the SPEI indices were below the -1 threshold, which corresponds to moderate-to-extreme drought. During the historical reference period, the BCC, ensemble of the models, MPI-HR and MRI had an equivalent median value as observed under SSP1-2.6. The ensemble mean distribution was similar to what was identified in the GMFD. GISS, MIROC6 and MIROC-ES2L had medians (≈ 0.2) slightly greater than zero and skewed positively. The other models had means below zero, indicating a drying signal with more than 75 % of the SPEI indices below zero. The driest model was CanESM5 which had a median value below the -1 threshold. The HadGEM-LL model was the wettest during the historical period for all the scenarios. More than 85 % of the models and their ensemble mean indicated a robust drying occurred during the historical reference under SSP2-4.5 and 5-8.5. MIRCO6 had the widest spread, and its median was closer to the observed than any model under the SSP2-4.5 and 5-8.5 scenarios. Model projections indicated robust wetting in the future (NF, MF and FF) under SSP2-4.5 and 5-8.5. This is because close to 85 % of models and their ensemble mean have a good agreement on the trajectory of change. MIROC6 and HadGEM-LL are models that deviate from all the others. HadGEM-LL projected an intensification of drought in all future periods under SSP2-4.5 and 5-8.5, while MIROC6 showed that about 25 % of the SPEI indices would be below the threshold during the NF and FF under SSP5-8.5 and the FF under SSP2-4.5. Similar patterns were observed in DM2 (Figure 4.33), DM3 (Figure 4.34) and DM4 (Figure 4.35). Projections of drought

in the future under SSP1-2.6 told a different story. About 66 % of models were in agreement with a shift from normal or drier conditions to wetter conditions in the Near term from the past when compared with the GMFD. Similar to the Near term, not much deviation is seen among models in the Mid term from their behaviour in the NF. Models such as GISS, HadGEM-LL, the ensemble mean of the models, MIROC6 and MRI show a general shift to dryness, with more than 25 % of the drought indices indicating moderate to severe drought. A comparison of models to their historical reference in DM1 revealed that about 53 % of the models projected decreasing drought events in all future periods. The BCC, MIROC-ES2L and MPI-HR models projected the NF would decrease while the MF and FF increased, and MIROC6 projected an increase in the NF and FF and a decrease in the MF. Also, HadGEM-LL and GISS indicated a gradual increment in drought over all the terms, and MRI and the Ensemble mean projected a decrease in drought events in the NF and MF while also showing an increase in the FF. In DM2, DM3 and DM4, the majority of the models show a decreasing trend in the occurrence of drought below the threshold throughout. Models that showed deviation are the BCC and HadGEM-LL projected increase in drought events in all future terms in DM2, DM3 and DM4. MIROC-ES2L projected a decrease in drought events in the NF and MF and an increase in the FF in DM2 and DM4 while MRI showed a decrease in NF and MF and an increase in the FF in both DM3 and 4. GISS showed a decrease in the NF and MF, and an increase in the FF in DM3 and, a decrease in the NF and an increase in the MF and FF in DM4. MPI-HR also projected a decrease in drought events in the NF and FF and an increase in the MF in DM3, and the vice-versa in DM4 while MIROC6 showed a decrease in the NF and MF and an increase in the FF in both DM3 and DM4. Most models generally project more normal to near normal conditions ($-1 < SPEI < 1$) in the future under SSP1-2.6 than observed in other scenarios.

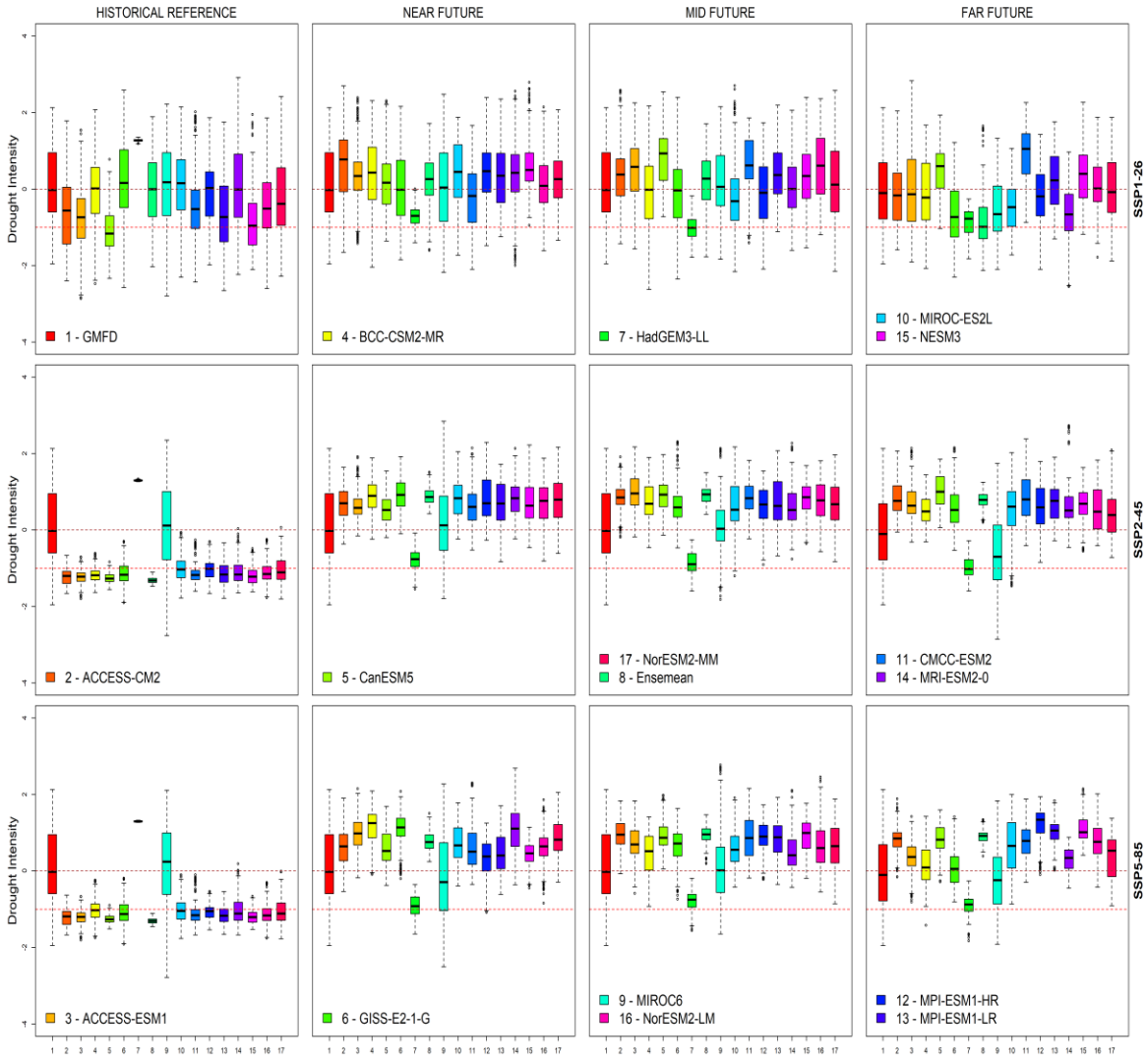

Figure 4.32: Historical and projected drought intensity (moderate-to-extreme drought) of all the models and GMFD (observation data) under the SSP1-2.6, SSP2-4.5 and SSP5-8.5 for Drought Mode One (DM1)

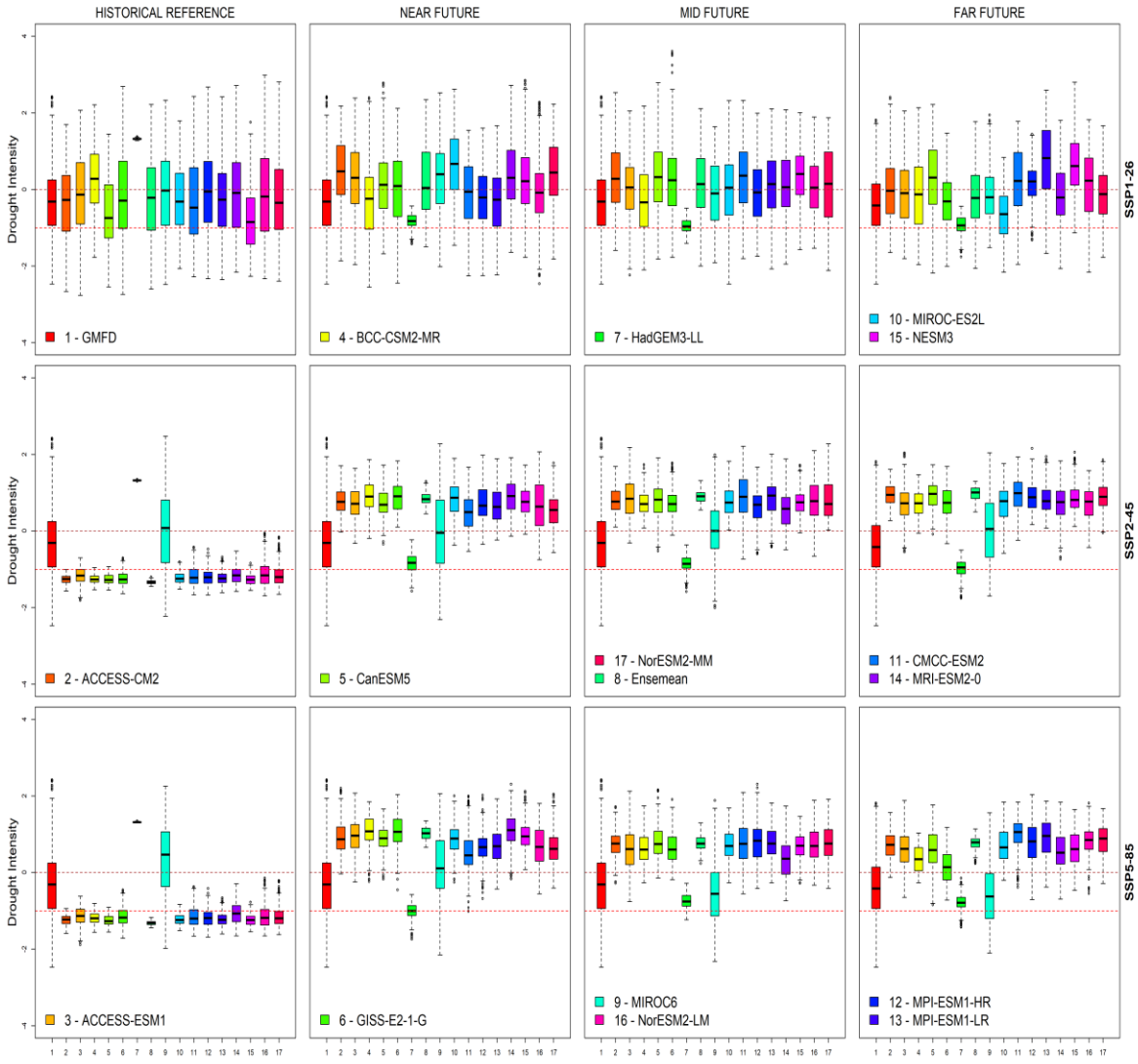

Figure 4.33: The same as Figure 4.32 but for Drought Mode Two (DM2)

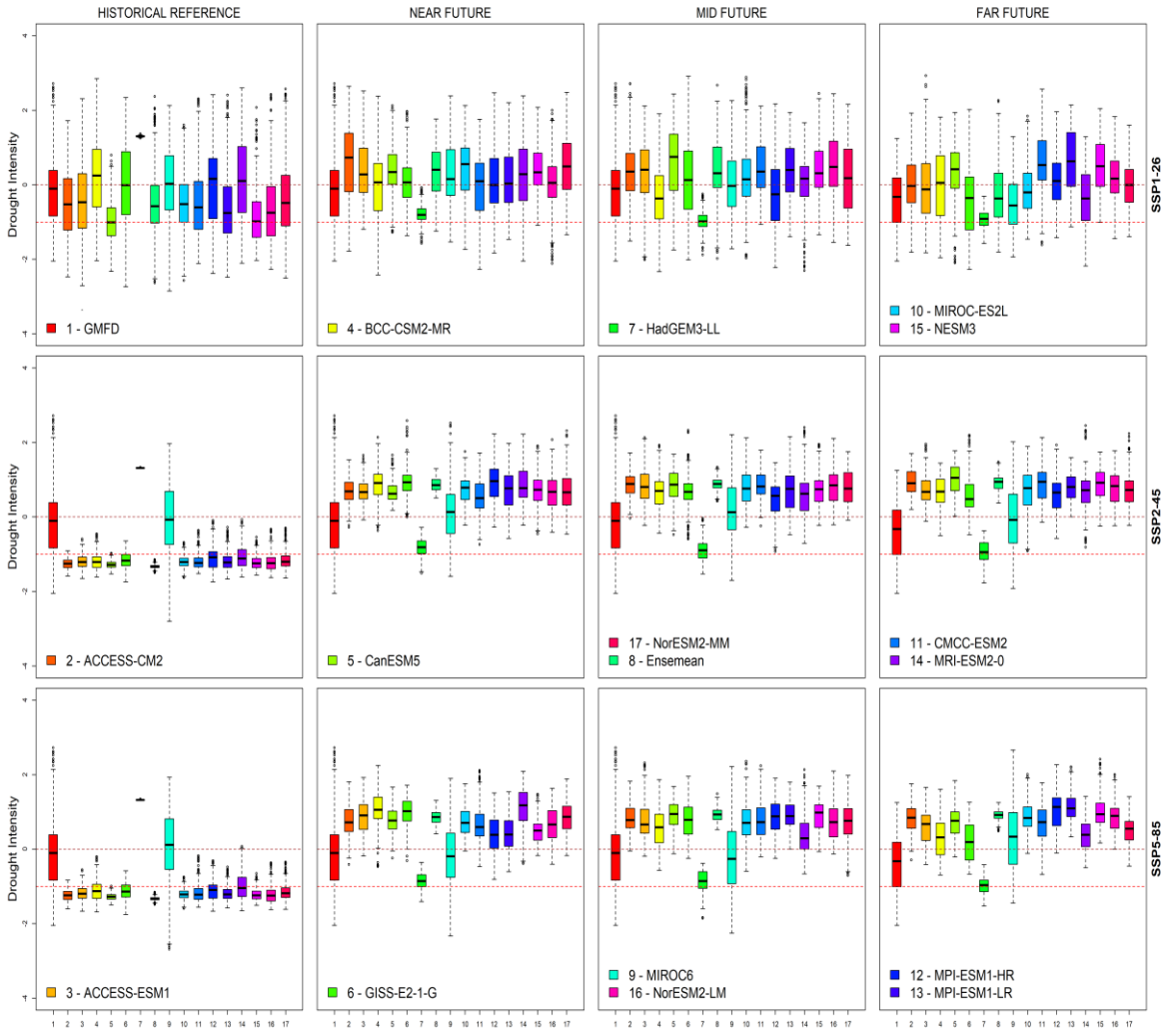

Figure 4.34: The same as Figure 4.32 but for Drought Mode Three (DM3)

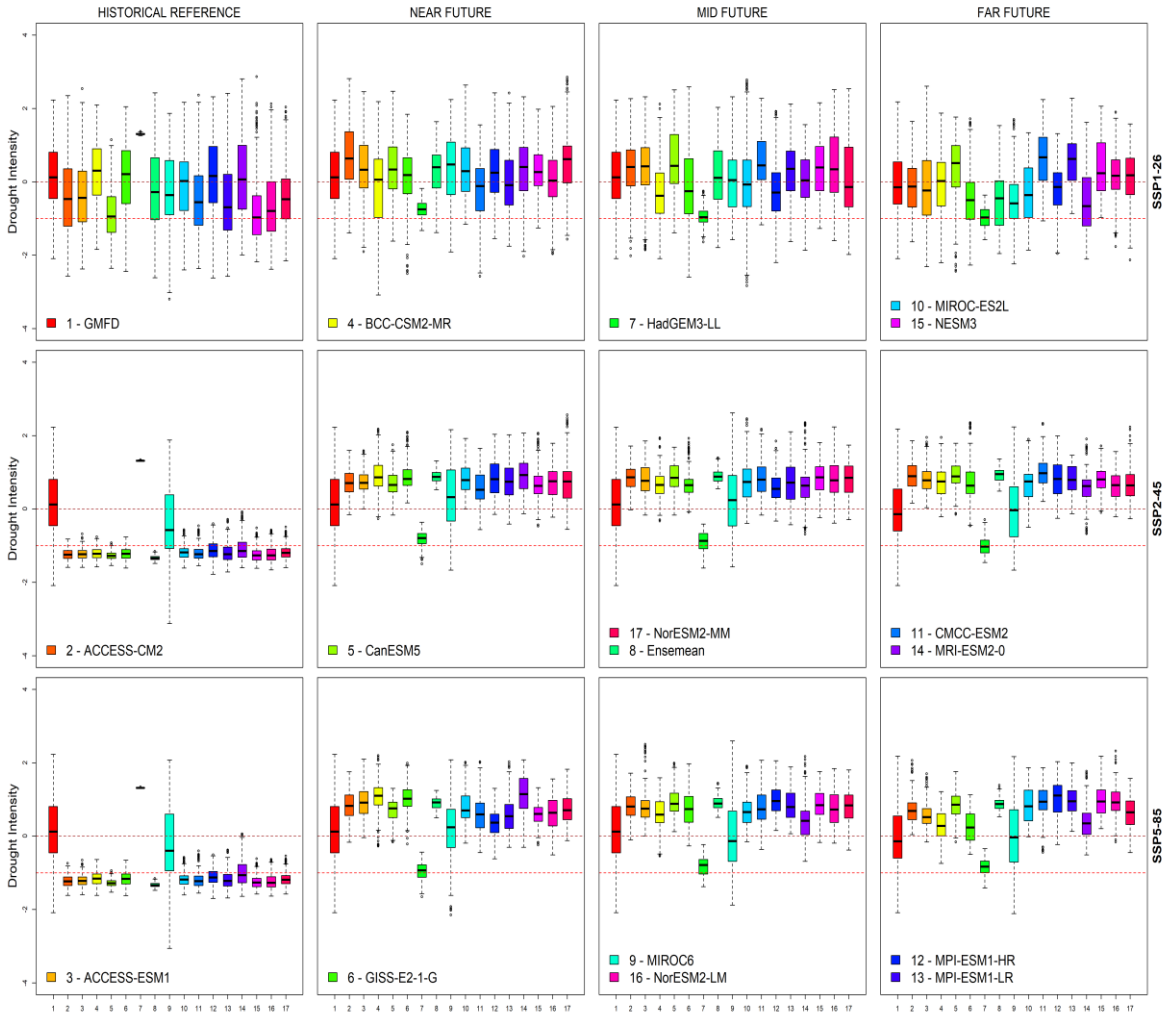

Figure 4.35: The same as Figure 4.32 but for Drought Mode Four (DM4)

To better understand the impact of climate change on some drought characteristics, Run's Theory was performed on the observation data (GMFD) and the Ensemble of the models utilised in this study (Table 4.2). The results indicate that 9, 17, 18 and 18 continuous drought events have occurred in DM1, DM2, DM3 and DM4 respectively during the reference period. Also, SSP1-2.6 results generally underestimated the number of continuous events in all DMs except in DM3 where it had the same value as the observed. Similarly, the number of continuous drought events reduced in all future terms for all DMs except for the FF and DM1. Generally, the SSP1-2.6 overestimate slightly the mean severity (6.93), intensity (1.3), duration and return period of drought in the historical series. DMs portray distinct drought characteristics in the future. For instance, in the NF under SSP1-2.6, the DM1 is projected to have the highest mean severity and intensity with an average of 5 months' duration and the longest return period of 120 months. Similarly, DM3 is projected to have the highest mean severity and intensity in the MF and DM1 in the FF. The mean severity (12.15) and duration of drought increased in the FF in DM1 than the historical value but the intensity was lower than simulated observed values. In DM2, the mean characteristics of drought except for the return period of drought reduced in all future terms. In DM3, drought severity and intensity decreased in the NF and FF but increased in the MF. Mean severity and intensity reduced in the DM4 for the NF and MF while a slight increment in severity of 0.32 was observed in the FF. This increment did not exacerbate the intensity of drought. The SSP2-4.5 and 5-8.5 overestimated drought events where all the months were under drought conditions during the reference period. In addition, no drought event was recorded in the future. This could be attributed to the high increase in precipitation projected in the Ensemble of the models under these scenarios as discussed earlier. This is supported by the findings of Almazroui *et al.* (2020) who found that precipitation is

expected to increase in the Near and Far term under these scenarios. The results of this study deviate from the findings of Oguntunde *et al.* (2017) in which the authors suggested that drought would increase in the future (2046 -2065 and 2081-2100) when they studied drought frequency and intensity using CMIP5 climate models downscaled by RCA regional climate models. The disagreement could be associated with the difference in the Global Climate models used as CMIP6 projections of precipitation and temperature are higher than projections made by CMIP5 models (Almazroui *et al.*, 2020).

Table 4.2: Drought Characteristics of the Observed and Ensemble of the Models averaged over the time periods under SSP1-2.6, 2-4.5 and 5-8.5

Climate Data	Scenarios	Time Period	DM1					DM2					DM3					DM4				
			Severity	Intensity	Duration	Interarrival	No. Event	Severity	Intensity	Duration	Interarrival	No. Event	Severity	Intensity	Duration	Interarrival	No. Event	Severity	Intensity	Duration	Interarrival	No. Event
GMFD		Reference Period	5.94	1.23	4.33	38	9	7.43	1.27	4	21.19	17	4.94	1.25	3.78	16.12	18	4.51	1.27	3.4	36	18
	SSP126	Reference Period	10.98	1.35	7.5	15.63	8	12.27	1.37	5.75	28.42	12	8.16	1.28	4.78	17.39	18	10	1.36	6.07	25.57	14
		NF	6.93	1.24	5.33	120	3	2.2	1.15	1.89	32.67	9	2	1.08	1.83	51.67	6	3.49	1.19	2.83	69	6
		MF	5.57	1.2	4.29	39.17	7	8.58	1.33	4.88	43.43	7	9.23	1.4	5.5	69.5	2	4.82	1.23	2.91	27.7	11
		FF	12.15	1.22	8.23	18.42	13	8.91	1.36	5.63	30	8	5.47	1.29	2.3	23.7	10	10.32	1.3	6.73	21.82	11
	SSP245	Reference Period	472.63	1.31	360	0	1	481.23	1.34	360	0	1	478.55	1.33	360	0	1	480.24	1.33	360	0	1
		NF	0	0	0	0	0	0	0	0	0	0	0	0	0	0	0	0	0	0	0	0
		MF	0	0	0	0	0	0	0	0	0	0	0	0	0	0	0	0	0	0	0	0
		FF	0	0	0	0	0	0	0	0	0	0	0	0	0	0	0	0	0	0	0	0
	SSP585	Reference Period	470.09	1.31	360	0	1	475.26	1.32	360	0	1	478.41	1.33	360	0	1	480.24	1.33	360	0	1
		NF	0	0	0	0	0	0	0	0	0	0	0	0	0	0	0	0	0	0	0	0
ENSEMEAN		MF	0	0	0	0	0	0	0	0	0	0	0	0	0	0	0	0	0	0	0	0
		FF	0	0	0	0	0	0	0	0	0	0	0	0	0	0	0	0	0	0	0	0

4.6 Assessment of SWATplus Model Performance in the Volta River Basin

4.6.1 Calibration and validation of the SWATplus model

The SWATplus model was setup for the VRB basin using the 1992 land use map, the SRTM DEM, climate data from the GMFD, and the FAO soil map. Figure 4.36 presents the results obtained during the calibration and validation of the SWATplus model. The calibration was conducted between 1987 and 1995, with the initial 2 years being the warmup period. Results of the calibration from the Nawuni, Saboba, Sabari and Bamboi gauging stations revealed that stations Nawuni, Saboba and Sabari present in the White Volta and Oti Basin performed well. For example, the coefficient of determination (R^2) for Nawuni, Saboba and Sabari were 0.72, 0.91 and 0.69, respectively, which indicated a strong performance of the model to simulate the hydrology of the VRB at these stations (Figure 4.36). Using the criteria recommended by Moriasi *et al.* (2007), the Nash-Sutcliffe efficiency (NSE) value obtained for Saboba (0.81) was very good, and that of Nawuni and Sabari was good. In addition, the PBIAS statistics of the Nawuni (-9.1 %) and Sabari (-1.9 %) were very good, and that of the Sabobo was good when compared to the recommended values in Table 4.3. The Bamboi station, which was selected for the calibration of the Black Volta, showed an unsatisfactory performance in the NSE (0.101) but performed satisfactorily when the PBIAS (22.7 %) and the R^2 were considered. Most hydrological studies (Akpoti *et al.*, 2016; Aziz, 2017; Amisigo *et al.*, 2018; Logah *et al.*, 2023) that have been conducted in the Black Volta Basin have primarily utilised the Bui station data record for calibration. In this study, the inclusion of the reservoir into the SWATplus model during model delineation removed any channel corresponding to the Bui gauging for delineation. The simulated streamflow of Channel 188, which was directly downstream of the Bui dam, was compared with the

streamflow of the Bui gauging station. The results showed that the NSE (0.34) was better than that of Bamboi, and the hydrograph shows an overestimation of streamflow, which is expected as the channel was downstream of the Bui gauging station. The R^2 (0.71) was considerably better than the value obtained for the Bamboi gauging station. During the validation period (1996 to 2003), the NSE values of Saboba (0.73) and Sabari (0.69) were good based on the recommendations made in Table 4.3, while that of Nawuni (0.58) and Bamboi (0.51) were satisfactory. PBIAS of Bamboi (-7.7 %) was very good, Saboba (-11.1 %) was good, and Nawuni (18 %) and Sabari (-21.6 %) were satisfactory. The R^2 values of all the stations were good and were higher than 0.65. From these results, the SWATplus model developed for the Volta River Basin was suitable for application in understanding the impact of climate change on the hydrology of the VRB.

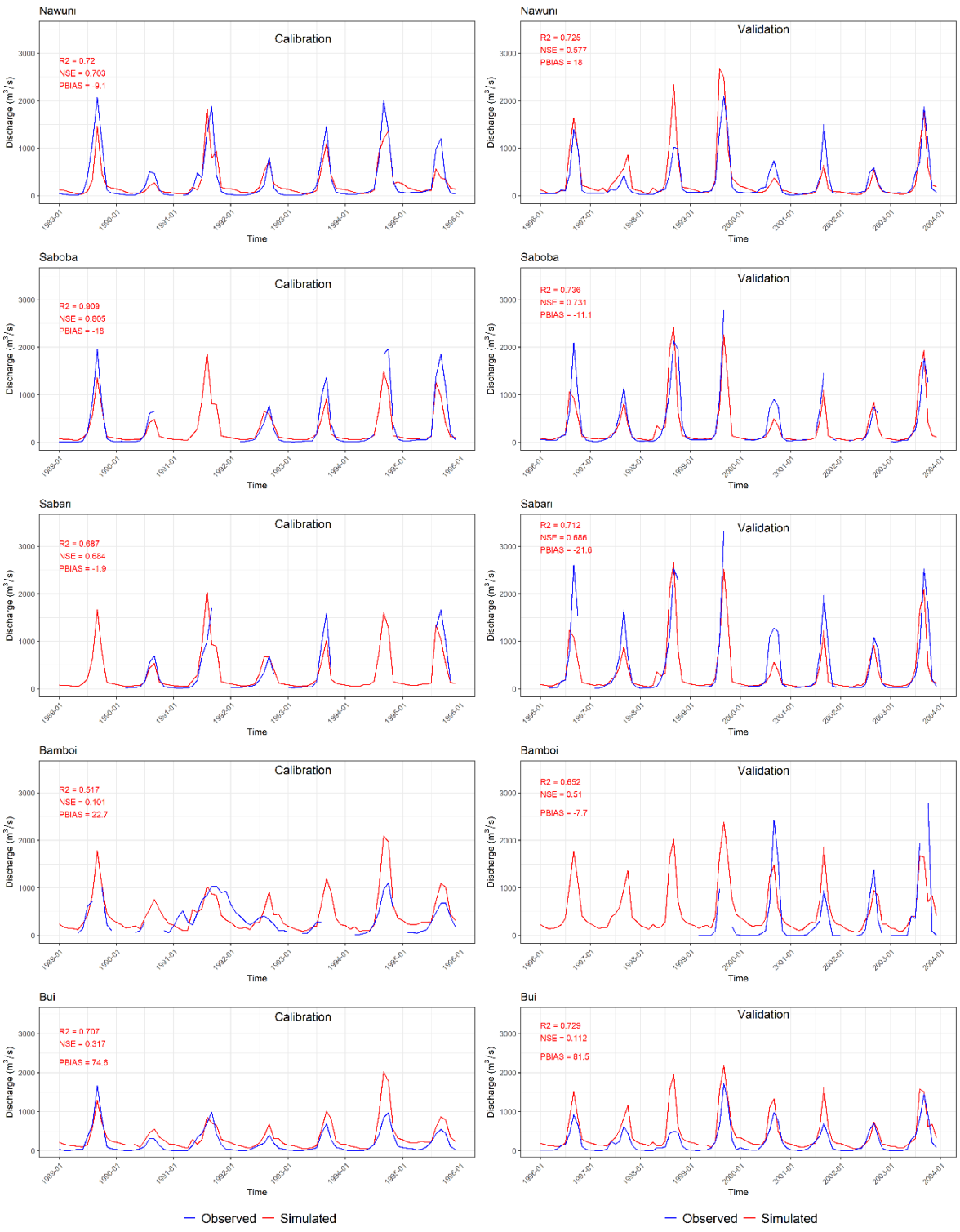

Figure 4.36: Calibration (1989-1995) and Validation (1996-2003) plots for each gauging station and their simulated SWATplus streamflow results

Table 4.3: Performance evaluation criteria for SWAT model assessment using monthly time step

Performance Rating	RSR	NSE	PBIAS (%)		
			Streamflow	**Sediment**	**N, P**
Very good	$0.00 \leq RSR \leq 0.50$	$0.75 \leq NSE \leq 1.00$	PBIAS < ±10	PBIAS < ±15	PBIAS < ±25
Good	$0.50 < RSR \leq 0.60$	$0.65 < NSE \leq 0.75$	±10 ≤ PBIAS < ±15	±15 ≤ PBIAS < ±30	±25 ≤ PBIAS < ±40
Satisfactory	$0.60 < RSR \leq 0.70$	$0.50 < NSE \leq 0.65$	±15 ≤ PBIAS < ±25	±30 ≤ PBIAS < ±55	±40 ≤ PBIAS < ±70
Unsatisfactory	RSR > 0.70	NSE ≤ 0.50	PBIAS ≥ ±25	PBIAS ≥ ±55	PBIAS ≥ ±70

RSR is the ratio of the RMSE and standard deviation of measured data, NSE is the Nash-Sutcliffe Efficiency, and PBIAS is the Percent Bias.

Source: Moriasi *et al*. (2007)

4.6.2 Sensitivity analysis

The sensitivity of SWATplus model parameters was assessed for the VRB. The regression model, the Sobol and the Morris OAT (MOAT) global sensitivity methods were applied after calibration using the understanding from global sensitivity analysis in SWAT_CUP. Because the SWATplus model has never been applied to the Volta River Basin previously, this study examines the sensitivity of thirty-five (35) model parameters that relate to hydrological response unit, channel routing, groundwater and soil. The results of the first MOAT analysis which represents 144 samples identified moist bulk density of soil (bd) and curve number (cn2) as the most sensitive, the next most sensitive parameters were percolation coefficient (perco) and soil depth (Z) (Figure 4.37). The PET coefficient (petco), pothole evaporation coefficient (cn3_swf and soil evaporation compensation factor (esco) also showed some sensitivity and, plant uptake compensation factor (epco), available water capacity of the soil layer (awc), lateral flow coefficient latq_co, soil saturated hydraulic conductivity (k), clay, epco and chl showed some slight sensitivity. The second MOAT analysis results with 720 samples identified cn2, cn3_swf and perco as the most sensitive, followed by esco, petco, Z, bd, awc, lat_len, k, clay and epco (Figure 4.37). Wang and Solomatine, (2019) demonstrated that the MOAT was efficient and converged faster at a smaller sampling size of 100. They iterated that the larger the sampling size the higher the improvement of the MOAT in identifying sensitive parameters. In addition, the Sobol was applied to Nawuni and Pwalugu using the SWAT+ Toolbox (Table 4.4) at seed amounts of 50 and 100 representing 2400 and 4800 samples, respectively. The results showed that the sampling size was small and did not make the Sobol analysis converge thereby generating 1st-order sensitivity negative indices for some parameters, which was unsatisfactory (Nossent *et al.*, 2011; Wang and Solomatine, 2019). Wang and Solomatine (2019) noted

that a large sampling size is required to make the Sobol sensitivity indices converge, leading to a considerable increase in computation time depending on the model complexities and number of parameters used. In the application of the Sobol technique in the SWAT+ Toolbox, the analysis took more than a month to complete the computation of sensitivity indices for 5 seeds for the VRB using a laptop with 32 GB RAM and 2.7 GHz processing speed. This made it computationally expensive to run Sobol analysis for a minimum of 10,000 samples reported by Wang and Solomatine (2019). Table 4.4 shows the result of the Sobol analysis for Nawuni and Pwalugu stations. Any parameter with a sensitivity index with three decimal places or less was considered significant in this study. From the results, cn2, petco, perco, revap_co, z, esco, flo_min, cn3_swf, and awc were classified as sensitive. Finally, the multi-regression analysis was performed to identify sensitive parameters after 500 model calibration simulations. The results are presented in Table 4.5. The results revealed that cn2, alpha, slope_len, cn3_swf, ch_clay, chl, revap_co, slope, bd, clay, chk, chd, silt and alb were the most sensitive parameters having a p-value less than 0.05 (Abbaspour, 2015). The cn2 was the most sensitive parameter in the basin identified in all the sensitivity analyses conducted.

Figure 4.37: Global Sensitivity analysis using MOAT at the repetition value of 4 (top) and 20 (down)

Table 4.4: Sensitivity Analysis of Nawuni and Pwalugu using the Sobol method

Station	Group	Change Type	Name	Unit	1st Order Sensitivity
Nawuni					
	hru	**Percent**	**cn2**		**0.10327010**
	hru	**Replace**	**petco**	**fraction**	**0.05128169**
	hru	**Replace**	**perco**	**fraction**	**0.01365749**
	aqu	**Replace**	**revap_co**		**0.00720238**
	sol	**Percent**	**z**	**mm**	**0.00671128**
	hru	**Replace**	**esco**		**0.00216661**
	rte	Percent	chn		0.00016490
	aqu	Replace	alpha	days	0.00004283
	hru	Percent	slope	m/m	0.00001601
	hru	Replace	epco		0.00001357
	sol	Percent	alb		0.00000800
	hru	Percent	lat_ttime	days	0.00000000
	rte	Percent	ch_bd	(g/cm**3)	0.00000000
	aqu	Percent	bf_max	mm	0.00000000
	hru	Percent	slope_len	m	0.00000000
	hru	Percent	ovn		0.00000000
	hru	Percent	canmx	mm/H20	-0.00000289
	hru	Percent	lat_len	m	-0.00001067
	sol	Percent	awc	mm_H20/mm	-0.00083892
	sol	Percent	k	mm/hr	-0.00091722
	aqu	Percent	flo_min	m	-0.00869976
	aqu	Percent	revap_min	m	-0.01158543
	hru	Percent	cn3_swf		-0.02145861
Pwalugu					
	hru	**Percent**	**cn2**		**0.2401097177**
	hru	**Replace**	**esco**		**0.0917247572**
	hru	**Percent**	**cn3_swf**		**0.0439971466**
	hru	**Replace**	**petco**	**fraction**	**0.0096150879**
	sol	**Percent**	**awc**	**mm_H20/mm**	**0.0051390746**
	aqu	**Percent**	**flo_min**	**m**	**0.0037510463**
	sol	**Percent**	**z**	**mm**	**0.0028505414**
	hru	**Replace**	**perco**	**fraction**	**0.0024702629**
	aqu	**Replace**	**revap_co**		**0.0011749411**
	rte	Percent	chn		0.0000478956
	hru	Percent	slope	m/m	0.0000166744
	hru	Replace	epco		0.0000087904
	sol	Percent	alb		0.0000001949
	hru	Percent	ovn		0.0000000000
	rte	Percent	ch_bd	(g/cm**3)	0.0000000000

Station	Group	Change Type	Name	Unit	1st Order Sensitivity
	hru	Percent	slope_len	m	0.0000000000
	hru	Percent	lat_ttime	days	0.0000000000
	aqu	Percent	bf_max	mm	0.0000000000
	hru	Percent	canmx	mm/H20	-0.0000001984
	hru	Percent	lat_len	m	-0.0000012057
	aqu	Replace	alpha	days	-0.0001654174
	sol	Percent	k	mm/hr	-0.0009983021
	aqu	Percent	revap_min	m	-0.0210382755

The parameters marked in red were identified as sensitive

Table 4.5: Global sensitivity of SWATplus parameters using Multi-regression analysis

SWAT Parameters	Description	Std. Error	t-stats	P-value	Significant Codes
cn2	SCS condition II curve number	2.66E-03	-14.198	2E-16	***
alpha	Baseflow alpha factor (1/days)	2.74E-01	-4.98	8.98E-07	***
alb	Moist soil albedo	1.87E-03	4.679	3.80E-06	***
slope_len	Average slope length for erosion (m)	1.76E-03	-4.276	2.31E-05	***
cn3_swf	Pothole evaporation coefficient	3.67E-03	3.463	0.000584	***
ch_clay	Channel clay percent of bank and bed	3.56E-03	-3.417	0.000689	***
chl	Channel length	2.26E-03	-3.054	0.002385	**
revap_co	Groundwater "revap" coefficient	2.62E-03	-2.787	0.005543	**
slope	Average slope steepness in HRU (m/m)	2.62E-03	2.671	0.00783	**
bd	Moist bulk density (Mg/m3 or g/cm3)	3.42E-03	-2.594	0.009774	**
clay	Clay content (% soil weight)	2.66E-03	-2.365	0.018448	*
chk	Channel bottom conductivity	2.34E-03	-2.19	0.029047	*
chd	Channel depth	3.62E-03	2.118	0.034709	*
silt	Silt content (% soil weight)	2.74E-03	-2.001	0.046025	*
ovn	Manning's 'n' value for overland flow	2.32E-03	1.949	0.051876	.
dis_stream	Average distance to stream	2.22E-06	1.933	0.053878	.
lat_len	Slope length for lateral subsurface flow	1.52E-03	-1.787	0.074559	.
chn	Channel Manning's n value	2.76E-03	-1.537	0.124987	
perco	Soil percolation coefficient	2.13E-01	-1.294	0.196258	
ch_bd	channel dry bulk density	3.35E-03	-1.199	0.231204	
latq_co	Lateral soil flow coefficient	3.08E-01	-1.054	0.29237	
petco	PET coefficient	3.44E-03	1.018	0.309039	
revap_min	Threshold depth of water in the shallow aquifer for “revap” or percolation to the deep aquifer to occur (mm H2O)	3.68E-03	-0.9	0.368576	
awc	Available water capacity of the soil layer (mm H2O/mm soil)	3.54E-03	0.889	0.374534	
esco	Soil evaporation compensation factor	2.78E-01	0.691	0.490051	

SWAT Parameters	Description	Std. Error	t-stats	P-value	Significant Codes
surlag	Surface runoff lag coefficient	9.15E-03	0.67	0.50295	
bf_max	maximum daily baseflow when all channels are contributing	9.22E-02	-0.657	0.511815	
flo_min	Minimum aquifer storage to allow return flow (m)	2.57E-03	-0.624	0.532936	
chs	Channel slope	1.74E-03	-0.623	0.533624	
canmx	Maximum canopy storage	2.51E-03	0.423	0.67275	
lat_ttime	Lateral flow travel time (days)	1.14E-03	-0.194	0.846274	
chss	Channel side slope	2.86E-03	0.134	0.893503	
epco	Plant water uptake compensation factor	2.11E-01	0.123	0.902347	
k	Saturated hydraulic conductivity (mm/hr)	3.24E-03	0.102	0.918405	
z	Depth from soil surface to bottom of layer (mm)	3.06E-03	-0.091	0.92738	

Significant codes: 0 = '***', 0.001 = '**', 0.01 = '*', and > 0.05 = '.'. t-stats = Student T-Statistics

The best values of parameters identified in each global sensitivity analysis during calibration were incorporated in the SWAT+ Toolbox and run in manual calibration mode. The integration of these parameters generated NSE and PBIAS values closer to the values obtained when all the parameters were utilised. Most parameters only present in the multi-regression sensitivity analysis were discarded except alpha because they did not improve the general model statistics when incorporated during the manual calibration. The parameters and their best calibration values utilised in the VRB's SWATplus model are listed in Table 4.6.

Table 4.6: The combined SWATplus parameters sensitive in the VRB

Type	Parameter	Change Type	Min Value	Best calibrated Value	Fitted_Value	Max Value	Unit
hru	cn2	Percent	-40	-16.6079	-16.6079	40	
hru	cn3_swf	Percent	-40	-17.0174	-17.0174	40	
hru	lat_len	Replace	1	4.00996	4.00996	150	m
hru	latq_co	Replace	0	0.16702	0.16702	1	
hru	esco	Replace	0	0.12735	0.12735	1	
hru	epco	Replace	0	0.79473	0.79473	1	
hru	perco	Replace	0	0.41248	0.41248	1	fraction
hru	petco	Percent	-40	-35.5287	-35.5287	40	fraction
sol	z	Percent	-40	26.8965	26.8965	40	mm
sol	bd	Percent	-40	-39.3494	-39.3494	40	mg/m**3
sol	awc	Percent	-40	-26.7193	-26.7193	40	mm_H20/mm
sol	k	Percent	-40	-36.9626	-36.9626	40	mm/hr
sol	clay	Percent	-40	-9.80593	-9.80593	40	
aqu	alpha	Replace	0	0.02292	0.02292	1	days
aqu	flo_min	Percent	-40	15.8323	15.8323	40	m
aqu	revap_co	Percent	-40	-1.53593	-1.53593	40	

4.7 Climate Change Impact on Hydrology and Hydrological Drought in the Volta River Basin

4.7.1 Climate change impact on hydrology

The impact of climate change on the hydrology of the VRB was assessed using the ACCESS-CM2 model as climate input for the calibrated SWATplus model of the VRB. Figure 4.38 illustrates the streamflow hydrograph of the annual cycle of the VRB during the ACCESS-CM2 historical, Near term, Mid term and Far term, and the observed streamflow records of Nawuni, Bamboi, Saboba and Sabari gauging stations. The results showed that the ACCESS-CM2 underestimated the peak streamflow from August to October and overestimated the streamflow during the low flow period from December to February period in all the stations during the baseline period. The model demonstrated robustness in capturing the annual cycle of streamflow in all the gauging stations during the historical periods. These performances were also observed in the future, especially in Nawuni, Sabari and Bamboi. Streamflow was projected to increase in the future (Near, Mid and Far term) by over 200 m^3/s. The characteristics of change during the future are distinct. For instance, the model projected more streamflow would be generated under scenario SSP1-2.6 in the NF more than the other scenarios and observed in all the stations. In addition, SSP2-4.5 projected more streamflow in the MF and FF in all the stations. Table 4.7 gives the streamflow change magnitude for the future terms and the observation at the baseline period. The streamflow projection suggested that Nawuni on the White Volta and Bamboi on the Black Volta would experience greater streamflow changes. Assessment of other hydroclimatological parameters such as water yield, potential evapotranspiration, actual evapotranspiration, lateral flow, surface runoff, soil water content and precipitation

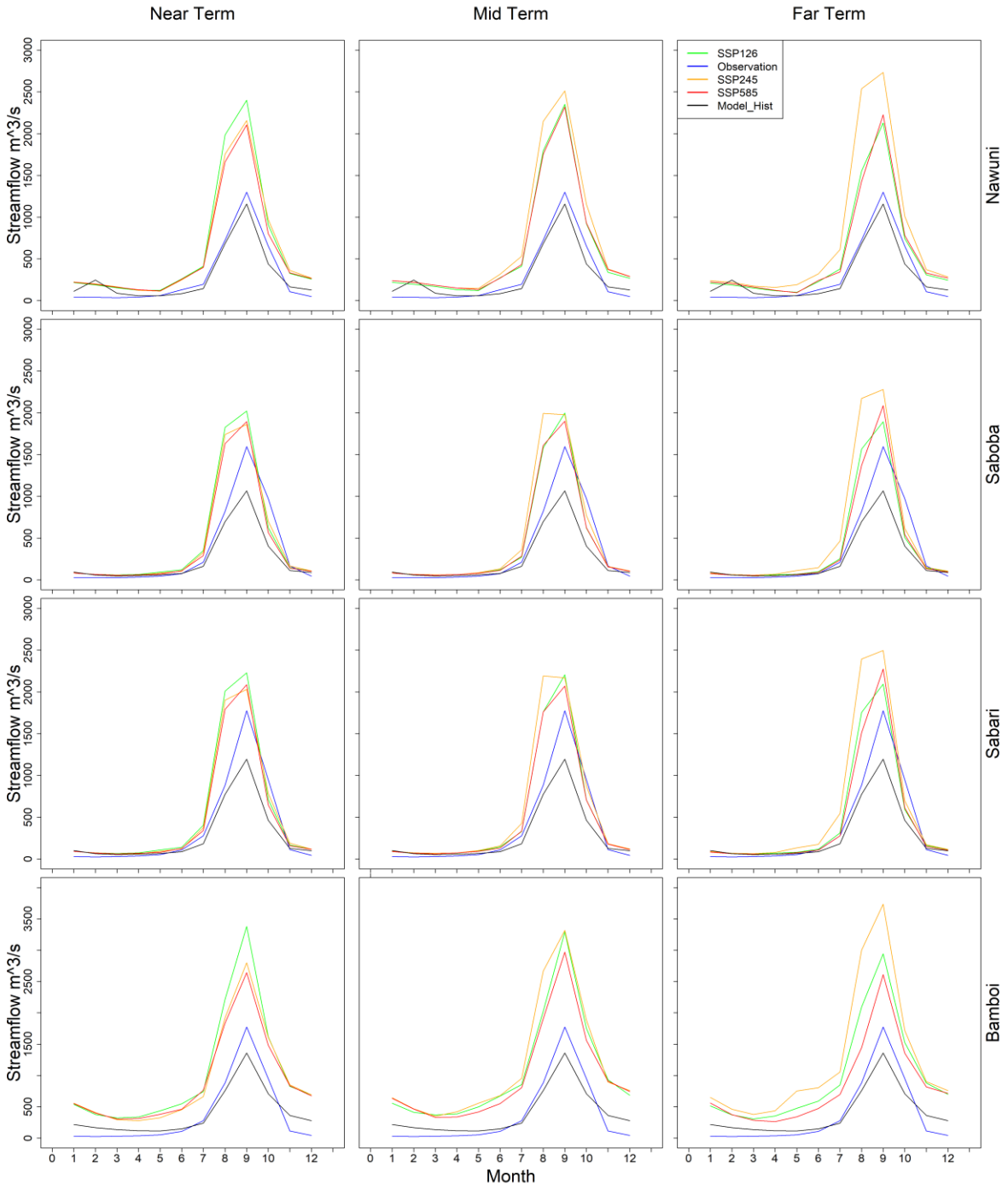

Figure 4.38: Hydrograph of the streamflow annual cycle of the observed hydrological gauge stations (Nawuni, Bamboi, Sabari and Saboba) and their simulated streamflow from the ACCESS-CM2 model's historical and Future periods (NF, MF and FF) and SSP1-2.6, 2-4.5 and 5-8.5

were carried out (Table 4.8). The result revealed that during the baseline period, average annual surface runoff and lateral flow contributed about 55 % and 45 % of the water yield. This changed in the future when more surface runoff (> 65 %) was generated in all the future periods as a result of the projected increment in precipitation. The largest water yield amounts were generated under SSP2-4.5 during the Mid and Far term. Similarly, the projection of precipitation by the ACCESS-CM2 model was higher during the MF and FF under scenario SSP2-4.5. Other parameters like the averaged deep percolation and soil water content also increased proportionally to the increment in precipitation. Average actual evapotranspiration (et) reduced throughout the future periods under all the climate change scenarios. The lowest et value was observed in the SSP1-2.6 during the FF. Potential evapotranspiration (PET) increased in all the scenarios with the greatest magnitude of change observed in the FF under SSP5-8.5. This is due to the model reaching its highest temperature record of 5 °C globally under SSp5-8.5 (Tebaldi *et al.*, 2021). Even though PET was increasing, the water balance (Pr – PET) suggests a reduction in the water deficit in all future periods except the FF period under SSP5-8.5 than witnessed in the baseline.

Table 4.7: Projected future changes in streamflow in the VRB for Near (2021-2050), Mid (2051-2080) and Far term (2081-2100) under SSPs 1-2.6, 2-4.5 and 5-8.5 scenarios

Station	Change in Streamflow Amount in the Future in m^3/s (percentage change)								
	NF			MF			FF		
	SSP1-2.6	SSP2 4.5	SSP5-8.5	SSP1-2.6	SSP2 4.5	SSP5-8.5	SSP1-2.6	SSP2 4.5	SSP5-8.5
Nawuni	3969.43 (117.4)	3616.83 (106.9)	3263.76 (96.5)	3818.26 (112.9)	4895.78 (144.8)	3917.95 (115.8)	2970.24 (87.8)	5469.12 (161.7)	3048.94 (90.1)
Saboba	1514.21 (37.5)	1305.31 (32.3)	1020.83 (25.3)	1158.05 (28.7)	1815.63 (45)	1086.69 (26.9)	834.59 (20.7)	2264.73 (56.1)	805.25 (19.9)
Sabari	1870.86 (43.4)	1585.02 (36.7)	1316.64 (30.5)	1516.54 (35.1)	2207.43 (51.2)	1355.77 (31.4)	1191.32 (27.6)	2706.52 (62.7)	1053.97 (24.4)
Bamboi	6295.78 (109.7)	5113.71 (89.1)	4907.95 (85.5)	6698.61 (116.7)	7854.61 (136.9)	5895.71 (102.7)	5860.26 (102.1)	8912.46 (155.3)	4191.06 (73)

NF refers to Near term, MF means Mid term and FF means Far term. The values in the bracket represent the percentage of the future from the observed.

Table 4.8: Average projected amounts of some hydro-climatological parameters in the VRB under SSP1-2.6, SSP2-4.5 and SSP5-8.5 scenarios

Future Period	pr (mm)	surface runoff (mm)	lateral Flow (mm)	wateryld (mm)	perc (mm)	et (mm)	sw_ave (mm)	pet (mm)	pr-pet (mm)	pr change (%)
SSP1-26										
Historical	967.37	56.84	46.89	103.78	75.96	781.9	336.33	1328.67	-361.3	
NF	1112.4	170.57	69.89	240.27	104.83	751.7	435.27	1352.67	-240.27	14.99
MF	1090.3	181.5	72.89	254.37	107.66	714.47	448.37	1381.67	-291.37	12.71
FF	1063.85	173.4	71.02	244.5	104.79	700.35	441.8	1382.5	-318.65	9.97
SSP2-4.5										
NF	1091.17	150.91	69.08	219.97	105.57	752.67	431.53	1350.33	-259.16	12.80
MF	1129.77	201.3	76.34	277.73	113	725.43	461.67	1382.33	-252.56	16.79
FF	1163	221.55	78.49	299.85	114.5	734	466.15	1401.5	-238.5	20.22
SSP5-8.5										
NF	1057.77	149.48	68.61	218.27	104.64	722.23	433.3	1358.67	-300.9	9.34
MF	1080.63	163.83	72.63	236.43	110.43	722.63	450.27	1407.33	-326.7	11.71
FF	1074.9	148.25	68.33	216.6	105.11	742.65	434	1482.5	-407.6	11.12

pr = precipitation, wateryld = water yield, perc = percolation into vadose zone, et = actual evapotranspiration from the soil, sw_ave = average soil moisture content and pet = potential evapotranspiration.

4.7.2 Climate change impact on hydrological drought occurrence

4.7.2.1 Historical and future patterns of hydrological drought

The observed Standardized Streamflow Index (SSFI) for Nawuni, Saboba, Sabari and Bamboi are shown in Figure 4.39. SSFI generally identifies hydrological drought in the 1970s, 1980s, 1990s and 2000s in all the gauging stations. The hydrological drought that occurred during the 1980s was the longest duration and the highest intensity in all the stations evaluated. The highest drought intensity was observed in the Bamboi station's SSFI drought indices on the Black Volta during the 1980s. These results correspond to the reported low inflow rates of Volta Lake which affected the hydropower generation in the Akosombo Dam (Bekoe and Logah, 2013). Bekoe and Logah (2013) reported that Volta Lake recorded the lowest intake volumes in the years 1983-1984, 1997-98, 2003 and 2006-2007 but found that hydrological drought accounted for low intake volume in 1983-1984, 1997 and 2006-2007. Figure 4.39 indicates that hydrological drought persisted longer than in 1983-1984 in all stations analysed. Also, 1997 was not a drought year but 2003 was rather a drought year from the findings of this study. The dissimilarities of the results could be a result of differences in the data utilised as well as the methodology employed since they used the Probability of Exceedance (POE) method while this study applied the SSFI. Gebrechorkos *et al*. (2022) identified that moderate drought severity was the highest during the 1980s in all subbasins and moderate drought severity decreased in the 1990s and 2000s in the Black Volta. The results of this study agree with their finding. For Instance, Bamboi (Fig 4.42d) on the Black Volta reveals a decreasing moderate drought intensity and duration from the 1980s to the 1990s and 2000s.

Figure 4.40 illustrates the result of the simulated Standardized Streamflow Index (SSFI) for Nawuni, Saboba, Sabari and Bamboi under scenarios SSP1-2.6, 2-4.5 and 5-8.5. From the results, the hydrological condition of the Volta River Basin during the historical period (1963 to 2014) alternated between dry and wet conditions. In all stations, drought conditions occurred during 1972 to 1975, 1982 to 1989, 1996 to 1997, 2002 to 2004 and 2006-2007 to 2008. The result partially agrees with Bekoe and Logah (2013), who stipulated that hydrological drought occurred only during 1983-1984, 1997 and 2006-2007. This affirms the ability of the bias-corrected and statistically downscaled ACCESS-CM2 model output to capture the historical hydrological drought in the VRB. The projection of hydrological drought in the VRB shows a shift from alternating dry and wet conditions to permanently wet conditions in the future. The trajectory of wet conditions indicates the presence of extreme wet indices from moderately, severe and extreme wet conditions in the VRB under all the scenarios at all the gauging stations utilised in the study. Jin *et al*. (2018) also found that streamflow would increase in the future from the 2050s while drought conditions persist before that period under RCP8.5. The departure of this study from their results is that extreme wet conditions occurred much earlier in the 2020s. Table 4.9 and 4.10 shows the number of wet and drought events in the historical and future (Near, Mid and Far term) periods. From the result, moderate drought was predominantly present in all the stations during the historical periods (Table 4.10). In the future, no drought events were projected under all the scenarios and all the stations. Generally, wetter events were projected under SSP2-4.5 more than all the scenarios at all the stations except for Bamboi where wetter events were greater in SSP5-8.5 (Table 4.9). Severe and extreme wet conditions would become a normal feature in all future terms in all the locations and under all the scenarios. In Nawuni, more extreme wet events would occur under SSP2-4.5 with the most extreme

events observed in the Far term and severe wet events in the Mid term. More wet events are projected under SSP5-8.5 than under SSP1-2.6 but they mostly consist of moderately wet conditions. In Saboba and Sabari in the Oti Basin, more wet events were simulated under SSP2-4.5 and also had the highest extreme wet events than all other scenarios. The number of severe wet events was greater under SSP1-2.6 in Saboba and under SSP2-4.5 in Sabari. More extreme wet events were projected at Bamboi under SSP1-2.6 and 2-4.5 with the highest number of events under SSP2-4.5 being slightly larger than events in SSP1-2.6. Even though more wet events were projected under SSP5-8.5 at Bamboi, they were mostly dominated by severe and extreme conditions, where the severe events were higher in all the scenarios but the number of extreme wet events was considerably lower than values observed under SSP1-2.6.

The Volta River Basin will be more flood-prone than drought-prone in the future. The projections of increases in wet events in the VRB can have both positive and negative effects on the inhabitants and their socioeconomic outlook. For instance, excess amount of rainfall can enhance agricultural activities and improve household income in the VRB (Dotse *et al*., 2023). Alternatively, the number and magnitude of wet events projected in the VRB could directly lead to frequent occurrence floods which can impact food security, infrastructure (i.e. housing, bridges, roads and many more), health and also claim lives. Balgah *et al*. (2023) found that flooding impacts food security through the destruction of crops, stored seeds, loss of livestock and farm infrastructure. The major economic activity of the inhabitants of the VRB is agriculture and therefore the occurrence of flooding may have dire consequences on their livelihood and income (Lawanson *et al*., 2023). Flooding could also affect human capital by affecting their health through communicable and non-communicable water-borne diseases and vector-borne diseases (Saulnier *et al*., 2018).

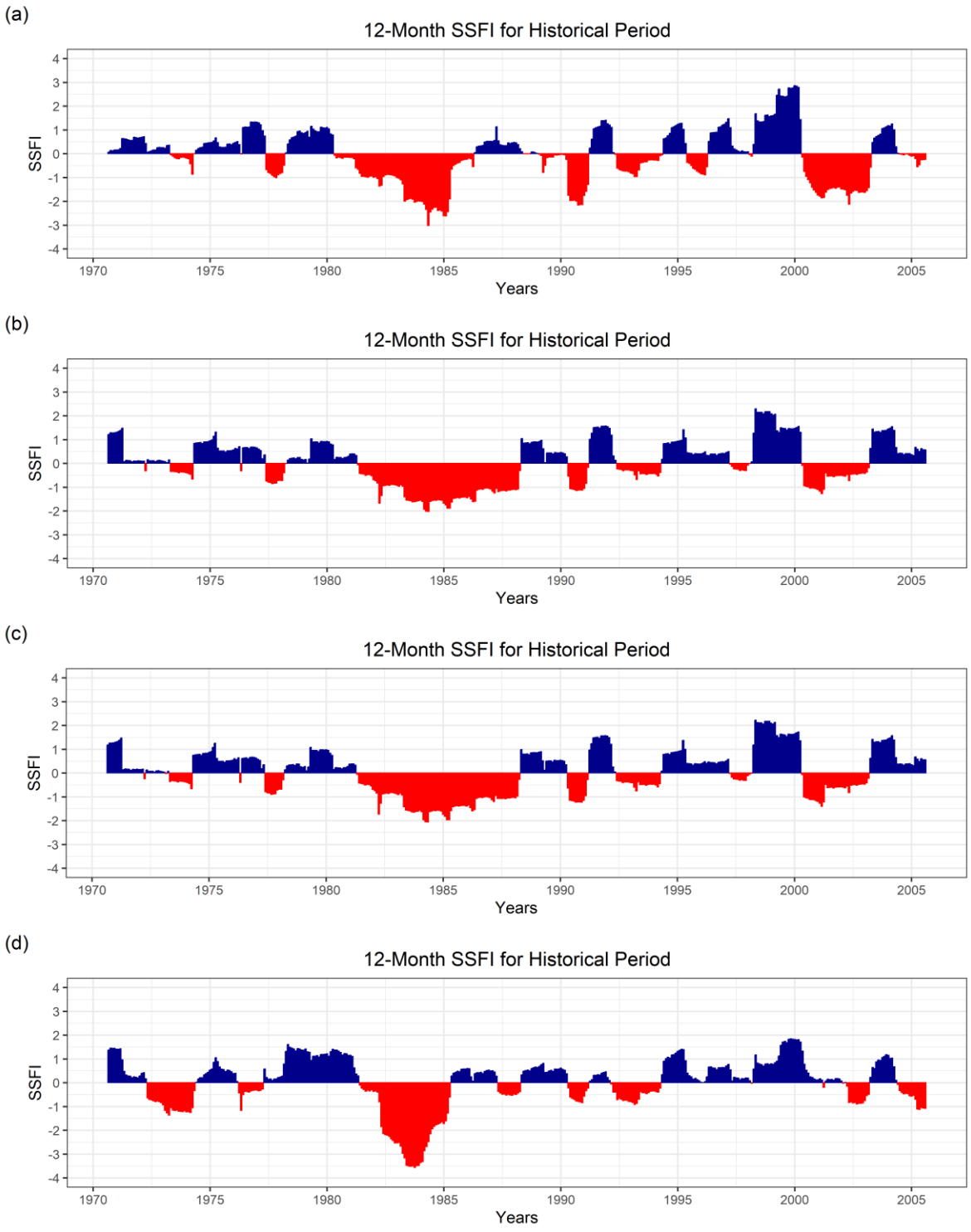

Figure 4.39: Historical Standardised Streamflow Index (SSFI) for Nawuni (a), Saboba (b), Sabari (c) and Bamboi (d) hydrological gauging stations

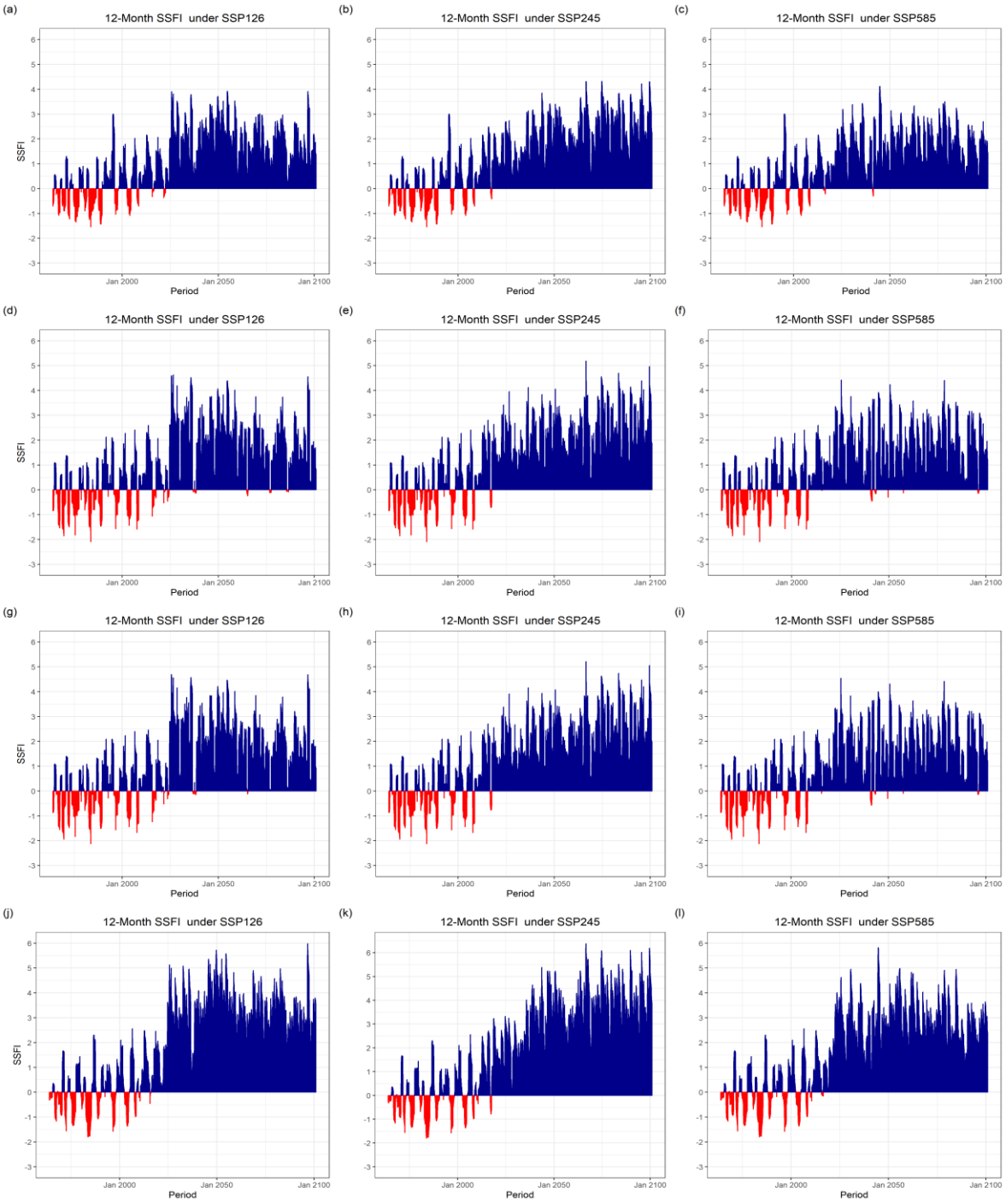

Figure 4.40: Simulated drought indices (Standardised Streamflow Index) for stations Nawuni (a, b & c), Bamboi (j, k & l), Sabari (g, h, & i) and Saboba (d, e & f) under SSP1-2.6, 2-4.5 and 5-8.5 scenarios

Dotse *et al*. (2023) suggest that the increments in rainfall amount directly leading to an increase in streamflow will increase hydropower generation in the VRB. Even though this assessment is valid, flooding could lead to soil erosion and land degradation which will ultimately increase the sediment load in the Volta River and may adversely affect the lake volume and the dam structure.

Table 4.9: Assessment of the occurrence of moderate, severe and extreme wet conditions in the Volta River Basin during the Near, Mid and Far term under SSP1-2.6, 2-4.5 and 5-8.5

		Number of Wet Events											
	Gauging Stations	**Nawuni**			**Saboba**			**Sabari**			**Bamboi**		
Scenarios	**Time Period**	Moderate (> 1)	Severe (> 2)	Extreme (> 3)	Moderate (> 1)	Severe (> 2)	Extreme (> 3)	Moderate (> 1)	Severe (> 2)	Extreme (> 3)	Moderate (> 1)	Severe (> 2)	Extreme (> 3)
	Reference Period	41	11	1	55	5	0	55	5	0	57	12	0
SSP126	**NF**	97	134	57	56	127	86	55	120	97	42	64	227
	MF	150	145	24	124	155	36	114	157	45	7	100	253
	FF	113	72	12	98	75	23	99	73	31	12	99	129
	Reference Period	41	12	1	55	5	0	55	5	0	57	12	0
SSP245	**NF**	147	117	31	157	117	60	143	122	61	79	117	147
	MF	115	160	75	110	134	96	97	139	107	6	57	297
	FF	59	103	78	53	99	88	47	104	89	0	21	219
	Reference Period	41	12	1	55	5	0	55	5	0	57	12	0
SSP585	**NF**	155	98	22	99	91	65	104	95	67	67	148	135
	MF	159	158	21	142	109	46	144	109	49	17	138	205
	FF	131	65	5	102	66	25	100	67	27	43	134	63

Table 4.10: Assessment of the occurrence of moderate, severe and extreme drought conditons in the Volta River Basin during the Near, Mid and Far term under SSP1-2.6, 2-4.5 and 5-8.5

		Number of Drought Events											
	Gauging Stations	**Nawuni**			**Saboba**			**Sabari**			**Bamboi**		
Scenarios	**Time Period**	Moderate (< -1)	Severe (< -2)	Extreme (< -3)	Moderate (< -1)	Severe (< -2)	Extreme (< -3)	Moderate (<-1)	Severe (<- 2)	Extreme (< -3)	Moderate (<-1)	Severe (< -2)	Extreme (< -3)
	Reference Period	50	0	0	49	1	0	45	1	0	72	0	0
SSP126	**NF**	0	0	0	0	0	0	0	0	0	0	0	0
	MF	0	0	0	0	0	0	0	0	0	0	0	0
	FF	0	0	0	0	0	0	0	0	0	0	0	0
	Reference Period	50	0	0	49	1	0	45	1	0	72	0	0
SSP245	**NF**	0	0	0	0	0	0	0	0	0	0	0	0
	MF	0	0	0	0	0	0	0	0	0	0	0	0
	FF	0	0	0	0	0	0	0	0	0	0	0	0
	Reference Period	50	0	0	49	1	0	45	1	0	72	0	0
SSP585	**NF**	0	0	0	0	0	0	0	0	0	0	0	0
	MF	0	0	0	0	0	0	0	0	0	0	0	0
	FF	0	0	0	0	0	0	0	0	0	0	0	0

4.7.2.2 Relationship between Meteorological and Hydrological Drought

The relationship between meteorological and hydrological drought was assessed. Using Oguntunde *et al*. (2017) as a reference, the 12-month SPEI was correlated with 12-month SSFI indices to understand the propagation of meteorological to hydrological drought in all four stations (Nawuni, Saboba, Sabari and Bamboi) in the VRB. Shukla and Wood (2008) also found that there was a high correlation between 12-month accumulated SPEI and 12-month SSFI indices. The cross-correlation between the SPEI and 12-month SSFI indices is present in Figure 4.41 at different lag times. The lag series with the maximum correlation was considered the propagation time. From the result, the maximum correlation was greater than 0.5 and occurred at lag -1 in Nawuni, Saboba and Sabari. This suggests that the 12-month meteorological drought lags the hydrological drought by one month. At Bamboi, the highest correction value was less than 0.3 indicating a poor correlation between the SPEI and SSFI indices. The maximum correlation occurred at lag -2 suggesting hydrological drought leads meteorological drought by 2 months. This result is contrary to the findings of Oguntunde *et al*. (2017) where meteorological drought leads hydrological drought by 2-3 months. Ho *et al*. (2021) found that other factors apart from precipitation could affect hydrological drought leading to runoff and evapotranspiration deficits preceding that of precipitation.

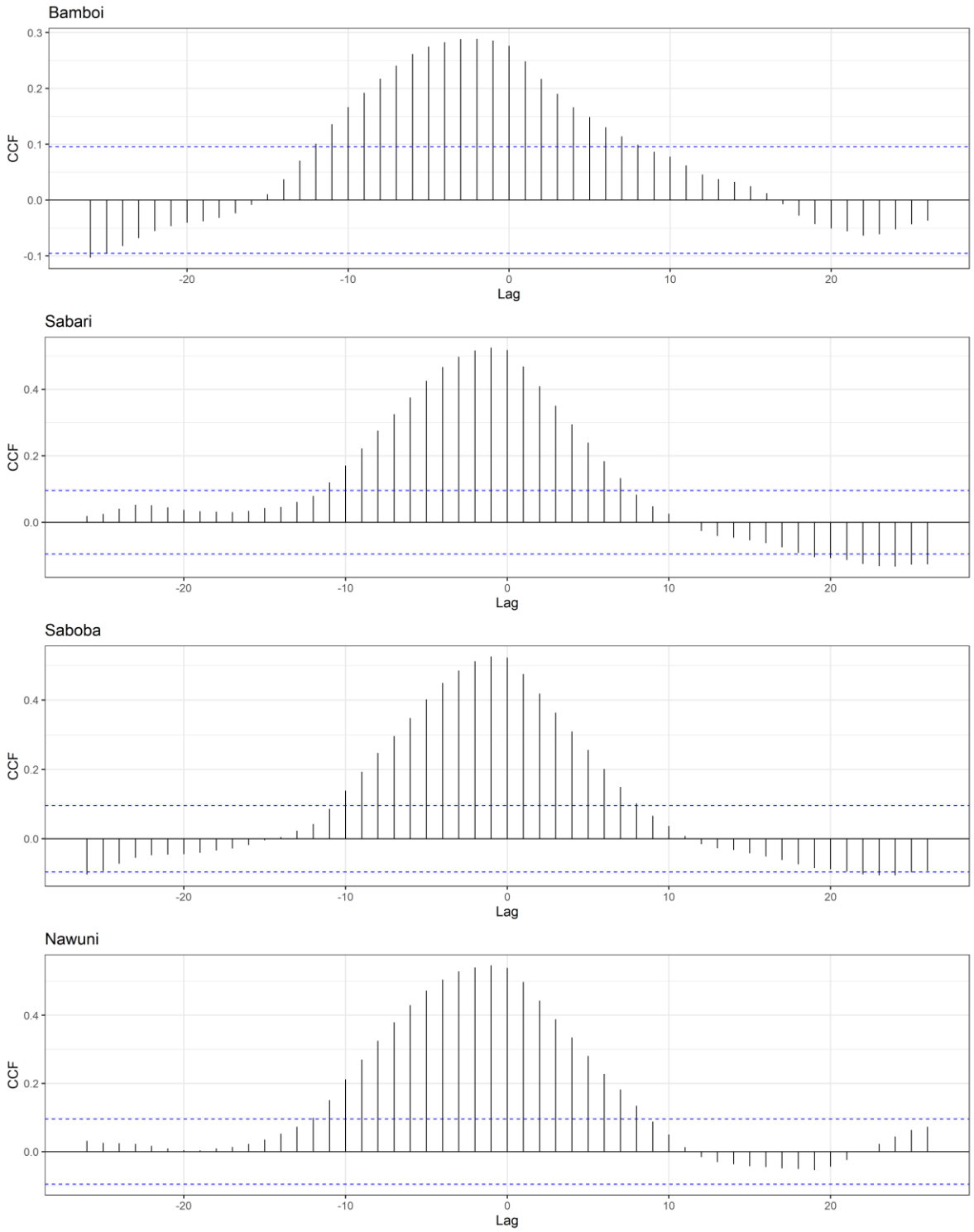

Figure 4.41: Cross-correlation between Standardised Precipitation-Evapotranspiration Index (SPEI) and Standardised Streamflow Index (SSFI) at a 12-month accumulation period

CHAPTER FIVE

5.0 CONCLUSION AND RECOMMENDATIONS

5.1 Conclusion

5.1.1 Potential impact of climate change on spatiotemporal characteristics of meteorological drought and the performance of model outputs

The following conclusions are derived from this research on the potential impact of climate change, spatiotemporal drought characteristics as well as performance of CMIP6 and NEX-GDDP models.

- Evaluation of GMFD precipitation reveals that it performs well comparable to CRU when assessed against in-situ stations.
- NEX-GDDP outperforms CMIP6 in capturing the spatial patterns and annual cycle of climatic variables with higher pattern correlation and less spatial bias in the VRB. Only CMIP6 model, NorESM2-MM reasonably captured the peak rainfall months in the Guinea Coast zone.
- There is little agreement between GCM models on the spatiotemporal characteristics of precipitation and temperature change. Historical trends in precipitation and temperature indicate a decreasing (-2.5 mm/year^2) and increasing (0.01 – 0.05 °C/year) trends respectively. NEX-GDDP models generally simulated increasing historical precipitation and temperature trend which was evident in the ensemble mean except for GISS with decreasing trend in precipitation.
- Majority of models projected more precipitation change under SSP5-8.5 in the NF and FF while more precipitation is expected under SSP2-4.5 in the MF.

- Four Drought modes (DMs) identified in the VRB explains 85 % and 87 % of the variability of 12- and 24-month scale SPEI respectively. These DMs are associated with different cycles ranging from 1 to 16 years that links to either predominantly wet or dry periods in the basin.
- NEX-GDDP models such as ACCESS-CM2, ACCESS-ESM1, GISS and BCCC performed slightly better in reproducing DMs than their CMIP6 versions. Nevertheless, bias correction and statistical downscaling in NEX-GDDP models does not improve their ability to reproduce all DMs.
- Ensemble mean of models projects potential decrease in meteorological drought events and intensities in the future under SSP2-4.5 and 5-8.5 but rather plagued by extreme wetter conditions. More normal conditions are observed under SSP1-2.6.

5.1.2 Performance of SWATplus model in simulating the water balance of the Volta River Basin

- SWATplus model was calibrated, validated and found to reasonably simulate the hydrology of the VRB.

5.1.3 Projections of climate change impact on streamflow and hydrological drought in the Volta River Basin

- Simulation suggest significantly increase in the future streamflow due to a projected increase in rainfall amount in the future. Consequently, hydrological drought events and its characteristics are projected to decrease drastically in the future.

Hydrological drought leads meteorological drought by one month in all stations. The major issue that will pose a greater threat to the VRB is flooding.

5.2 Limitations of the Study

The research utilised the NEX-GDDP CMIP6 output to assess the impact of climate change on meteorological and hydrological drought in the VRB. The models utilised showing a good performance in capturing some aspects of the climate of the VRB, they remain projections of the future and are characterised by large uncertainties which can affect the result of this study. Another limitation relates to the acquisition of in-situ datasets. These datasets can be plaques by systematic and random errors which can affect the accuracy of the results of this study. Finally, the author's inability to assess adequate information to model reservoir operations and irrigation in this research could impact the results obtained in this study.

5.3 Contribution to Knowledge

1. The research provided valuable insights into climate change impacts in the Volta River Basin.
2. The extensive use of climate and hydrological models have added to the body of knowledge on meteorological and hydrological droughts on the far and short term basis in the Volta River Basin.
3. Valuable information for guided decision making and planning to safeguard the Volta River Basin's vital services and resources has been provided.

5.4 Recommendations

The findings of this study provides valuable insights into the climate change impacts on the VRB and provide information for informed decision-making and planning to safeguard the basin's vital services and resources.

The increase in flood events will pose a major risk to agriculture, infrastructure, transportation and quality of human lives. Concerted effort and planning must be undertaken in the VRB to improve adaptation and mitigation to climate change impact specifically more importance must be placed on reducing the impacts of floods.

Areas for further studies

The findings of this research could be improved by simulating the impact of land use or cover change impact on streamflow. This will help enrich our understanding of how vegetation can play a key role in mitigating the effect of climate change in the VRB. In addition, reservoir operations and irrigation could be included to enhance the robustness of the results. Also, future studies can focus on climate change's impact on drought using dynamically downscaled CMIP6 outputs under different global warming levels (GWL).

REFERENCES

Abbaspour, K. C. (2015). SWAT calibration and uncertainty programs—a user manual. *Swiss Federal Institute of Aquatic Science and Technology: Eawag, Switzerland*

Abbaspour, K. C., Yang, J., Maximov, I., Siber, R., Bogner, K., Mieleitner, J., Zobrist, J., & Srinivasan, R. (2007). Modelling hydrology and water quality in the pre-alpine/alpine Thur watershed using SWAT. *Journal of hydrology*, *333*(2-4), 413-430.

Abiodun, B. J., Salami, A. T., Matthew, O. J. & Odedokun, S. (2013). Potential impacts of afforestation on climate change and extreme events in Nigeria. *Clim Dyn, 41*(2), 277–293. https://doi.org/10.1007/s00382-012-1523-9

Abramowitz, M. & Stegun, I. A. (1965). *Handbook of Mathematical Functions with Formulas, Graphs, and Mathematical Tables*. Dover, New York.

Adefisan, E. A., Gbuyiro, S. O. and Bayo, J. O. (2007). Development of irrigation requirement and water scheduling model for West Africa. *Agric. J., 2,* 577-582.

Adeyeri, O. E., Lawin, A. E., Laux, P., Ishola, K. A., & Ige, S. O. (2019). Analysis of climate extreme indices over the Komadugu-Yobe basin, Lake Chad region: Past and future occurrences. *Weather and climate extremes*, *23*, 100194. https://doi.org/10.1016/j.wace.2019.100194

Agyekum J., Annor T., Quansah E., Lamptey B., Okafor G. (2022). Extreme precipitation indices over the Volta Basin: CMIP6 model evaluation. *Scientific African, 16,* e01181, ISSN 2468-2276, https://doi.org/10.1016/j.sciaf.2022.e01181.

Akinsanola, A. A., Zhou, W., Zhou, T., & Keenlyside, N. (2020). Amplification of synoptic to annual variability of West African summer monsoon rainfall under global warming. *Npj Climate Atmosphere Science*, *3*(1), 21. https://doi.org/10.1038/s41612-

020-0125-1

Akpoti, K., Antwi, E. O., & Kabo-bah, A. T. (2016). Impacts of rainfall variability, land use and land cover change on stream flow of the black Volta Basin, West Africa. *Hydrology, 3*(3), 26. https://doi.org/10.3390/hydrology3030026

Allard, T., Caddy, A., Duffy, B., Fallow, P., Groffen, H., Grover, D., Hodgens, P., Joseph, L., Lau, J., Leo, V., Lowry, R., Mulder, E., Spindler, R., & Legge, S. M. (2023). Immediate and longer-term responses of conservation NGOs to the 2019–2020 wildfires. In S. van Leeuwen, B. A. Wintle, J. C. Z. Woinarski, L. Rumpff, & S. M. Legge (eds.), *Australia's Megafires: Biodiversity Impacts and Lessons from 2019-2020,* 313-327.

Almazroui, M., Saeed, F., Saeed, S., Nazrul Islam, M., Ismail, M., Klutse, N. A. B., & Siddiqui, M. H. (2020). Projected change in temperature and precipitation over Africa from CMIP6. *Earth Systems and Environment, 4*(3), 455-475. https://doi.org/10.1007/s41748-020-00161-x

Amisigo, B. A. (2005). *Modeling riverflow in the Volta Basin of West Africa: a data-driven framework*. Ph.D Thesis. Ecology and Development Series No.34. ZEF: Bonn, Germany. Cuvillier Verlag: Göttingen, Germany.

Amisigo, B. A., Logah, F. Y., Obuobie, E., & Kankam-Yeboah, K. (2018). Impacts of Climate Change on Stream Inflows into the Volta Lake. *Ghana Journal of Science, 58*, 23-33.

Ampomah, B. Y., Adjei, B. A., & Youkhana, E. (2008). *The transboundary water resources management regime of the Volta Basin*. ZEF Working Paper Series, (No. 28), University of Bonn, Center for Development Research (ZEF), Bonn, https://nbn-resolving.de/urn:nbn:de:0202-20080911287

Andah, E. I., van de Giesen, N., & Biney, C. A. (2003). Water, climate, food, and environment in the Volta Basin. Adaptation strategies to changing environments. *Contribution to the project ADAPT. Adaptation strategies to changing environments.* http://www.weap21.org/downloads/ADAPTVolta.pdf"

Andreini, M., Giesen, N., Edig, A., Fosu, M., & Andah, W. (2000). *Volta Basin water balance* (No. 21). ZEF discussion papers on development policy. Development Research, Bonn, Germany.

Arneth, A., Barbosa, H., Benton, T., Calvin, K., Calvo, E., & Connors, S. (2019). Climate change and land: summary for policymakers. An IPCC Special Report on Climate Change, Desertification, Land Degradation, Sustainable Land Management, Food Security, and Greenhouse Gas Fluxes in Terrestrial Ecosystems, 43.

Arnold, J. G., Kiniry, J. R., Srinivasan, R., Williams, J. R., Haney, E. B., & Neitsch, S. L. (2011). Soil and water assessment tool input/output file documentation, version 2009 (Texas Water Resources Institute Technical Report No. 365). Texas A&M University.

Arnold, J., Bieger, K., White, M., Srinivasan, R., Dunbar, J., & Allen, P. (2018). Use of Decision Tables to Simulate Management in SWAT+. *Water*, *10*(6), 713. MDPI AG. http://dx.doi.org/10.3390/w10060713

Arora, N. K. (2019). Impact of climate change on agriculture production and its sustainable solutions. *Environmental Sustainability*, *2*(2), 95-96.

Associated Programme on Flood Management (APFM) (2020). Information on the Volta Basin. Available from: https://www.floodmanagement.info/volta-basin/ [Accessed: 13th July 2023]

Ayugi, B., Eresanya, E. O., Onyango, A. O., Ogou, F. K., Okoro, E. C., Okoye, C. O., Anoruo, C. M., Dike, V. N., Ashiru, O. R., Daramola, M. T., Mumo, R., & Ongoma,

V. (2022). Review of meteorological drought in Africa: historical trends, impacts, mitigation measures, and prospects. *Pure and Applied Geophysics*, *179*(4), 1365-1386. https://doi.org/10.1007/s00024-022-02988-z

Aziz, F. (2017). *Modelling the Impact of Climate and Land Use/Land Cover Change on Streamflow and Sediment Yield in the Black Volta River Basin* [Doctoral dissertation, Université d'Abomey-Calavi]. WASCAL.

Bader, J., & Latif, M. (2011). The 1983 drought in the West Sahel: a case study. *Climate dynamics*, *36*, 463-472.

Balgah, R. A., Ngwa, K. A., Buchenrieder, G. R., & Kimengsi, J. N. (2023). Impacts of floods on agriculture-dependent livelihoods in Sub-Saharan Africa: An assessment from multiple geo-ecological zones. *Land*, *12*(2), 334. https://doi.org/10.3390/land12020334

Barry, B., Obuobie, E., Andreini, M., Andah, W., & Pluquet, M. (2005). *The Volta River Basin: comprehensive assessment of water management in agriculture, comparative study of river basin development and management* (unpublished draft report). International Water Management Institute (IWMI), Colombo, Sri Lanka.

Beguería, S., & Vicente-Serrano, S. M. (2023). SPEI: calculation of the standardised precipitation-evapotranspiration index. R package version 1.8.1, https://CRAN.R-project.org/package=SPEI.

Beguería, S., Vicente-Serrano, S. M., Reig, F., & Latorre, B. (2014). Standardized precipitation evapotranspiration index (SPEI) revisited: parameter fitting, evapotranspiration models, tools, datasets and drought monitoring. *International journal of climatology*, *34*(10), 3001-3023.

Bekoe, E. O., & Logah, F. Y. (2013). The Impact of Droughts and Climate Change on

Electricity Generation in Ghana. *Environmental Sciences, 1*(1), 13–24.

Bennett, B. M., & Barton, G. A. (2018). The enduring link between forest cover and rainfall: a historical perspective on science and policy discussions. *Forest Ecosystems, 5*(5), 1-9. https://doi.org/10.1186/s40663-017-0124-9

Bessah, E., Amponsah, W., Ansah, S. O., Afrifa, A., Yahaya, B., Wemegah, C. S., ... & Agyare, W. A. (2022). Climatic zoning of Ghana using selected meteorological variables for the period 1976–2018. *Meteorological Applications, 29*(1), e2049.

Bieger, K., Arnold, J. G., Rathjens, H., White, M. J., Bosch, D. D., Allen, P. M., ... & Srinivasan, R. (2017). Introduction to SWAT+, a completely restructured version of the soil and water assessment tool. *JAWRA Journal of the American Water Resources Association*, *53*(1), 115-130.

Biney, C. (2010). Connectivities and linkages within the Volta Basin. *The Global Dimensions of Change in River Basins*, 91.

Blamey, R. C., Kolusu, S. R., Mahlalela, P., Todd, M. C., & Reason, C. J. C. (2018). The role of regional circulation features in regulating El Niño climate impacts over southern Africa: A comparison of the 2015/2016 drought with previous events. *International journal of climatology*, *38*(11), 4276-4295.

Bonnesoeur, V., Locatelli, B., Guariguata, M. R., Ochoa-Tocachi, B. F., Vanacker, V., Mao, Z., Stokes, A., & Mathez-Stiefel, S.-L. (2019). Impacts of forests and forestation on hydrological services in the Andes: A systematic review. *Forest Ecology and Management*, *433*, 569–584. https://doi.org/https://doi.org/10.1016/j.foreco.2018.11.033

Brands, S., Taboada, J. J., Cofino, A. S., Sauter, T., & Schneider, C. (2011). Statistical downscaling of daily temperatures in the NW Iberian Peninsula from global climate

models: validation and future scenarios. *Climate Research*, *48*(2-3), 163-176.

Caminade, C., & Terray, L. (2010). Twentieth century Sahel rainfall variability as simulated by the ARPEGE AGCM, and future changes. *Climate dynamics*, *35*, 75-94.

Cao, J., Wang, B., Yang, Y. M., Ma, L., Li, J., Sun, B., ... & Wu, L. (2018). The NUIST Earth System Model (NESM) version 3: description and preliminary evaluation. *Geoscientific Model Development*, *11*(7), 2975-2993. https://doi.org/10.5194/gmd-11-2975-2018

Cotillon, S. E., & Tappan, G. G. (2016). Landscapes of West Africa: A window on a changing world. United States Geological Survey, Garretson. https://pubs.usgs.gov/book/2016/70176549/70176549.pdf

Cotton, W. R., Bryan, G., & van den Heever, S. C. (2011). Clouds, Storms, and Global Climate. *In International Geophysics*, *99*, 753-767. Academic Press. https://doi.org/10.1016/B978-0-08-102975-6.00002-9

Cui, L., Chen, X., An, J., Yao, C., Su, Y., Zhu, C., & Li, Y. (2023). Spatiotemporal Variation Characteristics of Droughts and Their Connection to Climate Variability and Human Activity in the Pearl River Basin, South China. *Water*, *15*(9), 1720.

Dai, A. (2011). Drought under global warming: a review. *Wiley Interdisciplinary Reviews: Climate Change*, *2*(1), 45-65.

Dai, A., & Zhao, T. (2017). Uncertainties in historical changes and future projections of drought. Part I: estimates of historical drought changes. *Climatic Change*, *144*, 519-533.

Darko, D., Adjei, K. A., Odai, S. N., Obuobie, E., Asmah, R., & Trolle, D. (2019). Recent climate trends for the Volta Basin in West Africa. *Weather, 74*(S1), S13–S22. https://doi.org/10.1002/wea.3303

Davarpanah, S., Erfanian, M., & Javan, K. (2021). Assessment of climate change impacts on drought and wet spells in Lake Urmia Basin. *Pure and Applied Geophysics*, *178*(2), 545-563.

Defourny, P., Kirches, G., Brockmann, C., Boettcher, M., Peters, M., Bontemps, S., Lamarche, C., Schlerf, M. and Santoro, M. (2017). *Land cover CCI. Product User Guide Version 2.0* (report CCI-LC-PUGV2). http://maps.elie.ucl.ac.be/CCI/viewer/download/ESACCI-LC-Ph2-PUGv2_2.0.pdf

Dembélé, M., Vrac, M., Ceperley, N., Zwart, S. J., Larsen, J., Dadson, S. J., ... & Schaefli, B. (2022). Contrasting changes in hydrological processes of the Volta River basin under global warming. *Hydrology and Earth System Sciences*, *26*(5), 1481-1506.

Diasso, U., & Abiodun, B. J. (2017). Drought modes in West Africa and how well CORDEX RCMs simulate them. *Theoretical and Applied Climatology*, *128*, 223-240.

Diasso, U., & Abiodun, B.J. (2018). Future impacts of global warming and reforestation on drought patterns over West Africa. *Theor Appl Climatol*, *133*, 647–662. https://doi.org/10.1007/s00704-017-2209-3

Donat, M. G., Lowry, A. L., Alexander, L. V., O'Gorman, P. A., & Maher, N. (2016). More extreme precipitation in the world's dry and wet regions. *Nature Climate Change*, *6*(5), 508-513.

Dong, W., Cui, B., Liu, Z., & Zhang, K. (2014). Relative effects of human activities and climate change on the river runoff in an arid basin in northwest China. *Hydrological processes*, *28*(18), 4854-4864.

Dosio, A., Jury, M. W., Almazroui, M., Ashfaq, M., Diallo, I., Engelbrecht, F. A., ... & Tamoffo, A. T. (2021). Projected future daily characteristics of African precipitation based on global (CMIP5, CMIP6) and regional (CORDEX, CORDEX-CORE) climate

models. *Climate dynamics*, *57*(11-12), 3135-3158.

Dotse, S. Q., Larbi, I., Limantol, A. M., Asare-Nuamah, P., Frimpong, L. K., Alhassan, A. R. M., ... & Ayisi-Addo, A. K. (2023). Rainfall Projections from Coupled Model Intercomparison Project Phase 6 in the Volta River Basin: Implications on Achieving Sustainable Development. *Sustainability*, *15*(2), 1472. https://doi.org/10.3390/su15021472

Ellison, D., Morris, C. E., Locatelli, B., Sheil, D., Cohen, J., Murdiyarso, D., Gutierrez, V., van Noordwijk, M., Creed, I. F., Pokorny, J., Gaveau, D., Spracklen, D. V., Tobella, A. B., Ilstedt, U., Teuling, A. J., Gebrehiwot, S. G., Sands, D. C., Muys, B., Verbist, B., Springgay, E., Sugandi, Y. &Sullivan, C. A. (2017). Trees, forests and water: cool insights for a hotworld. *Global Environ Chang, 43,* 51–61.

European Environment Agency (2015). Water scarcity and drought. *Fact sheet*

European Environment Agency. (2017). Climate change adaptation and disaster risk reduction in Europe. https://www.eea.europa.eu/publications/climate-change-adaptation-and-disaster/at_download/file

European Space Agency (ESA) (2017). Land Cover CCI Product User Guide Version 2. Tech. Rep. Available at: maps.elie.ucl.ac.be/CCI/viewer/download/ESACCI-LC-Ph2-PUGv2_2.0.pdf

Eyring, V., Bony, S., Meehl, G. A., Senior, C. A., Stevens, B., Stouffer, R. J., & Taylor, K. E. (2016). Overview of the Coupled Model Intercomparison Project Phase 6 (CMIP6) experimental design and organization. *Geoscientific Model Development*, *9*(5), 1937-1958.

Fang, G. H., Yang, J., Chen, Y. N., & Zammit, C. (2015). Comparing bias correction methods in downscaling meteorological variables for a hydrologic impact study in an

arid area in China. *Hydrology and Earth System Sciences*, *19*(6), 2547-2559.

Food and Agriculture Organization of the United Nations (FAO) – United Nations Educational, Scientific and Cultural Organization (UNESCO) (2003). Digital Soil Map of the World and Derived Soil Properties. CD-ROM, Version 3.6. Information Division, FAO, Viale delle Terme di Caracalla, 00100 Rome, Italy. https://www.fao.org/soils-portal/data-hub/soil-maps-and-databases/faounesco-soil-map-of-the-world/en/

FAO –UNESCO (1974). FAO-UNESCO soil map of the World. 1, 59. Legend. UNESCO, Paris,

FAO (2017). Drought & Agriculture. http://www.fao.org/3/i7378e/i7378e.pdf

Flato, G., Marotzke, J., Abiodun, B., Braconnot, P., Chou, S. C., Collins, W., ... & Rummukainen, M. (2014). Evaluation of climate models. In Climate change 2013: the physical science basis. Contribution of Working Group I to the Fifth Assessment Report of the Intergovernmental Panel on Climate Change. 741-866. Cambridge University Press.

Ford, J. D., Keskitalo, E. C. H., Smith, T., Pearce, T., Berrang-Ford, L., Duerden, F., & Smit, B. (2010). Case study and analogue methodologies in climate change vulnerability research. *Wiley Interdisciplinary Reviews: Climate Change*, *1*(3), 374-392.

Fuwape, J. A., & Onyekwelu, J. C. (2011). Urban forest development in West Africa-Benefits and challenges. *Journal of Biodiversity and Ecological Sciences (JBES)*,*1*(1), 77–94.

Gan, Y., Duan, Q., Gong, W., Tong, C., Sun, Y., Chu, W., ... & Di, Z. (2014). A comprehensive evaluation of various sensitivity analysis methods: A case study with

a hydrological model. *Environmental modelling & software, 51*, 269-285.

Gebrechorkos, S. H., Pan, M., Lin, P., Pritchard, D., Forsythe, N., Fowler, H., & Sheffield, J. (2021). *Modelling hydrological droughts and floods in the Volta Basin, West Africa.* No. EGU21-7992, Copernicus Meetings.

Gebrechorkos, S.H., Pan, M., Lin, P., Anghileri, D., Forsythe, N., Pritchard, D.M., Fowler, H.J., Obuobie, E., Darko, D. and Sheffield, J., (2022). Variability and changes in hydrological drought in the Volta Basin, West Africa. *Journal of hydrology: Regional Studies, 42*, 101143. https://doi.org/10.1016/j.ejrh.2022.101143

Ghosh, S., & Misra, C. (2010). Assessing hydrological impacts of climate change: modeling techniques and challenges. *The Open Hydrology Journal*, *4*(1), 115–121. https://doi.org/10.2174/1874378101004010115

Gore, M., Abiodun, B. J., & Kucharski, F. (2020). Understanding the influence of ENSO patterns on drought over southern Africa using SPEEDY. *Climate Dynamics, 54*(1-2), 307-327. https://doi.org/10.1007/s00382-019-05002-w

Graetz, R.D. (1991). Desertification: A tale of two feedbacks. In H. A. Mooney (Ed.), *Ecosystem Experiments* (59-87). John Wiley & Sons Ltd. http://hdl.handle.net/102.100.100/252489?index=1

Grose, M. R., Narsey, S., Delage, F. P., Dowdy, A. J., Bador, M., Boschat, G., Chung, C., Kajtar, J. B., Rauniyar, S., Freund, M. B., Lyu, K., Rashid, H., Zhang, X., Wales, S., Trenham, C., Holbrook, N. J., Cowan, T., Alexander, L., Arblaster, J. M., & Power, S. (2020). Insights from CMIP6 for Australia's future climate. *Earth's Future, 8*, e2019EF001469. https://doi.org/10.1029/2019EF001469

Guha-Sapir, D., Below, R., & Hoyois, P. (2021). EM-DAT: The CRED/OFDA International Disaster Database [dataset], Université Catholique de Louvain, Brussels,

Belgium.

Guo, H., Hu, Q., & Jiang, T. (2008). Annual and seasonal streamflow responses to climate and land-cover changes in the Poyang Lake basin, China. *Journal of hydrology*, *355*(1-4), 106-122.

Guo, L. Y., Gao, Q., Jiang, Z. H., & Li, L. (2018). Bias correction and projection of surface air temperature in LMDZ multiple simulation over central and eastern China. *Advances in Climate Change Research*, *9*(1), 81-92.

Gutiérrez, J. M., San-Martín, D., Brands, S., Manzanas, R., & Herrera, S. (2013). Reassessing statistical downscaling techniques for their robust application under climate change conditions. *Journal of Climate*, *26*(1), 171-188.

Hajima, T., Watanabe, M., Yamamoto, A., Tatebe, H., Noguchi, M. A., Abe, M., ... & Kawamiya, M. (2020). Development of the MIROC-ES2L Earth system model and the evaluation of biogeochemical processes and feedbacks. *Geoscientific Model Development*, *13*(5), 2197-2244. https://doi.org/10.5194/gmd-13-2197-2020

Haque, M. K., Azad, M. A. K., Hossain, M. Y., Ahmed, T., Uddin, M., & Hossain, M. M. (2021). Wildfire in Australia during 2019-2020, Its impact on health, biodiversity and environment with some proposals for risk management: a review. *Journal of Environmental Protection*, *12*(6), 391-414.

Hargreaves, G. H., & Samani, Z. A. (1985). Reference crop evapotranspiration from temperature. *Applied engineering in agriculture*, *1*(2), 96-99.

Hassan, I., Kalin, R. M., White, C. J., & Aladejana, J. A. (2020). Evaluation of daily gridded meteorological datasets over the Niger Delta region of Nigeria and implication to water resources management. *Atmospheric and Climate Sciences*, *10*(1), 21-39.

Hirsch, R. M., Slack, J. R., & Smith, R. A. (1982). Techniques of trend analysis for monthly

water quality data. *Water resources research*, *18*(1), 107-121

Ho, S., Tian, L., Disse, M., & Tuo, Y. (2021). A new approach to quantify propagation time from meteorological to hydrological drought. *Journal of hydrology, 603*, 127056. https://doi.org/10.1016/j.jhydrol.2021.127056

Hoerling, M., Hurrell, J. W., Eischeid, J., & Phillips, A. S. (2006). Detection and attribution of twentieth-century northern and southern African rainfall change. *J Clim 19*,3989–4008. https://doi.org/10.1175/JCLI3842.1

Im, E. S., Pal, J. S., & Eltahir, E. A. (2017). Deadly heat waves projected in the densely populated agricultural regions of South Asia. *Science advances, 3*(8), e1603322.

Intergovernmental Panel on Climate Change (IPCC) (2014). Climate Change 2014: Impacts, Adaptation, and Vulnerability. Part A: Global and Sectoral Aspects. In C. B. Field, V. R. Barros, D. J. Dokken, K. J. Mach, M. D. Mastrandrea, T. E. Bilir, M. Chatterjee, K. L. Ebi, Y. O. Estrada, R. C. Genova, B. Girma, E. S. Kissel, A. N. Levy, S. MacCracken, P. R. Mastrandrea, and L. L. White (Eds.). Cambridge University Press.

Iooss B, Veiga SD, Janon A, Pujol G, Broto wcfB, Boumhaout K, Delage T, Amri RE, Fruth J, Gilquin L, Guillaume J, Herin M, Idrissi MI, Le Gratiet L, Lemaitre P, Marrel A, Meynaoui A, Nelson BL, Monari F, Oomen R, Rakovec O, Ramos B, Roustant O, Sarazin G, Song E, Staum J, Sueur R, Touati T, Verges V, Weber F (2022). sensitivity: Global Sensitivity Analysis of Model Outputs. R package version 1.28.0, https://CRAN.R-roject.org/package=sensitivity

IPCC (2007). Climate Change 2007 - The physical science basis: Working Group I Contribution to the Fourth Assessment Report of the IPCC. In Solomon, S., Qin, D., Manning, M., Chen, Z., Marquis, M., Averyt, B., Tignor, M., Miller, H. L. (Eds.).

Cambridge University Press, Cambridge.

Jin, L., Whitehead, P.G., Addo, K.A., Amisigo, B., Macadam, I., Janes, T., Crossman, J., Nicholls, R.J., McCartney, M. and Rodda, H.J., (2018). Modeling future flows of the Volta River system: Impacts of climate change and socio-economic changes. *Science of the Total Environment*, *637*, 1069-1080.

Jung, J. (2006). *Regional Climate Change and the Impact on Hydrology in the Volta Basin of West Africa* [Doctoral dissertation, Institut für Meteorologie und Klimaforschung Bereich Atmosphärische Umweltforschung (IMK-IFU), Forschungszentrum Karlsruhe in der Helmholtz-Gemeinschaft].

Kang, H., & Sridhar, V. (2017). Combined statistical and spatially distributed hydrological model for evaluating future drought indices in Virginia. *Journal of hydrology*: Regional Studies, *12*(June), 253–272. https://doi.org/10.1016/j.ejrh.2017.06.003

Kasei, R.A., (2009). Modelling impacts of climate change on water resources in the Volta Basin, West Africa [Doctoral dissertation, Rheinischen Friedrich-Wilhelms Universität Bonn], Bonn.

Kelley, M., Schmidt, G. A., Nazarenko, L. S., Bauer, S. E., Ruedy, R., Russell, G. L., ... & Yao, M. S. (2020). GISS-E2. 1: Configurations and climatology. Journal of Advances in Modeling Earth Systems, 12(8), e2019MS002025. https://doi.org/10.1029/2019MS002025

Kendall, M. (1975). *Multivariate analysis*. Charles Griffin.

Knoben, W. J., Freer, J. E., & Woods, R. A. (2019). Inherent benchmark or not? Comparing Nash–Sutcliffe and Kling–Gupta efficiency scores. *Hydrology and Earth System Sciences*, *23*(10), 4323-4331.

Knutti, R., & Sedláček, J. (2013). Robustness and uncertainties in the new CMIP5 climate

model projections. *Nature Climate Change*, *3*(4), 369-373.

Kossi, A., Towanou, H., Habou, R., Novinyo, S. K., Elikplim, A. K., Nathalie, J. B., ... & Ali, M. (2019). Challenges of conservation and sustainable management of African rosewood (*Pterocarpus erinaceus*) in West Africa. In E. R. Rhodes & H. Naser (eds.), *Natural Resources Management and Biological Sciences* (289-316). IntechOpen. http://dx.doi.org/10.5772/intechopen.88796

Kunstmann, H., & Jung, G. (2005). Impact of regional climate change on water availability in the Volta basin of West Africa. In *Regional Hydrological Impacts of Climatic Variability and Change* (pp. 75-85). Symposium S6 held during the Seventh International Association of Hydrological Sciences Scientific Assembly at Foz do Iguaçu, April 2005, Volume 295. IAHS Publication, Brazil. https://www.academia.edu/download/30692044/Kunstmann_jung_2005.pdf

Lawanson, O. I., Proverbs, D., & Ibrahim, R. L. (2023). The impact of flooding on poor communities in Lagos State, Nigeria: The case of the Makoko urban settlement. *Journal of Flood Risk Management, 16*(1), e12838. https://doi.org/10.1111/jfr3.12838

Lawrence, D., & Vandecar, K. (2015). Effects of tropical deforestation on climate and agriculture. *Nature Clim Change, 5*, 27–36. https://doi.org/10.1038/nclimate2430

Le, P. V., Phan-Van, T., Mai, K. V., & Tran, D. Q. (2019). Space–time variability of drought over Vietnam. *International journal of climatology, 39*(14), 5437-5451.

Lehner, B., Verdin, K., Jarvis, A. (2008). New global hydrography derived from spaceborne elevation data. *Eos, Transactions, American Geophysical Union, 89*(10), 93–94. https://doi.org/10.1029/2008eo100001

Leng, G., Tang, Q., & Rayburg, S. (2015). Climate change impacts on meteorological,

agricultural and hydrological droughts in China. *Global and Planetary Change, 126,* 23-34.

Leroux, L., Baron, C., Zoungrana, B., Traoré, S. B., Seen, D. Lo & Bégué, A. (2016). Crop Monitoring Using Vegetation and Thermal Indices for Yield Estimates: Case Study of a Rainfed Cereal in Semi-Arid West Africa. *IEEE Journal of Selected Topics in Applied Earth Observations and Remote Sensing, 9*(1), 347-362.

Li, C., Sinha, E., Horton, D. E., Diffenbaugh, N. S., & Michalak, A. M. (2014). Joint bias correction of temperature and precipitation in climate model simulations. *Journal of Geophysical Research: Atmospheres, 119*(23), 13-153.

Li, H., Sheffield, J., & Wood, E. F. (2010). Bias correction of monthly precipitation and temperature fields from Intergovernmental Panel on Climate Change AR4 models using equidistant quantile matching. *Journal of Geophysical Research: Atmospheres, 115*(D10). https://doi.org/10.1029/2009JD012882

Liersch, S., Koch, H., Abungba, J. A., Salack, S., & Hattermann, F. F. (2023). Attributing synergies and trade-offs in water resources planning and management in the Volta River basin under climate change. *Environmental Research Letters, 18*(1), 014032. https://doi.org/10.1088/1748-9326/acad14

Lima, L. S., Coe, M. T., Soares Filho, B. S., Cuadra, S. V., Dias, L. C. P., Costa, M. H., Lima, L. S., & Rodrigues, H. O. (2014). Feedbacks between deforestation, climate, and hydrology in the Southwestern Amazon: Implications for the provision of ecosystem services. *Landscape Ecology 29,* 261-274. https://doi.org/10.1007/s10980-013-9962-1

Limantol, A. M., Larbi, I., Dotse, S. Q., Okafor, G. C., Asare-Nuamah, P., Frimpong, L. K., Alhassan, A. R. M., Angmor, E., Premkumar, J. P. J., Lutterodt, G., Asiamah, T. A,

Atta-Darkwa, T., Kumi, N., & Prempeh, N. A. (2023). An increase in temperature under the shared socioeconomic scenarios in the Volta River Basin, West Africa: implications for economic development. *Journal of Water and Climate Change, 14*(8), 2808-2824. https://doi.org/10.2166/wcc.2023.141

Logah, F. Y., Amisigo, A. B., Obuobie, E., & Kankam-Yeboah, K. (2017). Floodplain hydrodynamic modelling of the Lower Volta River in Ghana. *Journal of hydrology: Regional Studies, 14*, 1-9.

Logah, F. Y., Obuobie, E., Adjei, K. A., Gyamfi, C., & Odai, S. N. (2023). Capability of satellite rainfall products in simulating streamflows in the Black Volta Basin. *Sustainable Water Resources Management, 9*(3), 1-14.

Lovato, T., Peano, D., Butenschön, M., Materia, S., Iovino, D., Scoccimarro, E., ... & Navarra, A. (2022). CMIP6 simulations with the CMCC Earth system model (CMCC-ESM2). *Journal of Advances in Modeling Earth Systems, 14*(3), e2021MS002814. https://doi.org/10.1029/2021MS002814

Mahlalela, P. T., Blamey, R. C., Hart, N. C. G., & Reason, C. J. C. (2020). Drought in the Eastern Cape region of South Africa and trends in rainfall characteristics. *Climate dynamics, 55*, 2743-2759.

Mann, H. B. (1945). Nonparametric tests against trend. *Econometrica: Journal of the Econometric Society*, 245–259.

Martin, N. (2005*). Development of a water balance for the Atankwidi Catchment, West Africa–A case study of groundwater recharge in a semi-arid climate* [Doctoral dissertation, University of Göttingen]. Cuvillier Verlag, Göttingen, Germany. https://cuvillier.de/uploads/preview/public_file/3979/3865378854.pdf

Masih, I., Maskey, S., Mussá, F. E. F., & Trambauer, P. (2014). A review of droughts on

the African continent: a geospatial and long-term perspective. *Hydrology and Earth System Sciences*, *18*(9), 3635-3649.

Masters J. (2013). Top ten global weather events of 2012. Weather Underground. https://www.wunderground.com/blog/JeffMasters/topten-global-weather-events-of-2012.html

McCartney, M., Forkuor, G., Sood, A., Amisigo, B., Hattermann, F., & Muthuwatta, L. (2012). The water resource implications of changing climate in the Volta River Basin. (*IWMI Research Report Vol. 146*), International Water Management Institute, Colombo, Sri Lanka. doi:10.5337/2012.219,

Mechoso, C. R., & Arakawa, A. (2015). General Circulation Models. In G. R. North, J. Pyle, & F. Zhang (Eds.), Encyclopedia of Atmospheric Sciences (Second Edition) (153-160). Academic Press.

Meher-Homji, V. M. 1991. Probable impact of deforestation on hydrological processes. *Climatic Change*, *19*, 163-73. http://ciesin.org/docs/002-159/002-159.html

Meinshausen, M., Nicholls, Z. R., Lewis, J., Gidden, M. J., Vogel, E., Freund, M., ... & Wang, R. H. (2020). The shared socio-economic pathway (SSP) greenhouse gas concentrations and their extensions to 2500. *Geoscientific Model Development*, *13*(8), 3571-3605.

Miao, C., Su, L., Sun, Q., & Duan, Q. (2016). A nonstationary bias-correction technique to remove bias in GCM simulations. *Journal of Geophysical Research: Atmospheres*, *121*(10), 5718-5735.

Mishra, A. K., & Singh, V. P. (2010). A review of drought concepts. *Journal of hydrology*, *391*(1-2), 202-216.

Mishra, A. K., & Singh, V. P. (2011). Drought modeling–A review. *Journal of*

hydrology, 403(1-2), 157-175.

Modarres, R. (2007). Streamflow drought time series forecasting. *Stochastic Environmental Research and Risk Assessment, 21*, 223–233. DOI: 10.1007/s00477-006-0058-1

Mohammed, S., Alsafadi, K., Enaruvbe, G. O., Bashir, B., Elbeltagi, A., Széles, A., ... & Harsanyi, E. (2022). Assessing the impacts of agricultural drought (SPI/SPEI) on maize and wheat yields across Hungary. *Scientific Reports, 12*(1), 8838.

Moriasi, D. N., Arnold, J. G., Van Liew, M. W., Bingner, R. L., Harmel, R. D., & Veith, T. L. (2007). Model evaluation guidelines for systematic quantification of accuracy in watershed simulations. *Transactions of the ASABE, 50*(3), 885-900.

Morris, M. D. (1991). Factorial sampling plans for preliminary computational experiments. *Technometrics, 33*(2), 161-174.

Moulin, C., & Chiapello, I. (2004). Evidence of the control of summer atmospheric transport of African dust over the Atlantic by Sahel sources from TOMS satellites (1979–2000). *Geophysical research letters, 31*(2). https://doi.org/10.1029/2003GL018931

Mul, M., Obuobie, E., Appoh, R., Kankam-Yeboah, K., Bekoe-Obeng, E., Amisigo, B., ... & McCartney, M. (2015). *Water resources assessment of the Volta River Basin* (Report Vol. 166). International Water Management Institute (IWMI), Colombo, Sri Lanka.

Naik, M., & Abiodun, B. J. (2016). Potential impacts of forestation on future climate change in Southern Africa. *International journal of climatology*, *36*(14), 4560-4576.

Navarro-Racines, C., Tarapues, J., Thornton, P., Jarvis, A., & Ramirez-Villegas, J. (2020). High-resolution and bias-corrected CMIP5 projections for climate change impact assessments. *Scientific data, 7*(1), 7.

Ndehedehe, C. E., Awange, J. L., Corner, R. J., Kuhn, M., & Okwuashi, O. (2016). On the potentials of multiple climate variables in assessing the spatio-temporal characteristics of hydrological droughts over the Volta Basin. *Science of The Total Environment, 557,* 819-837.

Neitsch, S. L., Arnold, J. G., Kiniry, J. R., & Williams, J. R. (2011). *Soil and water assessment tool theoretical documentation version 2009* (Texas Water Resources Institute Technical Report No. 406), Texas A & M University System College Station, Texas 77843-2118.

Nicholson, S. E. (1979). Revised rainfall series for the West African subtropics. Monthly *Weather Review, 107*(5), 620-623.

Nicholson, S. E. (2013). The west african sahel: A review of recent studies on the rainfall regime and its interannual variability. *International Scholarly Research Notices: Meteorology, 2013*, 1–32. https://doi.org/10.1155/2013/453521

Nicholson, S. E., & Grist, J. P. (2001). A conceptual model for understanding rainfall variability in the West African Sahel on interannual and interdecadal timescales. *International journal of climatology*: *A Journal of the Royal Meteorological Society, 21*(14), 1733-1757.

Nicholson, S. E., Tucker, C. J., & Ba, M. B. (1998). Desertification, drought, and surface vegetation: An example from the West African Sahel. *Bulletin of the American Meteorological Society, 79*(5), 815-830.

Nikulin, G., Lennard, C., Dosio, A., Kjellström, E., Chen, Y., Hänsler, A., ... & van Meijgaard, E. (2018). The effects of 1.5 and 2 degrees of global warming on Africa in the CORDEX ensemble. *Environmental Research Letters, 13*(6), 065003.

National Oceanic and Atmospheric Administration (NOAA) – National Centers for

Environmental Information (NCEI) (2018). U.S. Billion-Dollar Weather and Climate Disasters. Retrieved from [https://www.ncdc.noaa.gov/billions/events/US/2012]

Nobre, C. A., Marengo, J. A., Seluchi, M. E., Cuartas, L. A., Alves, L. M. (2016). Some characteristics and impacts of the drought and water crisis in southeastern Brazil during 2014 and 2015. *J Water Res Prot, 8,* 252–262

Nosrati, K., Eslamian, S., Shahbazi, A., Ostad-Ali-Askari, K., & Singh, V. (2018). Climate Impact on Hydrological Drought. *International Journal of Civil Engineering, 4*, 9–13. https://doi.org/10.20431/2454-8693.0404002

Nossent, J., Elsen, P., & Bauwens, W. (2011). Sobol' sensitivity analysis of a complex environmental model. *Environmental Modelling & Software, 26*(12), 1515-1525.

Obuobie, E. (2008). *Estimation of groundwater recharge in the context of future climate change in the White Volta River Basin, West Africa* [Doctoral dissertation, University of Bonn].

Obuobie, E., Barry, B., & Agyekum, W. (2016). Groundwater resources of the Volta Basin. In T. O. Williams, M. Mul,, C. A. Biney & V. Smakhtin (eds.), *The Volta River Basin* (46-61). Routledge.

Obuobie, E., Amisigo, B., Logah, F., & Kankam-Yeboah, K. (2017). Analysis of changes in downscaled rainfall and temperature projections in the Volta River Basin. In Y. Ntiamoa-Baidu, B. Y. Ampomah & E. A. Ofosu (eds.), *Dams, Development and Downstream Communities: Implications for Re-optimising the Operations of the Akosombo and Kpong Dams in Ghana*, 157-184.

Ofori-Sarpong, E. (1986). The 1981–1983 drought in Ghana. *Singapore journal of tropical geography, 7*(2), 108-127.

Ogunrinde, A. T., Olasehinde, D. A., & Olotu, Y. (2020). Assessing the sensitivity of

standardized precipitation evapotranspiration index to three potential evapotranspiration models in Nigeria. *Scientific African, 8,* e00431. https://doi.org/10.1016/j.sciaf.2020.e00431

Oguntunde, P. G. (2004). Evapotranspiration and complementarity relations in the water balance of the Volta Basin: Field measurements and GIS-based regional estimates. *Ecology and Development Series* (No. 22). Cuvillier Verlag.

Oguntunde, P. G., Friesen, J., van de Giesen, N., & Savenije, H. H. (2006). Hydroclimatology of the Volta River Basin in West Africa: Trends and variability from 1901 to 2002. *Physics and Chemistry of the Earth, Parts a/b/c*, *31*(18), 1180-1188.

Oguntunde, P. G., Abiodun, B. J., & Lischeid, G. (2017). Impacts of climate change on hydro-meteorological drought over the Volta Basin, West Africa. *Global and Planetary Change, 155*, 121-132.

Oguntunde, P. G., Abiodun, B. J., Lischeid, G., & Abatan, A. A. (2020). Droughts projection over the Niger and Volta River basins of West Africa at specific global warming levels. *International journal of climatology*, *40*(13), 5688-5699.

Okafor, G., Annor, T., Odai, S., & Agyekum, J. (2019). Volta basin precipitation and temperature climatology: evaluation of CORDEX-Africa regional climate model simulations. *Theoretical and Applied Climatology*, *137*, 2803-2827.

Omotosho, J. B., & Abiodun, B. J. (2007). A numerical study of moisture build-up and rainfall over West Africa. *Meteorological Applications*: *A journal of forecasting, practical applications, training techniques and modelling, 14*(3), 209-225.

Ouedraogo, I., Tigabu, M., Savadogo, P., Compaoré, H., Odén, P. C., & Ouadba, J. M. (2010). Land cover change and its relation with population dynamics in Burkina Faso,

West Africa. *Land Degradation and Development, 21*(5), 453–462. https://doi.org/10.1002/ldr.981

Pattnayak KC, Gloor E, Tindall JC, Brienen RJW, Barichivich J, Baker JCA, Spracklen DV, Cintra BBL, Coelho CAS (2018) Adding new evidence to the attribution puzzle of the recent water shortage over Sao Paulo (Brazil). *Tellus a: Dyn Meteorol Oceanograp 70*(1):1–14

Peirce, A. M., Espira, L. M., & Larson, P. S. (2022). Climate change related catastrophic rainfall events and non-communicable respiratory disease: a systematic review of the literature. *Climate, 10*(7), 101. https://doi.org/10.3390/cli10070101

Pienaar, L. O. U. W., & Boonzaaier, J. O. H. A. N. N. (2018). Drought policy brief Western cape agriculture. *Western Cape Department of Agriculture (WCDoA) and the Bureau for Food and Agricultural Policy (BFAP),* Elsenburg.

Reinhart, V., Fonte, C. C., Hoffmann, P., Bechtel, B., Rechid, D., & Böhner, J. (2021). Comparison of ESA climate change initiative land cover to CORINE land cover over Eastern Europe and the Baltic States from a regional climate modeling perspective. *International Journal of Applied Earth Observation and Geoinformation, 94*, 102221. doi:10.1016/j.jag.2020.102221

Rouault, M., & Richard, Y. (2005). Intensity and spatial extent of droughts in southern Africa. *Geophysical research letters, 32*, 2–51. https://doi.org/10.1029/2005GL022436

Rummukainen, M. (2012). Changes in climate and weather extremes in the 21st century. *Wiley Interdisciplinary Reviews: Climate Change, 3*(2), 115-129.

Salvi, K., Kannan, S., & Ghosh, S. (2011, September*). Statistical downscaling and bias-correction for projections of Indian rainfall and temperature in climate change*

studies. 4th International Conference on Environmental and Computer Science (Vol. 19, 16-18).

Sandwidi, W. J. P. (2007). Groundwater potential to supply population demand within the Kompienga dam basin in Burkina Faso (Doctoral dissertation, University of Bonn).

Saulnier, D. D., Hanson, C., Ir, P., Mölsted Alvesson, H., & Von Schreeb, J. (2018). The effect of seasonal floods on health: analysis of six years of national health data and flood maps. *International journal of environmental research and public health, 15*(4), 665. https://doi.org/10.3390/ijerph15040665

Seland, Ø., Bentsen, M., Olivié, D., Toniazzo, T., Gjermundsen, A., Graff, L. S., ... & Schulz, M. (2020). Overview of the Norwegian Earth System Model (NorESM2) and key climate response of CMIP6 DECK, historical, and scenario simulations. *Geoscientific Model Development*, *13*(12), 6165-6200. https://doi.org/10.5194/gmd-13-6165-2020

Sen, P.K. (1968). Estimates of the regression coefficients based on Kendall's tau. *Journal of the American Statistical Association, 63*(324), 1379–1389. doi: 10.1080/01621459.1968.10480934

Shahbazi, A. N. (2015). Climate change impact on meteorological droughts in watershed scale (case study: southwestern Iran). *International Journal of Engineering & Technology, 4*(1), 1.

Sheffield, J., & Wood, E. F. (2008). Projected changes in drought occurrence under future global warming from multi-model, multi-scenario, IPCC AR4 simulations. *Climate dynamics*, *31*(1), 79-105.

Sheffield, J., Goteti, G., & Wood, E. F. (2006). Development of a 50-year high-resolution global dataset of meteorological forcings for land surface modeling. *Journal of*

Climate, *19*(13), 3088-3111.

Sheil, D., & Murdiyarso, D. (2009). How Forests Attract Rain: An Examination of a New Hypothesis. *BioScience, 59*, 341–347. https://doi.org/10.1525/bio.2009.59.4.12

Shiru, M. S., Shahid, S., Dewan, A., Chung, E. S., Alias, N., Ahmed, K., & Hassan, Q. K. (2020). Projection of meteorological droughts in Nigeria during growing seasons under climate change scenarios. *Scientific reports*, *10*(1), 10107.

Shukla, S., & Wood, A. W. (2008). Use of a standardized runoff index for characterizing hydrologic drought. *Geophysical research letters*, *35*(2), 1-7. https://doi.org/10.1029/2007GL032487

Sivakumar, M., Stone, R., Sentelhas, P. C., Svoboda, M., Omondi, P., Sarkar, J., & Wardlow, B. (2011). *Agricultural drought indices: summary and recommendations*. In Agricultural drought indices Proceedings of an expert meeting (2-4).

Sultan, B., & Gaetani, M. (2016). Agriculture in West Africa in the Twenty-First Century: Climate Change and Impacts Scenarios, and Potential for Adaptation. *Frontiers in Plant Science, 7*, 1262. doi: 10.3389/fpls.2016.01262

Swart, N. C., Cole, J. N., Kharin, V. V., Lazare, M., Scinocca, J. F., Gillett, N. P., ... & Winter, B. (2019). The Canadian earth system model version 5 (CanESM5.0.3). *Geoscientific Model Development*, *12*(11), 4823-4873. https://doi.org/10.5194/gmd-12-4823-2019

Sylla, M. B., Elguindi, N., Giorgi, F., & Wisser, D. (2016). Projected robust shift of climate zones over West Africa in response to anthropogenic climate change for the late 21st century. *Climatic Change*, *134*(1-2), 241-253.

Sylla, M. B., Faye, A., Klutse, N. A. B., & Dimobe, K. (2018). Projected increased risk of water deficit over major West African river basins under future climates. *Climatic*

Change, *151*(2), 247-258.impacts

Tabrizi, A. A., Khalili, D., Kamgar-Haghighi, A. A., & Zand-Parsa, S. (2010). Utilization of Time-Based Meteorological Droughts to Investigate Occurrence of Streamflow Droughts. *Water Resour Manage, 24*, 4287–4306. https://doi.org/10.1007/s11269-010-9659-z

Takata, K., & Hanasaki, N. (2020). The effects of afforestation as an adaptation option: A case study in the upper Chao Phraya River basin. *Environmental Research Letters, 15*(4). https://doi.org/10.1088/1748-9326/ab7462

Taylor, J. C., van de Giesen, N., & Steenhuis, T. S. (2006). West Africa: Volta discharge data quality assessment and use 1. *JAWRA Journal of the American Water Resources Association*, *42*(4), 1113-1126.

Tebaldi, C., Ranasinghe, R., Vousdoukas, M., Rasmussen, D. J., Vega-Westhoff, B., Kirezci, E., ... & Mentaschi, L. (2021). Extreme sea levels at different global warming levels. *Nature Climate Change*, *11*(9), 746-751.

Telesca, L., Lovallo, M., Lopez-Moreno, I. &Vicente-Serrano, S. (2012). Investigation of scaling properties in monthly streamflow and Standardized Streamflow Index time series in the Ebro Basin (Spain). *Physica A: Statistical Mechanics and its Applications, 391*(4): 1662–1678. DOI: 10.1016/j.physa.2011.10.023

Tew, Y. L., Tan, M. L., CHUN, K. P., Samat, N., & Mahamud, M. A. (2022). Analysis of the relationship between climate change and land use change using the ESA CCI land cover maps in Sungai Kelantan basin, Malaysia. *Sains Malays, 51*(2), 437-449.

Thrasher, B., Wang, W., Michaelis, A., Melton, F., Lee, T., & Nemani, R. (2022). NASA global daily downscaled projections, CMIP6. *Scientific data*, *9*(1), 262. https://doi.org/10.1038/s41597-022-01393-4

Torrence, C., & Compo, G. P. (1998). A practical guide to wavelet analysis. *Bulletin of the American Meteorological society, 79*(1), 61-78.

Ujeneza, E. L., & Abiodun, B. J. (2015). Drought regimes in Southern Africa and how well GCMs simulate them. *Climate dynamics*, *44*(5), 1595-1609.

United Nations Convention to Combat Desertification (2022). Drought in numbers 2022: Restoration for readiness and resilience. Retrieved on [04 July 2023] from [https://www.unccd.int/resources/publications/drought-numbers]

United Nations Department of Economic and Social Affairs, Population Division (2022). World Population Prospects 2022, Online Edition. Retrieved from [https://population.un.org/wpp/]

United Nations Environment Program – Global Environment Facility (UNEP-GEF) Volta Project (2013). Volta Basin Trans-Boundary Diagnostic Analysis. *UNEP/GEF/Volta/RR4/2013*. UNION Publishing: Nairobi

Van De Giesen, N., Liebe, J., & Jung, G. (2010). Adapting to climate change in the Volta Basin, West Africa. *Current Science*, *98*(8), 1033-1037.

van Eeden, L. M., Nimmo, D. G., Mahony, M., Herman, K., Ehmke, G., Driessen, J., O'Connor, J., Bino, G., Taylor, M., & Dickman, C. R. (2020). *Impacts of the unprecedented 2019-2020 bushfires on Australian animals* (Report prepared for WWF-Australia), WWF-Australia. DOI: 10.13140/RG.2.2.16157.74726

van Loon, A. F. (2015). Hydrological drought explained. Wiley Interdisciplinary Reviews: *Water*, *2*(4), 359-392.

Vicente-Serrano, S. M., Beguería, S., & López-Moreno, J. I. (2010). A multiscalar drought index sensitive to global warming: the standardized precipitation evapotranspiration index. *Journal of Climate*, *23*(7), 1696-1718.

Vicente-Serrano, S. M., López-Moreno, J. I., Beguería, S., Lorenzo-Lacruz, J., Azorin-Molina, C., & Morán-Tejeda, E. (2012). Accurate computation of a streamflow drought index. *Journal of Hydrologic Engineering, 17*(2), 318-332.

Volta Basin Authority (VBA) (2010). Strategic plan 2010-2014. VBA, Ouagadougou. http://www.gefvolta.iwlearn.org/project-resources/studies-reports/vba-strategic-plan/vba-strategic-plan-final-english

Wang, A., & Solomatine, D. P. (2019). Practical Experience of Sensitivity Analysis: Comparing Six Methods, on Three Hydrological Models, with Three Performance Criteria. *Water, 11*(5), 1062. http://dx.doi.org/10.3390/w11051062

Wang, A., Lettenmaier, D. P., & Sheffield, J. (2011). Soil moisture drought in China, 1950–2006. *Journal of Climate*, *24*(13), 3257-3271.

Wilhite, D. A., & Pulwarty, R. S. (2017). Drought and water crises: Lessons drawn, some lessons learned, and the road ahead. *In Drought and Water Crises* (515-528). CRC Press.

Williams, T. O., Mul, M., Biney, C. A., & Smakhtin, V. (Eds.). (2016). *The Volta River Basin: Water for food, economic growth and environment.* London, UK: Routledge. https://doi.org/10.4324/9781315707334

Williams, K. D., Copsey, D., Blockley, E. W., Bodas-Salcedo, A., Calvert, D., Comer, R., ... & Xavier, P. K. (2018). The Met Office global coupled model 3.0 and 3.1 (GC3. 0 and GC3. 1) configurations. *Journal of Advances in Modeling Earth Systems, 10*(2), 357-380. https://doi.org/10.1002/2017MS001115

Wintle, B. A., Legge, S., & Woinarski, J. C. (2020). After the megafires: What next for Australian wildlife? *Trends in Ecology & Evolution, 35*(9), 753-757.

Wu, T., Lu, Y., Fang, Y., Xin, X., Li, L., Li, W., ... & Liu, X. (2019). The Beijing Climate

Center climate system model (BCC-CSM): The main progress from CMIP5 to CMIP6. *Geoscientific Model Development*, *12*(4), 1573-1600. https://doi.org/10.5194/gmd-12-1573-2019

Yang, B., Kang, S., Ljungqvist, F. C., He, M., Zhao, Y., & Qin, C. (2014). Drought variability at the northern fringe of the Asian summer monsoon region over the past millennia. *Climate Dynamics*, 43(3-4), 845-859. https://doi.org/10.1007/s00382-013-1962-y

Yeboah, K.A., Akpoti, K., Kabo-bah, A.T., Ofosu, E.A., Siabi, E.K., Mortey, E.M. and Okyereh, S.A., (2022). Assessing climate change projections in the Volta Basin using the CORDEX-Africa climate simulations and statistical bias-correction. *Environmental Challenges*, *6*, 100439. https://doi.org/10.1016/j.envc.2021.100439

Yevjevich, V. M. (1967). Objective approach to definitions and investigations of continental hydrologic droughts (Doctoral dissertation, Colorado State University).

Yin, J., He, F., Xiong, Y. J., & Qiu, G. Y. (2017). Effects of land use/land cover and climate changes on surface runoff in a semi-humid and semi-arid transition zone in northwest China. *Hydrology and Earth System Sciences*, *21*(1), 183-196.

Yuan, F., Ma, M., Ren, L., Shen, H., Li, Y., Jiang, S., ... & Kong, H. (2016). Possible future climate change impacts on the hydrological drought events in the Weihe River basin, China. *Advances in Meteorology*, *2016*, 1-14.

Yue, S., & Wang, C. (2004). The Mann-Kendall test modified by effective sample size to detect trend in serially correlated hydrological series. *Water resources management*, *18*(3), 201-218.

Yukimoto, S., Kawai, H., Koshiro, T., Oshima, N., Yoshida, K., Urakawa, S., ... & Ishii, M. (2019). The Meteorological Research Institute Earth System Model version 2.0,

MRI-ESM2. 0: Description and basic evaluation of the physical component. *Journal of the Meteorological Society of Japan. Ser. II*, *97*(5), 931-965. https://doi.org/10.2151/jmsj.2019-051

Zhang, J., Li, L., Wu, Z., & Li, X. (2015a). Prolonged dry spells in recent decades over north-central China and their association with a northward shift in planetary waves. *International journal of climatology*, *35*(15), 4829-4842.

Zhang, L., Nan, Z., Xu, Y., & Li, S. (2016). Hydrological impacts of land use change and climate variability in the headwater region of the Heihe River Basin, Northwest China. *PloS one, 11*(6), e0158394. https://doi.org/10.1371/journal.pone.0158394

Zhang, X. Y., Trame, M. N., Lesko, L. J., & Schmidt, S. (2015b). Sobol sensitivity analysis: a tool to guide the development and evaluation of systems pharmacology models. *CPT: pharmacometrics & systems pharmacology*, *4*(2), 69-79.

Zhiña, D., Montenegro, M., Montalván, L., Mendoza, D., Contreras, J., Campozano, L., & Avilés, A. (2019). Climate change influences of temporal and spatial drought variation in the Andean High Mountain basin. *Atmosphere*, *10*(9), 558. https://doi.org/10.3390/atmos10090558

Zhou, T., Song, F., & Chen, X. (2013). Historical evolution of global and regional surface air temperature simulated by FGOALS-s2 and FGOALS-g2: How reliable are the model results? *Advances in Atmospheric Sciences*, *30*, 638-657. https://doi.org/10.1007/s00376-013-2205-1

APPENDICES

APPENDIX 1: Map of Volta River Basin indicating the main subbasins (Black Volta, White Volta, Oti and Lower Volta Basins)

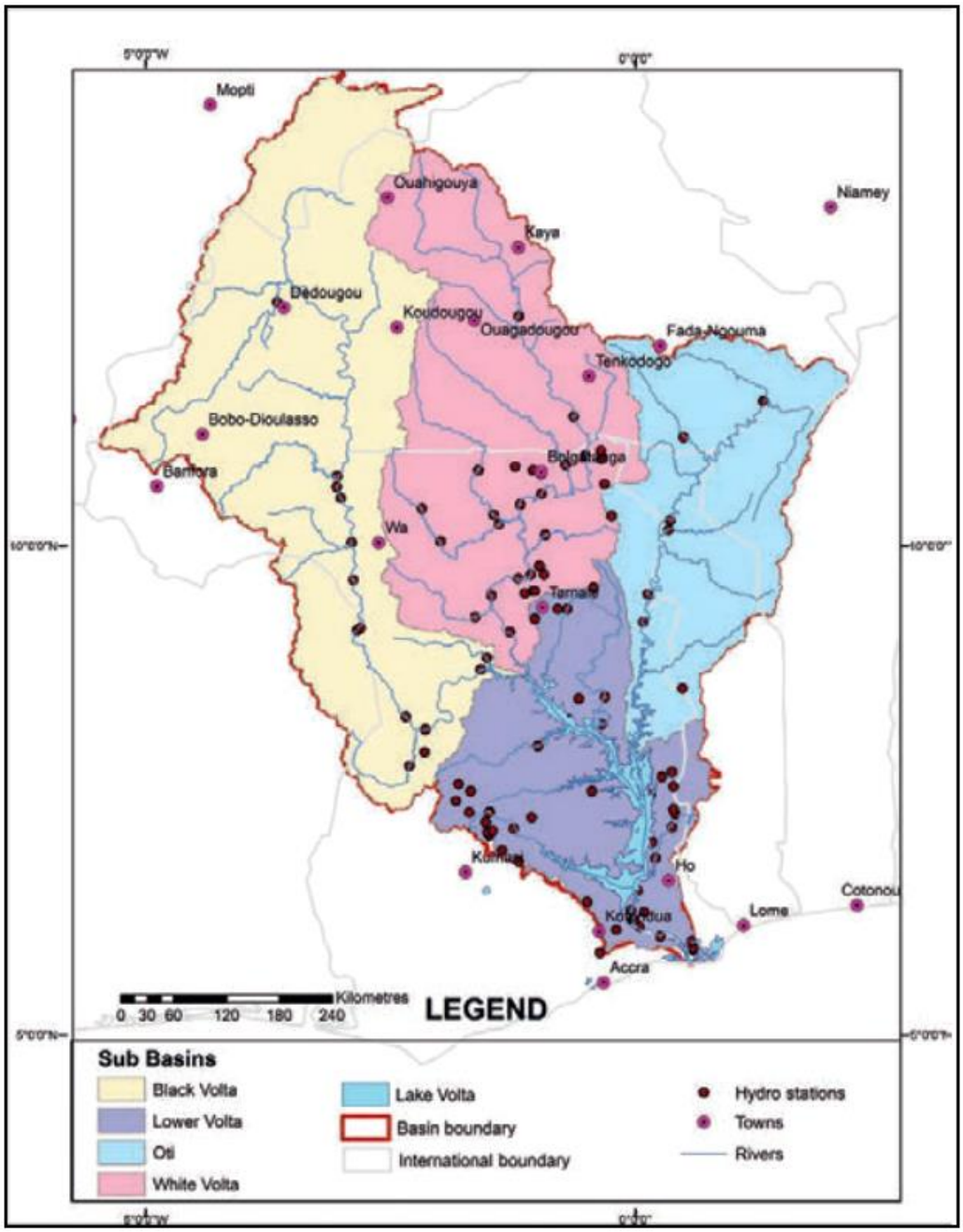

Source: Williams *et al*. (2016)

APPENDIX 2: Soil types and characteristics of the Volta River Basin

Dominant Soil Group	Soil Name	Sub_Type	No. LAYERS	Hydrological Group	TEXTURE	Area	Area (km^2)	Area Percentage (%)
Acrisols	Af18-1a-1024	Ferric	2	C	SANDY_LOAM	333.89		
	Af2-1025	Ferric	2	C	SANDY_CLAY_LOAM	1602.65		
	Ao10-1a-1048	Orthic	2	C	SANDY_LOAM	200.33		
	Ao11-b-1051	Orthic	2	D	LOAM	333.89		
	Ao13-1052	Orthic	2	D	LOAM	66.78	7479.05	1.81
	Ao1-ab-1046	Orthic	2	D	SANDY_CLAY_LOAM	1535.88		
	Ao46-a-1058	Orthic	2	C	SANDY_CLAY_LOAM	1335.54		
	Ao59-a-1063	Orthic	2	C	SANDY_CLAY_LOAM	1201.99		
	Ap22-2a-1074	Plinthic	2	C	SANDY_CLAY_LOAM	868.1		
Cambisols	Be1-1081	Eutric	2	D	LOAM	667.77		
	Be25-1083	Eutric	2	D	CLAY_LOAM	6744.5		
	Be42-2-3b-1093	Eutric	2	D	CLAY_LOAM	267.11		
	Be7-1b-1096	Eutric	2	C	SANDY_LOAM	400.66		
	Bf5-2-3ab-1102	Ferralic	2	C	CLAY_LOAM	333.89	12353.78	3
	Bv2-1138	Vertic	2	D	CLAY	1602.65		
	Bv2-3a-1140	Vertic	2	D	CLAY	1068.44		
	Bv3-1141	Vertic	2	D	CLAY	267.11		
	Bv6-1145	Vertic	2	D	CLAY	1001.66		
Gleysols	G1-3a-1192		2	C	CLAY	801.33		
	G4-a-1198		2	C	LOAM	600.99		
	G5-a-1199		2	D	CLAY_LOAM	1001.66	2604.31	0.63
	G6-a-1200		2	C	LOAM	200.33		
Lithosols	I-60		2	C	LOAM	1736.21		
	I-Ao-1227	Orthic Cambisols	2	D	LOAM	4540.85	41268.3	10.01
	I-b-1323		2	C	LOAM	2203.65		

Dominant Soil Group	Soil Name	Sub_Type	No. LAYERS	Hydrological Group	TEXTURE	Area	Area (km^2)	Area Percentage (%)
	I-Be-1230	Eutric Cambisols	2	D	LOAM	267.11		
	I-Be-a-1232	Eutric Cambisols	2	D	LOAM	9081.7		
	I-G-1253	Gleysols	2	C	LOAM	1535.88		
	I-Lf-1255	Ferric Luvisols	2	C	SANDY_CLAY_LOAM	1068.44		
	I-Lf-c-1270	Ferric Luvisols	2	C	SANDY_CLAY_LOAM	3272.08		
	I-Lf-Lp-1257	Ferric Luvisols	2	D	SANDY_CLAY_LOAM	801.33		
	I-Lf-Rd-1264	Ferric Luvisols-Dystric Regosols	2	D	LOAM	13088.33		
	I-Rd-79	Dystric Regosols	2	D	LOAM	200.33		
	I-Re-b-1294	Eutric Regosols	2	C	LOAM	2604.31		
	I-Ws-1298	Solodic Planosols	2	D	LOAM	868.1		
Fluvisols	J2-a-1327		2	C	LOAM	5075.07	5676.06	1.38
	Je1-1359	Eutric	2	C	LOAM	600.99		
Luvisols	Lf1-1a-1423	Ferric	2	C	LOAMY_SAND	3472.41		
	Lf1-1a-1424	Ferric	2	C	LOAMY_SAND	11151.79		
	Lf12-1a-1427	Ferric	2	C	SANDY_LOAM	734.55		
	Lf12-a-1429	Ferric	2	C	SANDY_CLAY_LOAM	267.11	5742.84	1.39
	Lf12-b-1431	Ferric	2	C	SANDY_CLAY_LOAM	6744.5		
	Lf13-1432	Ferric	2	C	SANDY_CLAY_LOAM	734.55		
	Lf18-1434	Ferric	2	C	SANDY_CLAY_LOAM	3806.3		
	Lf20-1a-1436	Ferric	2	C	SANDY_LOAM	13689.32		

Dominant Soil Group	Soil Name	Sub_Type	No. LAYERS	Hydrological Group	TEXTURE	Area	Area (km^2)	Area Percentage (%)
	Lf25-1438	Ferric	2	C	SANDY_CLAY_LOAM	1135.21		
	Lf26-a-1442	Ferric	2	C	SANDY_CLAY_LOAM	333.89		
	Lf26-a-1443	Ferric	2	C	SANDY_CLAY_LOAM	200.33		
	Lf26-a-1444	Ferric	2	C	SANDY_CLAY_LOAM	17362.07		
	Lf30-132	Ferric	2	C	SANDY_CLAY_LOAM	1135.21		
	Lf30-1a-1450	Ferric	2	C	SANDY_LOAM	3205.31		
	Lf31-a-1453	Ferric	2	C	SANDY_CLAY_LOAM	28113.2		
	Lf32-1a-1457	Ferric	2	C	SANDY_LOAM	600.99		
	Lf32-a-1458	Ferric	2	C	SANDY_CLAY_LOAM	1535.88		
	Lf34-a-1459	Ferric	2	C	SANDY_CLAY_LOAM	2270.42		
	Lf35-1460	Ferric	2	C	SANDY_CLAY_LOAM	4006.63		
	Lf37-1463	Ferric	2	C	SANDY_CLAY_LOAM	4340.52		
	Lf38-1464	Ferric	2	C	SANDY_CLAY_LOAM	133.55		
	Lf41-2a-1469	Ferric	2	C	SANDY_CLAY_LOAM	133.55		
	Lf7-a-1492	Ferric	2	C	SANDY_CLAY_LOAM	9081.7		
	Lf8-a-1494	Ferric	2	C	SANDY_CLAY_LOAM	12954.77		
	Lg10-1499	Gleyic	2	C	SANDY_CLAY_LOAM	66.78		
	Lg1-1495	Gleyic	2	C	SANDY_CLAY_LOAM	1135.21		
	Lg12-1501	Gleyic	2	C	SANDY_CLAY_LOAM	1402.32		
	Lg1-3a-1496	Gleyic	2	C	CLAY	5475.73		
	Lg23-a-1508	Gleyic	2	C	SANDY_CLAY_LOAM	600.99		
	Lg28-1a-1513	Gleyic	2	C	SANDY_LOAM	7479.05		
	Lg3-1a-785	Gleyic	2	C	SANDY_LOAM	1602.65		
	Lg3-2a-786	Gleyic	2	C	SANDY_CLAY_LOAM	4340.52		
	Lg5-2a-1515	Gleyic	2	C	SANDY_CLAY_LOAM	7946.49		
	Lg5-3a-1516	Gleyic	2	C	SANDY_CLAY	2270.42		
	Lg8-1520	Gleyic	2	C	SANDY_CLAY_LOAM	1201.99		
	Lg9-1522	Gleyic	2	C	SANDY_CLAY_LOAM	2537.53		
	Lp10-1a-1527	Plinthic	2	C	SANDY_LOAM	133.55		
	Lp2-1529	Plinthic	2	C	SANDY_CLAY_LOAM	2136.87		
	Lp2-a-1530	Plinthic	2	C	SANDY_CLAY_LOAM	22771.02		

Dominant Soil Group	Soil Name	Sub_Type	No. LAYERS	Hydrological Group	TEXTURE	Area	Area (km^2)	Area Percentage (%)
	Lp3-a-1956	Plinthic	2	D	SANDY_CLAY_LOAM	1068.44		
	Lp4-1532	Plinthic	2	D	SANDY_CLAY_LOAM	3205.31		
	Lp4-1533	Plinthic	2	D	SANDY_CLAY_LOAM	9949.8		
	Lp5-1534	Plinthic	2	D	SANDY_CLAY_LOAM	267.11		
	Lp5-1a-1536	Plinthic	2	C	SANDY_LOAM	17495.62		
	Lp6-1a-1540	Plinthic	2	C	SANDY_LOAM	13221.88		
	Lp7-1541	Plinthic	2	D	SANDY_CLAY_LOAM	5141.84		
	Lp8-1542	Plinthic	2	D	SANDY_CLAY_LOAM	5809.62		
	Lp9-1543	Plinthic	2	D	SANDY_CLAY_LOAM	2537.53		
Nitosols	Nd1-1544	Dystric	2	C	LOAM	1135.21		
	Nd3-1565	Dystric	2	C	LOAM	133.55		
	Nd7-1570	Dystric	2	C	LOAM	2203.65	5742.84	1.39
	Nd9-1574	Dystric	2	C	SANDY_CLAY_LOAM	200.33		
	Ne21-b-1589	Eutric	2	C	LOAM	667.77		
	Ne6-2b-1592	Eutric	2	C	LOAM	1402.32		
Arenosols	Qc1-1598	Cambic	2	B	SAND	2203.65		
	Ql1-1a-1614	Luvic	2	B	SAND	10350.46	13756.1	3.34
	Ql3-1a-1630	Luvic	2	C	SANDY_LOAM	801.33		
	Ql7-1637	Luvic	2	B	LOAMY_SAND	400.66		
Regosols	Rd1-1a-1647	Dystric	2	C	LOAMY_SAND	133.55		
	Re24-1665	Eutric	2	C	LOAM	1602.65		
	Re24-1667	Eutric	2	C	LOAM	333.89		
	Re24-1a-1669	Eutric	2	C	SANDY_LOAM	267.11		
	Re33-1673	Eutric	2	C	SANDY_CLAY_LOAM	1469.1		
	Re33-1674	Eutric	2	C	SANDY_CLAY_LOAM	6343.83	43739.06	10.61
	Re33-1a-1676	Eutric	2	C	SANDY_LOAM	600.99		
	Re33-1a-1677	Eutric	2	C	SANDY_LOAM	17695.95		
	Re34-1a-1680	Eutric	2	C	SANDY_LOAM	3873.08		
	Re35-1a-1684	Eutric	2	C	LOAMY_SAND	2136.87		
	Re35-1a-1685	Eutric	2	C	LOAMY_SAND	2604.31		
	Re36-1a-1687	Eutric	2	C	SANDY_LOAM	6677.72		

Dominant Soil Group	Soil Name	Sub_Type	No. LAYERS	Hydrological Group	TEXTURE	Area	Area (km^2)	Area Percentage (%)
Vertisols	Vc10-1717	Chromic	2	D	CLAY	1001.66		
	Vc11-1718	Chromic	2	D	CLAY	333.89		
	Vc1-1715	Chromic	2	D	CLAY	2403.98		
	Vc12-1719	Chromic	2	D	CLAY	2671.09		
	Vc1-3a-1716	Chromic	2	D	CLAY	868.1	15959.75	3.87
	Vc1-3a-954	Chromic	2	D	CLAY	1736.21		
	Vc4-1726	Chromic	2	D	CLAY	267.11		
	Vc8-1729	Chromic	2	D	CLAY	600.99		
	Vc9-1730	Chromic	2	D	CLAY	6076.72		
Water	WATER-1972		1	D	WATER	11886.34	11886.34	2.88
Planosols	Ws12-1a-1751	Solodic	2	C	SANDY_LOAM	267.11		
	Ws2-1752	Solodic	2	C	LOAM	66.78		
	Ws2-1a-1754	Solodic	2	C	SANDY_LOAM	2136.87		
	Ws4-1757	Solodic	2	D	LOAM	333.89	4874.73	1.18
	Ws4-1a-1758	Solodic	2	C	SANDY_LOAM	267.11		
	Ws6-1760	Solodic	2	D	CLAY_LOAM	934.88		
	Ws6-1a-1761	Solodic	2	D	SANDY_CLAY_LOAM	868.1		

APPENDIX 3: Description of Ghana Meteorological Agency synoptic stations used in this study

Station	Longitude	Latitude
Accra	-0.17	5.65
Ada Foah	0.61	5.79
Akatsi	0.80	6.12
Akim Oda	-0.97	5.93
Akuse	0.12	6.10
Axim	-2.24	4.87
Bole	-2.48	9.03
Kete Krachi	-0.17	7.80
Koforidua	-0.25	6.08
Kumasi	-1.62	6.68
Sunyani	-2.30	7.33
Takoradi	-1.77	4.88
Tamale	-0.85	9.43
Tema	0.02	5.70
Wa	-2.50	10.05
Wenchi	-2.10	7.74
Yendi	-0.02	9.45
Ho	0.48	6.61